eman ta zabal zazu

Universidad del País Vasco
Euskal Herriko Unibertsitatea

Doctoral Thesis

Lipid-protein interactions in autophagy: Exploring the role of LC3/GABARAP-family members

Marina Iriondo Nagore

2022

Supervisors: Prof. Alicia Alonso Izquierdo
Dr. Lidia Ruth Montes Burgos

Universidad del País Vasco Euskal Herriko Unibertsitatea

CSIC

Instituto Biofisika Institutua

eman ta zabal zazu

Universidad del País Vasco Euskal Herriko Unibertsitatea

Doctoral Thesis

Lipid-protein interactions in autophagy: Exploring the role of LC3/GABARAP-family members

Marina Iriondo Nagore

2022

Supervisors: Prof. Alicia Alonso Izquierdo
Dr. Lidia Ruth Montes Burgos

Instituto Biofisika (UPV/EHU, CSIC)

Department of Biochemistry and Molecular Biology

CONTENTS

ABBREVIATIONS

A_{400}	absorbance measured at 400 nm
A_{600}	absorbance measured at 600 nm
AC	alternating current
ACTB/β-actin	actin beta
AIM	Atg8 interacting motif
ALPS	amphipathic lipid packing sensor
AMBRA1	autophagy and beclin 1 regulator 1
Amp	ampicillin
AMPK	AMP-dependent protein kinase
ANTS	8-aminonaphthalene-1,3,6-trisulfonic acid, disodium salt
AP	autophagosome
ATG	autophagy-related
Atg8	autophagy-related 8
ATP	adenosine triphosphate
BAR	Bin–Amphiphysin–Rvs domain
BCA	bicinchoninic acid assay
BCL-2	B-cell CLL/lymphoma 2
BECN1	beclin-1
BEVS	baculovirus expression vector system
BNIP3	BCL-2 interacting protein 3
BSA	bovine serum albumin

CCCP	carbonyl cyanide m-chlorophenyl hydrazone
cDNA	complementary DNA
Cer	ceramide
CHAPS	3-[(3-Cholamidopropyl)dimethylammonio]-1-propanesulfonate
Chol	cholesterol
CL	cardiolipin
Cryo-EM	cryo-electron microscopy
DAG	diacylglycerol
DLS	dynamic light scattering
DMEM	Dulbecco's modified Eagle's medium
DMSO	dimethyl sulfoxide
DNA	deoxyribonucleic acid
DOG	dioleoylglycerol
DOPE	1,2-dioleoyl-sn-glycero-3-phosphoethanolamine
DPX	*p*-xylene-bis-pyridinium bromide
DsDNA	double-stranded DNA
DsRed	*Discosoma* red fluorescent protein
DTT	D,L- dithiothreitol
EBSS	Earle's balanced salt solution
EDTA	ethylenediaminetetraacetic acid
ePC	L-α-phosphatidylcholine from hen egg yolk
ER	endoplasmic reticulum
ESCRT	endosomal sorting complex required for transport
FBS	fetal bovine serum

FCS	Fluorescence correlation spectroscopy
FIP200	focal adhesion kinase family interacting protein of 200 kDa
FKBP8	FKBP prolyl isomerase 8
FRET	Förster resonance energy transfer
FT	flow-through
FYCO1	FYVE and coiled-coil domain containing 1)
GABARAP	GABA type A receptor associated protein
GABARAPL1	GABA type A receptor associated protein like 1
GABARAPL2	GABA type A receptor associated protein like 2
GCS	glucosylceramide synthase
GFP	green fluorescent protein
GIR	galectin-8 interacting region;
GLS	glycolsphingolipid
GST	glutathione S-Transferase
GTP	guanosine triphosphate
GUV	giant unilamellar vesicle
Hepes	2-[4-(2-hydroxyethyl)piperazin-1-yl]ethanesulfonic acid
HII	inverted-hexagonal lipid phase
HIV	human immunodeficiency viruses
HOPS	homotypic fusion and protein sorting
HRP	horseradish peroxidase
IMM	inner mitochondrial membrane
Ip	Input
iPCR	inverse polymerase chain reaction

IPTG	isopropyl-β-D-1-thiogalactopiranoside
ITO	indium–tin–oxide
LAMP2	lysosomal-associated membrane protein 2
LB	Luria Broth or Luria-Bertani medium
LC3A/MAP1LC3A	microtubule associated protein 1 light chain 3 alpha
LC3B/MAP1LC3B	microtubule associated protein 1 light chain 3 beta
LC3C/MAP1LC3C	microtubule associated protein 1 light chain 3 gamma
LIR	LC3-interacting region
Lo	liquid-ordered lamellar lipid phase
LUV	large unilamellar vesicle/s
lysoPC	lysophosphatidylcholine
Lα	fluid, liquid-disordered or liquid-crystalline lamellar lipid phase
Lβ	gel or solid-ordered lamellar lipid phase
Lβ´	oblique Lβ lamellar lipid phase
MLV	multilamellar vesicle
mTORC1	mammalian target of rapamycin complex 1
NBD	7-nitrobenz-2-oxa-1,3-diazol-4-yl
NBD-PE	1,2-dioleoyl-*sn*-glycero-3-phosphoethanolamine-N-(7-nitro-2-1,3-benzoxadiazol-4-yl)
NBDtail-PE	N-(7-nitrobenz-2-oxa-1,3-diazol-4-yl)-1,2-dihexadecanoyl-sn-glycero-3-phosphatidylethanolamine
NME4/NDPK-D/Nm23-H4	NME/NM23 nucleoside diphosphate kinase 4
NRBF2	nuclear receptor-binding factor 2
NTA	nitrilotriacetic acid
O/A	oligomycin A + antimycin A
O/N	overnight

OMM	outer mitochondrial membrane
OPTN	optineurin
PA	phosphatidic acid
PBS	phosphate buffered saline
PC	phosphatidylcholine
PCR	polymerase chain reaction
PE	phosphatidylethanolamine
PEmal	1,2-dioleoyl-sn-glycero-3-phosphatidylethanolamine-p-maleimidomethyl-cyclohexanecarboxamide
PFA	paraformaldehyde
PG	phosphatidylglycerol
PH	pleckstrin homology
PI	liver phosphatidylinositol
PI3K	Phosphatidylinositol 3-kinase
PI3K Vps34	Phosphatidylinositol 3-kinase encoded by the yeast *VPS34* gene
PI3KC1/3	class I or III phosphatidylinositol-3-kinase
PI3P	phosphatidylinositol-3-phosphate
PI4P	phosphatidylinositol-4-phosphate
PINK1	PTEN induced putative kinase 1
PM	Plasma membrane
PROPPIN	*β*-propeller that bind polyphosphoinositides
PS	phosphatidylserine
PtdIns3P	phosphatidylinositol-3-phosphate
PtdIns4P	phosphatidylinositol-4-phosphate
PVDF	polyvinylidene fluoride

PX	Phox homology domain
Rab	Ras-related GTP-binding protein
rBv	recombinant baculovirus
Rho	rhodamine
Rho-PE	1,2-dioleoyl-*sn*-glycero-3-phosphatidylethanolamine-N-lissamine rhodamine B sulfonyl
RNA	ribonucleic acid
ROS	reactive oxygen species
RT	room temperature
SBL	supported bilayer
SDS-PAGE	sodium dodecyl sulfate polyacrylamide gel electrophoresis
siRNA	small interfering RNA
SM	sphingomyelin
SNAP	soluble *N*-ethylmaleimide-Sensitive Factor Attachment Proteins
SNARE	SNAP soluble NSF attachment protein receptor
SUV	small unilamellar vesicle/s
TBST	mixture of Tris-Buffered Saline and Tween 20
TCEP	Tris (2-carboxyethyl) phosphine
Tm	Primer Melting Temperature
Tris	2-Amino-2-(hydroxymethyl)-1,3-propanediol
UBL	ubiquitin-like system
ULK 1/2	Uncoordinated-51 (unc-51)-like kinase 1 or 2
UVRAG	UV-radiation resistance associated gene
WIPI	WD repeat domain phosphoinositide-interacting protein
YFP	Yellow fluorescent protein

INDEX OF FIGURES

CHAPTER 1:

CHAPTER 2:

CHAPTER 3:

CHAPTER 4:

CHAPTER 5:

CHAPTER 6:

INDEX OF TABLES

CHAPTER 1:

CHAPTER 2:

INDEX OF EQUATIONS

CHAPTER 1:

CHAPTER 2:

INDEX OF EXPERIMENTAL PROTOCOLS

CHAPTER 1
INTRODUCTION AND AIMS

CHAPTER 1. Introduction and aims

1.1. Autophagy

1.1.1. History

Autophagy (from the Greek *auto*-, "self" and *phago*, "to eat") is a general biological process conserved among eukaryotes that allows the regulated lysosomal degradation of unnecessary or dysfunctional cellular materials. The term "autophagy" was invented in 1963 by the Nobel Laureate discoverer of lysosomes and peroxisomes, Christian de Duve (De Duve, 1963; Klionsky, 2008). He used it to describe the presence of single- or double-membrane intracellular vesicles (**Figure 1.1**) that contain part of the cytoplasm and organelles in various states of disintegration (Yang & Klionsky, 2010).

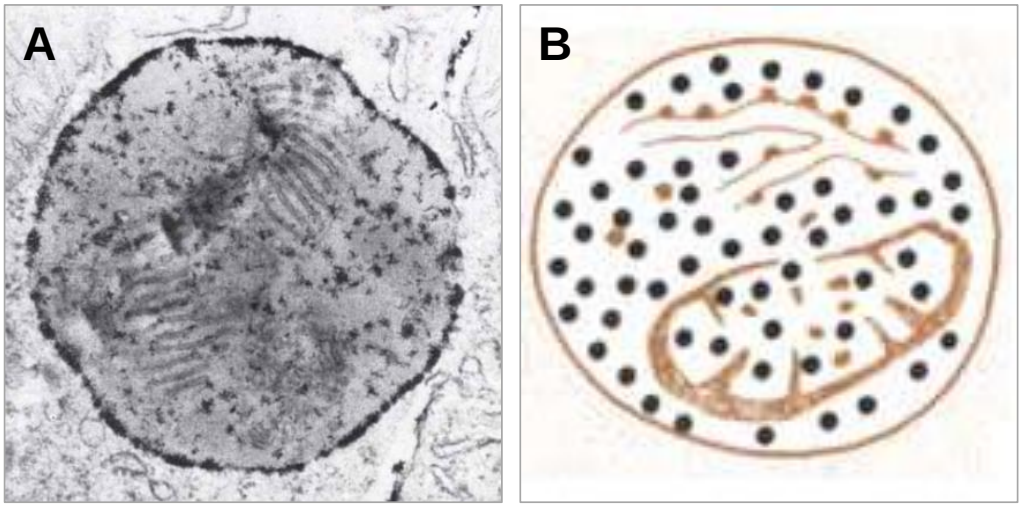

Figure 1.1. The "Autophagic Vacuole". (A) Electron micrograph (Magnification x55000) (**B)** Outline of the residual body. Both taken from De Duve (1963).

However, it was not until the early 1990s when the cell biologist Yoshinori Oshumi identified and characterized the autophagy machinery, AuTophaGy-related (Atg) genes, in yeast (Tsukada & Ohsumi, 1993). For that reason, he was awarded the Nobel Prize in Physiology or Medicine in 2016. Over the past decades, our understanding of the process has made enormous progress (Ohsumi, 2014), not only in terms of the molecular mechanism but also in relation to its physiological roles and relevance to health and disease. The progression shown on **Figure 1.2** has scaled up in the last years with the result that the number of papers associated to autophagy in 2021 was of 10500.

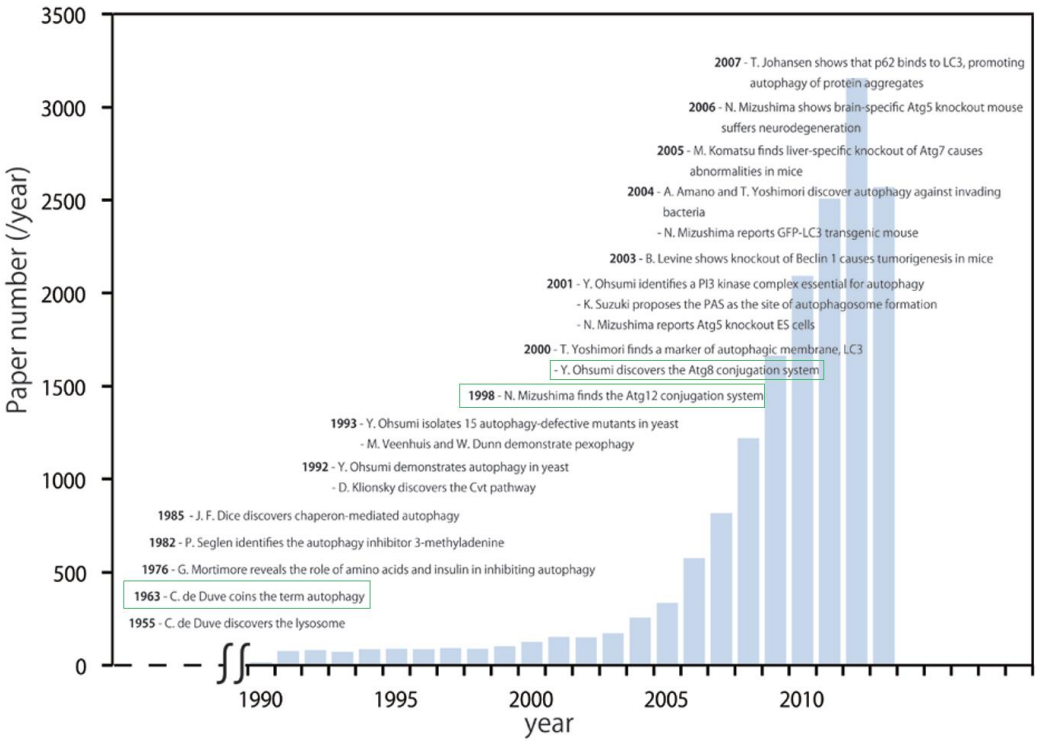

Figure 1.2. The growth of autophagy research and historical landmarks. Taken from Ohsumi (2014).

1.1.2. Autophagy in health and disease

Autophagy is a central regulation point that controls the homeostasis of the human body. It allows cellular maintenance and survival thanks to its ability to promote:

- **survival to environmental challenges,** such as amino acid or nitrogen starvation (Kuma *et al.*, 2004) by the recycling of cellular components that are further used for *de novo* synthesis of cellular building blocks and energy production.
- **response to intracellular challenges,** *e.g.* oxidative or ER stress, for example degradation of ROS producing mitochondria (Scherz-Shouval & Elazar, 2011).
- **cellular preservation,** by clearing defective proteins or organelles, toxic protein aggregates (Ravikumar *et al.*, 2002) or invading intracellular pathogens (Ravenhill *et al.*, 2019), autophagy could work as an anti-aging process.
- **cellular remodeling,** by degradation of cell constituents during development (Yue *et al.*, 2003) and cellular differentiation (Tanida *et al.*, 2006).

Not surprisingly, insufficient or defective autophagy underlies a wide range of pathological conditions (**Figure 1.3**) (Klionsky *et al.*, 2021). Some examples include:

- **neurodegenerative diseases.** Huntington disease (Martinez-Vicente *et al.*, 2010), Alzheimer disease (Nixon *et al.*, 2005) and Parkinson disease (Lynch-Day *et al.*, 2012) are linked to an accumulation of toxic misfolded protein aggregates in the brain that had not been degraded due to an impaired autophagy (Vidal *et al.*, 2014).

- **oncogenesis and cancer.** Impaired autophagy had been found during malignant transformation of cancer cells and deletion of several proteins involved in autophagy had been associated with cancer susceptibility (Levine & Kroemer, 2019). However, autophagy activation could also help in the survival of transformed cells from low-vascularized established tumors, therefore inhibition of autophagy in those cells could block tumor growth (Galluzzi *et al.*, 2015).
- **infectious diseases.** Impaired autophagy promotes the survival of pathogens (bacteria, viruses and parasites), creating a protective environment for them (Deretic, 2011).
- **aging.** Some autophagy-related genes are down-regulated in aging people and most of the proteins whose degradation is hindered during aging have been found to be the substrates of lysosomal degradation (Cuervo *et al.*, 2005).
- **diabetes and obesity.** Increased adiposity and insulin resistance are attributed to defective mitochondria, impaired degradation of mitochondria via autophagy can promote the development of those disorders (Yang *et al*., 2010).
- **lysosomal storage disorders.** Impaired autophagy has been associated to the defective removal of components stored in lysosomes, such as fatty acids or cholesterol (Settembre *et al.*, 2008).

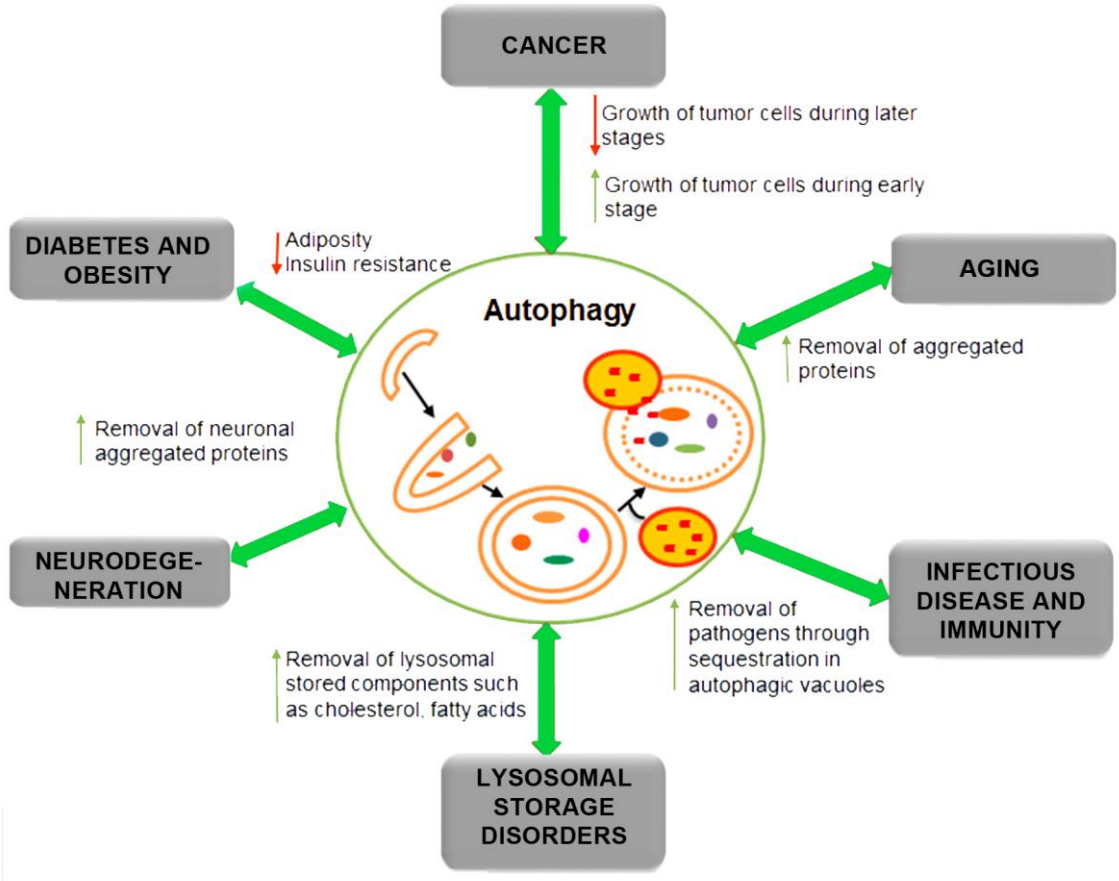

Figure 1.3. Autophagy in health and disease. Adapted from Saha *et al*. (2018).

Nowadays, pharmacological agents or dietary interventions that activate or inhibit autophagy have a great potential as novel therapies for multiple human disorders and pathophysiological conditions (Galluzzi *et al.*, 2017).

1.1.3. Types of autophagy

Three different types of autophagy have been described in mammalian cells (Okamoto, 2014) (**Figure 1.4**):

a) **macroautophagy** is the main autophagic pathway, occurring mainly to eradicate damaged cell organelles or unused proteins. This involves the formation of a double membrane around cytoplasmic substrates resulting in the organelle known as autophagosome. The autophagosome travels through the cytoplasm to a lysosome, and the two organelles fuse; intersection with endosomal pathways also occurs. Within the lysosome, the contents of the autophagosome are degraded via acidic lysosomal hydrolases. This pathway is conserved from yeast to humans.

b) **microautophagy** involves the direct engulfment of cytoplasmic material by the lysosome. This occurs by invagination, meaning the inward folding of the lysosomal membrane. It is also conserved from yeast to humans.

c) **chaperone-mediated autophagy** refers to the chaperone-dependent selection of soluble cytosolic proteins that are then targeted to a lysosome and directly translocated across the lysosomal membrane for degradation. It is only found in mammals and contributes to the regulation of cellular metabolism.

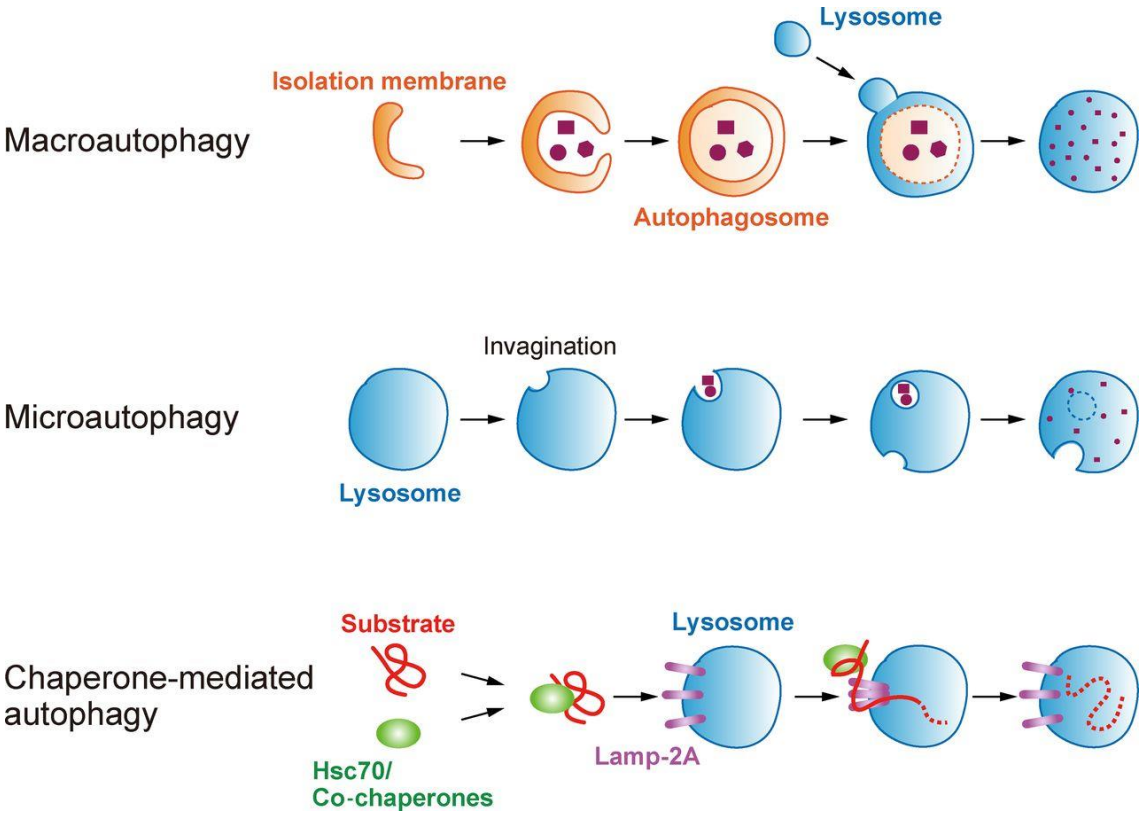

Figure 1.4. Types of autophagy. Taken from Okamoto (2014).

Autophagy can also be classified into selective or bulk autophagy (**Figure 1.5**), depending on whether there are signals to degrade a specific cellular component or else it is a bulk process. This is particularly important for the cell when only some specific organelles are damaged (Sica *et al.*, 2015).

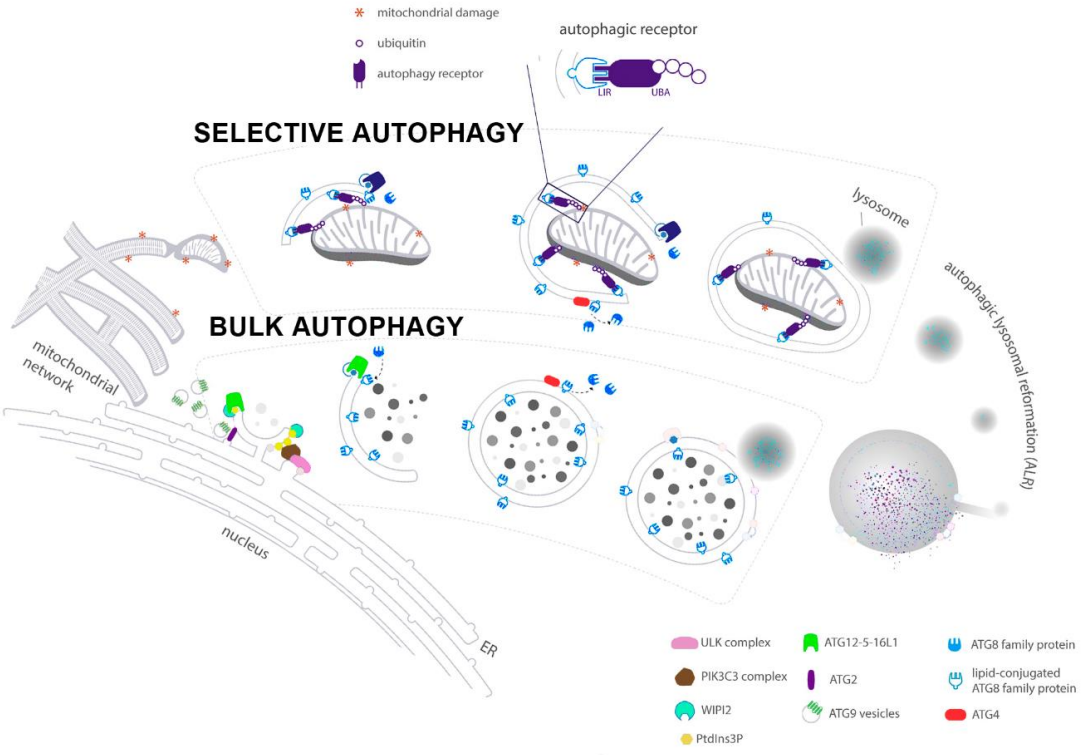

Figure 1.5. Selective and bulk autophagy. Adapted from de la Ballina *et al*. (2020).

Selective autophagy refers to turnover of specific cargo, such as superfluous or dysfunctional organelles, protein aggregates or invading pathogens (Levine & Kroemer, 2019). Cargo degradation relies on signals and receptors, that allow the interaction between cargo and autophagosomal membrane (Galluzzi *et al.*, 2017). As discussed in Chapter 3, the main proteins bridging between cargo and autophagosome during cargo recognition are the LC3/GABARAP proteins. Many types of selective autophagy have been described, for instance, mitochondria (mitophagy), peroxisome (pexophagy), lipid droplets (lipophagy), nucleus (nucleophagy), lysosome (lysophagy), ER (reticulophagy), ribosomes (ribophagy), proteasomes (proteaphagy), protein aggregates (aggrephagy), or bacteria or viruses (xenophagy).

This thesis is devoted to the process of autophagosome biogenesis and cargo recognition during the selective macroautophagy of mitochondria (mitophagy), thus in the context of this work, autophagy is to be understood as macroautophagy, the most widely studied form of autophagy.

1.1.4. Macroautophagy

The landmark event in macroautophagy, hereafter autophagy, is the formation of a double-membrane structure called autophagosome (AP) (Noda & Inagaki, 2015). The first step for this process is the generation of an 'isolation membrane' or 'phagophore'. The origin of the initial membrane is yet unknown, but some evidence suggests as possible sources the ER, the ER-Golgi intermediate compartment, endosomes, the plasma membrane or even mitochondria (Ktistakis & Tooze, 2016). How the phagophore expands and forms the autophagosome is still not clear. The adhesion and fusion of membrane structures, together with lipid transfer from donor membranes, is necessary for autophagosome expansion (Melia *et al.*, 2020). While membrane material is conforming the phagophore, cellular contents that need to be degraded start reaching this preformed structure. In a final step, the autophagosome closes and, upon fusion with a lysosome, the inside contents are degraded by lysosomal hydrolases (**Figure 1.6**).

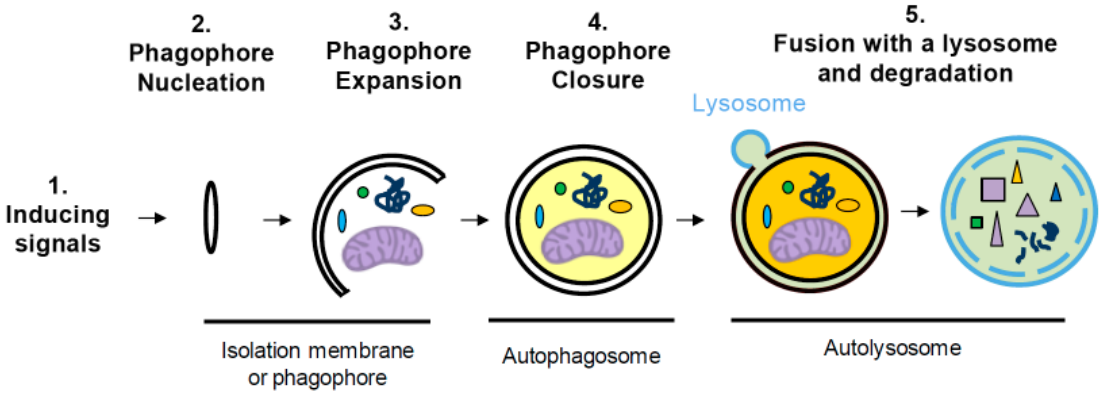

Figure 1.6. Outline of the general process of macroautophagy. From Iriondo *et al.* (2021).

1.1.4.1. Molecular machinery of macroautophagy

Although in humans the process is more complex and less studied than in yeast, autophagic functions are well conserved from yeast to human proteins. To date, at least 20 autophagy-related (ATG) genes have been identified and related to the process (Nakatogawa, 2020). They can be divided into several groups depending on their function during AP biogenesis. **Table 1.1** contains a summary of global and specific functions of each group, together with the differences between yeast and human proteins. Important AP biogenetic elements in humans include:

- **ULK protein kinase complex,** an initiator kinase complex that serves as a scaffold to recruit downstream factors and regulates their functions via phosphorylation of threonine or serine residues (Bach *et al.*, 2011). The mammalian ULK complex is composed of ATG13, FIP200, ATG101 and ULK1 or ULK2. To initiate autophagosome biogenesis, multiple copies of the ULK complex

are assembled, and this functions as a platform for the recruitment of other ATG proteins (Mercer & Tooze, 2021; Nakatogawa, 2020).

- **ATG9-containing vesicles.** ATG9 is a multispanning transmembrane protein. It is transported through the endomembrane system and localizes to plasma membrane, cytoplasmic vesicles or tubules. This ATG9 trafficking is regulated by Rab GTPases (Kakuta *et al.*, 2017). ATG9 containing membranes have been suggested to contribute to the generation of AP precursors (Yamamoto *et al.*, 2012).

- **Autophagy-specific phosphatidylinositol 3-kinase (PI3K) complex I.** The PI3K complex I involved in AP biogenesis is formed by class III PI3K VPS34, p150, BECN1, ATG14L and NRBF2. It produces phosphatidylinositol 3-phosphate (PtdIns3P) in nascent autophagosome membranes, where different PtdIns3P-binding proteins are recruited to regulate the process (Cheng *et al.*, 2014).

- **ATG2-WD repeat protein interacting with phosphoinositides (WIPI) complex.** ATG2 interacts with WIPI proteins. WIPIs are PtdIns3P-binding proteins, as they belong to the PROPPIN (beta-propellers that bind phosphoinositides) protein family (Proikas-Cezanne *et al.*, 2015). The ATG2-WIPI complex acts as a membrane tether and it also has a lipid transfer activity (Valverde *et al.*, 2019).

- **ATG12 ubiquitin-like system.** This system is formed by ATG7, ATG10, ATG12, ATG5, and ATG16L1 proteins (see section 1.3). The ubiquitin-like protein ATG12 is conjugated to a lysine in ATG5. Then the conjugate interacts with ATG16L1 to form the homodimeric ATG12–ATG5-ATG16L1 complex (Mizushima *et al.*, 1998). This complex interacts with WIPI2b via ATG16L1 and localizes to the phagophore membrane depending on WIPI2b interaction with PtdIns3P produced by PI3K complex I (Dooley *et al.*, 2014). There, it exerts its E3 enzyme activity, to promote the lipid conjugation of the LC3/GABARAP proteins.

- **LC3/GABARAP ubiquitin-like system.** This system is formed by the LC3/GABARAP proteins, ATG4, ATG7 and ATG3 (see section 1.3). The ubiquitin-like LC3/GABARAP family proteins (orthologs to the yeast Atg8) are conjugated to the amino group of the lipid phosphatidylethanolamine (PE) in a membrane (Ichimura *et al.*, 2000). Once anchored to the membrane, they can drive membrane expansion, help in the transport and fusion of the AP to lysosomes, and also mediate cargo recognition during selective autophagy (Johansen & Lamark, 2020). ATG4 is also able to catalyze LC3/GABARAP protein delipidation for their recycling.

Of the above, the present thesis is focused on the behavior and roles of the ATG12 and LC3/GABARAP ubiquitin-like systems (See sections 1.3 and 1.4). The possible different functions of LC3/GABARAP-family members (Chapters 3 and 4) and the effect of ATG12-ATG5-ATG16L1 (E3) complex (product of the ATG12 system) will be studied (Chapters 4 and 5).

Atg1/ULK complex		
Recruiting and regulating AP formation-related proteins		
Yeast	*Mammal*	*Function*
Atg1	ULK1 ULK2	Ser/Thr kinases that mediate mTOR signaling and Atg9/ATG9 cycling
Atg13	ATG13	Complex formation and bridging complexes
Atg17 Atg11	FIP200	Scaffold protein
Atg29 Atg31	ATG101	Complex stabilization, interacts with Atg21/ULK1 and Atg13/ATG13
Atg9/ATG9-containing vesicles		
Membrane source to generate AP precursors and to drive isolation membrane expansion		
Yeast	*Mammal*	*Function*
Atg9	ATG9A	Targeting the vesicles to AP formation sites
PI3K complex I		
Producing PtdIns3P in AP biogenesis-related membranes		
Yeast	*Mammal*	*Function*
Vps34	VPS34	PI3K, catalytically active subunit of the complex
Atg6	BECN1	Complex stabilization and a hub for Vps34/VPS34 regulation. Role in initiation, formation and maturation
Vps15	p150	Ser/Thr kinase required for Vps34/VPS34 activity. Recruits the PI3K complex to membranes
Atg14	ATG14L	Targeting the complex to AP biogenesis-related membranes
Atg38	NRBF2	Complex stabilization
Atg2-Atg18/**ATG2-WIPI complex**		
Tethering the AP precursor/isolation membrane to the ER and transferring lipids		
Yeast	*Mammal*	*Function*
Atg2	ATG2A ATG2B	Membrane tethering and lipid transfer
Atg18	WIPI1 WIPI2 WIPI3 WIPI4	PtdIns3P binding proteins that target the complex to the AP precursor/isolation membrane
Atg12/ATG12 conjugation system: Atg12–Atg5-Atg16/ATG12–ATG5-ATG16L1 (E3) complex		
Stimulating Atg8/LC3/GABARAP protein lipidation		
Yeast	*Mammal*	*Function*
Atg12	ATG12	Ubiquitin-like protein conjugated to Atg5/ATG5, activation of Atg3/ATG3
Atg7	ATG7	E1 for Atg12/ATG12 and Atg8/LC3/GABARAP conjugation systems
Atg10	ATG10	E2 for Atg12/ATG12 conjugation to a Lys residue in Atg5/ATG5
Atg5	ATG5	Conjugation target of Atg12/ATG12
Atg16	ATG16L1	Forms a homodimeric complex with the ATG12–ATG5 conjugate Bridging Atg5/ATG5 and Atg21/WIPI2b directing Atg8/LC3/GABARAP conjugation to AP precursor
Atg8/LC3/GABARAP conjugation system: Atg8/LC3/GABARAP–PE conjugate		
Exerting multiple roles in autophagy: Cargo recruitment, AP expansion, AP shaping…		
Yeast	*Mammal*	*Function*
Atg8	LC3A LC3B LC3C GABARAP GABARAPL1 GABARAPL2	Ubiquitin-like protein conjugated to phosphatidylethanolamine (PE)
Atg4	ATG4A ATG4B ATG4C ATG4D	C-terminal processing/delipidation of Atg8-family proteins
Atg7	ATG7	E1 for Atg12/ATG12 and Atg8/LC3/GABARAP conjugation systems
Atg3	ATG3	E2 for Atg8/LC3/GABARAP conjugation systems

Table 1.1 Atg/ATG proteins involved in AP biogenesis. Adapted from Nakatogawa (2020).

1.1.4.2. Macroautophagy steps

Step 1. Initiation of autophagosome biogenesis

Autophagy induction is controlled by a complex regulatory mechanism. Different signals such as nutrient deficiency (aminoacids, glucose, phosphate, iron…), stress (oxidative stress, hypoxia…), protein aggregates, damaged organelles or microbial infection induce autophagosome biogenesis (He & Klionsky, 2009).

The assembly of multiple ULK complexes is the common first step (Nakatogawa, 2020). Many signals converge at the level of the mammalian target of rapamycin complex 1 (mTORC1), a Ser-Thr kinase (Wirawan *et al.*, 2011) that is able to phosphorylate the ULK complex and therefore block autophagosome biogenesis. Repression of mTORC1 by nutrient deprivation or rapamycin treatment is commonly used to activate autophagy (Noda & Fujioka, 2015). Other signals such as hypoxia, ER stress or microbial infection are able to stimulate PI3K complex I (Corona Velazquez & Jackson, 2018) in order to upregulate autophagosome formation.

During selective autophagy, the cargo is the element emitting signals for autophagy initiation. As mentioned in section 1.1.3, in most cases, cargo receptors are needed. It has been shown that some receptors are able to interact with the ULK complex subunit FIP200 to initiate *de novo* AP formation around the cargo (Ravenhill *et al*., 2019; Turco *et al.*, 2019). In addition, cargo receptors have LIR or GIR (LC3/GABARAP interacting regions) allowing recruitment of LC3/GABARAP proteins to the cargo and facilitating its sequestration and degradation (Montava-Garriga & Ganley, 2020). This, at least in some cases, acts as an ‘amplification’ mechanism rather than a ‘triggering’ mechanism in selective autophagy and it is important for accurate recognition of cargos (Mizushima, 2020).

Step 2. Phagophore nucleation

Once autophagy is induced and multiple copies of the ULK complex are assembled, the latter serve as a scaffold for the recruitment of other ATG proteins (Koyama-Honda *et al*., 2013) to sites where the phagophore will be generated. The main candidate sites in mammalian cells are the endoplasmic reticulum subdomains associated with mitochondria (Hamasaki *et al.*, 2013).

One of the proteins recruited at the earliest stages is ATG9, which is present on cytoplasmic mobile vesicles that serve as a seed to form the phagophore (Nishimura *et al.*, 2017). In parallel, the PI3K complex I produces PtdIns3P, helping in the recruitment of PtdIns3P-binding proteins (such as WIPIs) (Obara *et al.*, 2008). This promotes ATG12–ATG5-ATG16L1 complex recruitment to the phagophore membrane where it binds to WIPI2b (Dooley *et al.*, 2014; Fracchiolla *et al.*, 2020). The ATG12–ATG5-ATG16L1 complex interacts with the E2 enzyme ATG3 to induce covalent binding of LC3/GABARAP proteins to membranes (See section 1.3 for details) (Hanada *et al.*, 2007).

Step 3. Phagophore expansion

Once the initial phagophore is formed, new membrane lipids must be added in order to support its growth, to surround the cargo and produce the final AP. To form a 400-nm AP, around 3 x 10^6 lipids are required, therefore distinct mechanism for lipid delivery are expected to exist.

Many results suggest that LC3/GABARAP proteins are involved in the expansion of the phagophore (See Chapter 4) once they are bound to the membrane, most likely via mediating the tethering and fusion of membrane-supplying vesicles (Landajuela *et al.*, 2016; Nakatogawa *et al.*, 2007; Weidberg *et al.*, 2010). But LC3/GABARAP proteins also act together with other fusogenic factors, such as SNARE proteins, in a mechanism where lipid composition and membrane curvature are thought to be important (Nair *et al.*, 2011).

Recent studies proposed that ATG2 could also participate in phagophore expansion process. This protein forms a complex with WIPI and localizes in the site of phagophore formation, depending on its interaction with PtdIns3P. Once there, ATG2 is able to extract lipids from the ER and transfer them to the AP precursor through its long hydrophobic groove (Maeda *et al.*, 2019; Osawa *et al.*, 2019; Valverde *et al.*, 2019). Moreover, recent results with yeast protein suggest that phospholipids delivered by Atg2 are translocated from the cytoplasmic to the luminal leaflet by Atg9, thereby driving autophagosomal membrane expansion (Matoba *et al.*, 2020).

Step 4. Phagophore closure

Once the phagophore has grown and adopted a spherical shape, a small pore remains, and it needs to be closed to form the AP. Phagophore closure is a process that involves fission of the inner and outer membrane of the phagophore edge (Knorr *et al.*, 2015) (See Section 1.2.4 for details). The endosomal sorting complexes required for transport (ESCRT) machinery participate in the process (Takahashi *et al.*, 2019; Zhen *et al.*, 2020). It is not clear how is it targeted to the unsealed phagophore, but it seems that the ULK complex could play a role (Zhou *et al.*, 2019). Moreover, other unknown mechanisms must exist to obtain a highly constricted membrane neck in which ESCRT proteins can promote the scission step.

Step 5. AP fusion with a lysosome and degradation

The AP travels along the cytoplasm microtubules using the dynein-dynactin motor complex and fuses with a lysosome (Shen & Mizushima, 2014). The outer AP membrane fuses with the lysosome so that the inner membrane and its contents come into contact with the lysosomal hydrolases and lipases. LC3/GABARAP and other proteins such as, LAMP2, Rab, HOPS, SNAREs, ESCRT, FYCO1 and UVRAG-C-Vps tethering complex, take part in the autophagosome-lysosome fusion event (Itakura *et al.*, 2012; Wirawan *et al.*, 2011). The result of the autophagy degradation process is the generation of recycled amino acids, fatty acids and nucleosides that will come back to the cytosol for new anabolic reactions. This renewal of nutrient supply via the autophagic degradation of cellular components reactivates mTORC1, leading to the end of autophagy (Yu *et al.*, 2010).

1.2 Autophagy and aspects related to membrane architecture and dynamics

As shown in the previous section, autophagy is a complex process that involves the participation of a large amount of proteins and lipids. During autophagy, a new membrane organelle is formed. New lipids are needed to form and expand an initial membrane. Protein-protein and protein-lipid interactions, membrane bending, fusion and fission are happening during the process. Moreover, selective autophagy involves the recognition of other organelles mediated via protein-protein or protein-lipid interactions.

1.2.1. Cell membranes

Cell membranes are composed of a thin double layer of lipid molecules with large amounts of embedded proteins (Goñi, 2014; Singer & Nicolson, 1972). Membrane lipids are amphipathic molecules containing a hydrophobic tail and a polar head group, and can often self-assemble into lipid bilayers (**Figure 1.7**). When exposed to a water solvent, these lipids can be spontaneously arranged so that the hydrophilic head groups interact with the water molecules isolating the hydrophobic tails from the water environment (Israelachvili *et al.*, 1980). Thus, lipids in cell membranes characteristically adopt a bilayer structure with the hydrophobic tails facing each other and the polar heads interacting with the cytoplasm or extracellular medium.

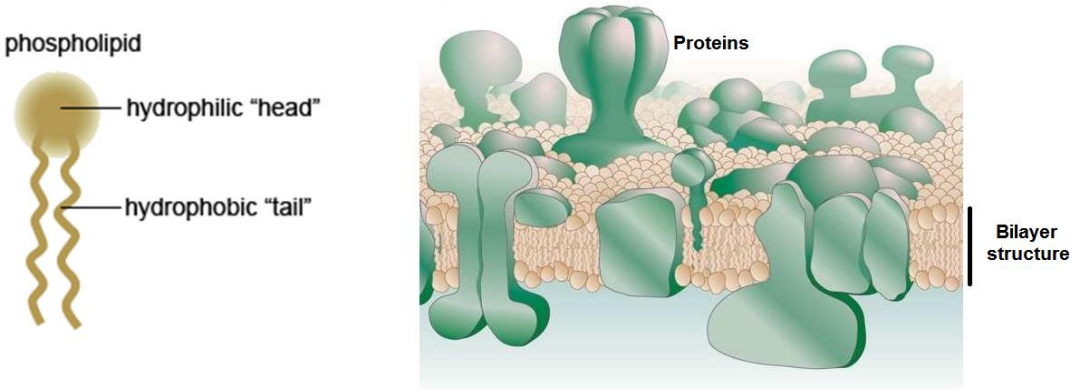

Figure 1.7. Phospholipids and an updated Singer and Nicolson "fluid mosaic model". Taken from Engelman (2005).

Proteins accommodate along the membrane extension, usually making up to 50% of the plasma membrane mass. In this context, Singer and Nicolson proposed the current view of cell membranes as a fluid mosaic, in which lipids and proteins can rotate and diffuse easily along the plane of the membrane. Subsequent adjustments and evolutions of this model have emerged in the following decades (Engelman, 2005; Goñi, 2014) (**Figure 1.7**). For example, it has been pointed out that membranes are crowded with proteins embedded in the phospholipid bilayer; they are asymmetric as a consequence of the restricted transbilayer movement, the asymmetry being controlled by flippase or scramblase proteins; membranes may contain laterally separated domains, composed of specific proteins or lipids; membranes are not flat and non-bilayer lipid structures can

be formed. Implications of these phenomena in autophagy will be discussed in the next sections.

1.2.2. Lipid Distribution and Asymmetry

Eukaryotic cells contain well over 1000 different lipid species in the membranes. Variation in headgroups and aliphatic chains of each kind of lipid generates this enormous lipid diversity (**Figure 1.8**).

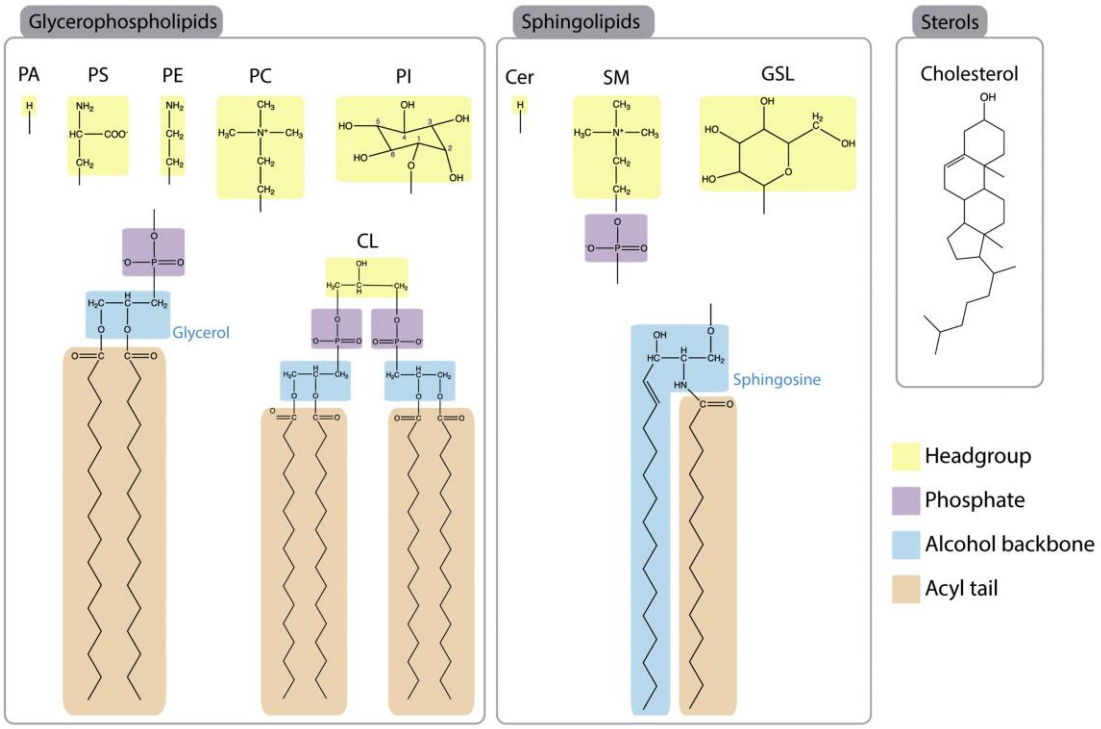

Figure 1.8. Lipids in eukaryotic membranes. They can be divided into glycerophospholipids, sphingolipids and sterols. Phosphatidic acid (PA), phosphatidylserine (PS), phosphatidylethanolamine (PE), phosphatidylcholine (PC), phosphatidylinositol (PI), cardiolipin (CL) ceramide (Cer), sphingomyelin (SM), glycosphingolipids (GLS). Taken from de la Ballina *et al.* (2020).

Phospholipids, sphingolipids and sterols are not distributed homogeneously throughout the main organelles of mammals, heterogeneity of lipid composition conferring special characteristics to them (**Figure 1.9**). This segregation reflects the different physiological role, local lipid metabolism of each lipid in the cell, and specific physico-chemical membrane properties generated by differences in lipid composition. For example, sphingomyelin and cholesterol are mainly found in the plasma membrane, while cardiolipin can be found almost exclusively in the inner mitochondrial membranes.

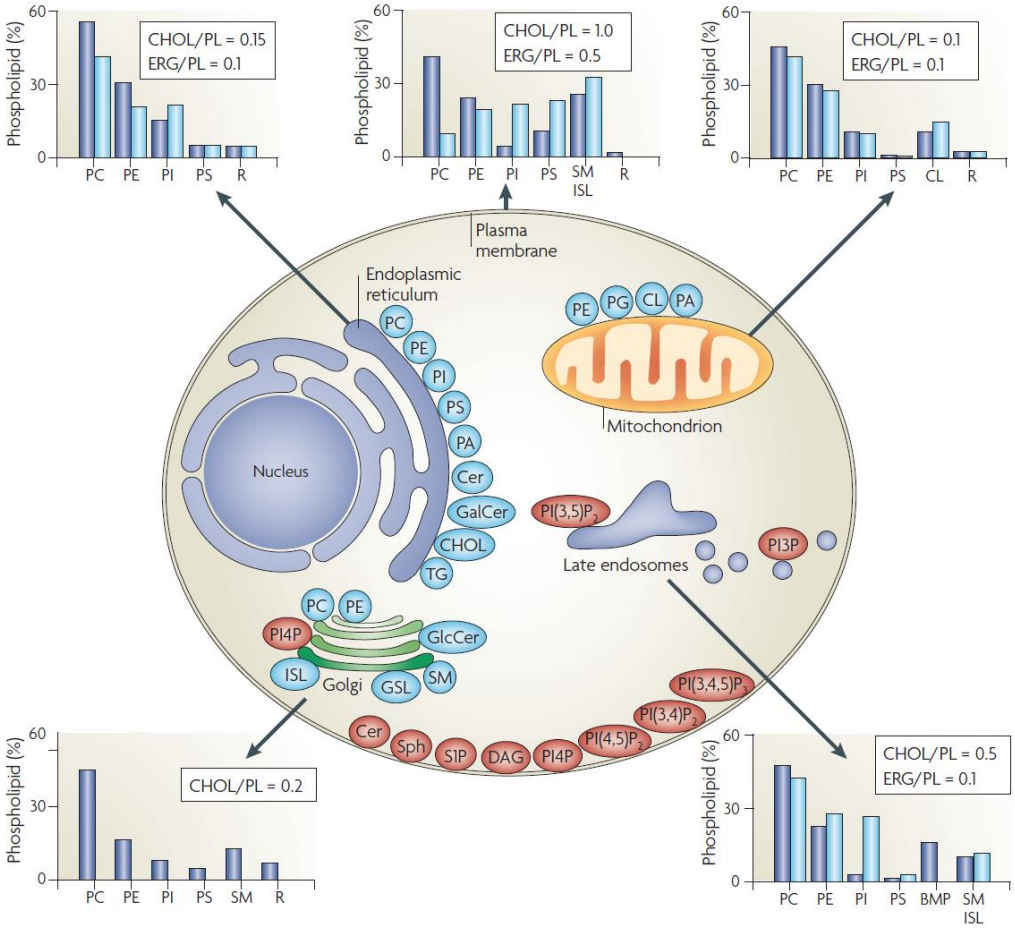

Figure 1.9. Lipid composition of different membranes within the cell. The lipid compositional data are expressed as a percentage of the total phospholipid in mammals (blue) and yeast (light blue). Taken from Van Meer *et al*. (2008).

Furthermore, lipid heterogeneity is not only present between different membranes in the cell, but also within single membranes. Lipids can be asymmetrically distributed between the two monolayers of a lipid bilayer (Van Meer *et al.*, 2008). This lipid transversal asymmetry is a necessary feature of all cell membranes in order to be functional. The main reason for lipid composition differences between both monolayers is the asymmetric synthesis of certain lipids or the presence of transporters that allow unidirectional lipid translocation.

Among the different intracellular membranes, this thesis deals with the phagophore membrane that will evolve into the double membrane AP, in particular with the zones that could allow fusion of new vesicles to expand the initial phagophore (Chapter 4) and with the external membrane of the mitochondria once it is damaged (Chapter 3).

1.2.3. Lipid polymorphism and geometry

Biological membranes under equilibrium conditions are composed of a lipid bilayer in a lamellar configuration. Lipids in membranes are said to adopt the lamellar or L phase. A lipid phase is a thermodynamic concept related to the specific structural pattern(s) that

a lipid or a lipid mixture adopts in aqueous solution. The most relevant lamellar lipid phases are: L_α (fluid phase), L_β (gel phase), and L_o (liquid-ordered phase).

Fluid, or liquid-crystalline, or liquid-disordered phase: Lipids in the L_α phase are free to diffuse laterally and rotationally, and display their acyl chains in a disordered state with high flexibility. Most membrane lipids occur in the liquid-disordered phase.

Gel phase: Lipids in the L_β phase have highly ordered acyl chains, being almost immobile and not allowing lateral or rotational motion. The gel phase is seldom, if ever, encountered in cell membranes.

Liquid-ordered phase: Lipids in the L_o phase are characterized by free rotational and translational diffusion, with highly ordered acyl chains. The L_o phase occurs in the presence of high concentrations of sterols.

Although cell membranes are basically organized in a virtually one-dimensional lamellar structure, some crucial events are characterized by the formation of more complex non-lamellar structures, such as the inverted hexagonal phases. From macromolecule transversal motion across the membrane to cell division, many processes require the generation of these unstable structures (Epand, 1998). Membrane fusion and fission processes, essential in autophagosome generation, growth and closure, are good examples of energetically unfavorable events that require the transient formation of non-lamellar structures (Gilbert, 2016; Kozlov & Chernomordik, 2015). The formation of some non-lamellar structures is strongly influenced by the lipid molecular geometry. About 30% of membrane lipids can adopt or induce non-lamellar structures in model systems.
Differences in the cross-sectional areas between the polar head group and the hydrophobic tail could determine the overall structure that lipids adopt when they self-assemble (Israelachvili *et al.*, 1980). From this point of view, lipids are mainly classified into 3 groups: lipids with conical, cylindrical or inverted-conical shapes (**Figure 1.10)**.

These shapes could be described by the morphological parameter S:

$$S = V/Ao \cdot Lc$$

Equation 1.1. Morphological parameter S.

where: V is the volume of the lipid molecule, Ao is the area of the molecule at the lipid-water interface and Lc is the length of the extended acyl chain.

Taking into account these parameters and the lipid cross-sectional area of the hydrophobic tail(s) (AH), which would reflect a volume of $V = AH \cdot Lc$ for a lipid of cylindrical shape, the different morphological geometries can be reviewed as:

- $Ao = AH$ ($S = 1$): The molecule presents a cylindrical shape, intrinsic curvature = 0.
- $Ao < AH$ ($S > 1$): The molecule presents a conical shape, intrinsic curvature <0.
- $Ao > AH$ ($S < 1$): The molecule presents an inverted-conical shape, intrinsic curvature >0.

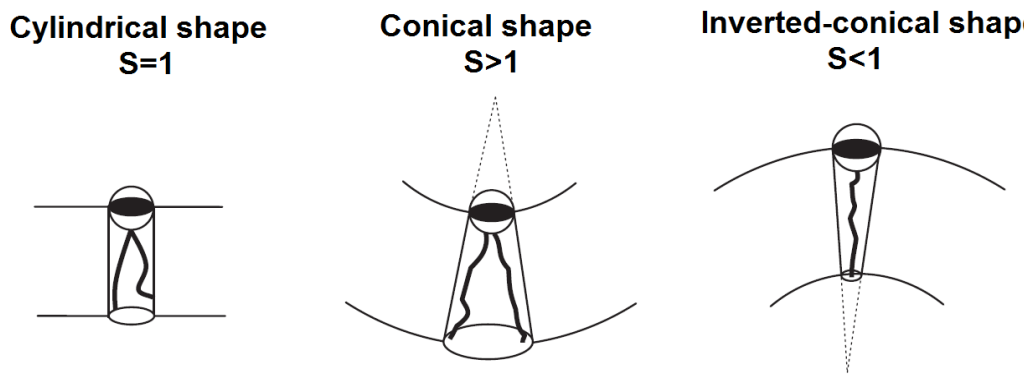

Figure 1.10. Molecular shapes of membrane lipids, according to Israelachvili. Adapted from Goñi (2014).

Note, however, that it is difficult to quantitatively define the shape and curvature of the phases adopted by lipids, since the area and volume of the molecules also depend on factors such as the amount of water present, ionic strength, pH, temperature, divalent cations and proteins.

Pure lipids in aqueous solutions will self-aggregate into different structures depending on their molecular geometry (**Figure 1.11)**:

- **Cylindrical shaped** lipids as PC or SM will become organized in the form of lamellar bilayers.
- **Cone shaped** lipids as PE, DAG or sterols will tend to form “hexagonal” (tubular) arrangements, (strictly speaking DAG or sterols will not form hexagonal phases by themselves, they can induce an inverted hexagonal phase in lipid mixtures).
- **Inverted-cone-shaped** lipids as is the case of lysophospholipids (*e.g.* lysoPC) will aggregate into micelles.

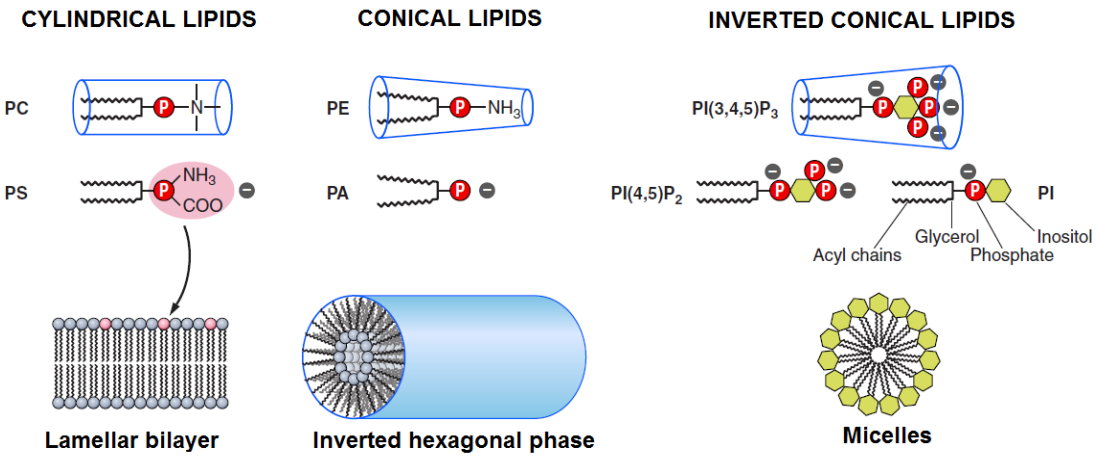

Figure 1.11. Molecular geometry of lipid and structures formed. Taken from Suetsugu *et al*. (2014).

However, these non-cylindrical lipids could be part of a lipid bilayer structure whenever lipids such as PC, SM or PS are present. For instance, 20–50 mol% cylindrical lipids are necessary when mixed with conical lipids in order to have an overall lamellar structure (Cullis *et al*., 1986b).

1.2.4. Fusion and fission processes

Membrane fusion occurs in cells whenever two vesicles coalesce giving rise to a single compartment. The "vesicles" may be two liposomes, two cells (*e.g.*, sperm and ovum), one virus and one cell (*e.g.*, HIV particle and T-lymphocyte), or one intracellular vesicle and the plasma membrane (*e.g.*, in the release of neurotransmitters), as examples of the multitude of possible membrane fusion events. In the context of autophagy, membrane fusion events occur to promote the expansion of the growing phagophore, and when the AP fuses with the lysosome.

Lipid polymorphism plays an essential role in membrane fusion (Cullis *et al.*, 1986a). Even if lipids in cell membranes adopt the disposition of lamellar phases (Goñi, 2014; Singer & Nicolson, 1972), the mechanism of fusion of two apposed lipid bilayers necessarily requires the formation of a transient non-lamellar intermediate. This intermediate has been called the "stalk" (Leikin *et al.*, 1987; Markin & Albanesi, 2002). (**Figure 1.12**). The canonical form of stalk-mediated fusion (Chernomordik *et al.*, 1995; Landajuela *et al.*, 2016), requires the independent demonstration of vesicle aggregation, inter-vesicular mixing of total membrane lipids, mixing of inner monolayer lipids, and mixing of aqueous contents in the absence of vesicular content leakage or spill out. Ideally, aggregation, total lipid mixing, inner lipid mixing, and contents mixing should start in the said order, i.e., should exhibit increasing lag times.

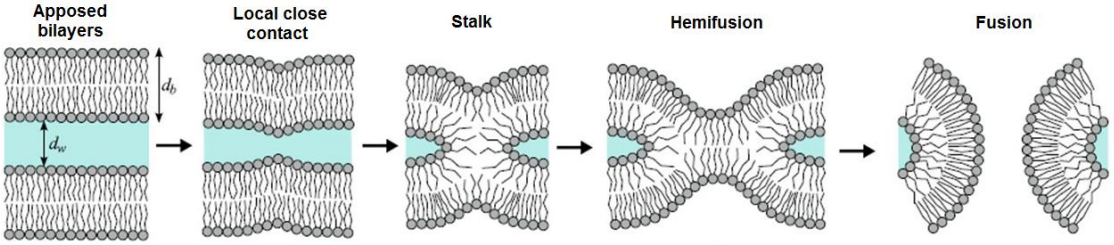

Figure 1.12. Schematic representation of the stalk fusion model. Adapted from Aeffner *et al*., (2009).

Much experimental evidence shows that model membranes enriched in negatively curved lipids favor fusion processes, whereas incorporation of positively curved lipids hinder fusion (Kozlovsky *et al.*, 2002). In natural membranes, proteins inserted into the bilayer may also contribute in overcoming the energy barrier required for membrane fusion. Several authors have approached the fusion processes leading to autophagosomal growth, using model membrane systems consisting of vesicles of defined lipid compositions and LC3/GABARAP proteins. Landajuela *et al.* (2016) demonstrated that lipids with an intrinsic negative curvature (*e.g.*, DAG, CL) facilitated stalk formation, thus membrane fusion (Basáñez, *et al*., 1996a,b), as well as the opposite, *i.e*. an inhibitory effect of positive intrinsic-curvature lipids (*e.g.* lysoPC). The same considerations on intrinsic lipid curvature apply to the requirement of high

proportions of PE in the vesicle composition. In this thesis, the ability of the different LC3/GABARAP-family members to promote membrane fusion will be studied and the implications that these results could have in its participation in phagophore expansion will be discussed (See Chapter 4).

Autophagosome completion is achieved by closure of the elongated phagophore, giving rise to the double-membrane structure that is characteristic of autophagy. Phagophore closure is interesting from the point of view of the topological changes involved, since two separate aqueous domains are generated, separated by two membranes, where a single aqueous compartment existed. The geometry of this event has been described by Dimova and co-workers (Knorr *et al.*, 2015, 2017). The critical step in phagophore closure had often been interpreted in terms of membrane fusion. However, in fusion, two separate aqueous compartments merge into one. The opposite happens in phagophore closure, *i.e.* aqueous compartment separation. Thus, the relevant membrane event is an example of scission, or fission, rather than fusion (**Figure 1.13**). Fusion and scission are topologically, but not energetically, opposite processes, because they are characterized by different energy barriers (Knorr *et al.*, 2017).

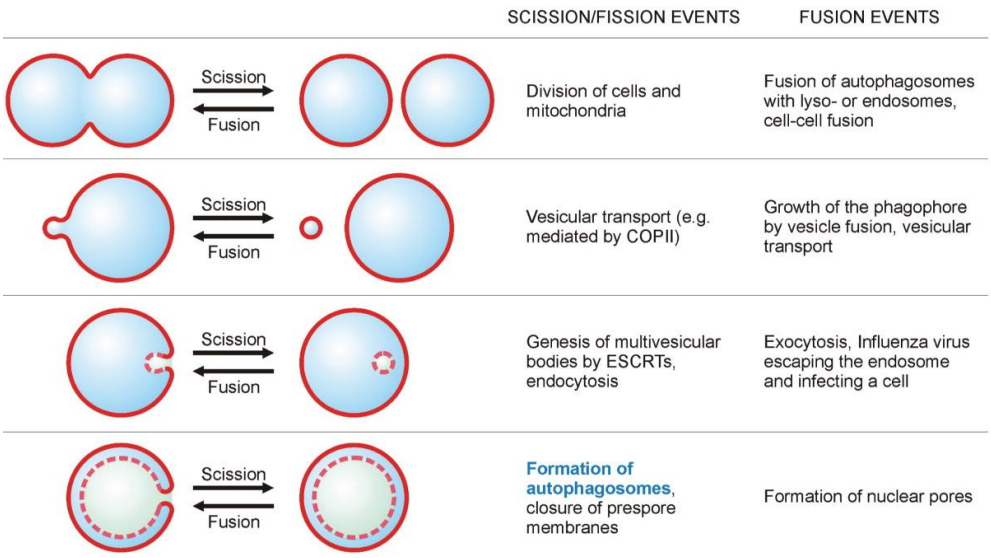

Figure 1.13. Scission and fusion events. Taken from Knorr *et al.* (2015).

1.2.5. Membrane curvature

Membrane curvature represents a global property of the membrane, and it should not be confused with the intrinsic molecular curvature of lipids, discussed above (section 1.2.3), typically related to the molecular geometry and strongly influenced by the environment (Bassereau *et al.*, 2018).

Acyl chain saturation also influences membrane curvature. Unsaturated lipids can tolerate high membrane curvature, whereas the shapes of saturated lipids are cylindrical, making membranes containing them thicker. ER membranes are enriched in unsaturated phospholipids, enabling high membrane curvature. This facilitates protein secretion from the ER. In contrast, PM membranes are more tightly packed, due to the abundance of

saturated phospholipid, which creates a thick boundary between the cell and its environment (Bigay & Antonny, 2012).

The overall membrane curvature is the result of a complex interplay among membrane proteins, lipids, and physical forces that are applied to the membrane surface (Simunovic *et al.*, 2015) (**Figure 1.14**).

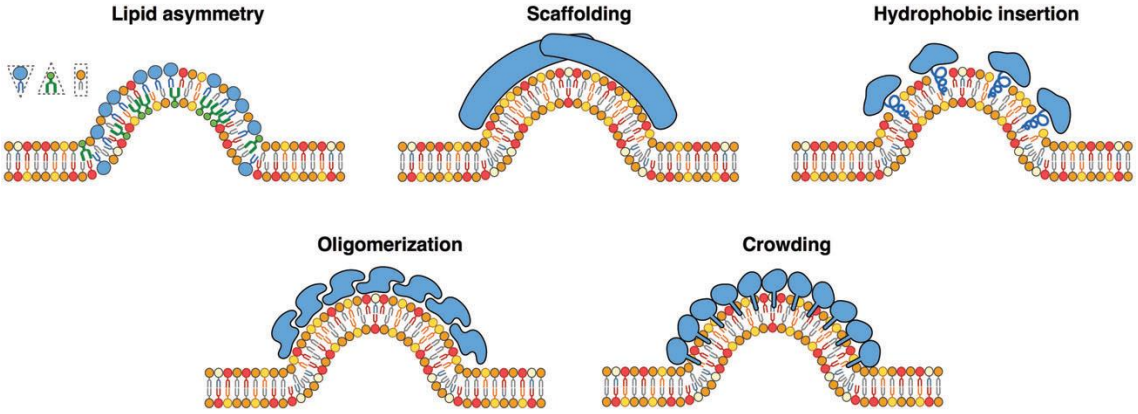

Figure 1.14. Membrane curvature can be induced by different mechanisms. Taken from Chabanon *et al*. (2017).

In general, a high membrane curvature (short vesicle radius) helps in protein binding to the bilayer convex side, because curvature is usually accompanied by a decreased density of lipid polar heads at the bilayer convex surface. Consequently, local lipid-packing defects occur, and the hydrophobic membrane core becomes more accessible to any hydrophobic stretches, *e.g.* amphipathic helices, that could exist in the protein. A number of proteins involved in AP generation have been shown to bind preferentially highly curved membranes.

1.2.6. Lipid-protein interactions

As mentioned in section 1.2.1, each particular bilayer contains a specific pool of proteins that confers to it some particular properties (Goñi, 2014; Singer & Nicolson, 1972). Membrane proteins are commonly classified as peripheral or integral proteins:

- **Integral (also called intrinsic)** proteins contain one or more segments embedded in the phospholipid bilayer. Most integral proteins contain hydrophobic residues that interact with the fatty acyl chains of phospholipids in order to anchor the protein to the membrane. The multispanning membrane protein ATG9 is an integral membrane protein. However, the polypeptide chain does not always enter the phospholipid bilayer, as is the case of proteins anchored by covalent binding to fatty acids or other lipids. The latter is the case of LC3/GABARAP proteins, covalently bound to a PE molecule in the AP.

- **Peripheral (also called extrinsic)** proteins usually interact with the lipid polar head groups of lipids or of intrinsic proteins.

Moreover, a large amount of membrane proteins does not spend their whole life attached to the membrane. Some of them contact the lipid bilayer only under certain conditions, thereby remaining membrane bound (either as integral or as peripheral proteins) or returning promptly to the aqueous medium (non-permanent membrane proteins) (Goñi, 2002). In this regard, these **non-permanent proteins** can be classified according to:

- **The reversibility of the membrane contact:** there are some proteins that interact reversibly with the membrane and others with very long-lived (irreversible) contacts.
- **The nature of the interaction:** sorts the proteins into groups depending on the strength of the interaction, considering weak or strong associations, either in a transient or in a permanent way, with the membrane.

Protein binding to membranes is affected by three important physicochemical parameters: membrane electrostatics, lipid packing, and membrane curvature (Bigay & Antonny, 2012). Moreover, protein-membrane association can also rely on specific protein domains that recognize some peculiarities of the membrane, including regions with net electric charges. At least 10 different types of protein domains bind phospholipids at the membrane surface (Hurley, 2006). These interactions can fall into two classes:

- **Highly specific**: involving the recognition of a particular phospholipid in the membrane. For instance, C1, C2, PH, PX, FYVE or PROPPINs domains. This is the case of WIPI proteins, that are able to recognize PtIns in the membrane through a PROPPIN domain (Proikas-Cezanne *et al.*, 2015).
- **Non-specific:** implying a physical property of the membrane surface. Bin/Amphiphysin/Rvs (BAR) domains, Amphipathic Lipid Packing Sensor (ALPS) motifs or N-terminal amphipathic α-helices recognize physical properties such as membrane curvature (Antonny, 2011). Among the proteins that are sensitive to curvature, ATG3 facilitates LC3/GABARAP conjugation preferentially on membranes presenting packing defects due to its N-terminal amphipathic helix (Hervás *et al.*, 2017; Nath *et al.*, 2014).

Among all the lipid-protein interactions occurring in autophagy, the following are explored in this thesis:

- **Cardiolipin (CL) - LC3/GABARAP interaction (Chapter 3):** The ability of the different LC3-subfamily members to recognize CL will be compared, as LC3B was shown to interact with CL to promote the selective removal of damaged mitochondria (Antón *et al*., 2016; Chu *et al.*, 2013).

- **Phosphatidylethanolamine (PE) – LC3/GABARAP interaction (Chapters 4 and 5)**. The conjugation of the different LC3/GABARAP-family members to PE will be reconstituted (See 1.3) and the potential functions of these proteins once they are lipidated will be compared.

1.3. Ubiquitin-like systems

Among the six functional groups mentioned in section 1.1.4.1, the two UBL conjugation systems ATG12 and LC3/GABARAP deserve special attention. As in the case of ubiquitin, conjugation of LC3/GABARAP proteins to PE is achieved through a cascade of activities, catalyzed by E1 activating enzymes, E2 conjugating enzymes and E3 ligases (**Figure 1.15**). However, the UBL structural organization and some characteristics differ considerably from the canonical enzymes (Cappadocia & Lima, 2018). For example, one of the peculiarities of autophagy UBL systems is that a UBL-like protein conjugate with three ubiquitin-like folds serves as an E3 enzyme in the conjugation reaction of another ubiquitin-like system (Nakatogawa, 2013).

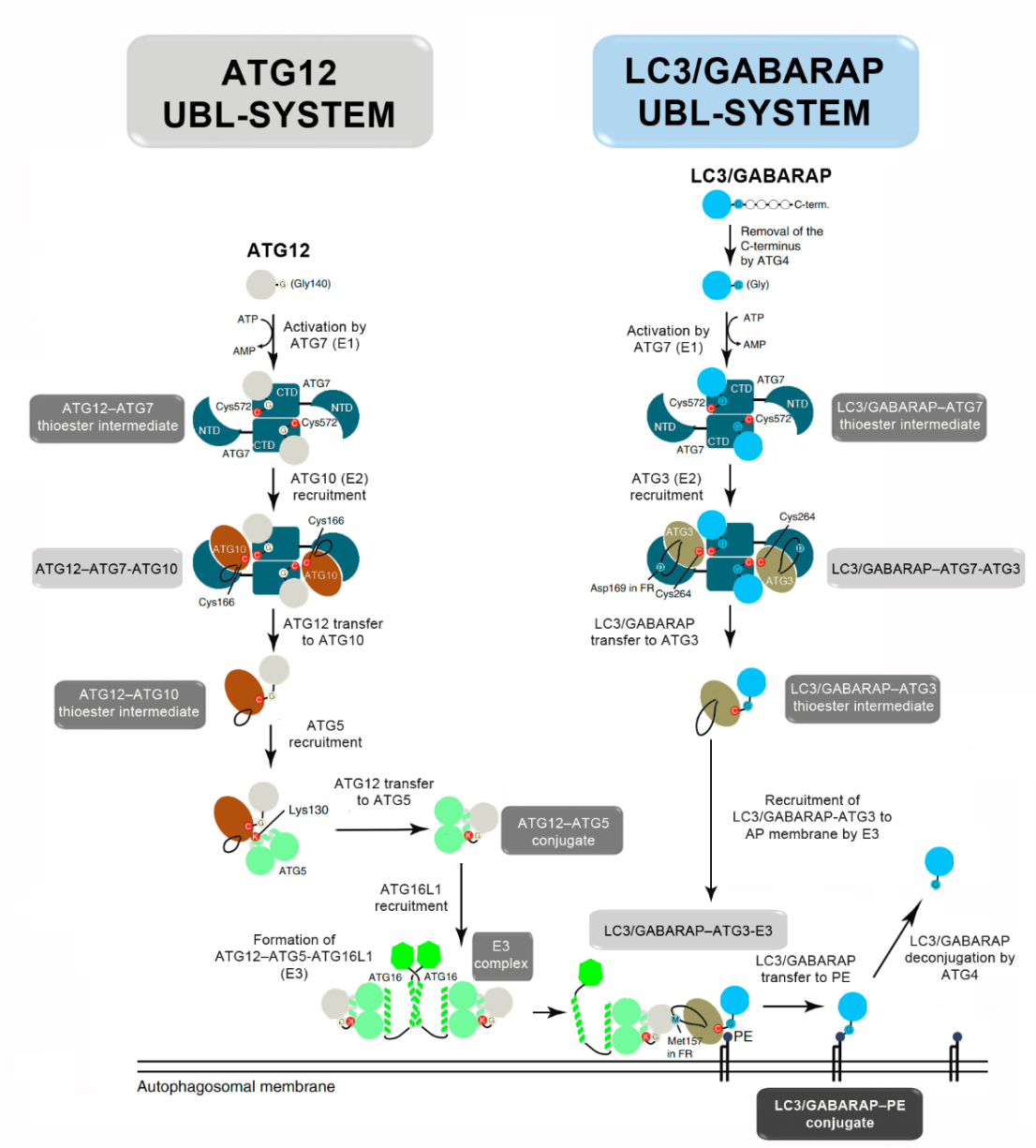

Figure 1.15. UBL conjugation systems in autophagy. E1, E2, E3 are presented as cartoon models. Residues involved in conjugation reactions are indicated. Asp 169 and Met 157 in ATG3^{FR} are critical for E1-E2 and E2-E3 interactions respectively. Adapted from Ohashi *et al*. (2019).

1.3.1. ATG12 UBL-system

Yeast Atg12 was the first ubiquitin-like Atg protein to be identified. Orthologues of each component of the yeast Atg12 system have been found in mice and humans, and they function similarly to their yeast counterparts (Kuma *et al.*, 2002; Mizushima *et al.*, 1999). In contrast to ubiquitin, which is conjugated to multiple targets in an inducible and reversible manner, ATG5 seems to be the only target of ATG12, and the conjugation of ATG12–ATG5 occurs constitutively. No processing enzyme is known that can cleave the isopeptide bond between ATG12 and ATG5 (Geng & Klionsky, 2008).

The ATG12 amino-acid sequence ends with a glycine residue and there is no protease involved in ATG12 conjugation (**Figure 1.15**). ATG7 acts as an E1-like enzyme activating ATG12 in an ATP-dependent manner. For that purpose, a thioester bond is formed between the C-terminal Gly 140 of ATG12 and the Cys 572 of ATG7. As ATG7 is a symmetric homodimer with two catalytic cysteine residues, it can activate two UBL-proteins and using its N-terminal domain interact with E2-like enzymes. This interaction promotes a conformational change that allows the juxtaposition of the active site in E2 with the one in E1 (Kaiser *et al.*, 2012).

Thereby, ATG12 is transferred from ATG7 to the Cys 166 of the E2-like enzyme ATG10, and this allows its conjugation to ATG5 at the Lys 130 through an isopeptide bond (Ohashi *et al.*, 2019). There is no E3 enzyme involved in this ATG12–ATG5 conjugation. Once it is formed, the ATG12–ATG5 conjugate is able to interact with ATG16L1 protein and form a homodimeric complex: the ATG12–ATG5-ATG16L1 complex (Otomo *et al.*, 2013), that will act as an E3 enzyme for the LC3/GABARAP UBL- system and participate in the determination of site of LC3/GABARAP lipidation (Nakatogawa, 2013). See Chapter 4 and 5 for details.

1.3.2. LC3/GABARAP UBL-system

Yeast Atg8 was the second ubiquitin-like Atg protein to be identified. In mammalian cells several orthologues of Atg8 (see section 1.4, LC3/GABARAP family) and of each component of the Atg8 UBL-system have also been found, and they function similarly to their yeast counterparts (Ichimura *et al.*, 2000; Tanida *et al.*, 2004). As explained above, rather than to another protein, in this system the UBL-protein is conjugated to a lipid.

All UBL proteins belonging to the LC3/GABARAP family are synthetized in the form of precursors (**Figure 1.15**). Therefore, several residues of their C-terminal region are cleaved by ATG4 family proteases to expose the glycine residue essential for subsequent reactions (Kirisako *et al.*, 2000). The processed LC3/GABARAP proteins are activated by the E1 enzyme ATG7 in an ATP-dependent reaction (same protein and mechanism as in the ATG12 system). It results in the covalent attachment of the LC3/GABARAP glycine terminal residue on the catalytic Cys 572 of ATG7 through a thioester bond (Noda *et al.*, 2011).

Then, the LC3/GABARAP protein should be transferred to ATG3. This protein consists of a canonical E2 domain and a flexible region ($ATG3^{FR}$) that allows the interaction with the N-terminal region of ATG7. Thus, the catalytic Cys 264 of ATG3 replaces the one in

ATG7, resulting in the transfer of the LC3/GABARAP family member to ATG3 (Ohashi *et al.*, 2019).

Finally, LC3/GABARAP members have to be transferred and conjugated to the head group of phosphatidylethanolamine (PE). For this last step ATG12–ATG5-ATG16L1 complex acts as an E3-like ligase enzyme to promote LC3/GABARAP lipidation through the interaction between $ATG3^{FR}$ and a patch in ATG12 (Metlagel *et al.*, 2013). This allows that the C-terminal carboxyl group of LC3/GABARAP protein form an amide bond with the amino group in the hydrophilic head moiety of PE, anchoring the protein to membranes (Nakatogawa, 2013). Unlike the ATG12–ATG5 conjugate, LC3/GABARAP–PE can be cleaved by ATG4 to release free LC3/GABARAP (Kauffman *et al.*, 2018; Maruyama & Noda, 2017).

1.4. LC3/GABARAP family

The human LC3/GABARAP family is composed of at least 8 Atg8 orthologs (Schaaf *et al.*, 2016). They are usually divided into two subfamilies, LC3 (microtubule-associated proteins 1A/1B-light chain 3) and GABARAP (gamma-aminobutyric acid receptor-associated proteins). LC3A, LC3B, LC3B2 and LC3C constitute the LC3 subfamily, whereas GABARAP, GABARAPL1/GEC1, GABARAPL2/GATE-16 and GABARAPL3 comprise the GABARAP one (Weiergräber *et al.*, 2013). GABARAPL3 seems to be a pseudogene as its expression has been demonstrated at the transcriptional level only (Xin *et al.*, 2001) and LC3B2 has a low expression in human tissues (Bai *et al.*, 2012). Therefore, in general, when we talk about the LC3/GABARAP family we are referring to six members of this family, namely LC3A, LC3B, LC3C, GABARAP, GABARAPL1 and GABARAPL2.

These proteins are ubiquitous, despite differences in their levels of expression depending on tissue and stress conditions (Schaaf *et al.*, 2016; Shpilka *et al.*, 2011). To mention but a few examples: LC3C, which is transcribed at lower levels than other members of the LC3 subfamily, is expressed predominantly in the lung (He *et al*., 2003), GABARAPL1 is highly expressed in the central nervous system (Nemos *et al.*, 2003) and GABARAPL2 is strongly expressed in the brain (Xin *et al.*, 2001).

1.4.1. Evolution to the LC3/GABARAP-family members

In the course of evolution, after various transposition, translocation and recombination events, the six human orthologs of Atg8 were found to have different chromosomal locations (Schaaf *et al.*, 2016), LC3A, LC3B, LC3C, GABARAP, GABARAPL1 and GABARAPL2 are located on chromosome 20, 16, 1, 17, 2 and 16 respectively. The recent computational study of ATG8 proteins from 20 different species performed by Jatana *et al.* (2020) revealed 68 gene duplication events. Their phylogenetic analysis showed that, while LC3A-LC3B and GABARAP-GABARAPL1 originated from the same node, LC3C and GABARAPL2 proteins branched into separate clades (**Figure 1.16**).

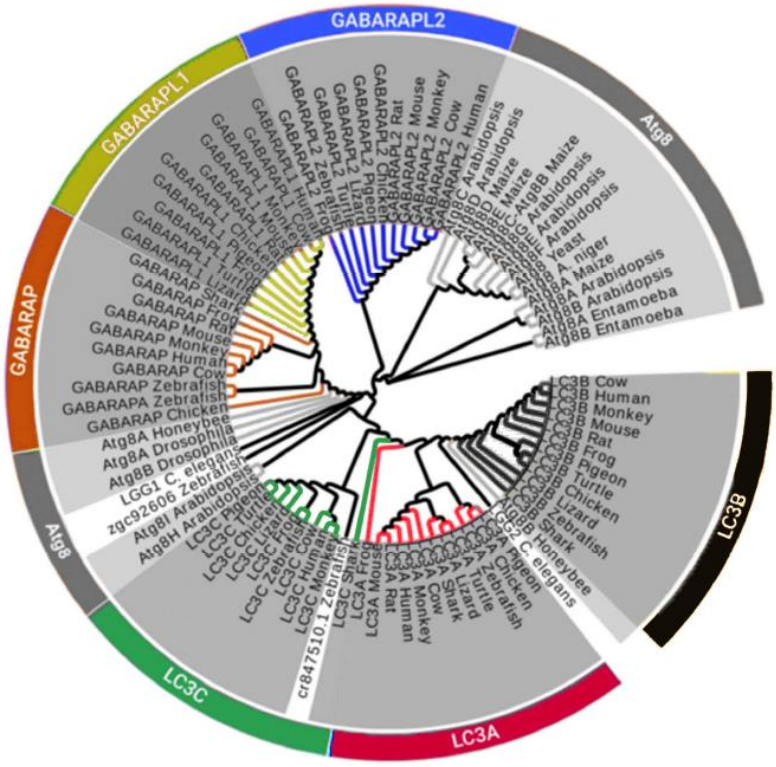

Figure 1.16. Phylogenetic tree of Atg8 orthologs. Adapted from Jatana *et al.* (2020).

Those results are in agreement with their different sequence identities (**Figure 1.17**). LC3/GABARAP family members share from 31 to 87% sequence identity between them. In the LC3 subfamily, LC3B are very similar to LC3A (83%), whereas LC3C is the one featuring highest diversity (55-59%). The GABARAP subfamily follows a similar pattern, with GABARAPL1 close to GABARAP (87%), and GABARAPL2 with a lower sequence identity (58-61%) (Jatana *et al.*, 2020).

	Atg8	LC3A	LC3B	LC3C	GABARAP	GABARAPL1	GABARAPL2
Atg8		39	40	40	55	55	56
LC3A			83	59	32	34	42
LC3B				55	31	32	39
LC3C					39	39	43
GABARAP						87	58
GABARAPL1							61
GABARAPL2							

Figure 1.17. Sequence identity matrix of LC3/GABARAP family members and Atg8. Adapted from Jatana *et al*. (2020).

Sequence alignment of the Atg8-family members from six different species reveals that these proteins are highly conserved and that there is a clear similarity for the proteins within individual subfamilies in certain zones (Wesch *et al.*, 2020). There is already an evolution-based sorting of Atg8 into LC3 and GABARAP subfamilies in lower eukaryotes as *C. elegans* proteins LGG-1 and LGG-2 were found to show structural and functional similarity to GABARAP and LC3 subfamilies (Wu *et al.*, 2015). It also indicates that the proteins from the GABARAP subfamily are evolutionarily more related to the Atg8

proteins than to those of the LC3 subfamily. This was supported by a coevolution measurement and molecular modelling performed by Jatana *et al.* (2020) that suggested that GABARAP subfamily has a lower propensity than LC3 to acquire new functions, LC3C being the isoform displaying the highest number of unique co-evolved residues, mostly harbored between N-terminal helices and ubiquitin fold (Jatana *et al.*, 2020). Therefore, there are substantial differences in the sequences not only between the subfamilies but also between the individual subfamily members that could be responsible of different behaviors. However, at present it is unclear which functions are associated to the particular sequence features.

1.4.2. Structure of LC3/GABARAP-family members

LC3/GABARAP-family members are soluble proteins formed by 117-147 aminoacids with a molecular mass of approximately 14-17 kDa. Despite the variability in sequence of LC3/GABARAP-family members, the structures determined experimentally showed very high structural similarity (**Figure 1.18**). Their structures could be overlaid upon each other with a root-mean-square deviation (RMSD) of 1.2 Å on backbone atoms (Wesch *et al.*, 2020). As mentioned in section 1.3.2 they are UBL-proteins, and the presence of two extra N-terminal helices is the main structural difference between ubiquitin and LC3/GABARAP proteins or Atg8 (**Figure 1.18)**.

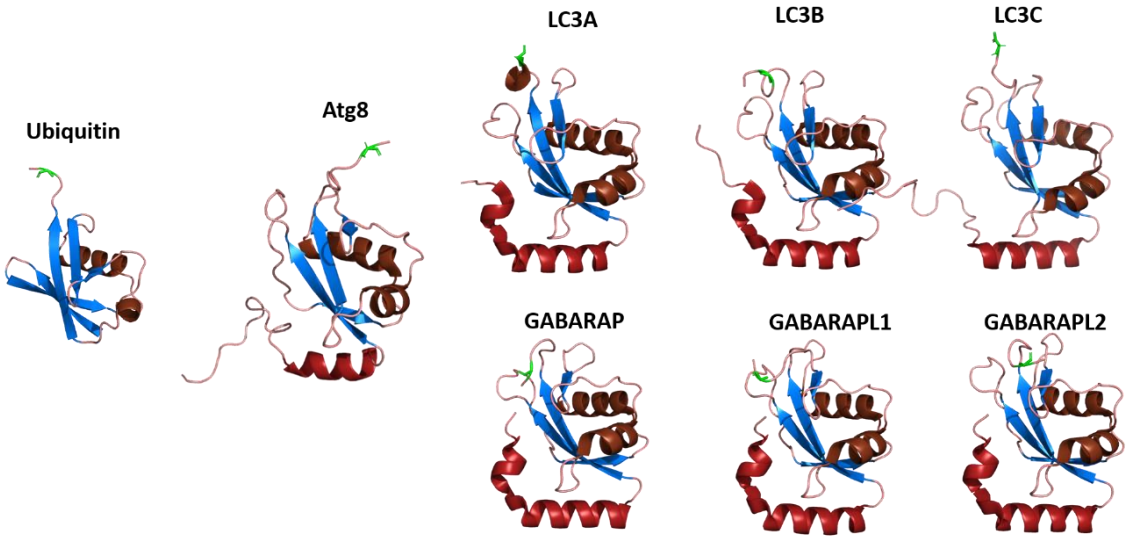

Figure 1.18. Comparison of Ubiquitin, Atg8 and LC3/GABARAP family-member structure. Structures were displayed with PyMOL. N-terminal regions appear in red, and the ubiquitin-like core is formed by four β-sheets (blue) and two α-helices (brown). In green, the conserved Gly C-terminal. PDB: Ubiquitin (1UBQ), Atg8 (2KQ7), PDB: LC3A (5CX3), LC3B (2ZJD), LC3C (2NCN), GABARAP (1GNU), GABARAPL1 (5LXI) and GABARAPL2 (4CO7).

LC3/GABARAP protein structure consists of two N-terminal α-helices (α1-α2) and a ubiquitin core formed by a four-stranded central β-sheet core (β1-β4) and two α-helices (α3-α4) shielding the concave face of the sheet (Weiergräber *et al.*, 2013) (**Figure 1.18 and 1.19**)

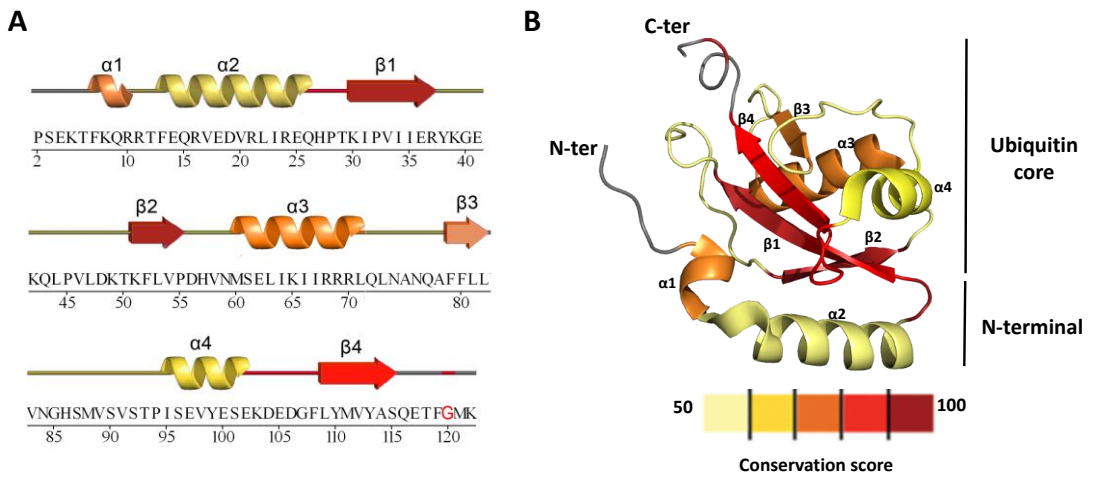

Figure 1.19. LC3B structure and sequence conservation score. **(A)** Secondary structure elements and the sequence of LC3B (PDBsum, 2ZJD) colored according to the conservation score displayed in Jatana *et al*. (2020). **(B)** Structure of LC3B PDB 2ZJD displayed by PyMOL colored according to the conservation score displayed in Jatana *et al*. (2020).

The largest variability is found in the N-terminal helices, β1-β2 and β2-α3 loops (Jatana *et al.*, 2020). The most highly conserved residues among the LC3/GABARAP members belong to the beta sheets of the Ub core. This region of the protein is responsible of is UBL-characteristics and contains its conserved Gly C-terminal that will allow LC3/GABARAP proteins conjugate to PE in the phagophore membrane (Cappadocia & Lima, 2018).

Other important zones in LC3/GABARAP proteins are two hydrophobic pockets (HP1 and HP2) (**Figure 1.20**) as they form a consensus zone of interaction with proteins that contain a "region of interaction with LC3/GABARAP" or LIR motif. This zone is called LDS (LIR docking site) and it usually accommodates large side chains of non-polar aromatic residues located in the LIR motif of the interacting proteins.

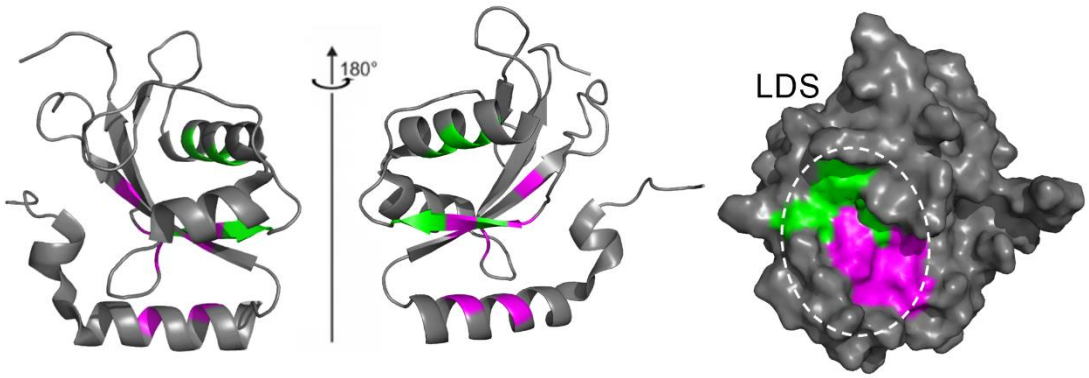

Figure 1.20. LIR docking site (LDS) in LC3/GABARAP family members. HP1 (pink) and HP2 (green). LC3B structures and surface displayed by PyMOL, PDB: 1V49. Redrawn from Wesch *et al.* (2020).

The existence of various LC3/GABARAP members that interact with different LIR-containing proteins (Behrends *et al.*, 2010), suggests some specificity of these interactions. Several techniques have been employed to investigate the specificity of LC3/GABARAP binding partners (Johansen & Lamark, 2020). They can be summarized in five categories: preference for LC3A/B, LC3C only, LC3C and GABARAP subfamilies, GABARAP subfamily, nonspecific binders and not enough data available to determine a preferential binding (Sora *et al.*, 2020).

1.4.3. Roles of LC3/GABARAP-family members

The LC3/GABARAP protein-family function is still not fully understood and even less are the possible different roles of the LC3/GABARAP members. They have been related to multiple functions during autophagosome formation (Martens, 2016; Mizushima, 2020; Nakatogawa, 2020) (**Figure 1.21**), such as cargo recognition, phagophore initiation, phagophore expansion and closure, autophagosomal trafficking, fusion between autophagosomes and lysosomes, and inner membrane degradation. Moreover, those proteins take part in autophagy-independent cellular processes, for example, LC3 interacts with microtubules (Mann & Hammarback, 1994) and GABARAP participates in membrane trafficking of GABA(A) receptors to the plasma membrane (Chen *et al.*, 2006; Leil *et al.*, 2004).

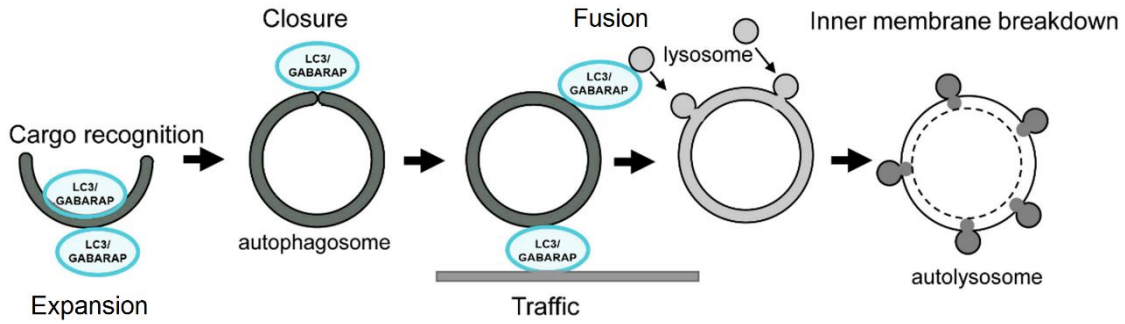

Figure 1.21. Proposed functions of LC3/GABARAP proteins during autophagy. Adapted from Mizushima (2020).

Among all these functions, this thesis intends to shed some light on the participation of the different LC3/GABARAP proteins in cargo recognition during CL-mediated mitophagy (Chapter 3) and in membrane expansion and shaping (Chapter 4 and 5).

HYPOTHESIS AND AIMS

The existence of at least six members of LC3/GABARAP protein family when there is only one in yeast is intriguing and suggests that each ortholog has different functions. We hypothesize that LC3/GABARAP family members could behave differently during CL-mediated mitophagy and during phagophore expansion and shaping. Therefore, the present work is aimed at obtaining a better understanding of the roles of each LC3/GABARAP family member. The molecular mechanism and specific roles of protein-lipid interactions, and the effect of these lipids and proteins on membrane properties constitute the basis of our interest. Quantitative biophysical approaches applying model membrane techniques well established in this laboratory, together with cell biology methods, have been used to advance the knowledge of these aspects of cell molecular biology.

The specific aims of this thesis are the following:

- To study and compare LC3 subfamily-member implications in CL-mediated mitophagy by studying their interaction with CL *in vitro* and their colocalization with mitochondria after autophagy treatments with CL externalization agents.

- To reconstitute *in vitro* the lipidation reaction of six LC3/GABARAP subfamily members in order to determine the capacity of the different LC3/GABARAP proteins to tether and fuse membranes in the absence and presence of E3 complex.

- To further study the E3 effect on GABARAPL1 lipid mixing ability by analysis of the potential formation of a protein scaffold in the membranes.

CHAPTER 2
EXPERIMENTAL TECNIQUES

CHAPTER 2. Experimental techniques

2.1. Materials

A full list of the required materials is given in the Materials and Methods section of each Results chapter.

2.2. Molecular Biology methods

Molecular biology techniques make possible to isolate, purify and modify DNA sequences encoding the protein of interest (Green & Sambrook, 2012). In this work, we have applied standard recombinant DNA techniques in order to be able to purify several autophagy related (ATG) proteins using bacterial and insect expression vectors as well as to perform mutations in their sequences for analyzing the implication of selected residues in the overall protein function.

2.2.1. DNA constructs

In order to express and purify the ATG protein of interest, its cDNA needs to be inserted into a self-replicating genetic element, generally a plasmid, also called the vector (**Figure 2.1**).

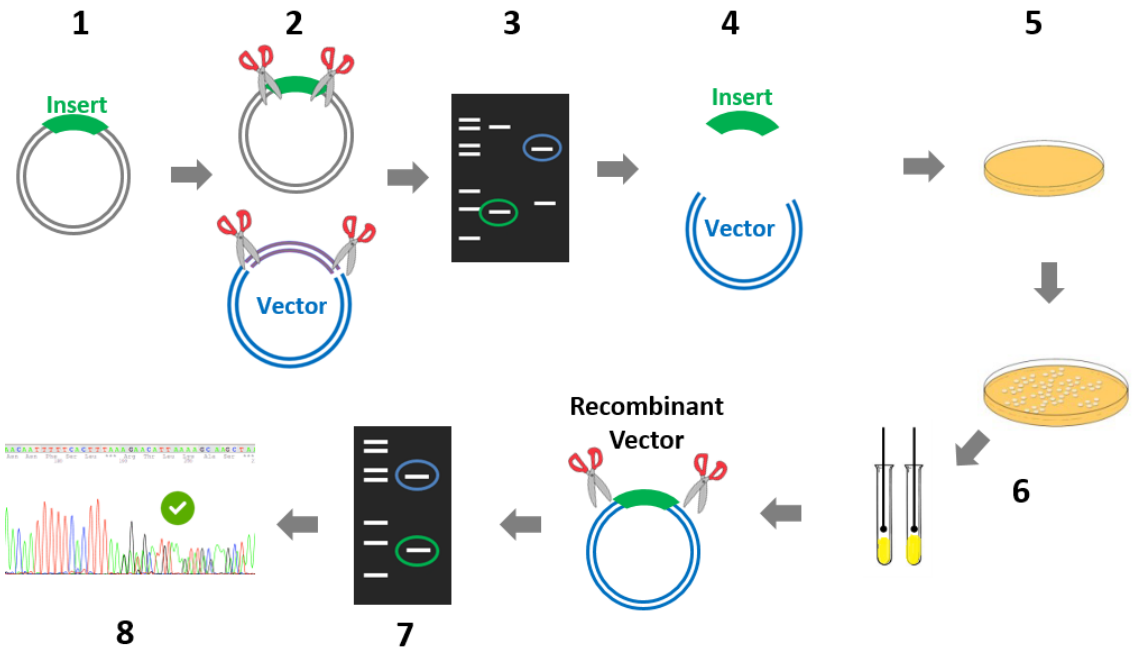

Figure 2.1. General cloning steps. The process can be divided in: 1) PCR Amplification and purification, 2) Digestion, 3) DNA purification, 4) Ligation, 5) Transformation in *E. coli* competent cells 6) Extraction of the plasmid DNA from *E. coli*, and 7-8) Confirmation of the presence of the insert in the vector.

In this thesis, the different plasmids used for expression and purification were provided by different research groups (see **Table 2.1** for details):

- The pGEX4T-1 plasmids for expression of the various Atg8 orthologs tagged with glutathione S-transferase (GST) were kindly provided by Dr. Ivanna Novak (School of Medicine, University of Split, Croatia). Each of them was a truncated form lacking the C-terminal Gly (Kirkin *et al.*, 2009). The ones used in this thesis (Table 2.1) were a version containing the Gly C-terminal exposed obtained by site direct mutagenesis (See section 2.2.3. for details).
- The pHAGE-N-eGFP plasmids for expression of several of the various Atg8 orthologs tagged with green fluorescent protein (GFP) (Stadel *et al.*, 2015) were kindly provided by Dr. Christian Behrends (Munich Cluster for Systems Neurology, Munich, Germany). Each of them contains the full-length sequence of the protein of interest.
- The pGEX6P-1 plasmid for expression of human ATG3 (Sou *et al.*, 2006) was kindly provided by Dr. Isei Tanida (National Institute of Infectious Diseases, Tokyo, Japan).
- The pGEX4T-1, pETDuet-1, pFast BacHT(B) and pGBdest plasmids for expression of GST, GFP, mouse ATG7 and ATG12–ATG5-ATG16 (E3) complex respectively, were kindly provided by Dr. S. Martens (Max Perutz Labs, Vienna, Austria) (Fracchiolla *et al.*, 2020).

Protein	Vector	Encoding
LC3A	pGEX4T-1	Human GST-THROMBINcs-LC3A-Gly(Δ1C)
LC3B	pGEX4T-1	Human GST-THROMBINcs-LC3B-Gly(Δ5C)
LC3C	pGEX4T-1	Human GST-THROMBINcs-LC3C-Gly(Δ21C)
GABARAP	pGEX4T-1	Human GST-THROMBINcs-GABARAP-Gly(Δ1C)
GABARAPL1	pGEX4T-1	Human GST-THROMBINcs-GABARAPL1-Gly(Δ1C)
GABARAPL2	pGEX4T-1	Human GST-THROMBINcs-GABARAPL2-Gly(Δ1C)
GFP-LC3A	pHAGE-N-eGFP	Human GFP-LC3A (full length)
GFP-LC3B	pHAGE-N-eGFP	Human GFP-LC3B (full length)
GFP-LC3C	pHAGE-N-eGFP	Human GFP-LC3C (full length)
GFP-GABARAPL2	pHAGE-N-eGFP	Human GFP-GABARAPL2 (full length)
ATG3	pGEX-6P-1	Human GST-PRESCISSIONcs-ATG3
ATG7	pFast BacHT(B)	Mouse 9xHis-TEVcs-ATG7
ATG12–ATG5-ATG16L1 (E3)	pGBdest	ATG12, (10xHis-TEVcs-)ATG5, 10xHis-TEVcs-ATG16L1-TEVcs-StrepII, ATG7, ATG10 (synthetic genes)
ATG12–ATG5-ATG16L1-GFP (GFP-E3)	pGBdest	ATG12, (10xHis-TEVcs-)ATG5, 10xHis-TEVcs-ATG16L1-GFP-TEVcs-StrepII, ATG7, ATG10 (synthetic genes)

Table 2.1. List of ATG constructs used in this thesis. Mutations for functional analysis were performed using them as a template.

2.2.2. DNA amplification and extraction

To amplify the ATG plasmids in order to store them we use *E. coli* DH5α strain. See **Protocol 1** for details.

Protocol 1. DNA amplification and extraction

1. Transformation of competent cells with the plasmid of interest

- a. Thaw 50 µl of cells in ice for 20 min.
- b. Add 1 µl the plasmid of interest (100 ng/µl) and keep 15 min on ice.
- c. Two methods:
  - i. Heat-shock:
    1. 90 sec 42ºC.
    2. Transfer immediately to ice.
  - ii. Electroporation (Electro-competent cells are required):
    1. Transfer to a electroporation cuvette.
    2. Apply a 2.5kV potential difference across the electrodes.
- d. Recover the cells by adding 950 µl of LB medium and incubate 1 hour at 37ºC to allow the synthesis of proteins for antibiotic resistance.
- e. Spin down the cells (2 min 9700 x g) and remove 900 µl.
- f. Resuspend the pellet, plate the cells on an agar plate containing the appropriate antibiotic and incubate overnight (O/N) at 37ºC.

2. Extraction of plasmid DNA from *E. coli*

- a. Choose a colony of the plate and grow it O/N in 5 ml of LB medium containing the appropriate antibiotic.
- b. Use the Kit "Gene Jet Plasmid Miniprep" (K0502, Thermo Fisher) and follow the instructions to extract the DNA.

3. Determination of DNA concentration

- a. Measure the A_{260nm} of the sample and check the purity with the A_{260}/A_{280} ratio, aiming for a ratio >2 in a Nanodrop spectrophotometer (Thermo Scientific).

2.2.3. Site-directed mutagenesis

In vitro site-directed mutagenesis is an invaluable technique for determining the contribution of individual amino acids to the structure and function of a given protein. The basic procedure utilizes an initial template double-stranded DNA (dsDNA) and two synthetic oligonucleotide primers containing the desired mutation (See **Table 2.2**). The oligonucleotide primers, each complementary to opposite strands of the vector, are extended during temperature cycling by PCR using a DNA polymerase. Incorporation of the oligonucleotide primers generates a mutated plasmid. Following temperature cycling, the product is treated with DpnI. The DpnI endonuclease (target sequence: 5´-Gm6ATC-3´) is specific for methylated and hemimethylated DNA and is used to digest the parental DNA template. The nicked vector containing the desired mutations is then transformed into *E. coli* competent cells.

In this thesis, we have used two different approaches to perform point mutations in the different members of the LC3/GABARAP subfamily (**Table 2.2**). All the primers used in order to perform site directed mutagenesis are detailed in **Table 2.3**.

	Quikchange Site-Directed Mutagenesis Kit	KOD-Plus mutagenesis kit
Characteristics	Site-directed mutagenesis	Inverse PCR (iPCR)-based site-directed mutagenesis
DNA polymerase	PfuTurbo DNA polymerase	KOD DNA polymerase
Design of primers	Mutation sites should be designed close to the middle in the sense and antisense primer	Mutation sites should be designed at the 5' terminal end of the sense primer.
Used for	Mutations to add the Gly C-terminal in LC3/GABARAP plasmids	Mutations to add point mutations in LC3 subfamily members (Chapter 3)

Table 2.2. Mutagenesis kits used in this thesis.

Mutant	Sense primer (5´→3´)	Antisense primer (5´→3´)
GST-LC3A Gly C-ter	AGGAAACCTTC**GGC**TGACTCGAGCG	CGCTCGAGTCAG**CCG**AAGGTTTCCT
GST-LC3B Gly C-ter	AGGAGACGTTC**GGG**TAACTCGAGCG	CGCTCGAGTTA**CCC**GAACGTCTCCT
GST-LC3C Gly C-ter	CAGGAGACATTT**GGC**TAGCTCGAGCG	CGCTCGAGCTA**GCC**AAATGTCTCCTG
GST-GABARAP Gly C-ter	CGAAAGTGTCTAC**GGT**TGACTCGAGCGGC	GCCGCTCGAGT**CAA**CCGTAGACACTTTCG
GST-GABARAPL1 Gly C-ter	GAGAGTGTCTAT**GGG**TGACTCGAGCGG	CCGCTCGAGTCA**CCC**ATAGACACTCTC
GST-GABARAPL2 Gly C-ter	GAGAACACTTTT**GGC**TGACTCGAGCGGC	GCCGCTCGAGTCA**GCC**AAAAGTGTTCTC
GST-LC3B^{E14A}	**GCC**CAAAGAGTAGAAGATGTCCGACTTATTCGAG	GAAGGTGCGGCGCTGCTTGAAGGTC
GST-LC3B^{E18K}	**AAG**GATGTCCGACTTATTCGAGAGCAGC	TACTCTTTGTTCGAAGGTGCGGCGC
GST-LC3B$^{E14A, E18K}$	**AAG**GATGTCCGACTTATTCGAGAGCAGC	TACTCTTTGGGCGAAGGTGCGGC
GST-LC3A^{A14E}	**GAA**GACCGCTGTAAGGAGGTACAGCAG	GAAGCTCCGCCGCTGCTTG
GST-LC3A^{K18E}	**GAA**GAGGTACAGCAGATCCGCGACC	ACAGCGGTCGGCGAAGCTC
GST-LC3A$^{A14E, K18E}$	**GAA**GAGGTACAGCAGATCCGCGACC	ACAGCGGTCTTCGAAGCTCCG
GST-LC3C^{A20E}	**GAG**ATCAGACAAGAGGAAGTTGCTGGAATCCGG	CAAGCTTTTCCTCTGCTTGAAGGGTCTGAC
GFP-LC3A^{G120A}	**GCC**TTCTGACCAACTTTCTTGTACAAAGTGGTTCG	GAAGGTTTCCTGGGAGGCGTAGACC
GFP-LC3B^{G120A}	**GCC**ATGAAATTGTCAGTGTAACCAACTTTCTTGTAC	GAACGTCTCCTGGGAGGCATAGACCA
GFP-LC3C^{G120A}	**GCC**TGCCTGGAGTCAGCAGCCC	AAATGTCTCCTGGGAGGCGTAGG
GFP-GABARAPL2^{G116A}	**GCC**TTCTGATGCCCAACTTTCTTGTACAAAGTG	AAAAGTGTTCTCTCCGCTGTAGGCCA

Table 2.3. List of primers used in this thesis

The general procedure selected in this work to perform point mutations in LC3 subfamily members is illustrated in **Figure 2.2** and described in **Protocol 2.**

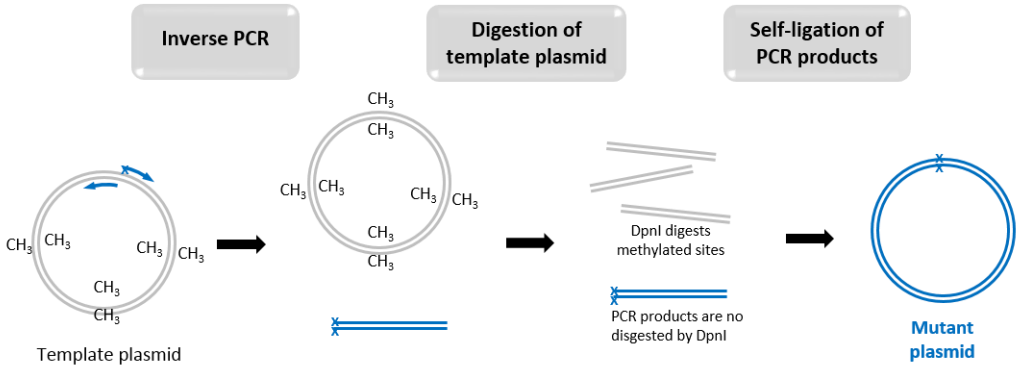

Figure 2.2. Flow chart of KOD-Plus Mutagenesis Kit. An inverse PCR-based site-directed mutagenesis.

Protocol 2. Site-directed mutagenesis (KOD-Plus polymerase)

1. Design of primers: Introduce the mutation in the 5´ of the sense primer. Primers can be synthesized and purified by sigma or IDT.
2. Mix (Total volume 25 µl).
    a. 17.5 µl PCR grade water
    b. 2.5 µl 10X buffer for iPCR
    c. 2.5 µl dNTPs (2mM)
    d. 0.75 µl Forward primer (10 pmol/µl)
    e. 0.75 µl Reverse primer (10 pmol/µl)
    f. 0.5 µl DNA Plasmid template (10 ng/µl)
    g. 0.5 µl KOD-Plus-DNA polymerase (1 U/µl)
3. Inverse PCR program:
    a. 2 min 94ºC
    b. Repeat the next steps X times depending on plasmid length (1 cycle/kb)
        i. 10 sec 98ºC
        ii. 30 sec at Tm – (5-10ºC)
        iii. Y min 68ºC: Time depends on plasmid length (1min/kb)
4. To digest the template plasmid, add 1 µl of DpnI restriction enzyme (10 U/µl) to the 25 µl of PCR product and incubate 1 hour at 37ºC.
5. To ligate the PCR product, prepare the following mix (total volume 15 µl) and incubate 1 hour at 16ºC:
    a. 1 µl DpnI-treated PCR product
    b. 3.5 µl PCR grade water
    c. 2.5 µl Ligation high (T4 Ligase + Buffer Mixture)
    d. 0.5 µl T4 polynucleotide Kinase (5 U/µl)
6. Transform 50 µl DH5α *E. coli* chemo-competent cells with 10 µl of ligation product (See **Protocol 1**).
7. Select 5 colonies and extract their DNA by miniprep (See **Protocol 1**) and sequence them to verify the presence of the desired mutation (Secugen, S.L.).

Adapted from KOD-Plus-Mutagenesis Kit manual (SMK-101).

The chimeras (LC3A/B, LC3C/B), the GFP-tagged double mutants (GFP-LC3A-EE, GFP-LC3B-AK) the LC3A^{R10,11A} mutant (GST- and GFP-tagged versions) (Chapter 3) together with the Cys mutated version of GST-LC3/GABARAP proteins (GST-LC3A^{C17S,G120}, GST-LC3B^{G120C}, GST-LC3C^{G126C}, GST-GABARAP^{G116C}, GST-GABARAPL1^{G116C}, GST-GABARAPL2^{C15S,G116C} (Chapter 4) were synthesized by GenScript (Genscript Europe, Rijswijk, Netherlands).

2.3. Expression of recombinant proteins in bacterial cells and purification

2.3.1. Protein expression in bacterial cells

Plasmids encoding His-GFP, GST, GST-ATG3, GST-LC3A, GST-LC3B, GST-LC3C, GST-GABARAP, GST-GABARAPL1, GST-GABARAPL2, and the corresponding mutant forms of the LC3/GABARAP-family members were transformed onto *E. coli* BL21 (λDE3) cells. Proteins were expressed as Glutathione S-transferase (GST)-tagged or Histidine (His)-tagged fusion proteins. First, cells were picked either from an *E.coli* BL21 (λE3) colony transformed with the plasmid of interest or from a glycerol stock. They were grown in a 50 ml flask containing LB-Ampicillin (Amp) medium. Then, they were incubated in an orbital shaker at 37ºC overnight. The culture was escalated by adding 10 ml of the overnight saturated culture to 1 L LB-Amp medium, and the mixture was incubated at 37ºC to 0.6-0.8 absorbance (A_{600}), then isopropyl-β-D-1-tiogalactopiranósido (IPTG) was added to start the induction of the recombinant protein expression. After IPTG addition, samples were incubated in an orbital shaker for 16 h at 20ºC and bacteria were collected by centrifugation (4500 x g for 15 min, 4ºC) in a Beckman Coulter centrifuge using a JLA-9.100 rotor (Beckman Coulter, Fullerton, California, U.S.A). The supernatant was discarded and the pellet with the cells expressing the protein was stored at -80ºC until the purification.

2.3.2. Purification of GST-tagged proteins from bacterial cells

ATG3, GST and LC3/GABARAP-family members with cleaved and uncleaved GST-tag were purified by affinity chromatography followed by a further size exclusion chromatography step. See **Protocol 3**, **Table 2.4** and **Table 2.5** for details.

Protocol 3. Purification of GST-tagged proteins from bacterial cells

1. Lysate the cells by resuspension in Breaking buffer (See **Table 2.4** for buffers details) and incubation at 4ºC in an orbital shaker for 40 min to allow disruption of the bacterial cell wall by lysozyme.
2. Sonicate on ice, to avoid overheating, 10 sec on / 10 sec off, 40 cycles.
3. Centrifuge at 30000 x g for 30 min at 4ºC in a Beckman Coulter centrifuge using a JA-25-50 rotor. Discard the pellet and filter the supernatant through 0.45 µm and 0.2 µm filters. Keep on ice for subsequent purification steps.
4. Wash the Glutathione Sepharose 4B beads (1ml for 4L of culture) by centrifugation, three times with ten bed volumes of distilled water and five times with Breaking buffer.
5. For the affinity chromatography step: mix the bacterial supernatant with washed beads and incubate the mixture for 3 h in an orbital rotator at 4ºC to allow binding of Glutathione S-Transferase (GST) tag to glutathione.

Continues in next page

6. Pack the beads with bound proteins in a gravity flow column PD10 (Bio-Rad), and remove the Flow-Through (FT). Then, wash the column with 5 bed volumes of the indicated washing buffer described in **Table 2.4.**

    a. For cutting the GST-tag: Prepare a mixture of cleavage buffer + protease (final volume 1500 µl), add to the beads in the column and transfer the beads to a 15 ml falcon tube (See **Table 2.5** for details). Transfer to the gravity flow column.

    b. For purification of the GST-tagged protein: Prepare a mixture of GST-elution buffer containing Glutathione reduced (G4251, Sigma) (final volume 5 ml), add to the beads in the column and transfer the beads to a 15 ml falcon tube, incubate 1h at RT in an orbital shake (See **Table 2.4** for details). Transfer to the gravity flow column.

7. Elute the protein from the gravity flow column with Elution buffer (See **Table 2.4** for details). Collect four fractions of 4 ml.

8. Analyse the fractions with SDS-PAGE analysis and Coomassie Brilliant Blue staining. Concentrate protein enriched fractions up to 500 µl using Amicon Ultra-4 Centrifugal Filter (4 mL, 3 kDa cut-off).

9. For the size exclusion chromatography step: Inject the protein in a Superdex75 10/300 GL size exclusion column previously equilibrated in Superdex Buffer (See **Table 2.4** for details).

10. Collect the fractions corresponding to the expected molecular weight and analyze with SDS-PAGE and Coomassie Brilliant Blue staining.

11. Concentrate protein enriched fractions up to the desired concentration. Put in aliquots, flash-freeze and store in 20% glycerol at -80ºC until further use.

Buffer	Buffer composition		
Breaking buffer	LC3/GABARAP	PBS 1x, 20 mM Tris-HCl pH 7, 150 mM NaCl, 1mM DTT supplemented with lysozyme, protease inhibitors and DNase	
	ATG3		
	GST/GST-LC3/GABARAP	50 mM Hepes pH 7.5, 300 mM NaCl, 1mM DTT supplemented with lysozyme, protease inhibitors and DNase	
Washing buffer	LC3/GABARAP	PBS 1x/ 50mM Tris pH 7,3, 1 mM DTT	
	ATG3	1	PBS 1x pH 7.4, 1 mM DTT
		2	PBS 1x, 50 mM Tris pH 8.7, 1 mM DTT
		3	PBS 1x, 50 mM Tris pH 8.7, 500 mM NaCl, 1 mM DTT
	GST/GST-LC3/GABARAP	1	50 mM Hepes pH 7.5, 300 mM NaCl, 1 mM DTT
		2	50 mM Hepes pH 7.5, 500 mM NaCl, 1 mM DTT
Cleavage buffer	LC3/GABARAP	Thrombin	140 mM NaCl, 2,7 mM KCl, 10 mM Na_2HPO_4, 1,8 mM KH_2PO_4, 1 mM DTT, pH 7,3
	ATG3	PreScission	50 mM Tris, 150 mM NaCl, 1 mM EDTA, pH 7,5
Elution	LC3/GABARAP	50 mM Tris pH 7.5,150 mM NaCl, 1 mM EDTA, 1 mM DTT	
	ATG3		
	GST/GST-LC3/GABARAP	50 mM Hepes pH 7.5, 300 mM NaCl, 1 mM DTT, 20 mM L-Gluthatione reduced	
Superdex	LC3/GABARAP	50 mM Tris pH 7.5, 150 mM NaCl, 1 mM EDTA, 1 mM DTT	
	ATG3		
	GST/GST-LC3/GABARAP	25 mM Hepes pH 7.5, 150 mM NaCl, 1 mM DTT	

Table 2.4. List of Buffers used for GST-tagged proteins purification.

CLEAVAGE STEP			
Protease	Proteins	Amount	Procedure
Thrombin protease	LC3A LC3B GABARAP GABARAPL2	45 µl (Stock: 1U/µl)	O/N RT (Falcon 15, immobile) →4 fractions (4ml)
	LC3C GABARAPL1	60 µl (Stock: 1U/µl)	O/N RT (Falcon 15, immobile) →4 fractions (4ml)
PreScission protease	ATG3	50 µl (Stock: 2U/µl)	4h 4ºC (Falcon 15, orbital rotator) →2 fractions (4ml) O/N 4ºC (Gravity flow column)→2 fractions (4ml)

Table 2.5. Differences in cleavage step among the proteins purified in this thesis.

2.3.3. Purification of His-tagged proteins from bacterial cells

GFP protein was purified by affinity chromatography followed by a further size exclusion chromatography step. See **Protocol 4** for details.

Protocol 4. Purification of His-tagged proteins from bacterial cells

1. Lysate the cells by resuspension in Breaking buffer (50 mM Hepes pH 7.5, 300 mM NaCl, 1mM TCEP supplemented with lysozyme, protease inhibitors and DNase) and incubate at 4ºC in an orbital shaker for 40 min to allow disruption of the bacterial cell wall by lysozyme.

2. Sonicate on ice, to avoid overheating, 10 sec on / 10 sec off 40 cycles.

3. Centrifuge at 30000 x g for 30 min at 4ºC in a Beckman Coulter centrifuge using a JA-25-50 rotor. Discard the pellet and filter the supernatant through 0.45 µm and 0.2 µm filters. Keep on ice for subsequent purification steps.

4. For the affinity chromatography step inject the bacterial supernatant to a 5-ml nickel-nitrilotriacetic acid (Ni-NTA) column (GE Healthcare).

5. Discard the Flow-Through (FT), wash the column with washing buffer (50 mM Hepes pH 7.5, 300 mM NaCl, 2 mM TCEP, 10 mM Imidazole) and elute the protein via a stepwise imidazole gradient (50, 75, 100, 150, 200, and 300 mM).

6. Analyze the fractions with SDS-PAGE analysis and Coomassie Brilliant Blue staining. Concentrate protein enriched fractions up to 500 µl using Amicon Ultra-4 Centrifugal Filter (4 mL, 3 kDa cut-off).

7. For the size exclusion chromatography step: Inject the protein in a Superdex75 10/300 GL size exclusion column previously equilibrated in Superdex Buffer (25 mM Hepes pH 7.5, 150 mM NaCl, 1 mM DTT).

8. Collect the fractions corresponding to the expected molecular weight and analyze with SDS-PAGE and Coomassie Brilliant Blue staining.

9. Concentrate protein enriched fractions up to the desired concentration. Put in aliquots, flash-freeze and store at -80ºC until further use.

2.4. Baculovirus expression system and recombinant protein purification

The baculovirus expression vector system (BEVS) was developed in the 1980s. This system can be used to express proteins in insect cell lines and produce valuable and functional proteins that are similar to mammalian cell proteins (Kost *et al.*, 2005).

2.4.1. Bac to bac system

Recombinant baculoviruses (rBV) were generated with a Bac-to-Bac system (**Figure 2.3**). This method is based on the transposition of the recombinant genes into the infective genome of the Baculovirus, which is present in a vector (called bacmid) multiplied in the *E. coli* DH10Bac strain (Luckow *et al.*, 1993). These cells, apart from the bacmid, contain a helper plasmid that carries the transposase gene responsible for the transposition of the GOI from the donor plasmid into the bacmid.

This system was used for the expression of recombinant mATG7 and ATG12–ATG5-ATG16 (E3) complex. Once the relevant gene is cloned in a donor plasmid (*e.g.* FastBAc or pGBdest), this plasmid will be used to transform *E. coli* DH10Bac bacteria, where the recombinant gene transposition into the bacmid will take place. Then, the recombinant colonies, containing the recombinant bacmid are selected, and the rBV are generated by insect cell transfection with the extracted bacmids. Finally, the bacmid-transfected cell supernatants, containing rBV, are used to infect new insect cells, where the rBV will be amplified and the protein of interest overexpressed (See section 2.4.2) (**Figure 2.3**).

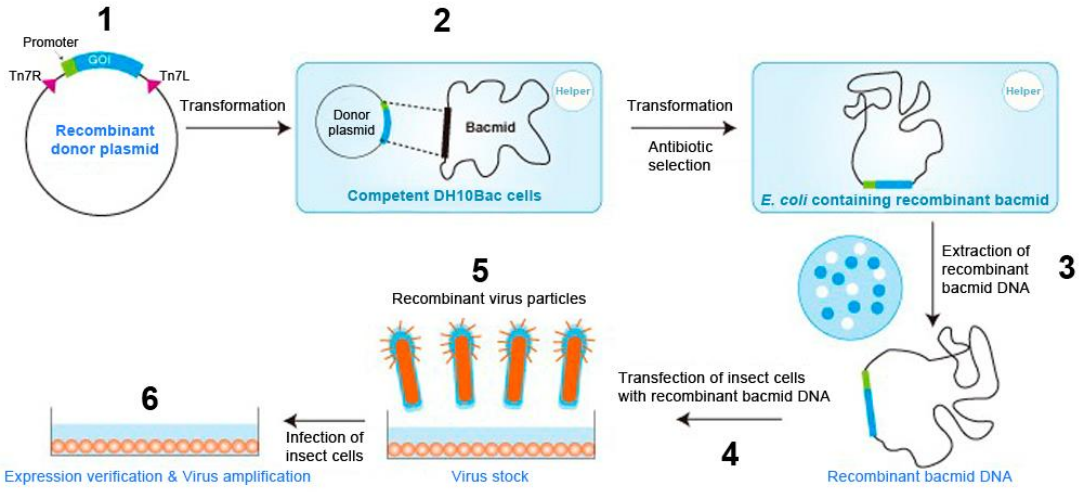

Figure 2.3. Bac to bac system: 1) Cloning of the gene of interest (GOI) into a donor plasmid (*e.g.* FastBAc, or pGBdest): These plasmids contain Tn7 target sites on both sides of the cloning site. 2) Transformation of the donor plasmid into *E. coli* DH10Bac cells. 3) Selection of cells that contain the recombinant bacmid with the GOI and extraction of the bacmid. 4) Transfection of insect cells with the bacmid to allow baculovirus production.5) Isolation of the produced recombinant baculovirus. 6) Infection of cells with the rBV to express the protein of interest. Adapted from Invitrogen™ manuals.

In order to generate, amplify and express the recombinant Baculoviruses (rBV) the Sf9 insect cell line (B82501, Thermo Fisher) was used. This cell line originated from the IPLBSF-21 cell line, derived from the pupal ovarian tissue of the fall armyworm, *Spodoptera frugiperda*. Sf9 cells were cultured in suspension at 27ºC in ESF 921 Insect Cell Culture Medium (Expression systems) supplemented with 10% penicillin/streptomycin (Merck). Details on the plasmids used to generate the mATG7 and E3 rBVs are in **Table 2.1**. Protocols for recombinant bacmid extraction and recombinant baculovirus productions can be found in **Protocol 5** and **Protocol 6**, respectively. See also Chapter 4 (Section 4.3.2).

Protocol 5. Transposition and bacmid extraction

1. Transform the donor plasmid with the gene of interest (GOI) into *E. coli* DH10BacY electrocompetent cells (an YFP containing strain) (See **Protocol 1**).
2. Plate them into plates containing:
    a. Kanamycin (50 µg/ml): resistance of the bacmid in *E. coli* DH10BacY cells.
    b. Gentamicin (7 µg/ml): resistance of the donor plasmid containing the GOI.
    c. Tetracycline (10 µg/ml): resistance of the helper plasmid.
    d. X-gal (200 µg/ml): artificial lactose substrate processed to galactose by the LacZ gene (β-galactosidase) present in the bacmid. The reaction turns the colonies blue.
    e. IPTG (165 µM): Inductor of the lactose operon in *E. coli* where the GOI should be integrated.
3. Let them grow for 48 hours:
    a. Blue colonies: No GOI integration, LacZ in the bacmid is intact and it can process X-gal to galactose and produce blue colonies.
    b. White colonies: LacZ is disrupted due to the integration of the GOI in the bacmid of the DH10Bac cells.
4. Check positive white colonies by PCR analysis using primers (M13) that bind to the transposition zone of the bacmid:
    a. Single band, 300bp: No insert, the band corresponds to the fragment between M13 primers→ Repeat.
    b. Two bands, 2430 bp + size of insert (GOI) and 300 bp: Mixed colonies→Repeat.
    c. Single band, 2430 bp + size of insert (GOI) → Positive colony; inoculate in 4 ml of LB + antibiotics [Kanamycin, gentamicin and tetracycline (same concentrations as before)].
5. Extraction of the bacmid:
    a. Centrifuge the bacteria from the O/N cultures.
    b. Use the Kit “Gene Jet Plasmid Miniprep” (K0502, ThermoFisher) (only the three first steps).
    c. Centrifuge 10 min, 15800 x g and transfer to a 2 ml tube containing 800 µl of isopropanol. Incubate 10 min on ice.
    d. Centrifuge 15 min, 15800 x g, remove the supernatant and add 500 µl of 70% EtOH. Invert the tube several times.
    e. Centrifuge 5 min, 15800 x g, remove the supernatant gently and let it dry.
    f. Resuspend in 40 µl of miliQ water and measure DNA concentration at 260 nm.
    g. The usual concentration is 900 ng/µl (between 500-2500 ng/µl is okay, less than 200 ng/µl is probably genomic DNA).
    h. Before use, incubate 10 min at 70ºC to make sure no bacteria remain.

Protocol 6. Recombinant Baculovirus production

1. Plate 10^6 Sf9 insect cells in a 6-well plate with 2.5 ml of insect cell medium containing penicillin/streptomycin (10^6 cells per well).

2. Transfection: Prepare a mixture with the transfection agent (FuGENE HD (E2311, Promega) and the bacmid. For each well:
    a. DNA mix: Dilute 2.5 µl of bacmid in 100 µl of medium without antibiotics.
    b. Transfection mix: Mix 5µl of FuGENE HD with 50 µl of medium. Incubate 5 min.
    c. Add the transfection mix to the DNA mix and incubate 10 min.
    d. Transfer the mix to the well in a dropwise manner.

3. Check three days later:
    a. Cells with the same size and no fluorescence → No transfection occurred.
    b. Cells are bigger, clumpier and show YFP fluorescence → Transfection occurred and "V0" baculovirus is being generated.

4. Harvest V0 baculovirus when almost all the cells are infected (normally 7 days after transfection) by taking the supernatant.

5. Infect a 30 ml suspension culture (10^6 cells/ml) with the V0 baculovirus.

6. Check the infection using two parameters:
    a. Fluorescence: Check the amount of fluorescent/infected cells.
    b. Cell viability: Using a cell counter that measures the ratio between live and trypan blue colored cells. When viability drops from 98% to 90% (4-5 days) it is time to harvest the V1 baculovirus.

7. Harvesting V1: Centrifuge at 700 g during 5 min and filter the supernatant. It can be store at 4ºC for up to 6 month.

2.4.2. Protein expression in insect cells

Recombinant baculoviruses (rBV) expressing His-tagged mATG7 or the needed proteins for E3 complex formation (ATG12, ATG7, ATG10, ATG5, Strep-tagged ATG16L) were used to infect Sf9 insect cells. Before infection, a preculture of 125 ml of Sf9 cells (10^6 cells/ml) was started and expanded by dilution until 10^6 cells/ml in 1 L of culture were obtained (normally 3 days after the first preculture). The next day, 1 ml of the baculovirus containing solution (V1) (See Protocol 6 for details) was added to the cells. Two days after infection the cell count, viability and fluorescence were checked every day. Once the cells were fluorescent and reached a viability of 85-90%, they were harvested (usually after 3-4 days). Insect cells expressing the protein of interest were collected by centrifugation (3315 x g for 10 min, 4ºC) in a Beckman Coulter centrifuge using a JLA-9.100 rotor. The supernatant was discarded and the pellet with the cells expressing the protein was washed with cold PBS1X and subjected to a further centrifugation step in order to completely remove the culture medium. Finally, the cells were flash frozen and kept at -80ºC until protein purification.

2.4.3. Purification of Strep-tagged proteins from insect cells

E3 and GFP-E3 complex were purified thanks to the presence of a Strep-tag in one of the components of the complex, ATG16L1 (Fracchiolla *et al.*, 2020). It was purified by affinity chromatography followed by a further size exclusion chromatography step. See **Protocol 7** and Chapter 4 (Section 4.3.2) for details.

Protocol 7. Purification of Strep-tagged proteins from insect cells

1. Resuspend the insect cells expressing the protein in ice-cold Breaking buffer (50 mM Hepes, pH 7.5, 300 mM NaCl, 2 mM $MgCl_2$, 1 mM DTT, supplemented with complete protease inhibitors (11836170001, Sigma), Protease Inhibitor Cocktail (P8849, Sigma), and Benzonase Nuclease (E1014, Sigma).
2. Lysate the insect cells by extrusion in a tissue homogenizer.
3. Centrifuge at 38398 x g for 60 min at 4ºC in a Beckman Coulter centrifuge using a JA-25-50 rotor. Discard the pellet and filter the supernatant through 0.45 µm and 0.2 µm filters, and finally keep on ice for subsequent purification steps.
4. For the affinity chromatography step, inject the insect cell supernatant to a 5-ml StrepTactin column (GE Healthcare) to promote the biding of Strep-tagged proteins.
5. Discard the Flow-Through (FT), wash the column with washing buffer (25 mM Hepes, pH 7.5, 300 mM NaCl, 1 mM DTT) and elute the protein with 2.5 mM D-Desthiobiotin (D1411, Sigma) in 25 mM Hepes, pH 7.5, 300 mM NaCl, and 1 mM DTT.
6. Analyze the fractions with SDS-PAGE analysis and Coomassie Brilliant Blue staining. Concentrate protein enriched fractions up to 500 µl using Amicon Ultra-15 Centrifugal Filter (15 mL, 30 kDa cut-off).
7. For the size exclusion chromatography step: Inject the protein in a Superose 6 column (Increase 10/ 300; GE Healthcare) previously equilibrated in SEC Buffer (25 mM Hepes pH 7.5, 300 mM NaCl, 1 mM DTT).
8. Collect the fractions corresponding to the expected molecular weight and analyze with SDS-PAGE and Coomassie Brilliant Blue staining.
9. Concentrate protein enriched fractions up to the desired concentration. Put in aliquots, flash-freeze and store at -80ºC until further use.

Techniques in **Protocols 5, Protocol 6** and **Protocol 7** were developed with the help of S. Martens and D. Fracchiolla during the author´s stay at Max Perutz Labs (Vienna, Austria) and implemented later at the Instituto Biofisika (UPV/EHU, CSIC).

2.4.4. Purification of His-tagged proteins from insect cells

Mouse ATG7 (mATG7) was purified thanks to the presence of a His-tag in its N-terminal region. It was purified by affinity chromatography followed by a further size exclusion chromatography step. See steps 1-3 from **Protocol 7** for insect cell lysis and steps 4 to 9 from **Protocol 4** for His-tagged purification. The size exclusion step was performed using a Superdex 200 10/300 (GE Healthcare).

2.5. Protein analysis

2.5.1. Protein concentration measurements

2.5.1.1. Absorbance at 280 nm

This measurement was performed to calculate the concentration of the proteins purified. It is based on the fact that proteins in solution absorb ultraviolet light with absorbance maxima at 280 nm, due to the presence of amino acids with aromatic rings. Protein concentration can be estimated using Lambert-Beer equation (**Equation 2.1**) where A is the absorbance, ε is the molar extinction coefficient, c is the concentration and l is the path length. The extinction coefficients needed for protein concentration measurements of the purified proteins used in this thesis are in **Table 2.6**

$$A = \varepsilon \, c \, l$$

Equation 2.1. Lambert-Beer equation.

Purified protein	Molecular weight (kDa)	Molar extinction coefficient, ε (M^{-1} cm^{-1})
LC3A Gly C-ter exposed	14.51	5960
LC3B Gly C-ter exposed	14.51	5960
LC3C Gly C-ter exposed	15.03	8940
GABARAP Gly C-ter exposed	13.82	11920
GABARAPL1 Gly C-ter exposed	14.30	14900
GABARAPL2 Gly C-ter exposed	13.91	18450
ATG3	35.86	45840
9His-mATG7	79.28	83310
ATG12–ATG5-ATG16L1-Strep (E3)	120.57	148280
Strep-GFP-E3	148.26	170170
His-GFP	29.11	23380
GST	25.50	42860
GST-LC3A C-ter exposed	40.66	48820
GST-LC3B C-ter exposed	40.66	48820
GST-LC3C C-ter exposed	41.17	51800
GST-GABARAP C-ter exposed	39.97	54780
GST-GABARAPL1 C-ter exposed	40.45	57760
GST-GABARAPL2 C-ter exposed	40.05	61310

Table 2.6. Extinction coefficients (ε) of the proteins purified in this thesis. Obtained with ProtParam (Expaxy).

2.5.1.2. Bicinchoninic acid Assay (BCA)

This measurement was performed to calculate the concentration of proteins present in cell lysates (See **Protocol 24**). The assay is performed using Pierce TM BCA protein assay kit (23227, Thermo Scientific) and following the manufacturer´s instructions. It is based on the fact that the presence of peptide bonds promotes the reduction of Cu^{2+} ions in a temperature dependent manner. The reduced Cu^{1+} is able to interact with bicicinchoninic acid and form a purple-colored complex that absorbs light at 562 nm. Therefore, the absorbance of the mixture at 562 nm is proportional to the amount of

protein present in the solution. A set of prediluted BSA protein assay standards allow the quantification of the concentration of proteins in the sample.

2.5.2. Protein electrophoresis

This technique was especially useful for the detection of proteins during their purification (See **Protocol 3, 4 and 7**) and in flotation assays (See **Protocol 16**). It is also a needed step for Western Blot analysis (see **Protocol 24**) and for the detection and quantification of lipidated-proteins during *in vitro* assays including the UBL-system components (See Lipidation assays in Chapter 4).

Protein separation was achieved by SDS-PAGE in 12.5 or 15% (w/v) acrylamide gels. Samples were mixed with Laemmli loading buffer (6x) supplemented with β-mercapthoethanol and heated at 90ºC for 5 min. Broad-range and precision (unstained and prestained) standards (Bio-Rad) were used as molecular weight markers. Electrophoresis was performed at 150 V in running buffer (3.028 g Tris, 14.41 g glycine, 1 g SDS and H_2O to 1 L). For quick protein visualization, the gel was stained for at least 10 min in a solution containing 0.1% (v/v) Coomassie Brilliant Blue R-250, 40% (v/v) methanol and 10% (v/v) acetic acid. Background staining was eliminated by washing with 10% (v/v) acetic acid solution and images were taken on a Gel Doc™ EZ Imager (Bio-Rad).

2.5.3. Determination of protein structure by circular dichroism (CD)

Circular Dichroism (CD) it is an excellent tool for rapid determination of the secondary structure and folding properties of peptides and proteins in physiological buffers (Martin & Schilstra, 2008). In the present thesis, CD spectroscopy in the far-UV has been used to obtain an estimation of the average secondary structure of LC3/GABARAP proteins as well as to assess the structural integrity of the mutant proteins. Measurements were performed in a thermally controlled Jasco J-810 spectropolarimeter (Jasco Spectroscopic Co. Ltd., Hachioji, Japan) at 37ºC using a 1 mm optical path quartz cuvette. Data were collected every 0.2 nm at 50 nm/min from 260 to 200 nm with a bandwidth of 2 nm, and results were averaged from 20 scans. Buffer contribution was subtracted, and data converted to mean residue molar ellipticity [θ].

2.5.4. Protein labelling

Different strategies can be used in order to detect proteins in experiments performed using microscopy techniques. In this thesis, to detect them in cells, LC3/GABARAP isoforms were transfected as GFP-fusion proteins (see Chapter 3 and **Protocol 23**). The GFP-tag included in one of the components of the E3 complex (ATG16L1) also allowed its detection (see Chapter 5).

For *in vitro* assays, there are many different fluorescent dyes available that can be chemically bound to the proteins. This is the case of Alexa Fluor 633 NHS Ester (A20005, Thermo Fisher). This dye is able to label primary amines of proteins. A protocol for LC3/GABARAP protein labelling is described in **Protocol 8.**

Protocol 8. Protein labelling with Alexa NHS Ester dye

1. Purify the protein in Labelling buffer (25 mM Hepes, 150 mM NaCl, pH 7.5). It is important that the buffer does not contain Tris (or any other amine-containing substances).
2. Mix 1 ml of protein (25 µM) with 5 µl of Alexa Fluor 633 (20 mM).
3. Incubate for 90 min at 37ºC with continuous stirring.
4. Centrifuge at 15800 x g for 3 min at 4ºC to discard aggregated dye.
5. Remove un-conjugated dye by gel filtration in Sephadex G-25M using labelling buffer as the eluent.
6. Determine the degree of labeling by measuring the absorbance of the protein-dye conjugate at 280 nm and that of the dye at 633 nm.
7. Load the labeled samples in a SDS-PAGE gel and visualize them using a VersaDoc MP 4000 Imaging System (Bio-Rad).

2.5.5. Protein-protein interaction

2.5.5.1.Analytical size exclusion chromatography

Size exclusion chromatography (SEC), commonly known as gel filtration, separate molecules according to differences in size and shape (hydrodynamic radius, Mr) as they pass through a gel filtration medium packed in a column. When molecules of various sizes flow into the column, smaller molecules flow more slowly because they penetrate deep into the pores, whereas larger molecules flow quickly through the column because they do not enter the pores. Consequently, larger molecules elute from the column sooner and smaller molecules later, which effectively sorts the molecules by size. SEC, as well as other methods such as two-hybrid approaches or pull down experiments, is a widely used technique for studying protein-protein interactions (S. S. Li & Giometti, 2007).

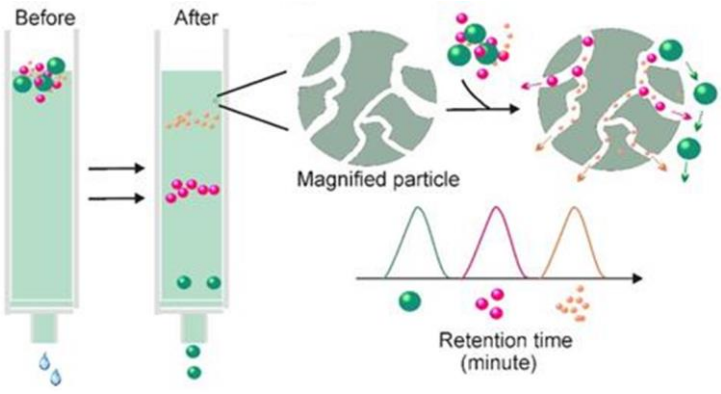

Figure 2.4. Principle for Size-exclusion chromatography. Taken from Yang *et al*., 2020.

In this thesis apart from its use as the final chromatography steps in purifications (See **Protocol 3**, **Protocol 4** and **Protocol 7**), it has been used as a preliminary approach to determine LC3/GABARAP potential oligomerization as it can provide valuable information about protein quaternary structure. The steps followed are summarized in **Protocol 9**.

Protocol 9. Analytical SEC: Oligomerization assays

1. Prepare vesicles of the desired lipid composition as described (**Protocol 13**). Perform a Fiske assay to determine the exact lipid concentration (**Protocol 11**).
2. Equilibrate a Superdex 75 10/300 in a Buffer containing 0.75% CHAPS (v/v).
3. Incubate proteins with liposomes (final volume 150 µl) under continuous stirring (1100 rpm) 30 min at 37ºC
4. Solubilize vesicles with 2% CHAPS [Add 20 µl of CHAPS (20% v/v)]
5. Inject 100 µl of sample in in a Superdex 75 10/300. Keep 10 µl of the input sample and mix with LB6X.
6. Collect fractions of 500 µl.
7. Analyze the chromatogram: Check the appearance of new peaks.
8. Load the fractions in a SDS-PAGE gel and analyze with Coomassie Brilliant Blue staining.

2.5.5.2. Microscope-based bead protein–protein interaction assay

This technique (Fracchiolla *et al.*, 2020) was used to assess the interaction between E3 complex and LC3/GABARAP proteins. See **Protocol 10** for the basic procedure.

Protocol 10. Microscopy-based bead protein–protein interaction assay

1. Centrifuge (90 s, 1500 x g, 4ºC) Glutathione Sepharose 4B beads (GE Healthcare, 17-0756-01) to remove ethanol and equilibrate in buffer.
2. Incubate the “bait protein” (GST-tagged protein) with beads on a rotating wheel for 1 hour at 4ºC.
3. Clean non-bound GST-proteins by successive rounds of centrifugation and new buffer addition.
4. Prepare 100 µl of the “prey protein” at the desired concentration in a 8-well IBIDI chamber previously blocked with BSA.
5. Add 5 µl of the beads with the “bait protein” into the IBIDI well and incubate 30 min at room temperature.
6. Get images on a Leica SP5 confocal microscope (Leica Microsystems, Wetzlar, Germany) with a 63× Plan Apochromat 1.4 NA objective.

This technique was developed with the help of S. Martens and J. Sawa-Makarska during the author´s stay at Max Perutz Labs (Vienna, Austria) and implemented later at the Instituto Biofisika (UPV/EHU, CSIC).

2.6. Membrane lipid model systems: Liposomes

The complexity of biological membranes, both from the structural and functional standpoint, presents numerous difficulties for their study. Therefore, numerous model membrane systems have been developed for studying the properties of pure lipids, lipid mixtures, and reconstituted lipid-protein systems. These model systems can be grouped as monolayers, planar bilayers, and liposomes or vesicles (Gennis, 1989). In the present work, lipid vesicles or liposomes have been used. Liposomes are lipid structures in a bilayer configuration enclosing an aqueous solution. Liposomes are spontaneously generated when dispersing cylindrical-shaped lipids in aqueous solutions, thus they constitute a convenient source of lipidic model membranes. Liposomes have been extensively used for measuring fusion, fission, solubilization, leakage, lipid flip-flop, lipid-protein binding and many more events.

Liposomes can be prepared to have a single or several bilayers or lamellae, being unilamellar vesicles the principal system used in this work. Multilamellar vesicles (MLV) are spontaneously formed after lipid hydration and sample shaking (**Figure 2.5**), usually containing between 7 and 10 concentric bilayers, each of them separated by a thin water layer. Vesicles are heterogeneous in size, displaying an average diameter of around 700 nm but ranging from 100 to 5000 nm. MLV are easy and fast to prepare, but they have an important drawback. When treating vesicles with a solubilizing agent, or when looking at a protein effect upon binding to the vesicle, only the effects of interaction with lipids on the external bilayer can be achieved, thus making difficult data analysis and interpretation. To overcome this issue, unilamellar vesicles are generally used (**Figure 2.5**). Unilamellar vesicles are classified according to their size, those with an average diameter of less than 60 nm being named SUV (small unilamellar vesicles), those with an average diameter between 80 and 500 nm are LUV (large unilamellar vesicles) and those with larger, micrometer-ranged diameters, are GUV (giant unilamellar vesicles). Apart from their size, they differ from each other in the method of preparation. See **Figure 2.5** and next sections for details.

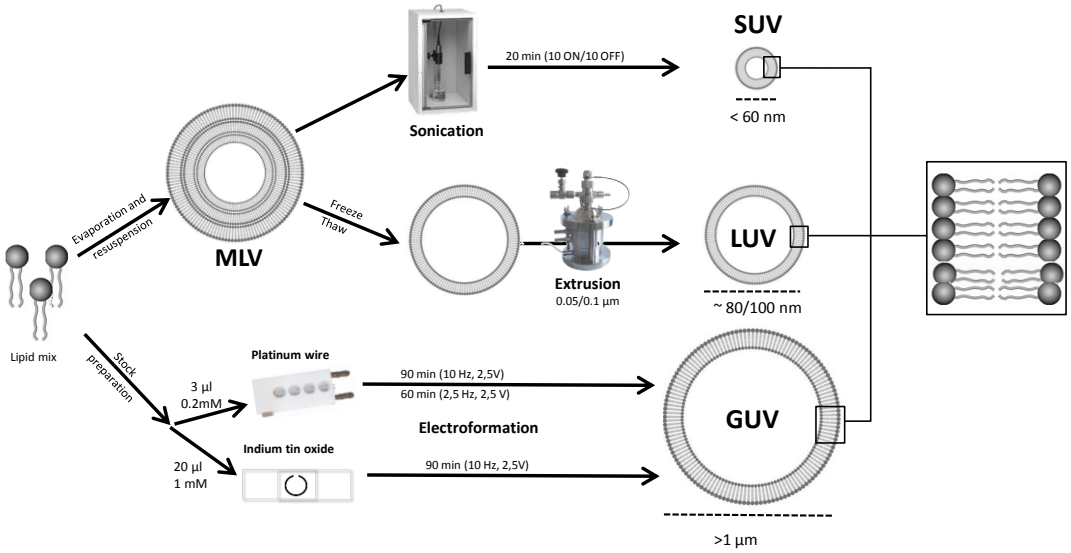

Figure 2.5. Characteristics of the different liposomes used in this thesis (SUV, LUV and GUV): Outline of the preparation method.

2.6.1. Determination of phospholipid concentration (FISKE Assay)

In order to determine the concentration of the lipid stocks needed to prepare liposomes or the concentration of lipids of our liposomes, we use the FISKE assay. It is a well-established method for the quantification of the concentration of phospholipids based on the quantitation of inorganic phosphorous. The approach is based on the initial procedure developed in 1925 by Fiske and Subbarow (1925) and later modified (Bartlett, 1959; Böttcher *et al.*, 1961). Briefly, it consists of hydrolyzing the phospholipids until the lipid phosphate group is free to interact with specific reagents that will color the solution in a concentration-dependent manner (**Protocol 11**).

Protocol 11. FISKE assay

1. Set up a phosphorous calibration curve from which the exact lipid sample concentration will be determined: pipette 0, 25, 50, 75 and 100 nmol phosphorous into duplicate separate test tubes from a 1 mM NaH_2PO_4 standard solution, which will be used to construct the calibration curve.

2. Pipette the sample into separate tubes (at least triplicates) to contain theoretically 50 nmol lipid phosphorous, which will be in the centre of the calibration curve. When pipetting samples in organic solution, use Hamilton syringes.

3. Add 500 µl of a 60% perchloric acid ($HClO_4$) to each tube. Vigorously vortex and introduce the tubes into a heating block at 205ºC for 45 min. This way phospholipid hydrolysis is achieved, leaving free inorganic phosphate.

4. Collect the tubes, cool down to room temperature and pipette the following solutions:

   a. 4 ml 1X ammonium heptamolybdate solution [$(NH_4)_6Mo_7O_{24}.4H_2O$].
   b. 500 µl 10% (v/v) ascorbic acid (add while vortexing).

5. The inorganic phosphate reacts with molybdate, which subsequently reacts with the ascorbic acid giving a yellow-colored solution.

6. Introduce the tubes into a boiling water bath and leave for 6 min. During that period, the solution color is blue-shifted depending on the amount of phosphorous.

7. Finally, cool the tubes down in water and measure the absorbance of each sample at 812 nm. In the present work, an Ultrospec 500 pro spectrophotometer from Amersham Biosciences (Piscataway, NJ, USA) was used for this purpose.

8. To obtain the sample phospholipid concentration, pot the standard absorbance against the phosphorous concentration and adjust to a straight line. Use the slope of the curve and the sample absorbance to find out the sample concentration.

2.6.2. Multilamellar Vesicles (MLV)

MLV generation is the simplest and fastest of all liposome formation methods. A detailed protocol for multilamellar vesicle preparation used in the present work is described below (**Protocol 11, Figure 2.5**).

Protocol 12. Multilamellar Vesicles (MLVs)

1. Prepare pure lipid stocks by dispersing lipids in powder in chloroform/methanol (2:1 v/v) to the desired concentration.
2. Pipette the desired amount of lipid from the stock in organic solution into a glass test tube.
3. Evaporate the organic solvent under a nitrogen gas flow.
4. Completely remove any traces of organic solvent of the sample by placing it into a high vacuum desiccator for 1 h to obtain a solvent-free dried lipid film at the bottom of the test tube.
5. Finally, hydrate the lipid by pipetting the desired amount of an aqueous solution at a temperature above the lipid main phase transition temperature. Shake the suspension by vigorous vortexing for lipid detachment from the bottom of the test tube. By increasing temperature, the lipid is hydrated faster and, when preparing vesicles with a mixture of lipids, a more homogeneous lipid composition through the vesicles can be expected by maintaining every lipid in the fluid phase state. This method is often enough for MLV preparation.
6. Assay the concentration of the vesicle suspension using the Fiske method (**Protocol 11**), because some lipid can be lost in the process.

2.6.3. Small Unilamellar Vesicles (SUV)

Due to their small diameter (smaller than 60 nm) SUV present a high curvature stress, which induces a lipid enrichment in the external monolayer as compared to the inner one (Szoka & Papahadjopoulos, 1980). Their curvature stress makes these vesicles good model membranes for the study of membrane fusion and/or fission related processes (Nieva *et al.*, 1989), because they may be subjected to such stress conditions *in vivo*.

Small unilamellar vesicles are usually prepared by sonication of MLV suspensions. This is basically done either by bath sonication or by probe tip sonication, in the latter case probes are immersed in the MLV suspension for sonication. In this way, large MLV are broken down into small unilamellar vesicles. In the present work, small unilamellar vesicles have been prepared by probe tip sonication. Thus, the protocol for SUV generation is that of the MLV (**Protocol 11**) but with final sonication of the vesicles for 20 min (10 s on / 10 s off) (**Figure 2.5**). Finally, SUV preparation is centrifuged at 15800 x g, 10 min, to remove aggregates and traces of the sonicator tip. SUV generation can be directly observed as the vesicle solution becomes transparent.

2.6.3.1.Vesicle Size Measurement by Dynamic Light Scattering (DLS)

In order to check the size of our liposomes, the quasi-elastic light scattering (QELS) technique, commonly known as dynamic light scattering (DLS), that is related to the Brownian motion of particles in solution was used (Minton, 2016). By the use of a laser beam focused within a small area in the solution, a measurement of the intensity fluctuations from the scattered light of sample particles crossing through the focused area is performed. The scattered light provides a correlation function from which, by the use of several algorithms, a vesicle size distribution in solution can be obtained (**Figure 2.6**). This value is accompanied by a polydispersity index (PDI), which gives information on the size heterogeneity of the sample. The PDI varies between 0 and 1, where values close to zero indicate homogeneous monodisperse solutions.

In this thesis, the size of liposomes was analyzed using a Malvern Zeta-Sizer Nano ZS (Malvern, Instruments, UK) with a detection range for sizes between 0.6 nm to 6 μm. 50 μl of the sample (around 0.4 mM in lipid) were placed in standard acryl cuvettes at room temperature with a He-Ne laser beam of 5 mW (λ = 633 nm) as the light source. The light scattered by the vesicles was detected with a photomultiplier and the results were analyzed by the commercial software of the instrument.

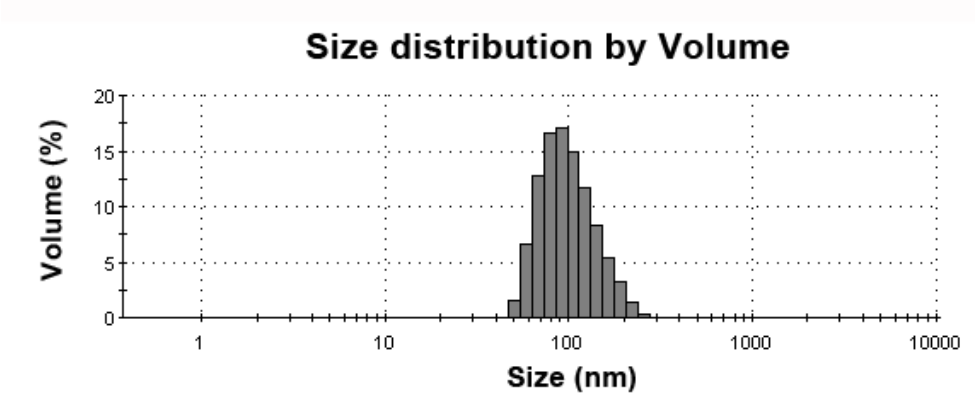

Figure 2.6. Example of a size distribution plot. ePC:DOPE:CL (33:33:33) vesicle population prepared using 100 nm polycarbonate filters.

2.6.4. Large Unilamellar Vesicles (LUV)

Large unilamellar vesicles present, in contrast to small vesicles, low curvature stress and so, when preparing LUV containing a mixture of lipid species, a homogeneous lipid distribution through both monolayers in stable lipid vesicles is generally obtained. In this way, LUV represent a very good model system for most studies. LUV are generally prepared by mechanical extrusion of MLV suspensions through polycarbonate porous filters of the desired pore size (Mayer *et al.*, 1986) (**Figure 2.5**). A detailed protocol (**Protocol 13**) is described below:

Protocol 13. Large Unilamellar Vesicles (LUVs)

1. Steps 1-5 of MLV preparation protocol (**Protocol 12**)
2. Perform 10 freeze/thaw cycles on the MLV solution in order to reduce the number of lamellae in the vesicles: place the vesicles in liquid nitrogen for 1 min, then place them in a water bath at a temperature above that of the lipid with the highest main transition temperature. Finally, vortex the suspension before starting the next cycle. Repeat 10 times.
3. Extrude the vesicles 10 times through polycarbonate filters of the desired diameter (usually between 0.05 and 0.1 μm), using a high-pressure extruder (nitrogen gas flow). The extruder can be connected to a water bath in order to maintain the vesicles at a high temperature if necessary.
4. Assay the concentration of the vesicle suspension using the Fiske method (**Protocol 11**), because some lipid can be lost in the process.
5. Finally, check vesicle size using dynamic light scattering (DLS) (see Section 2.6.3.1)

2.6.5. Giant Unilamellar Vesicles (GUV)

Giant unilamellar vesicles are nowadays one of the most promising model systems in the study of membrane heterogeneity. Their size, in the order of 5-100 micrometers as prepared by electroformation, i.e. comparable to a cell, allows performing direct microscopy on individual vesicles. In 1986, Angelova and Dimitrov developed a method for the generation of giant vesicles based on the exposure of dry lipid films to an aqueous solution under electric fields, which is the most generally applied procedure in the present (Angelova *et al.*, 1992; Angelova & Dimitrov, 1986) (**Figure 2.7**). Vesicle generation under electric fields is strongly dependent on the lipid composition, aqueous solution ionic strength and pH, and on the electric voltage and frequency conditions (Bagatolli, 2003).

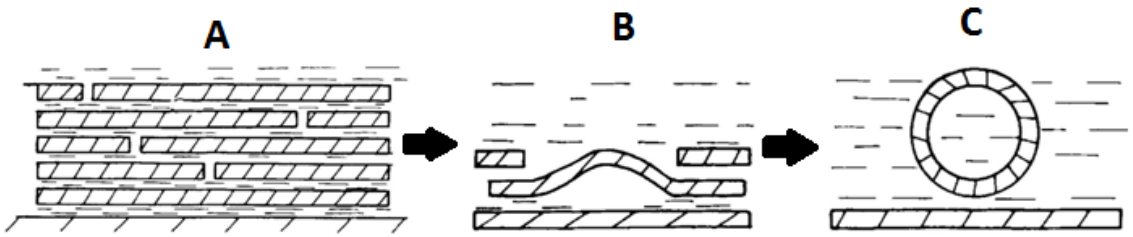

Figure 2.7. Outline of GUV electroformation. The electric field makes the lipid films **(A)** to grow/fuse **(B)** and detach **(C)** yielding GUV. Adapted from (Angelova & Dimitrov, 1986).

GUV in solution are formed and subsequently translated to visualization chambers. To enable their visualization, a high density sucrose solution is encapsulated in vesicles so that when transferred to chambers with an iso-osmotic solution, they sediment at the bottom of the chamber and can be imaged. To obtain giant vesicles in solution (Estes &

Mayer, 2005), two vesicle generation procedures have been applied in this thesis: i) Platinum wire (**Figure 2.5**, **Protocol 14**) or ii) Indium tin oxide (ITO) method (**Figure 2.5, Protocol 15**). A general overview for both procedures is given bellow. For a detailed specification on composition, buffer or microscopy conditions in a particular assay see Materials & Methods in Chapter 5.

Protocol 14. GUV formation: Platinum wire method

1. Prepare GUV lipid stocks of the desire composition by diluting the adequate lipid into a chloroform:dietilether:methanol (4:5:1 v/v) organic solution to a 0.2 mM final concentration.

2. Add 3 µl of the appropriate stock solution onto the surface of different platinum electrodes in a specially designed chamber (Industrias Técnicas ITC, Bilbao, Spain) containing four holes with two platinum electrodes each.

3. Introduce the chamber into a high vacuum desiccator for 1 h to remove any remaining solvent traces and equilibrate for 10 min at the desired temperature by an incorporated water bath.

4. Next, cover the platinum wires with 500 µl of a 300 mM sucrose solution previously equilibrated at the desired temperature. Cover the chamber holes with a glass held in place with vacuum grease to avoid evaporation during electroformation.

5. Connect the platinum electrodes to a function generator and apply the desired electric field (900 mV/10Hz, 2.5V) for 90 min. Vesicles are then generated enclosing sucrose. Temperature during preparation is always higher than that of the lipid with the highest main phase transition temperature.

6. Decrease the applied frequency (2.5 Hz, 2.5V) for 60 min to induce vesicle detachment from the electrodes.

7. Disconnect the electric field and water bath and leave the vesicles 30 min for equilibration.

8. Transfer the vesicle solution to microscopy chambers, which have been pre-treated with BSA (10 mg/ml) for 45 min and contain an iso-osmotic aqueous solution or buffer without sucrose (adjusted using an osmometer). In this way, vesicles sediment due to the higher density of the enclosed sucrose, and this allows direct fluorescent confocal microscopy measurements to be performed.

Protocol 15. GUV formation: ITO method

1. Prepare GUV lipid stocks of the desired composition by diluting the adequate lipid into a chloroform:dietilether:methanol (4:5:1 v/v) organic solution to a 1 mM final concentration.

2. Add 20 µl of the stock solution onto a delimited zone of the surface of indium tin oxide (ITO) coated glass electrodes (10 µl on each conducting surface).

Continues in next page

3. Introduce the glass electrodes into a high vacuum desiccator for 1 h to remove any remaining solvent traces.

4. Assemble the system by putting an O-ring between the ITO glass surfaces with dry lipid in the delimited zone.

5. Add a 300 mM sucrose solution previously equilibrated at the desired temperature inside the space created between the ITO surfaces (thanks to the spacer O-ring). Seal it with a silicone elastomer (Kiwik-cast) to avoid spilling and evaporation.

6. Connect the glass electrodes to a function generator and apply the desired electric field (900 mV/10Hz, 2.5V) for 90 min. Vesicles are then generated enclosing sucrose. Temperature during preparation is always higher than that of the lipid with the highest main phase transition temperature.

7. Transfer the vesicle solution to microscopy chambers, which have been pre-treated with BSA (10 mg/ml) for 45 min and contain an iso-osmotic aqueous solution or buffer without sucrose (adjusted using an osmometer). In this way, vesicles sediment due to the higher density of the enclosed sucrose, and this allows direct fluorescent confocal microscopy measurements to be performed.

2.7. Protein-Lipid interactions

In order to understand the molecular mechanisms by which a protein interacts with biological membranes, the affinity and specificity of the membrane-binding process and the protein topology or conformation in the lipid bilayer need to be studied. Techniques such as X-ray crystallography or electron crystallization are the methods of choice to obtain high-resolution structures of membrane proteins. In addition to this high-resolution techniques, a number of fluorometric, centrifugation, and microscopic assays are also available for studying the molecular mechanisms by which proteins interact with membranes (Zhao & Lappalainen, 2012).

2.7.1. Vesicle flotation assay

In the present work, vesicle flotation assays have been used to analyze the binding capacities of LC3/GABARAP family members to several autophagy-related lipids. Many factors need to be taken into account when designing an experiment for studying membrane interactions of a specific protein. These include: (i) vesicle lipid composition, (ii) protein:lipid ratio, (iii) membrane curvature, (iv) pH and (v) buffer salt concentration.

Liposome flotation assays are widely applied for studying the affinity and lipid specificity of protein binding to membranes (Antón *et al.*, 2016; Hervás *et al.*, 2017; Landeta *et al.*, 2011). In the liposome float-up experiment, the vesicles and bound proteins are enriched by density gradient centrifugation. During ultracentrifugation, due to their lower density, liposomes and liposome-bound proteins float-up to the top fraction of the gradient whereas free protein remains at the bottom (**Figure 2.8, Protocol 16**).

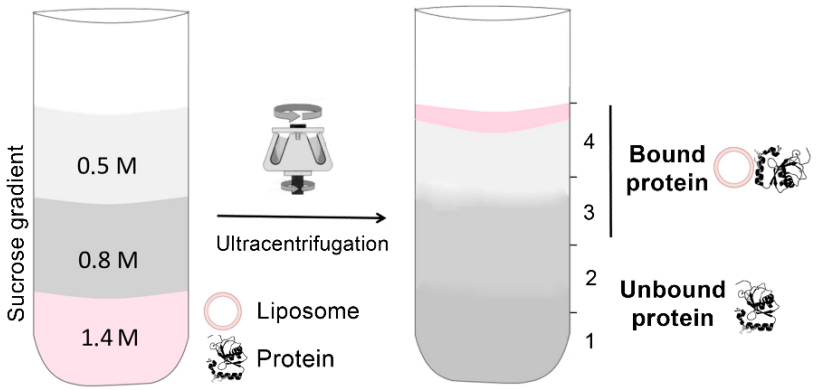

Figure 2.8. Representative scheme of a flotation assay in a sucrose-density gradient. Proteins are incubated with rhodamine-PE (Rho-PE)-labeled LUV and subsequently mixed within the 1.4 M (final concentration) layer of a discontinuous sucrose gradient. After ultracentrifugation, liposomes and liposome-bound protein float up while the unbound protein remains at the bottom. Four equal-volume fractions are collected, 1-4, starting from the bottom; protein found in fractions 3+4 is taken as bound protein.

Protocol 16. Flotation assay in sucrose gradient

1. Prepare LUVs or SUV containing 0.05 mol % Rho-PE and the desired lipid composition as previously described (**Protocol 13** or Section 2.6.3). A Fiske assay is performed to determine the exact lipid concentration (**Protocol 11**).
2. Incubate proteins with liposomes (final volume 200 µl) under continuous stirring (1100 rpm) at 37ºC.
3. Prepare a 2.4 M sucrose stock by mixing 10.69 g of sucrose and 6.25 ml of the assay buffer. Using this stock, prepare two more, with 0.8 and 0.5 M of sucrose.
4. Adjust the protein/lipid mix to 1.4 M of sucrose by mixing (vortex, do not use a pipette) 175 µl of 2.4 M sucrose and 125 µl of the incubation mix.
5. Transfer it to a 1 ml centrifuge tube and make the discontinuous sucrose gradient by adding a second layer (400 µl of 0.8 M sucrose) and then a third one (300 µl of 0.5 M sucrose).
6. Equilibrate the tubes (maximum 0.5 mg of difference) and ultracentrifuge in a TLA-120.2 rotor (Beckman Coulter) at 355040 x g (100000 rpm) 50 min at 4ºC.
7. Take 4 fractions of 250 µl starting from the bottom using a Hamilton syringe and transfer them into a 96-well plate.
8. To assure vesicle flotation, measure rhodamine (Rho-PE) fluorescence of the fractions in a microplate reader Synergy HT (BioTek Instruments/Agilent, Santa Clara, CA, USA). Signal should be detected in fractions 3 and 4.
9. Prepare samples by mixing 75 µl of the sample and 15 µl of 6X Loading Buffer. Load them in a SDS-PAGE gel and stain with Coomassie Brilliant Blue.
10. Analysis of results: Use Image J software to analyze protein bands in the different fractions. Calculate the percent liposome-bound protein from the band intensities measured in the third + fourth fractions (floating vesicle fractions), relative to the total sum of intensities measured in all fractions.

2.8. Vesicle tethering measurements

Lipid vesicles are found to tether/aggregate under a variety of conditions. Tethering/aggregation is usually assayed as an increase in turbidity (A_{400}) of the vesicle suspension that can be followed spectrophotometrically (**Figure 2.9**). The vesicle tethering may be a first step for vesicle-vesicle fusion so turbidity measurements can be used as a first approach in the study of fusion events. This assay has been performed in a Varian Cary 300 spectrophotometer (Agilent Technologies, Santa Clara, CA, USA) as described in the following protocol (**Protocol 17**).

Protocol 17. Vesicle tethering assay

1. Prepare LUVs at the desired lipid composition as previously described (**Protocol 13**). Determine the lipid concentration by the Fiske assay (**Protocol 11**).
2. Add 400 µl final volume of buffer containing 0.4 mM liposomes (in some conditions, mixed also with proteins) to cylindrical glass tubes (see **Figure 2.8A**).
3. Measure absorbance at 400 nm (A_{400}) under continuous stirring at 37ºC.
4. After 4 min stabilization, add the corresponding amount of protein or ATP to the cuvette in the smallest possible volume (no more than 20 µl) and record the time course of the reaction.
5. The aggregation time course is usually shown as a ΔA_{400}

$$\Delta A_{400} = A_t - A_0$$

Equation 2.2. Absorbance change calculation

Where: A_t is the measured absorbance of LUVs at time t,
A_0 is the measured absorbance of LUVs before protein/ATP addition.

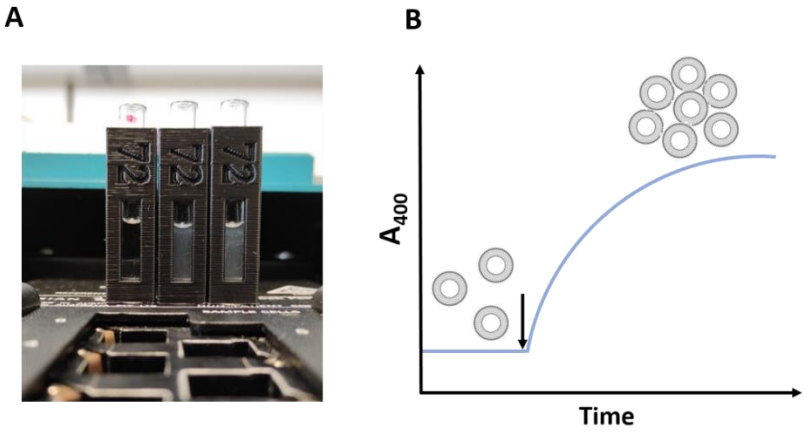

Figure 2.9. Schematic overview of a time-course of a vesicle tethering assay. (A) Tubes used for aggregation measurements**. (B)** Initially vesicles scarcely scatter light. Upon protein or ATP addition (arrow), aggregation occurs and turbidity increases, thus light scattering increases in parallel.

2.9. Fluorescence Spectroscopy techniques

2.9.1. Lipid mixing assay

Förster resonance energy transfer (FRET) is a distance-dependent interaction between the electronic excited states of two dye molecules in which excitation is transferred from a donor molecule to an acceptor molecule without emission of a photon. The efficiency of FRET is dependent of the inverse sixth power of the intermolecular separation, thus it can only occur when fluorophores are very close to each other.

In order to study vesicle-vesicle fusion, lipid mixing between vesicles was monitored using a FRET pair of fluorescently labeled lipids, a methodology developed by Struck *et al.* (1981). 7-nitrobenz-2-oxa-1,3-diazol-4-yl (NBD, excitation peak at 463 nm and emission peak at 536 nm) was used as the energy donor and rhodamine (Rho, excitation peak at 560 nm and emission peak at 583 nm) as the energy acceptor. The energy transfer takes place because the emission spectrum of the donor overlap the acceptor excitation spectrum. Each of the two fluorophores is coupled to the free amino group of a phosphatidylethanolamine to provide an analogue that can be incorporated into a lipid vesicle bilayer. When both fluorescent lipids are in LUV at the appropriate surface densities (ratio of fluorescent lipid to total lipid), efficient energy transfer is observed (**Figure 2.10A**). When such vesicles are fused with a population of unlabeled vesicles by the addition of a fusion-inducing agent, the two probes mix with the other lipids present to form a new membrane. This mixing reduces the surface density of the fluorophores and the energy transferred between molecules decreases, thus the fusion can be measured as an increase of NBD (donor) fluorescence (**Figure 2.10B**).

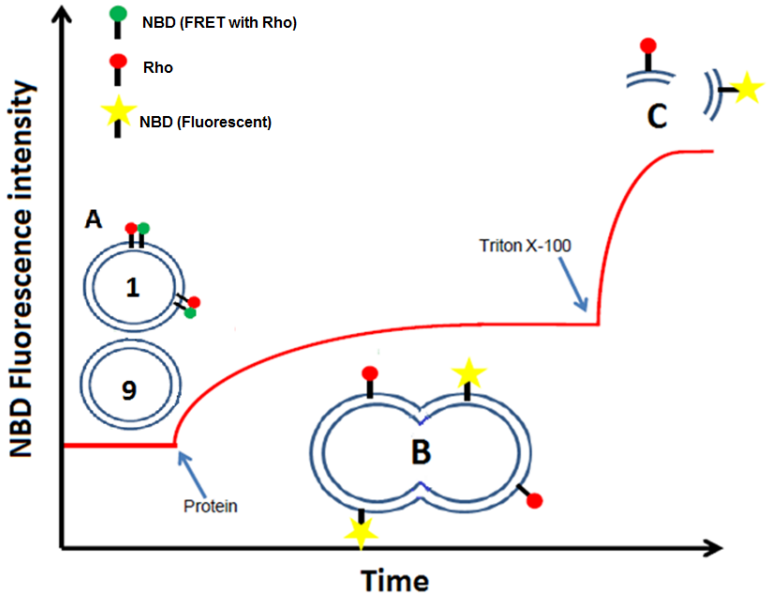

Figure 2.10. Schematic overview of an inter-vesicle lipid mixing assay. (A) Initially there are two populations of vesicles, one labelled with the FRET pair and the second unlabeled). **(B)** Upon protein addition, when fusion occurs lipids are mixed and the energy transferred between NBD and rhodamine decrease. **(C)** Triton X-100 is added to achieve vesicle complete solubilization, under these conditions 100% NBD fluorescence value is obtained.

Using this system, the ability of LC3/GABARAP proteins to induce lipid mixing in the presence of the UBL-system proteins and ATP has been studied (See Chapter 4). In addition, to determine whether the observed process was one of membrane hemifusion or of full fusion, total and inner lipid mixing studies were performed (**Protocol 18**).

Protocol 18. Total and Inner Lipid mixing assay

1. Prepare two LUV populations (**Protocol 13**) and determine the lipid concentration with the lipid phosphorous (Fiske) assay (**Protocol 11**):

   a. "non labelled" with no fluorescent probes
   b. "labelled" with 1.5 mol% NBD and 1.5 mol% Rho

2. (Only for inner lipid mixing assay): Reduction of outer leaflet fluorescence

   a. Prepare a fresh 100 mM stock solution of sodium dithionite in the same buffer as the vesicles. Keep in the dark at 4ºC.
   b. Place 400 µl of the labelled population in a cylindrical glass tubes (see **Figure 2.8A**) and add small amounts (1 – 3 µl) of dithionite to the sample until the fluorescence is quenched to half of the initial value by measuring NBD emission at 530 nm with the excitation wavelength set at 465 nm (slits at 4 nm).
   c. Pass the vesicle suspension immediately through a Sephadex G-25 column to remove dithionite. Steps c and d should be done as quickly as possible in order to avoid dithionite permeabilization into the vesicles.
   d. Determine the lipid concentration with the lipid phosphorous (Fiske) assay (**Protocol 11**).

3. Mix the two population of liposomes in a 1:9 (labelled:non labelled) ratio to a 0.4 mM total concentration with the adequate proteins (final volume 400 µl) in cylindrical glass tubes (see **Figure 2.8A**).

4. Measure NBD emission at 530 nm with the excitation wavelength set at 465 nm (slits at 4 nm) in a Fluorolog®-3 (Horiba Jobin Yvon, Edison, NJ, USA) spectrofluorometer with constant stirring at 37°C. Place a 515 nm cut-off filter between the sample and the emission monochromator to avoid scattering interference.

5. After 4 min stabilization, add protein/ATP and record the time course of the reaction.

6. Add 10 µL of 10% (v/v) Triton X-100 to disrupt the liposomes and obtain the maximum NBD fluorescence value.

7. Quantify the extent of inner lipid mixing on a percentage basis according to the equation:

$$\% \text{ Lipid mixing} = (F_t - F_0 / F_{100} - F_0) \times 100$$

Equation 2.3. % Lipid Mixing calculation

where: F_t is the measured NBD fluorescence of protein-treated LUVs at time t.
F_0 is the initial NBD fluorescence (maximum NBD-Rho energy transfer) of the LUV suspension before protein/ATP addition.
F_{100} is the maximum NBD fluorescence value after complete disruption of non reduced LUVs by addition of Triton X-100.

2.9.2. Vesicle contents efflux measurement (leakage) assay

This technique measures the ability of particular molecules to permeabilize the vesicle lipid bilayer. It is a simple approach in which vesicles are prepared enclosing fluorescent molecules. Upon specific molecule incubation, permeabilization is followed by changes in fluorescence. If vesicles are incubated with a detergent, a possible permeabilization could be followed by externalization of entrapped fluorescent molecules through unstable solubilized vesicle regions.

The basis of this approach is depicted in **Figure 2.11**. By entrapping both ANTS and DPX inside the vesicles, their close proximity allows DPX to interact with ANTS, quenching its fluorescence (**Figure 2.11A**). Upon externalization, both molecules are diluted into the external medium and they hardly interact, inducing an increase of ANTS fluorescence (**Figure 2.11B**). Thus, by following ANTS fluorescence, vesicle bilayer permeabilization, or solubilization in our case, can be followed. This approach was initially developed in 1985 (Ellens *et al.*, 1985) to measure vesicle fusion (see next section).

In the present study, the ability of LC3/GABARAP proteins in the presence of the UBL-system proteins and ATP to produce vesicle leakage in the process of vesicle aggregation, and the possible leakage in vesicle fusion processes were tested by following the externalization of the well-known low-molecular weight ANTS and its quencher DPX fluorescent molecules. A full description of the assay conditions is given in the **Protocol 19**.

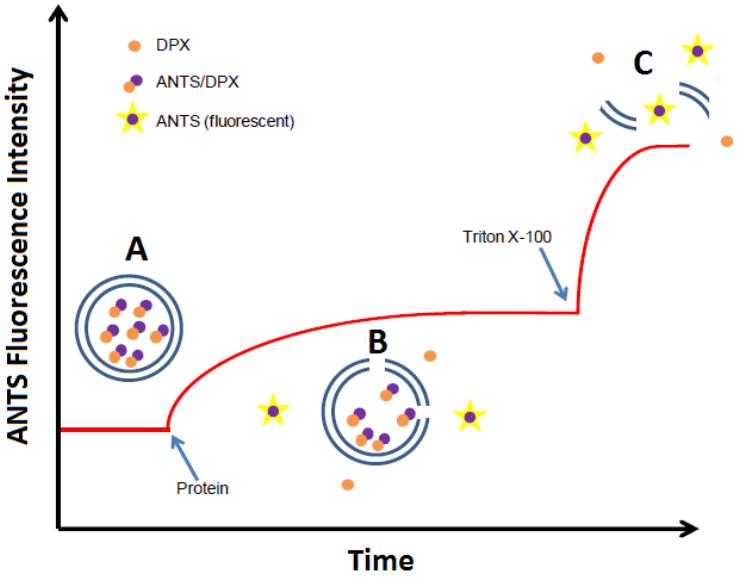

Figure 2.11. Schematic overview of the ANTS/DPX leakage assay. (A) Vesicles have coencapsulated ANTS and DPX. DPX is a quencher of ANTS fluorescence. (**B)** Upon addition of the protein, vesicle-enclosed ANTS and DPX are externalized through membrane defects. An increase on ANTS fluorescence is observed. (**C)** Triton X-100 is added for complete vesicle solubilization that gives the 100% leakage value (i.e. maximum ANTS fluorescence).

Protocol 19. Vesicle Contents Efflux Measurement (Leakage) Assay

1. Prepare large unilamellar vesicles (LUVs) as previously described (**Protocol 13**) in the following buffer containing both ANTS and DPX: 20 mM ANTS, 70 mM DPX, 50 mM Tris, 40 mM NaCl, pH 7.5. A high DPX/ANTS ratio is used to ensure complete quenching inside vesicles. Cover the samples with aluminium foil to protect fluorescent molecules from bleaching.

2. Pass the vesicle suspension through a Sephadex G-25 column to remove non-entrapped ANTS and DPX. Use a previously adjusted isosmotic buffer solution for this process (50 mM Tris-HCl, 150 mM NaCl, 1 mM DTT, pH 7.5). Determine lipid concentration as previously described (**Protocol 11**).

3. Add the ANTS/DPX-containing liposomes to a 0.4 mM total concentration together with the adequate proteins (final volume 400 µl) in cylindrical glass tubes (see **Figure 2.8A**).

4. Measure ANTS fluorescence at 520 nm with the excitation wavelength set at 355 nm (slits at 4 nm) in a Fluorolog®-3 (Horiba Jobin Yvon, Edison, NJ, USA) spectrofluorometer with constant stirring at 37°C.

5. After 4 min stabilization, add protein/ATP and record the time course of the reaction.

6. Add 10 µL of 10% (v/v) Triton X-100 to disrupt the liposomes and obtain the maximum ANTS fluorescence value.

7. Quantify the extent of leakage on a percentage basis according to the equation:

$$\% \text{ Leakage} = (F_t - F_0 / F_{100} - F_0) \times 100$$

Equation 2.4. % Leakage calculation

where F_t is the measured ANTS fluorescence of protein-treated LUVs at time t.
F_0 is the initial ANTS fluorescence (maximum ANTS-DPX quenching) of the LUV suspension before protein/ATP addition.
F_{100} is the maximum ANTS fluorescence value after complete disruption of LUVs by addition of Triton X-100.

2.9.3. Aqueous contents mixing assay

As mentioned in the previous section, before its use for testing the leakage ability of the molecules, the ANTS-DPX quenching assay can be used (Ellens *et al.*, 1985) in order to measure the capacity of particular molecules to promote full fusion of vesicles. In this case, both ANTS and DPX are entrapped into separate vesicle populations and their fusion is followed in terms of ANTS fluorescence quenching upon fusion and ANTS-DPX interaction [see (Goñi *et al.*, 2003; Nieva *et al.*, 1989)].

The basis of this approach is depicted in **Figure 2.12**. ANTS is entrapped in one vesicle population while DPX in a different vesicle population. Upon fusion between the two populations, the close proximity of the molecules caused by the mixing of contents will allow their interaction and an ANTS fluorescence decrease will be observed. Thus, by following ANTS fluorescence, vesicle bilayer full fusion can be followed.

In the present thesis, this technique was used together with total and inner lipid mixing assays to measure the ability of LC3/GABARAP proteins in the presence of the UBL-system proteins and ATP to produce full fusion (**Protocol 20)**.

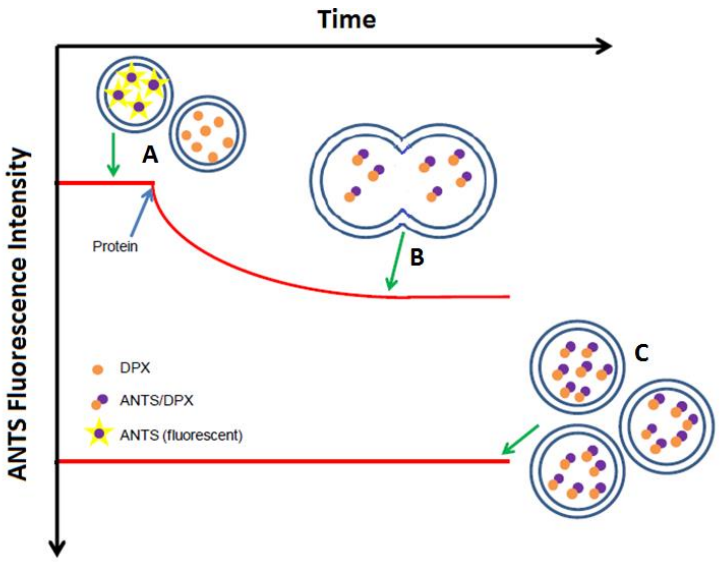

Figure 2.12. Schematic overview of an inter-vesicular aqueous contents mixing assay. (A) Initially, there are two populations of vesicles, one with ANTS and the second one with DPX. (**B**) Upon protein addition, when complete fusion occurs the aqueous contents of the vesicles are mixed and DPX can quench ANTS. **(C**) 100% fusion value is obtained measuring the fluorescence of a vesicle population containing both molecules.

Protocol 20. Aqueous Contents mixing Measurement Assay

1. Prepare three populations of large unilamellar vesicles (LUVs) as previously described (**Protocol 13**), each of them in one of the following buffers:
    a. ANTS population: 39 mM ANTS, 50 mM Tris, 72 mM NaCl, pH 7.5.
    b. DPX population: 140 mM DPX, 50 mM Tris, 10 mM NaCl, pH 7.5.
    c. ANTS/DPX population: 20 mM ANTS, 70 mM DPX, 50 mM Tris, 40 mM NaCl, pH 7.
2. Pass the vesicle suspensions through a Sephadex G-25 column to remove non-entrapped ANTS and DPX. Use a previously adjusted isosmotic buffer solution for this process (50 mM Tris-HCl, 150 mM NaCl, 1 mM DTT, pH 7.5).
3. Determine lipid concentration as previously described (**Protocol 11**).
4. Mix the ANTS and DPX populations in a (1:1) ratio to a 0.4 mM total concentration together with the adequate proteins (final volume 400 µl) in cylindrical glass tubes (see **Figure 2.8A**).
5. Measure ANTS fluorescence at 520 nm with the excitation wavelength set at 355 nm (slits at 1 nm) in a Fluorolog®-3 (Horiba Jobin Yvon, Edison, NJ, USA) spectrofluorometer with constant stirring at 37°C.
6. After 4 min stabilization, add protein/ATP and record the time course of the reaction.

Continues in next page

8. To calculate 100% content mixing, measure the ANTS fluorescence of the vesicles that have ANTS/DPX co-encapsulated.

9. Quantify the extent of aqueous content mixing on a percentage basis according to the equation:

$$\% \text{ Aqueous content mixing} = (-(F_t - F_0 / F_{100} - F_0)) \times 100$$

Equation 2.5. % Aqueous Content mixing calculation

where F_t is the measured ANTS fluorescence of protein-treated LUVs at time t.
F_0 is the initial ANTS fluorescence (minimum ANTS-DPX quenching) of the LUV suspension before protein/ATP addition.
F_{100} is the ANTS fluorescence (maximum ANTS-DPX quenching) of the LUV suspension with ANTS and DPX co-encapsulated.

2.10. Cryo-electron microscopy

Cryo-electron microscopy (cryo-EM) is a form of transmission electron microscopy (EM) where the sample is studied at cryogenic temperatures (generally liquid nitrogen temperatures). The main advantage of cryo-EM stems is the fact that this technique allows the observation of specimens that have not been stained or fixed in any way, showing them in their native form. The sample could be frozen from its native conditions, generally in an aqueous environment (aqueous buffer). This is in contrast to X-ray crystallography, which requires crystallizing the specimens, which can be a difficult task, and placing them in non-physiological environments, which can occasionally lead to functionally irrelevant conformational changes.

The biological material is spread on an electron microscopy grid and is preserved in a frozen-hydrated state by rapid freezing, usually in liquid ethane near liquid nitrogen temperature. By maintaining samples at or below liquid nitrogen temperature, they can be introduced into the high-vacuum of the electron microscope column. Most biological samples are extremely radiation-sensitive, so they must be imaged with low-dose techniques. Usefully, the low temperature of cryo-electron microscopy provides an additional protective factor against radiation damage.

In the present thesis, this technique was used to observe differences in liposome aggregation and fusion after LC3/GABARAP protein addition in the presence of the UBL-system components and ATP. The procedure followed to perform Cryo-EM measurements is summarized in **Protocol 21**.

Protocol 21. Cryo-electron microscopy

1. Prepare LUVs (**Protocol 13**) and determine lipid concentration as previously described (**Protocol 11**).

2. Mix and incubate the adequate protein and liposomes.

3. Vitrification of the samples:

    a. Use a LEICA GP2 automatic plunge freezer (LEICA Microsystems, Wetzlar, Germany) maintained at 8°C at a relative humidity close to saturation (90% rH) to prevent water evaporation from the sample.

    b. Using a tweezer put a freshly glow-discharged 300-mesh R2/2 Quantifoil holey carbon grid inside the vitrification chamber.

    c. Take 4 μl of the sample (mix before) and load into the grid.

    d. After 30 s incubation, blot with absorbent standard filter paper for 2 s, and plunge into a liquid ethane bath (-184ºC). Remove most of the liquid by careful blotting with absorbent filter paper to create a thin liquid film. Then, plunge the sample rapidly into liquid ethane and cool with liquid nitrogen to its melting temperature to obtain a vitrified film.

    e. Remove the vitrified grids from the plunger and store under liquid nitrogen.

4. Imaging of Cryo-EM samples:

    a. Transfer the grid to a JEM-2200FS/CR (JEOL Europe, Nieuw-Vennep, The Netherlands) transmission electron microscope operated at 200 kV.

    b. Record digital images on a GATAN K2 summit direct detection camera 4K × 4K (5 μm pixels) (Gatan Inc., Pleasanton, CA) using Digital Micrograph (Gatan Inc.) software, at a nominal magnification of 30,000×, resulting in final sampling of 1.3 Å/pixel.

This technique was performed in collaboration with I. Santos, M. Lázaro and M. Valle at CIC bioGUNE (Derio, Spain).

2.11. Atomic force microscopy

Atomic force microscopy (AFM) is a high-resolution imaging technique, part of the family of scanning probe microscopy. Its basic principle is that a tip, which is mounted at the end of a cantilever, is in contact with the sample surface across the XY axis and the sample topography is obtained by the movement of the tip over the surface (**Figure 2.13**). The movement of the tip is controlled by a scanner (piezoelectric material). The interaction between the sample and the tip is measured with a laser beam, which is focused on the top-end of the cantilever. The beam is reflected towards a position-sensitive four quadrant photodetector by the use of a mirror. The signal from the photodetector passes through a feedback circuit, which relates the movement in z-axis

needed by the scanner to maintain the cantilever deflection constant with the sample topography.

AFM is a widely used technique to obtain topographical information of biological membranes at a lateral resolution of less than 1 nm and at a vertical resolution between 0.1 and 0.2 nm. The set of biological samples ranges from the smallest biomolecules (phospholipids, proteins, DNA, RNA) to subcellular structures (membranes), all the way up to living cells and tissues. In addition, this technique allows the analysis of mechanical, chemical and functional properties of the sample (Alessandrini & Facci, 2005).

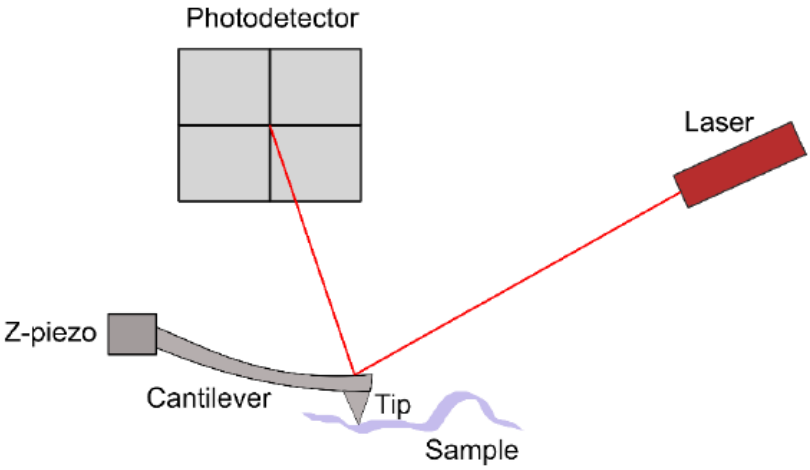

Figure 2.13. Basic principle of atomic force microscopy measurements: A fine tip is attached to a cantilever that scans the surface of a sample.

The tip and the cantilever play a crucial role in AFM. The tips can be rectangular or triangular, and usually have a metal coating for increased reflectivity. The quality of the data and the resolution of the AFM depend on a large extent of them, for that reason, it is important to select specifically the material, shape, coating, spring constant and resonance frequency of the tip. For example, silicon nitride cantilever tips are usually used to work in liquid, with a typical spring constant range from 0.01 N/m to 100 N/m. However, the softness of biological samples limits the force applied during the imaging process so the spring constant recommended is below 1 N/m (usually between 0.01-0.5 N/m).

In this thesis, AFM was used to study the formation of a possible protein scaffold on the top of a supported lipid bilayer (SLB) (See Chapter 5 for details). Among the different modes of operation, QI Mode was used because it ensures a lower tip-sample interaction than other methods available. This preserves the tip and the sample from damage. The protocol followed is summarized in **Protocol 22**.

Protocol 22. AFM measurements

1. Prepare SUV of the desired composition (as previously described in Section 2.6.3)
2. Attach mica substrate to a round 24 mm glass coverslip and cleave the mica before use.
3. Mount the freshly cleaved mica onto a JPK coverslip-based liquid cell for atomic force microscopy (AFM) measurements.
4. For supported lipid bilayer formation: Add 120 µl assay buffer containing 3 mM $CaCl_2$ and 80 µl of SUV onto the mica.
5. Leave the vesicles to adsorb and extent for 20 min at 37ºC.
6. Discard the non-adsorbed vesicles by washing the samples 10 times with assay buffer without $CaCl_2$, in order to remove remaining Ca^{2+} cations from the solution.
7. Collect AFM data for imaging in a NanoWizard ULTRA Speed (JPK BioAFM, Bruker Nano GmbH, Berlín, Germany) using the following settings:
    a. Tip: MLCT Silicon nitride cantilevers
    b. Set-point: 0.4 N/m
    c. QI mode
8. Incubate with proteins in two different modes:
    a. Addition of the protein mixture, incubation 20 min at 37ºC and imaging.
    b. Addition of the protein mixture with a syringe system and imaging every 5 min.

This technique was performed in collaboration with E. J. González Ramírez at Instituto Biofisika UPV/EHU, CSIC (Leioa, Spain)

2.12. Fluorescence confocal microscopy

Fluorescence microscopy is a widely used technique to obtain high contrast magnified images of a sample of interest. In a common epifluorescence microscope, a lamp is used as a light source and the illumination light passes through an excitation filter located before the objective, which selects an excitation wavelength. The objective collects fluorescence emission, which is separated from excitation light by a dichroic filter before it reaches the detector. The main disadvantage of an epifluorescence set up is that all planes in the sample are excited, collected and imaged at the same time, which makes it impossible to create resolved images of different focal planes.

The development of confocal microscopy during the late 70´s resulted in one of the major advances in optical microscopy. Specifically, fluorescence confocal microscopy allows the analysis of the fluorescence coming from an individual thin in-focus plane of the sample, and this enables the construction of real three-dimensional (3D) images. To discard fluorescence coming from out-of-focus planes, and in contrast to common epifluorescence microscopy, confocal imaging is achieved by introducing a pinhole next to the detector that allows only fluorescence coming from the in-focus plane to reach the detector. **Figure 2.14** shows a schematic picture of the central components of a fluorescence confocal microscope. Essentially, a laser beam is used as the excitation light, which is focused into a dichroic mirror that selects the light to be directed through

an objective into a small spot within the sample. However, this is not enough to build a 3D image of the specimen being measured. For this purpose, special mirrors are introduced to scan the laser beam on the x-y plane, thus building a special confocal microscopy known as laser scanning confocal microscopy. In this way, by precisely controlling the z sample movement, three-dimensional images can be constructed.

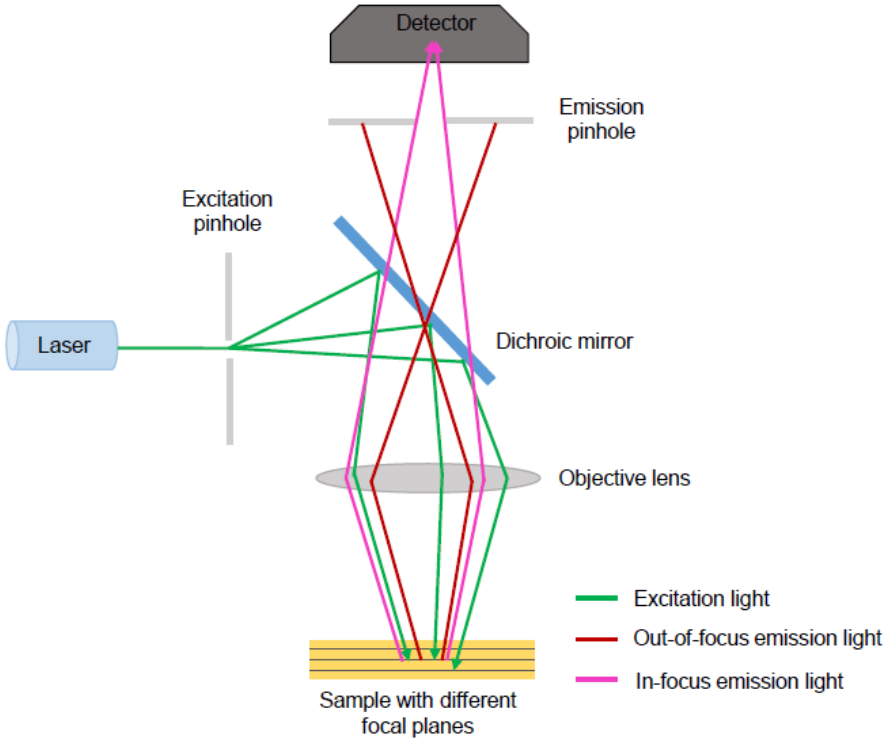

Figure 2.14. Central components of a fluorescence confocal microscope.

In the present work, laser scanning confocal microscopy has been applied to:

- **The study LC3/GABARAP participation in mitophagy**: (See next section and Chapter 3 for details): GFP-tagged LC3/GABARAP proteins were transfected into SH-SHY5 cells and mitochondria were labelled (MitoTracker or co-trasfection with DsRed). The colocalization of LC3/GABARAP proteins and mitochondria after a mitophagy inducing treatment was assessed.
- **The study of the interaction between LC3/GABARAP and E3**: (See **Protocol 10** and Chapter 5): GFP-tagged E3 was used to assess its binding to LC3/GABARAP covered beads.
- **The reconstitution of GABARAPL1 lipidation reaction in GUV in the presence or in the absence of E3 complex**: (See Chapter 5): GABARAPL1 labelled with Alexa 633 and E3 complex labelled with a GFP tag were mixed together with the rest of the UBL-system proteins, ATP and GUV (See **Protocol 14** and **Protocol 15**) to observe GABARAPL1 and E3 localization.

2.13. Mammalian cell culture

Cell cultures are one of the most frequently used experimental setup for the investigation of autophagy. In this thesis, they were used to study the participation of the LC3/GABARAP-family members in mitophagy, the specific autophagy of mitochondria (See Chapter 3). These techniques were performed in collaboration with A. Etxaniz at Instituto Biofisika UPV/EHU, CSIC (Leioa, Spain).

2.13.1. Cell culture and mitophagy-inducing treatments

SH-SY5Y neuroblastoma cell line (**Figure 2.15**) was kindly provided by Dr. I. Ramos (Innoprot, Derio, Spain). Cells were grown in an atmosphere of 5% CO_2 at 37ºC in RPMI 1640 medium containing 10% fetal bovine serum, non-essential amino acids and 1% penicillin-streptomycin.

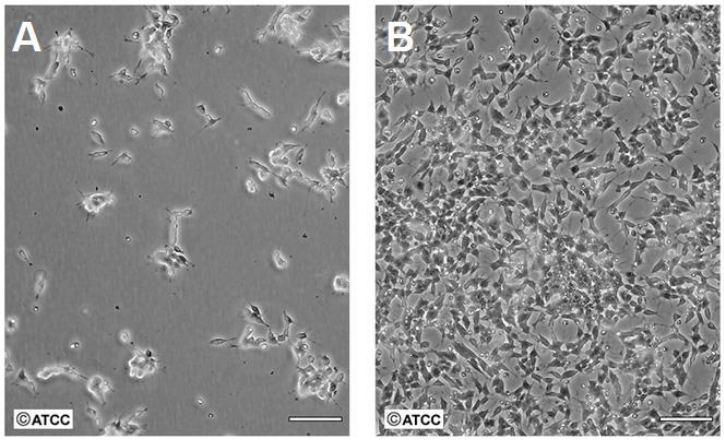

Figure 2.15. SH-SY5Y cells. (A) Low density. **(B)** High density. Adapted from ATCC (CRL-2266). Bar=100 µm

In order to activate mitophagy three different treatments (**Table 2.7**) previously used in other studies (Chu *et al.*, 2013; Kagan *et al.*, 2016; Nguyen *et al.*, 2016b) were used (See Chapter 3 for details).

Treatment	Concentration	Duration	Function
Rotenone	1 µM	6 h	Inhibitor of complex I of the respiratory chain
CCCP	20 µM	1 h	Proton ionophore commonly used as an uncoupling agent and inhibitor of photosynthesis
Oligomycin A + Antimycin A	10 µM/4 µM	6 h	Oligomycin A: ATP synthase inhibitor Antimycin A: mitochondrial electron transport inhibitor

Table 2.7. Mitophagy-inducing treatments used in this doctoral thesis.

2.13.2. Cell Transfection

In order to express the GFP-tagged LC3/GABARAP proteins, cells were transfected using Lipofectamine™ 2000 following the manufacturer's instructions (**See Protocol 23**). The plasmids used for mammalian cell transient transfection of LC3/GABARAP labelled with GFP had the full sequence of the proteins (see **Table 2.1**).

Protocol 23. Transient cell transfection

1. Seed cells 24 hours before the experiment to have cells at 70% confluence for the transfection. For example, in a µ-Slide 8-well chambered coverslips (Ibidi, 80826), seed 20.000 cell/well.
2. Prepare a mixture with the transfection agent (Lipofectamine™ 2000) and the DNA in a 2:1 ratio (µl:µg). For a µ-Slide 8-welll:
   a. DNA mix: Dilute 0.25 µg DNA in opti-MEM to a final volume of 25 µl.
   b. Transfection mix: Dilute 0.5 µl Lipofectamine 3000™ in opti-MEM to a final volume of 25 µl.
   c. Add the transfection mix to the DNA mix and incubate 5 min.
3. Transfer the mix to the well in a dropwise manner
4. Culture cells for 24 h at 37ºC and 5% CO_2 and analyze transfection efficiency.

2.13.2.1. RNA Silencing (siRNA)

This technique was used in order to address the role of LC3A and LC3B proteins in CCCP-induced mitophagy. The siRNAs were designed to target the same sequences used in other works (**Table 2.8**). Transfection protocol (see **Protocol 23**) was also used for RNA silencing. Cells were seeded the day before in 6-well plate (100000 cells/well). Transfection with the adequate siRNA (100nM) was performed. Then, the transfection protocol was repeated three times more, after 24 h, 48 h and 72 h. Efficiency of the silencing was checked by western blot (See next section).

Target protein	Description	Sequence	Reference
LC3A	Target sequence (5´→3´)	GGCUUCCUCUAUAUGGUCUACGCCU	(von Muhlinen *et al.*, 2012)
	Sense siRNA (5´→3´)	GGCUUCCUCUAUAUGGUCUACGCCUUU	
	Antisense siRNA (5´→3´)	AGGCGUAGACCAUAUAGAGGAAGCCUU	
LC3B	Target sequence (5´→3´)	CAAAGUUCCUUGUACCUGA	(Liu *et al.*, 2017)
	Sense siRNA (5´→3´)	CAAAGUUCCUUGUACCUGAUU	
	Antisense siRNA (5´→3´)	UCAGGUACAAGGAACUUUGUU	
Control	Target sequence (5´→3´)	UUCUCCGAACGUGUCACGUTT	(Liu *et al.*, 2017)
	Sense siRNA (5´→3´)	UUCUCCGAACGUGUCACGUUUUU	
	Antisense siRNA (5´→3´)	AAACGUGACACGUUCGGAGAAUU	

Table 2.8. siRNA synthesized by IDT to silence LC3A and LC3B proteins.

2.13.3. Cell lysis and Western blot

Western blot is a useful technique to detect autophagy activation in cells, as the appearance of a faster migrating LC3/GABARAP band is an indicator of their lipidation and binding to membranes and so, their participation in autophagy. Western Blot also allows the detection of mitochondrial proteins and therefore it permits the study of mitochondrial flux (See Chapter 3 for details). **Protocol 24** contains a schematic procedure of the steps needed to lyse the cells and detect the protein of interest by western blotting.

Protocol 24. Cell Lysis and Western Blot

For cell lysis:

1. Scrap the cells in phosphate buffer saline (PBS).
2. Centrifuge and collect them at 1500 x g for 10 min at 4ºC
3. Lyse the cells during 45 min using RIPA lysis buffer (R0278, Merck) supplemented with protease inhibition cocktail at 1X.
4. Centrifuge the lysates at 12000 x g for 10 min at 4ºC and collect supernatants.
5. Measure protein concentration using a BCA assay (see section 2.5.1.2)

For Western blot:

1. Load the same amount of protein in each well (20-30 µg/sample) and run the SDS-PAGE polyacrylamide gel.
2. Transference:
   a. Prepare a gel sandwich with Trans-Blot filter papers and a PVDF blotting membrane HybondTM (10600021), activated previously with methanol. Hydrate it with transference buffer (2.25 g glycine, 5.81 g Tris, pH 8, 0.375 g SDS, 200 mL MetOH and H_2O to 1L).
   b. Transfer the protein using a Trans-Blot Turbo® equipment (Bio-Rad) at 22 V for 30 min at room temperature
3. Blocking:
   a. Use 5% nonfat milk in TBST buffer (20 mM Tris-HCl, 150 mM NaCl, 0.1% Tween 20) 1h at room temperature.
4. Primary antibody incubation:
   a. Incubate the membranes with the specific primary antibodies in TBST buffer containing 1% of nonfat milk O/N at 4ºC.
5. Secondary antibody incubation:
   a. After washing with TBST, incubate blots with the specific secondary antibodies (1:5000) in TBST containing 1% nonfat milk for 1 h at room temperature, using HRP-conjugated antibodies.
6. Detection:
   a. After washing with TBST, add Immobilon® Forte Western HRP Substrate (WBLUF0100, Millipore) to the blot and visualize the protein bands using an iBright FL1500 Imaging System (Invitrogen- Thermo Fisher Scientific Inc, Waltham, MA, USA)

2.13.4. Mitochondrial isolation

Obtaining highly enriched mitochondria preparations is useful to evaluate the function of LC3/GABARAP proteins in mitophagy. Mitochondrial isolation is a typical procedure in many laboratories. **Protocol 25**, adapted from (Frezza *et al.*, 2007) illustrates a schematic diagram of a 1-hour step-by-step procedure to obtain functional mitochondria.

Protocol 25. Mitochondrial isolation

1. Growth cells in T175 flask at 70% confluence

Perform all following steps on ice. Cool centrifuge and buffers at 4°C

2. Wash the cells twice with cold PBS1X (137 mM NaCl, 2.7 mM KCl, 10 mM Na_2HPO_4, 2 mM KH_2PO_4, pH 7.4
3. Scrap the cells in 25 ml cold PBS.
4. Centrifuge cells 5 min, 950 x g at 4ºC
5. Discard the supernatant and resuspend the pellet in 4 ml ice cold mitochondrial isolation buffer (MIB) (10 mM HEPES, 70 mM sucrose, 210 mM mannitol, 1 mM EDTA, pH 7.5) supplemented with protease inhibitors.
6. Transfer cell suspension to a pre-cooled 5 ml glass-teflon Elvehjem potter for homogenization.
7. Homogenization (50 strokes)
8. Centrifuge the homogenate at 1500 x g for 10 min at 4ºC
9. Collect the supernatant
10. Centrifuge the supernatant at 10500 x g for 5 min at 4°C
11. Discard the supernatant and wash the purified mitochondria-containing pellet with MIB.
12. Resuspend the pellet in RIPA lysis buffer.
13. Check for adequate mitochondria isolation by immunodetection of COX-IV (only in the mitochondrial fraction).

CHAPTER 3

LC3 SUBFAMILY IN CARDIOLIPIN-MEDIATED MITOPHAGY: A COMPARISON OF THE LC3A, LC3B AND LC3C HOMOLOGS

CHAPTER 3. LC3 subfamily in cardiolipin-mediated mitophagy: A comparison of the LC3A, LC3B and LC3C homologs

3.1. Introduction

Mitochondria are essential organelles for energy transduction in the eukaryotic cell. Mitochondrial dysfunctions have been associated with a wide number of pathological conditions, including neurodegenerative diseases, myopathies, and cancer (Um & Yun, 2017). Cells have developed different quality control systems in order to maintain an optimal mitochondrial network, including processes that allow the removal of damaged or superfluous mitochondria without causing cell death (Pickles *et al.*, 2018). Among them, the selective degradation of mitochondria via macroautophagy is termed mitophagy (**Figure 3.1**).

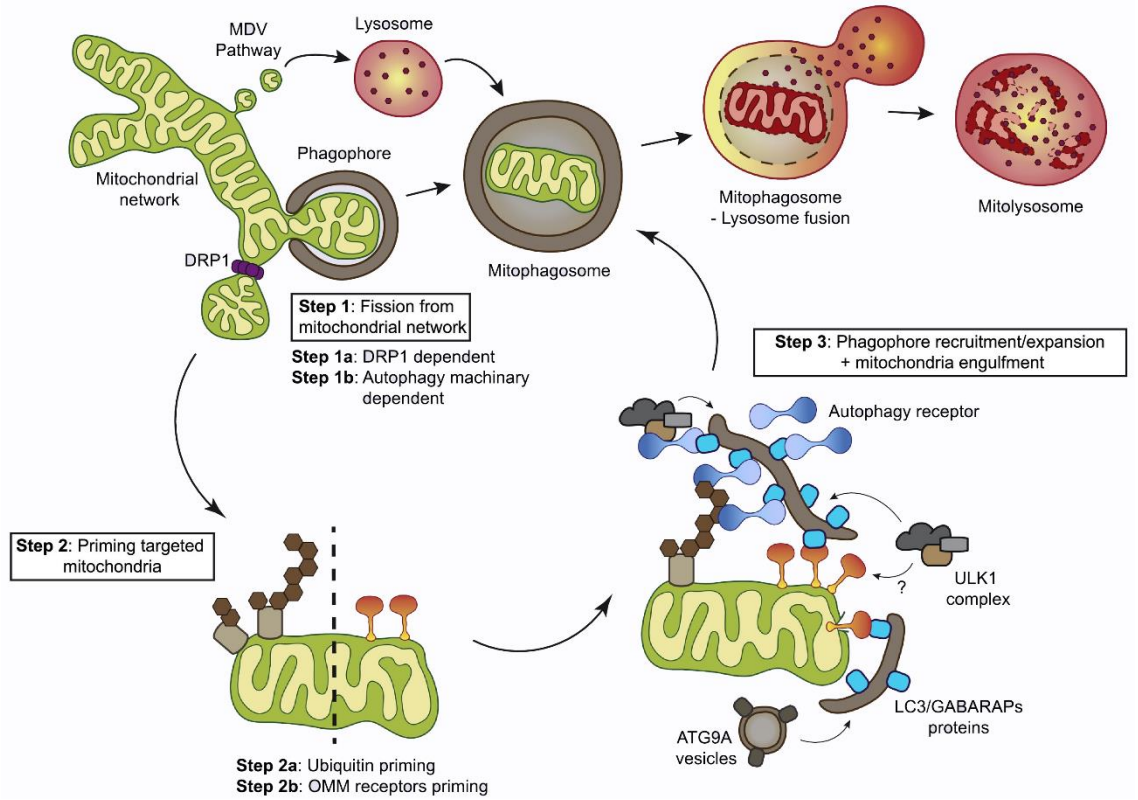

Figure 3.1. Molecular steps of mitochondrial degradation via mitophagy. Taken from Montava-Garriga & Ganley (2020).

Recognition of damaged or superfluous mitochondria is a key event in mitophagy. Many different indicators of mitochondrial damage are known. The PINK1-PRKN/Parkin axis, recognized as the main regulator of mitophagy (Nguyen *et al.*, 2016a), is characterized by the tagging of damaged mitochondria with ubiquitin chains that trigger their selective autophagy. This process requires the participation of different proteins such as OPTN (optineurin) and CALCOCO2/NDP52, which act as receptors. They are able not only to recognize the ubiquitin chain on the mitochondrial surface but also to bind LC3B in the phagophore membrane (Lazarou *et al.*, 2015). However, a growing body of evidence has shown that this pathway is not the only relevant one. Many mitophagy receptors, such as FUNDC1, BNIP3L/NIX, BNIP3, BCL2L13, AMBRA1 or FKBP8, that are found in the outer mitochondrial membrane (OMM), have shown the ability to recruit directly LC3/GABARAP proteins to mediate mitochondrial degradation, without ubiquitin signaling (Villa *et al.*, 2018). Most of these receptors have an LC3-interacting motif (LIR) that allows their association with LC3/GABARAP proteins (Johansen & Lamark, 2020). Lipids, such as ceramide (Sentelle *et al.*, 2012) or cardiolipin (Chu *et al*., 2013), can also serve as damaged mitochondrial signals/receptors.

The mitophagy mechanism mediated by the phospholipid cardiolipin (CL) is particularly intriguing. CL is essential for mitochondrial function and it is localized in the inner mitochondrial membrane (IMM) in healthy mitochondria (Dudek, 2017). In 2013, Chu found out that rotenone and other pro-mitophagic stimuli caused CL externalization to OMM, in turn inducing mitophagy (Chu *et al*., 2013). Furthermore, inhibition of CL synthesis or of CL externalization decreased the delivery of mitochondria to AP. Therefore, those authors proposed that CL would play a role in mitophagy; its externalization to the OMM upon mitochondrial injury would act as a signal for LC3 proteins to remove damaged mitochondria in neuronal cells, preventing CL oxidation and accumulation of proapoptotic signals (Chu *et al*., 2013).

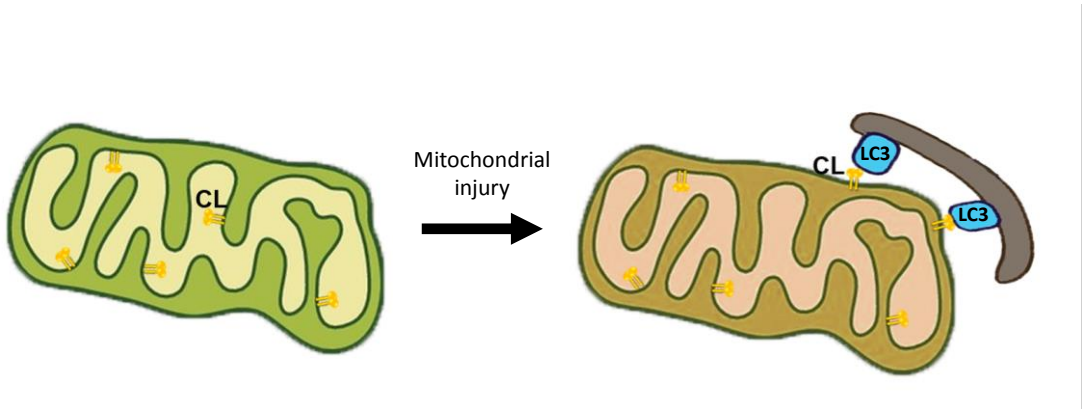

Figure 3.2. CL externalization acts as a signal for mitophagy. Adapted from Chu *et al.* (2013) and Montava-Garriga & Ganley (2020).

Recent studies have demonstrated that CL-externalization takes place also *in vivo*. Traumatic brain injury (TBI) model animals externalize CL to the OMM to a similar extent than rotenone-exposed mitochondria, thus underlining the importance of CL for mitophagy induction during the early response to TBI in human and rat brain (Chao *et al.*, 2019). Moreover, it is known that TAFAZZIN-deficiency-related perturbations in CL remodeling, found in the Barth syndrome, cause defective mitophagosome biogenesis

(Hsu *et al.*, 2015). In addition, it seems that externalized CL could interact with SNCA/alpha-synuclein (Ryan *et al.*, 2018), a protein associated with Parkinson disease. For these reasons, studying this mechanism of CL-mediated mitophagy could lead to interpreting some neurodegenerative diseases as mitophagy-related diseases (Chu, 2019; Lizama & Chu, 2021).

Chu *et al*. (2013) demonstrated the importance of two conserved residues (R10, R11) located in the N-terminal region of LC3 proteins for its interaction with CL. They proposed a mode of interaction between LC3 proteins and CL based on the recognition of damaged mitochondria by the protein N-terminal region, while their C-terminal region would target the autophagosomal membrane. These results were extended by studies in our laboratory (Antón *et al.*, 2016) that explored the molecular basis of LC3-CL interaction. It was shown that LC3B was able to interact preferentially with CL over other di-anionic lipids, and that after protein binding to CL-enriched membranes the C-terminus of LC3B remained exposed to the hydrophilic environment allowing its interaction with the phagophore. Thus, CL appeared to serve as a specific mitophagy receptor for LC3 proteins, ultimately leading to the removal of damaged mitochondria. However, although Chu *et al*. (2013) showed that LC3A and LC3B interacted with CL-containing liposomes, no comparative study was available on the CL- and mitochondria-binding abilities of the LC3 subfamily members LC3A, LC3B, and LC3C.

In the present chapter, first, a comparative analysis of the LC3-subfamily members' interaction and specificity for CL-containing model membranes was performed. Then, some mutants were designed to investigate the protein regions implicated in CL recognition. Their ability to translocate to mitochondria upon CL-externalizing treatments was also assessed and the capacity of the mutants to mediate mitophagy was analyzed, as well as the recognition of oxidized CL by LC3A and LC3B.

3.2. Materials and methods

3.2.1. Materials.

L-α-phosphatidylcholine from hen egg yolk (ePC; 840051), bovine heart cardiolipin (CL; 90% tetralinoleoylcardiolipin, 5% tetraoleoylcardiolipin, 5% unknown; 840012), brain phosphatidylinositol-4-phosphate (PtdIns4P; 840045), egg phosphatidic acid (PA; 840101), hen egg L-α-phosphatidylglycerol (PG; 841138), 1,2-dioleoyl-*sn*-glycero-3-phosphatidylethanolamine-N-lissamine rhodamine B sulfonyl (Rho-PE; 810150), and 1,2-dioleoyl-*sn*-glycero-3-phosphatidylethanolamine (DOPE; 850725) were purchased from Avanti Polar Lipids, Inc. *E. coli* BL21(λDE3) cells (C600003), RPMI 1640 medium (61870-10), Opti-MEM medium (11058-011), Lipofectamine™ 2000 (11668027), Lipofectamine™ 3000 (L3000008), MitoTracker™ Red CMXRos (M7512), fetal bovine serum (10270106) were purchased from Thermo Fisher Scientific. Anti-LC3A (ab26628), anti-LC3B (ab51520) anti-LC3C (ab150367) anti-COX4I/COX-IV (ab14744) antibodies and rotenone (ab143145) were purchased from Abcam. Anti-ACTB/actin (sc-8432), HRP-conjugated anti-mouse (sc-516102), HRP-conjugated anti-rabbit (sc-2357) antibodies, carbonyl cyanide m-chlorophenylhydrazone (CCCP; sc-202984) and oligomycin A (sc-201551) were purchased from Santa Cruz Biotechnology. DMEM medium (D5796), isopropyl-β-D-thiogalactoside (IPTG; I6758), DL-dithiothreitol (DTT; D0632), paraformaldehyde (PFA; 158127), non-essential amino acids (M7145), 1% penicillin-streptomycin (P4333), RIPA lysis buffer (R0278), antimycin A (A8674), Immobilon®Forte Western HRP Substrate (WBLUF0100), Thrombin Protease (27-0846-01), cOmplete™, EDTA-free Protease Inhibitor Cocktail (5056489001) and sucrose (84097) were purchased from Merck.

3.2.2. DNA constructs and site-directed mutagenesis.

The pGEX4T-1 plasmids for expression of several of the various LC3/GABARAP proteins tagged with GST (glutathione S-transferase) (human LC3A, human LC3B, human LC3C and human GABARAPL2) were kindly provided by Dr. Ivanna Novak (School of Medicine, University of Split, Croatia). Note that each of these LC3/GABARAP proteins was a truncated form lacking the C-terminal Gly. The Gly-exposed forms (**Table 2.1**), such that no ATG4-mediated pre-processing was necessary, that were used in this work, were constructed using a QuikChange site-directed mutagenesis kit (Agilent, 200514) (**Table 2.2**). The green fluorescent protein (GFP) plasmids (pHAGE-N-eGFP) (**Table 2.1**). were kindly provided by Dr. Christian Behrends (Munich Cluster for Systems Neurology, Munich, Germany.) Each of these GFP-tagged LC3/GABARAP-family members contains the full-length sequence of the proteins. For the preparation of the mutant proteins LC3A^{A14E} (LC3A-EK), LC3A^{K18E} (LC3A-AE), LC3A^{A14E,K18E} (LC3A-EE), LC3B^{E14A} (LC3B-AE), LC3B^{E18K} (LC3B-EK), LC3B^{E14A,E18K} (LC3B-AK), LC3C^{A20E}, GFP-LC3A^{G120A}, GFP-LC3B^{G120A}, GFP-LC3C^{G126A} and GFP-GABARAPL2^{G116C}, an inverse PCR-based site-directed mutagenesis using the KOD-Plus mutagenesis kit (Toyobo, SMK-101) was employed, following the instructions of the manufacturer. The sequences in all mutant constructs were confirmed by DNA sequencing analysis (Secugen S.L) (**Protocol 2**). The primers used for making the different mutants are listed in **Table 2.3**. The chimeras (LC3A/B, LC3C/B), the GFP-tagged double mutants (GFP-LC3A-EE, GFP-LC3B-AK) and the LC3A^{R10,11A} mutant (GST- and GFP-tagged versions) were

obtained by subcloning (synthesized by GenScript). Circular dichroism analysis of native and mutant proteins was performed. The results indicated that the mutations did not appreciably affect the protein secondary structure (data not shown).

3.2.3. Recombinant protein expression and purification.

LC3/GABARAP proteins and their mutants were purified (**Protocol 3**) from soluble fractions of bacterial extracts obtained in the absence of detergents, and they were >90% pure as evaluated by Coomassie Brilliant Blue-stained SDS-PAGE. *E. coli* BL21(λDE3) cells were transformed with appropriate plasmids, they were grown to OD_{600}=0.8 and induced with 0.5 mM IPTG for 16 h at 20ºC. Following centrifugation at 4,500 x g for 15 min, the pellet was resuspended and sonicated in Breaking Buffer (PBS 1x, 20 mM Tris-HCl pH 7, 150 mM NaCl, 1mM DTT with lysozyme, protease inhibitors mixture and DNase) (See also **Table 2.4**). After removal of cellular debris by centrifugation at 30,000 x g for 30 min at 4ºC, the sample supernatant fraction was incubated with 1 ml Glutathione Sepharose 4B (GE Healthcare, 17-0756-01) for 3 h at 4ºC to bind GST-tagged proteins. Bound proteins were cleaved with Thrombin Protease (See also **Table 2.5**) overnight at room temperature in Thrombin Buffer (140 mM NaCl, 2.7 mM KCl, 10 mM Na_2HPO_4, 1.8 mM KH_2PO_4, pH 7.3 with freshly added 1 mM DTT). After cleavage, they were eluted in Elution Buffer (50 mM Tris-HCl, pH 7.5, 150 mM NaCl, 1 mM EDTA with freshly added 1 mM DTT), then concentrated to 500 µl using Amicon Ultra-4 (4 mL, 3 kDa cut-off; Millipore, UFC800324), and loaded onto a Superdex 75 10/300 GL size exclusion column (GE Healthcare, GE17-5174-01) equilibrated in Elution Buffer supplemented with freshly added 1 mM DTT. Proteins were distributed in aliquots, flash-frozen and stored in 20% glycerol at -80ºC until further use.

3.2.4. Liposome preparation.

The appropriate lipids were mixed in organic solution and the solvent was evaporated to dryness under a N_2 stream. Then the sample was kept under vacuum for 1 h to remove solvent traces. The lipids were swollen in Assay Buffer in order to obtain multilamellar vesicles (MLV) (**Protocol 12**). Large unilamellar vesicles (LUV) (**Protocol 13**) were produced from MLV according to the extrusion method described by Mayer *et al*. (1986). They were subjected to 10 freeze/thaw cycles, and then extruded using a LIPEX Liposome Extrusion System (Evonik Health Care, Essen, Germany) with a 0.1-µm pore size Nuclepore filters (Whatman, 110605). Small unilamellar vesicles (SUV) (**Section 2.6.3**) were obtained by sonicating MLV with a probe tip sonicator (MSE Soniprep 150, MSE, UK) for 20 min (10 sec on, 10 sec off) on ice. Vesicle size was checked by quasi-elastic light scattering using a Malvern Zeta-Sizer 4 spectrometer (Malvern Instruments, Malvern, UK). LUV had an average diameter of ≈100 nm, and SUV average diameter was ≈50 nm. Phospholipid concentration was determined by phosphate analysis (**Protocol 11**) (Böttcher *et al.*, 1961).

3.2.5. Vesicle flotation assay.

Protein interaction with membranes was assessed using flotation in sucrose gradients (**Protocol 16**). Liposomes (3 mM), containing 0.05 mol% Rho-PE for detection, were incubated with 10 µM of the different purified proteins, for 1 h at 37ºC in Assay Buffer under continuous stirring (1100 rpm). The protein/lipid mix was adjusted to 1.4 M sucrose concentration in 300 µl and transferred to a centrifuge tube. This first (bottom) layer was overlaid with successive solutions containing 0.8 M (400 µl) and 0.5 M (300 µl) sucrose. The three-layer gradients were centrifuged in a TLA-120.2 rotor (Beckman Coulter, Brea, CA, US) at 355040 x g for 50 min at 4ºC. After centrifugation, four 250-µl fractions were collected, starting from the bottom. Proteins were detected in SDS-PAGE gels by using Coomassie Brilliant Blue staining, and the presence of liposomes was monitored by measuring rhodamine (Rho-PE) fluorescence in a microplate reader Synergy HT (Bio-Tek, Winooski, VT, USA). Densitometry of the protein bands was performed using ImageJ software, and the percent liposome-bound protein was calculated from the band intensities measured in the third + fourth fractions (floating vesicle fractions), relative to the total sum of intensities measured in all fractions.

3.2.6. Cell culture.

SH-SY5Y neuroblastoma cells (ATCC®, CRL-2266™) obtained from Innoprot S.L. (Derio, Spain) were cultured in RPMI 1640 medium containing 10% fetal bovine serum, non-essential amino acids and 1% penicillin-streptomycin at 37ºC in a humidified atmosphere with 5% CO_2. Cells were transfected with Lipofectamine™ 3000 following the manufacturer's instructions (**Protocol 23**).

3.2.7. Fluorescence confocal microscopy.

SH-SY5Y cells were grown on µ-Slide 8-well chambered coverslips (Ibidi, 80826). 24 h post-transfection, cells were stained with MitoTracker Red CMXRos (100 nM 1 h 37ºC) or co-transfected with DsRed2-Mito-7 plasmid (Addgene, 55838; deposited by Michael Davidson). Cells were treated with rotenone (1 µM 6 h), CCCP (20 µM 1 h) or O/A (oligomycin A 10 µM + antimycin A 4 µM, 6 h) in serum-free medium and then fixed with 4% paraformaldehyde (PFA) for 10 min. Samples were visualized in an inverted confocal fluorescence microscope (Nikon Eclipse C1, Nikon Inc., Melville, NY, USA) with a x60 oil immersion objective. The excitation wavelengths used were 488 nm for GFP and 561 nm for MitroTracker Red, and emitted fluorescence was recorded using band pass filters BP515 and BP593 respectively. Autophagy vesicles and their colocalization with mitochondria were analyzed using Just Another Colocalization Plugin Software (JaCoP) in ImageJ (Bolte & Cordelières, 2006). At least 30 cells were analyzed per condition.

3.2.8. Cell lysis and western blot.

Cells were scraped in PBS and collected after centrifugation at 1500 x g for 10 min at 4ºC. They were lysed using the commercial RIPA lysis buffer supplemented with protease inhibition cocktail at 1X for 45 min. Afterwards, cell lysates were centrifuged at 12000 x g for 10 min at 4ºC and supernatants were collected. Samples were separated by SDS-PAGE, using 15% polyacrylamide gels, and then transferred onto PVDF blotting

membranes with a 0.2-µm pore size (Amersham™ Hybond™, 10600021). Membranes were blocked with 5% nonfat milk in TBST buffer (20 mM Tris-HCl, pH 7.4, 150 mM NaCl, 0.1% Tween 20 [Sigma-Aldrich, P7949]). Western blots were performed incubating the membranes with primary antibodies in TBST buffer containing 1% of nonfat milk overnight at 4ºC. The primary antibodies employed were: anti-LC3A (rabbit) 1:1000 (Abcam, ab26628); anti-LC3B (rabbit polyclonal) 1:10000 (Abcam, ab51520); anti-LC3C (rabbit monoclonal) 1:1000 (Abcam, ab150367); anti-COX4I/COX-IV (mouse monoclonal) 1:1000 (Abcam, ab14744); anti-ACTB/actin (mouse monoclonal) 1:1000 (Santa Cruz Biotechnology, sc-8432). After washing, blots were incubated with secondary antibodies in TBST containing 1% nonfat milk for 1 h at room temperature, using HRP-conjugated anti-mouse 1:5000 (Santa Cruz Biotechnology, sc-516102) or HRP-conjugated anti-rabbit 1:5000 (Santa Cruz Biotechnology, sc-2357) as required. Blots were then washed in TBST and bands were visualized using Immobilon®Forte Western HRP Substrate in an iBright 1500 equipment (Invitrogen, California, CA, USA). See also **Protocol 24**.

3.2.9. siRNA.

SH-SY5Y cells were transfected with 100 nM siRNA using Lipofectamine™ 2000 in Opti-MEM medium according to manufacturer instructions. Opti-MEM was replaced with complete RPMI 1640 medium after 6-h incubation. This incubation was repeated after 24 h, for a period of 72 h. siRNAs were designed to target the sequences used in other works (Liu *et al*., 2017; von Muhlinen *et al*., 2012) for the specific silencing of LC3A and LC3B proteins and are indicated in **Table 2.5**.

3.2.10. Mitochondrial isolation.

Cells were collected and resuspended in mitochondrial insolation buffer (MIB; 10 mM Hepes, 70 mM sucrose, 210 mM mannitol, 1 mM EDTA, pH 7.5) supplied with protease inhibitors and homogenized (50 strokes) with a Potter-Elvehjem homogenizer (Fischer Scientific, 10373143). The homogenate was centrifuged at 1500 x g for 10 min at 4°C and the post-nuclear supernatant was collected. Supernatants were mixed and centrifuged at 10500 x g for 5 min at 4°C. The pellet containing purified mitochondria was washed once with MB, and finally resuspended in RIPA lysis buffer supplemented with protease inhibition cocktail at 1X. Samples were examined by western blot. Immunodetection of COX4I only in mitochondrial fractions was considered as a control of mitochondrial isolation. See also **Protocol 25**.

3.2.11. Statistical analysis.

Statistical analyses were performed using the Student's t-test. Results in Figure 3.11 were analyzed with ANOVA.

3.3. Results

3.3.1. The similarity of predicted CL-interacting residues in LC3-subfamily members suggests similar functions.

Despite the extensive structural similarities (**Figure 3.3A**), a marked variation between LC3/GABARAP family members is found in the N-terminal region (See also section 1.4). It has been shown that, while the first α-helix of LC3 subfamily is strongly basic, in the GABARAP subfamily this region is acidic (Sugawara *et al.*, 2004) (**Figure 3.3A, B**). These differences are relevant because the N-terminal region of these proteins might be important for specific functions during autophagy, playing an important role in protein-protein interactions, lipid-protein interactions, or via post-translational modifications (Lee & Lee, 2016).

Previous studies from this laboratory have focused on the potential different roles of these two subfamilies, both in cargo recognition (Antón *et al.*, 2016) and during autophagosome expansion (Landajuela *et al.*, 2016). Regarding cargo recognition, several aspects of the mitophagic mechanism initiated by CL externalization remain obscure. Previous work from this laboratory (Antón *et al.*, 2016) compared the behavior of LC3B with that of GABARAP subfamily members. The study explored the differences in residues putatively involved in LC3B interaction with CL (**Figure 3.3B**). *In vitro*, the GABARAP-subfamily members showed less binding to CL than LC3B and this corresponded with the absence of translocation to mitochondria in cells.

Taking into account the similarity between the predicted CL-interacting residues in LC3B and those in LC3A and LC3C (**Figure 3.3B**), it could be assumed that all three LC3-subfamily members would be involved in CL recognition. This hypothesis was experimentally tested as follows.

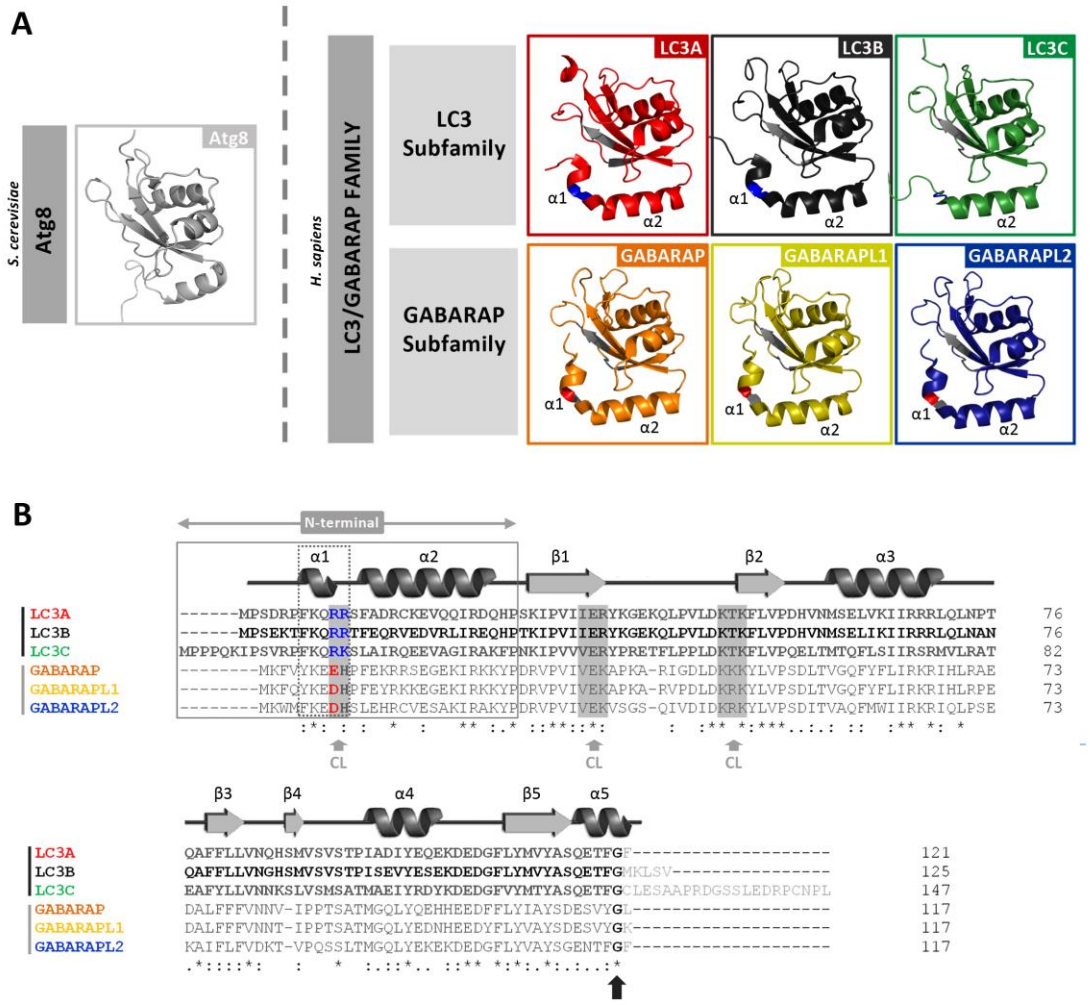

Figure 3.3. LC3/GABARAP-family members and their interaction with CL. (**A**) Schematic representation of the 3D structures of yeast Atg8 and of each LC3/GABARAP protein in solution, displayed with PyMOL. PDB: Atg8 (2KQ7), LC3A (5CX3), LC3B (2ZJD), LC3C (2NCN), GABARAP (1GNU), GABARAPL1 (5LXI) and GABARAPL2 (4CO7). The thermodynamically preferred residues for cardiolipin binding on LC3B, identified by docking analysis (Chu *et al*., 2013), and their equivalents in the other LC3/GABARAP-family members are highlighted in gray [See (B)]. Among them, the two residues in the α1 N-terminal region proposed to be essential for the interaction, and their equivalents in the LC3 subfamily, are colored in blue (positively charged). The amino acid corresponding to R10 of LC3B is a negatively charged residue in the GABARAP subfamily, colored in red (See Figure 1B). (**B**) Sequence alignment of the human orthologs of Atg8 obtained with Clustal W. UniProt: LC3A (Q9GZQ8), LC3B (Q9GZQ8), LC3C (Q9BXW4), GABARAP (O95166), GABARAPL1 (Q9H0R8) and GABARAPL2 (P60520). The secondary structure elements of LC3B (PDBsum, 2ZJD) are indicated above the alignment as an example. The N-terminal and α-helix 1 (α1) of the two subfamilies are boxed. As in (A), the thermodynamically preferred residues for cardiolipin binding of LC3B, and their equivalents in the other members of the LC3/GABARAP family are highlighted in gray (gray arrow). The two positively charged α1 N-terminal residues proposed to be essential for the interaction of LC3B with CL and their equivalents are colored; blue: positively charged, red: negatively charged. The C-terminal glycine (black arrow) is conserved in all the LC3/GABARAP-family members.

3.3.2. LC3A and LC3C, as well as LC3B, interact with CL-containing model membranes.

To determine whether members of the LC3 subfamily other than LC3B were also able to bind CL-enriched model membranes, the binding of LC3A and LC3C to large unilamellar vesicles (LUV) containing CL was measured. For this purpose, a vesicle flotation assay (**Protocol 16**) was performed (Antón *et al.*, 2016), in which protein association with membranes was assessed by the protein ability to float together with the vesicles after equilibrium in sucrose-gradient centrifugation (**Figure 2.8**). A highly unsaturated (mainly tetralinoleoyl) CL was chosen based on the results by Antón *et al.* (2016), who compared the LC3B binding affinities towards CL containing acyl chains with different degrees of unsaturation. CL concentration in these experiments intended to mimic the one of the interaction zones formed in the OMM after CL exposure, and it was based on the CL levels used in similar studies with other proteins (Landeta *et al.*, 2011; Ryan *et al.*, 2018; Stepanyants *et al.*, 2015).

In fact, the *in vitro* interaction of LC3A and LC3C with CL was higher than that of LC3B. Almost all of the LC3C was bound to membranes when CL was present, and, while not all LC3A interacted with CL, it nearly doubled the proportion of bound LC3B (**Figure 3.4**). Binding of the three proteins was dependent on both vesicle curvature (the proteins bound more highly curved SUV better than LUV) and CL concentration in the bilayers (**Figure 3.5**). Consistent with previous results (Antón *et al.*, 2016) GABARAPL2 did not reach the binding level of the LC3 proteins to CL-containing membranes (**Figure 3.4**). The results indicated that LC3B was not the only member of the LC3 subfamily able to bind CL in lipid bilayers, thus perhaps LC3B might not be the only one capable of recognizing externalized CL in damaged mitochondria.

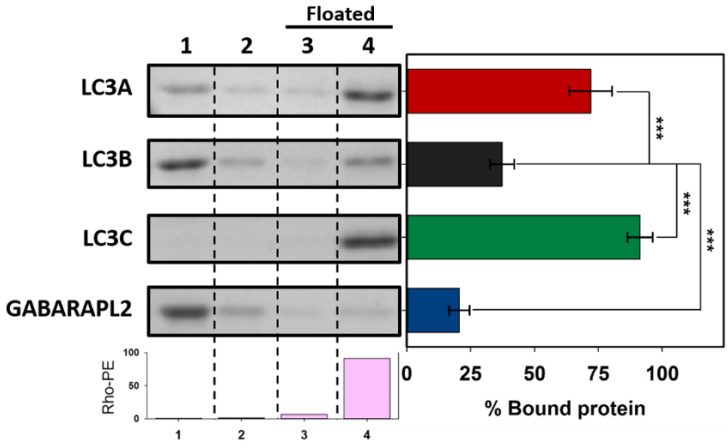

Figure 3.4. LC3A and LC3C, as well as LC3B, interact with CL-containing model membranes. Interaction of LC3A, LC3B, LC3C and GABARAPL2 with LUV containing CL using a vesicle flotation assay. LUV were composed of ePC:DOPE:CL (33:33:33 mol ratio) + 0.05% Rho-PE. The presence of vesicles and proteins in the different fractions was probed by Rho-PE fluorescence emission and by SDS-PAGE/Coomassie Brilliant Blue staining respectively. Bars at the bottom: Rho-PE emission was detected only in fractions 3-4 (i.e., floating fractions). The bars at the right-hand side correspond to the percentage of bound protein, taken as protein co-floating with vesicles and calculated by gel densitometry. Data are means ± SD ($n \geq 9$). ***$p < 0.001$.

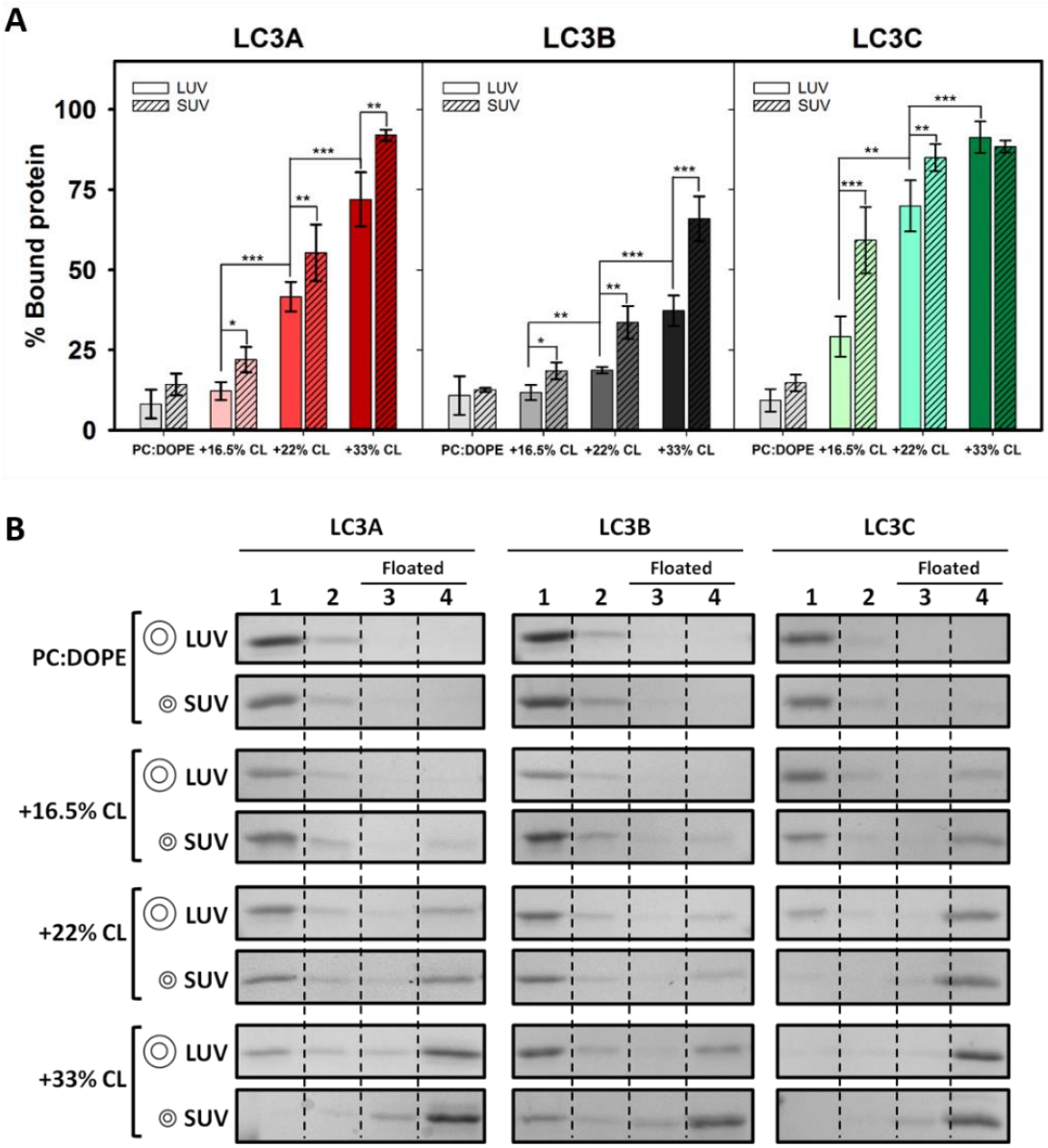

Figure 3.5. LC3 binding to liposomes is enhanced by membrane curvature and, in a dose-dependent manner, by CL. Interaction of LC3 proteins with vesicles of different radii and/or CL contents was measured by a vesicle flotation assay. (**A**) Binding of LC3A, LC3B, and LC3C to liposomes, quantified by gel densitometry. LUV (100 nm) or SUV (50 nm) were composed either of ePC:DOPE (50:50 mol ratio) or of ePC:DOPE:CL. In the latter case, the percent lipid proportions were 49.5:33:16.5, 44:33:22 or 33:33:33. Data shown are means ± SD (n ≥ 3). ***p < 0.001, **p < 0.01, *p < 0.05 **(B)** Representative SDS-PAGE Coomassie Brilliant Blue-stained gels of the fractions obtained from LC3A, LC3B, and LC3C vesicle flotation assays, whose quantitative results are summarized in Figure 3.5A. Bound protein is computed as the proportion retrieved in fractions 3+4 (See Figure 2.8).

3.3.3. LC3A and LC3B interact preferentially with CL over other negatively charged phospholipids.

To determine whether LC3 proteins interaction with membranes was specific for CL, the binding of these proteins to LUV of different lipid compositions was investigated (**Figure 3.6**).

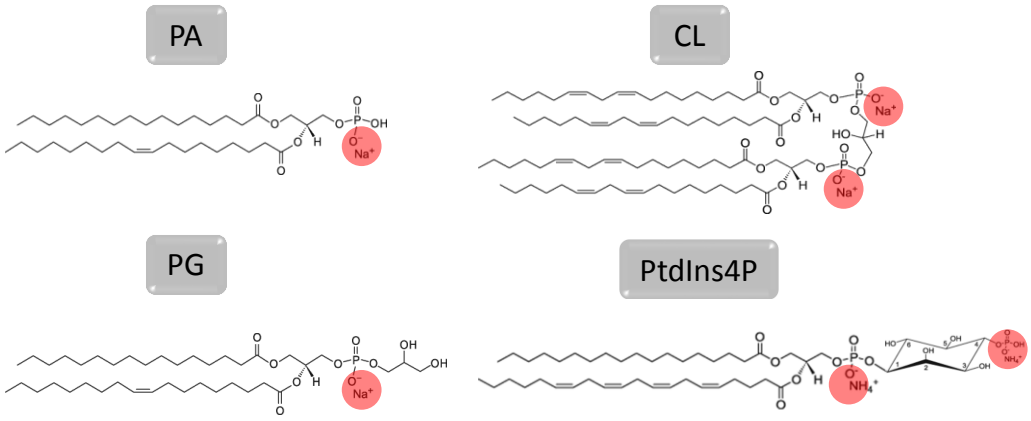

Figure 3.6. Structures of relevant negatively charged phospholipids. Egg phosphatidic acid (PA), egg phosphatidylglycerol (PG), heart cardiolipin (CL), brain phosphatidylinositol-4-phosphate (PtdIns4P).

None of the LC3-subfamily members was able to float in the absence of vesicles, or in the presence of liposomes composed of electrically neutral phospholipids (egg phosphatidylcholine [PC] or dioleoyl phosphatidylethanolamine [DOPE]) (**Figure 3.7A**). Moreover, the interaction of LC3 proteins with membranes containing egg phosphatidic acid (PA) or egg phosphatidylglycerol (PG), phospholipids that are structurally and metabolically related to CL, was assayed. PA and PG are also negatively charged, but they contain ≈1 charge per molecule under physiological conditions, vs. ≈ 2 in the case of CL (Kates *et al.*, 1993). Neither LC3A nor LC3B did interact with PA- or PG-containing membranes. LC3C was able to bind PA-containing bilayers, albeit the interaction was lower than with CL-vesicles. PG did not increase LC3C binding to liposomes (**Figure 3.7**).

In addition, the interaction with brain phosphatidylinositol-4-phosphate (PtdIns4P) was measured. PtdIns4P contains two negative charges per molecule, as in the case of CL, but two fatty acyl chains per molecule, vs. four in the case of CL. None of the LC3-subfamily members showed the ability to interact with PtdIns4P-containing membranes, suggesting that the interaction could not be explained by purely electrostatic forces (**Figure 3.7**). Note that PtdIns4P generation in autophagosomes was shown to be critically important for GABARAP-mediated fusion with lysosomes (Wang *et al.*, 2015), another example of differentiation in the LC3/GABARAP-protein family. In summary, the above results suggest that all three LC3-subfamily members interact preferentially with CL over other negatively charged lipids, although LC3C displays also a rather high affinity towards PA, which suggests that this protein is not as specific for CL as the other LC3 homologs.

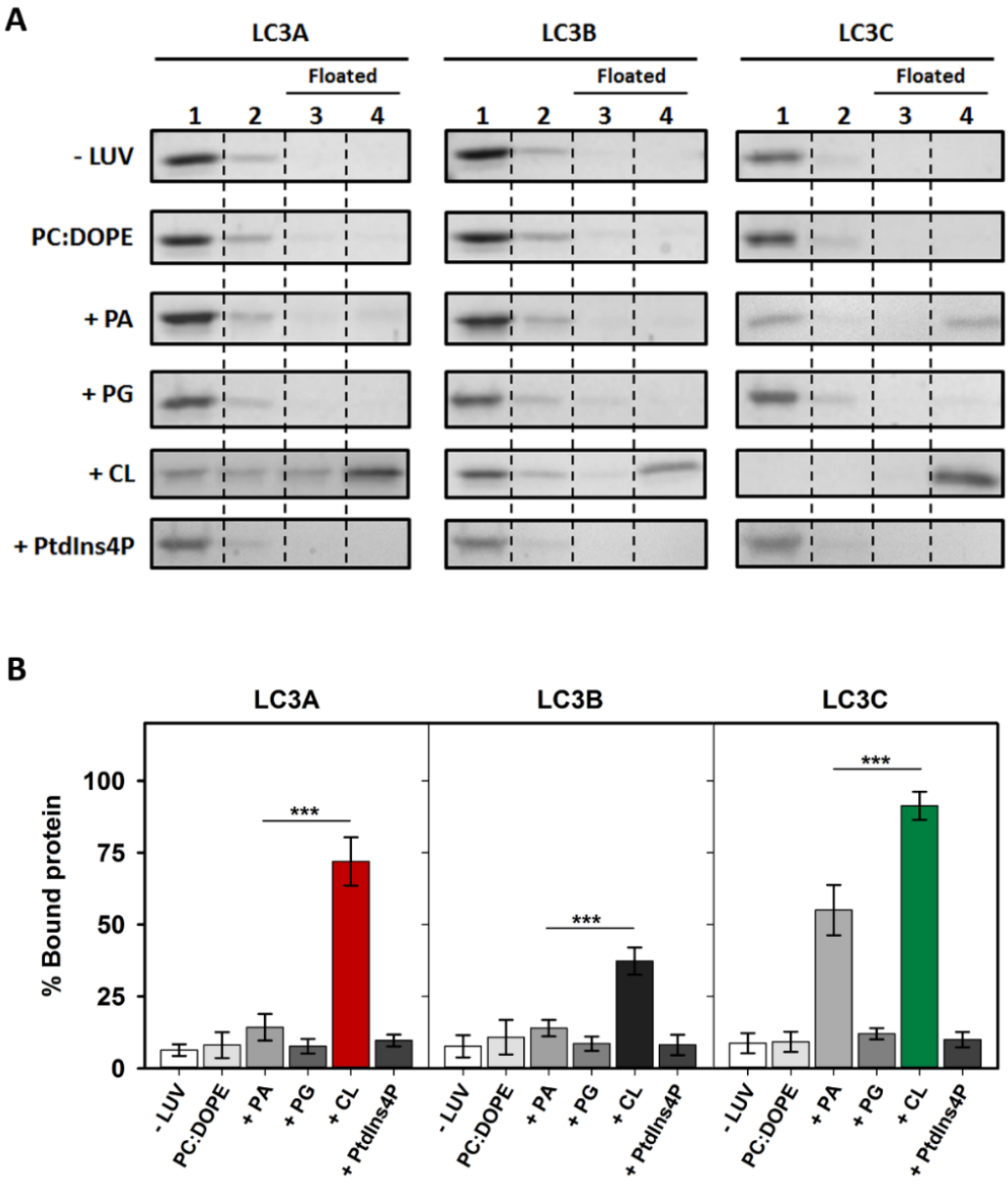

Figure 3.7. LC3A and LC3B exhibit a marked specificity for CL. Interaction of LC3 proteins with membranes of different compositions, measured by a vesicle flotation assay. (**A**) Representative SDS-PAGE Coomassie Brilliant Blue-stained gels of the fractions obtained from LC3A, LC3B or LC3C vesicle flotation assays performed without liposomes (-LUV) or with liposomes of different compositions, either ePC:DOPE (50:50) or ePC:DOPE:X (33:33:33 mol ratio) where X was PA, PG, CL or PtdIns4P. Bound protein was computed as the proportion retrieved in fractions 3+4 (See Figure 2.8). (**B**) Binding of LC3A, LC3B, and LC3C to liposomes quantified by gel densitometry. Data are means ± SD (n ≥ 3). ***p< 0.001.

3.3.4. The higher capacity of LC3C to interact with CL resides in its N-terminal region.

To determine the characteristics that made LC3C interact with CL with a higher affinity than LC3B, a sequence alignment of LC3C and LC3B was performed. LC3C exhibited large differences with LC3B in its amino acid sequence (46/72% identity/similarity) (**Figure 3.8A**). The main differences were found in the N terminal region. This observation was consistent with the previously mentioned role of the N-terminal region in the interaction with CL (Antón *et al*., 2016; Chu *et al.*, 2013). Therefore, the possibility that this region could participate in the interaction with CL was tested. For this purpose, a chimera protein was constructed, containing the LC3C N-terminal region (1-33) and the LC3B 29-120 residues (**Figure 3.8B**). The proportion of this chimera bound to CL-containing liposomes was larger than that of LC3B, reaching the level of LC3C (**Figure 3.8C, D**), thus implying that the N-terminal region of LC3C alone was enough to explain the higher degree of interaction with CL observed with LC3C.

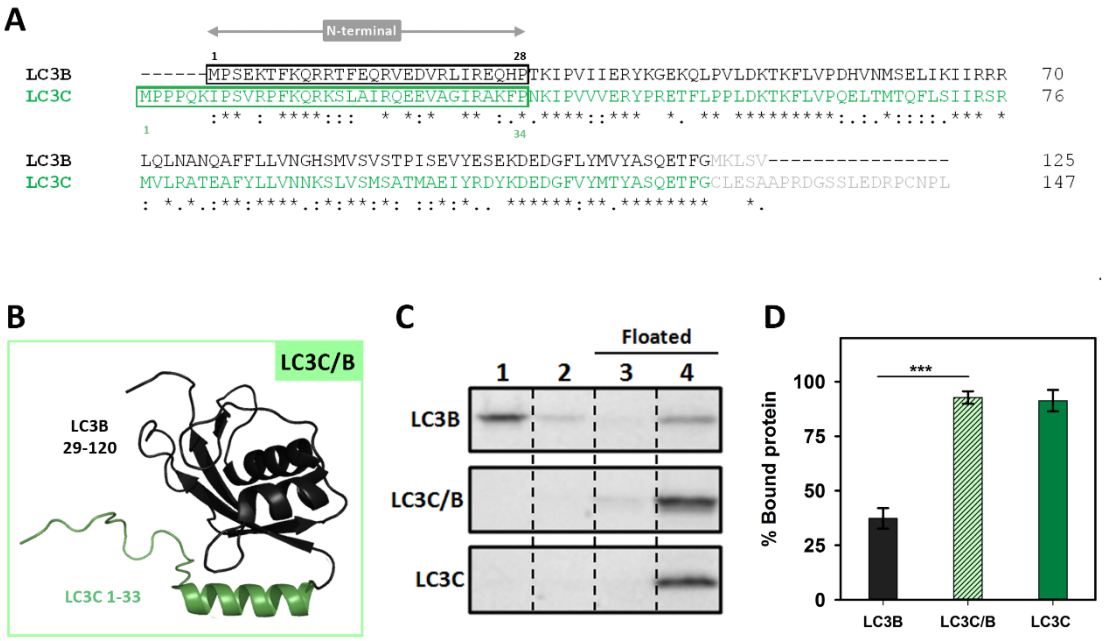

Figure 3.8. The higher capacity of LC3C to interact with CL resides in its N-terminal region. (**A**) Clustal W alignment of LC3B and LC3C amino acid sequences. The N-terminal region of both proteins is boxed. Residues processed by ATG4 and not present in our recombinant proteins are in light gray. (**B**) 3D outline of the LC3C/B chimera composed of the structures of the LC3C N-terminal region (1-33 amino acids) and 29-120 residues of LC3B. (**C**) Representative SDS-PAGE/Coomassie Brilliant Blue-stained gels of the fractions obtained from LC3B, LC3C/B or LC3C vesicle flotation assays performed with CL-containing liposomes (ePC:DOPE:CL (33:33:33 mol ratio)). Bound protein was computed as the proportion retrieved in fractions 3+4 (See Figure 2.8) (**D**) Binding of LC3B, LC3C/B, and LC3C to CL-containing liposomes quantified by gel densitometry. Data are means ± SD (n ≥ 7). ***p < 0.001.

3.3.5. The N-terminal regions of LC3A and LC3B are important for their differential interaction with CL.

The reason why LC3A interacted with CL with a higher affinity than LC3B was also explored. These two proteins exhibited a 79/92% identity/similarity when their amino acid sequences were compared (**Figure 3.9A**) and the main differences were also found in the N-terminal region. Therefore, the implication of this region in LC3A interaction with CL was tested. In this case, a chimera composed of the LC3A N-terminal region (1-28) and the LC3B protein 29-120 residues was designed (**Figure 3.9B**). The chimera showed a higher interaction with cardiolipin than LC3B, even if it did not reach LC3A binding levels (**Figure 3.9C, D**). These results suggested a mode of interaction with CL involving other regions of the protein apart from its N terminus, similar to the mechanism proposed for LC3B, but not to the one observed with LC3C. The increased CL interaction with the LC3A/B chimera, as compared to that of LC3B, suggests that LC3A might contain some residues in its N-terminal region allowing a stronger interaction with that phospholipid.

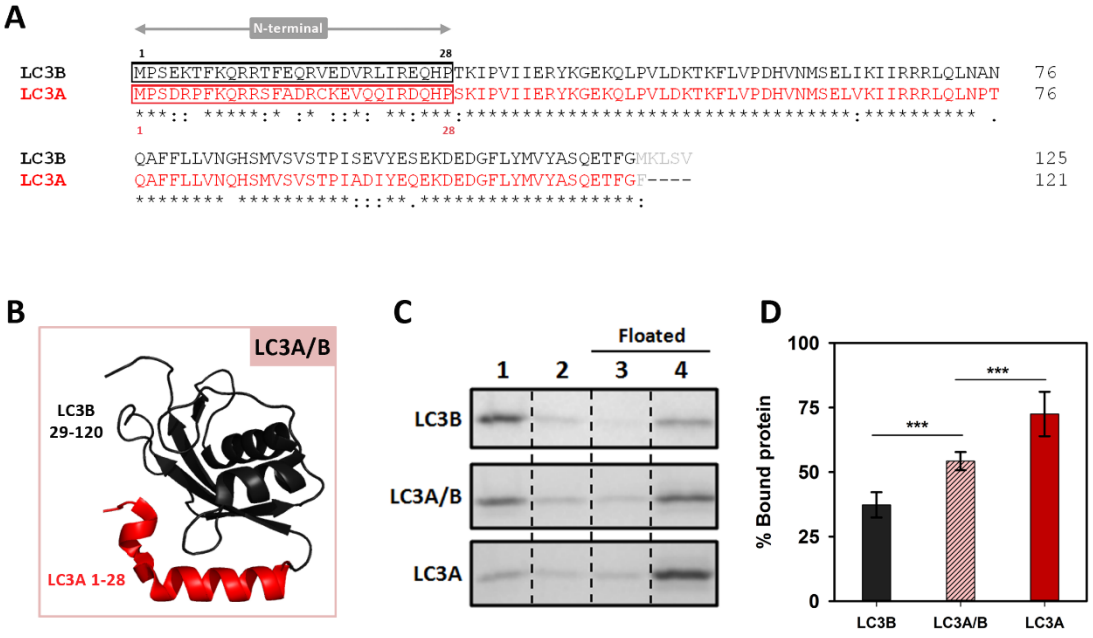

Figure 3.9. The N-terminal regions of LC3A and LC3B are important for their differential interaction with CL. (**A**) Clustal W alignment of LC3B and LC3A amino acid sequences. The N-terminal region of both proteins is boxed. Residues processed by ATG4 and not present in our recombinant proteins are in light gray (**B**) 3D outline of the LC3A/B chimera composed of the structures of the LC3A N-terminal region (1-28 amino acids) and 29-120 residues of LC3B. (**C**) Representative SDS-PAGE/Coomassie Brilliant Blue-stained gels of the fractions obtained from LC3B, LC3A/B or LC3A vesicle flotation assays performed with CL-containing liposomes (ePC:DOPE:CL (33:33:33 mol ratio). Bound protein was computed as the proportion retrieved in 3+4 (See Figure 2.8) (**D**) Binding of LC3B, LC3A/B, and LC3B to CL-containing liposomes quantified by gel densitometry. Data are means ± SD (n ≥ 8) ***p < 0.001.

3.3.6. A14 and K18 residues in LC3A N-terminal region are key for its higher interaction with CL.

To further analyze the importance of specific residues in the N terminus of LC3A, a sequence alignment focusing on this region of LC3B and LC3A proteins was performed. This comparison revealed that residues shown by Chu (Chu *et al*., 2013) to be involved in the interaction with CL were the same in both proteins (R10, R11), suggesting that the cause for the different behavior had to be found elsewhere.

Taking into account that the object of the study was an interaction with a negatively charged phospholipid an analysis of the isoelectric points (pI) of the proteins (**Figure 3.10A**) was performed. The effect of ionic strength was assessed using either the standard buffer (150 mM NaCl) or a buffer containing 300 mM NaCl. A decreased LC3 binding in the presence of high-ionic-strength buffer was observed in all cases (**Figure 3.10B, C)**, pointing to an implication of electrostatic interactions in LC3 proteins binding to CL-containing bilayers. Moreover, the fact that this decrease was more marked for LC3A could indicate the implication of charged amino acids in the differential interaction of LC3A and LC3B.

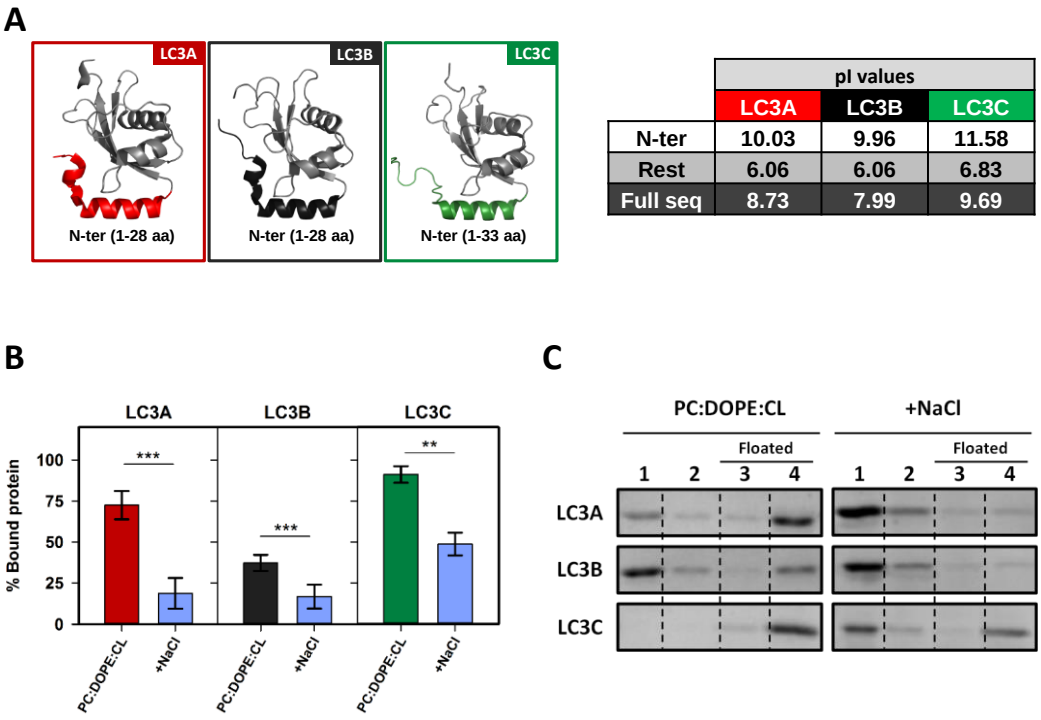

Figure 3.10. Increasing ionic strength of the medium decreases the binding of LC3 to CL. Effect of the increased ionic strength on the interaction of LC3 proteins with CL-containing membranes, measured by a vesicle flotation assay. (**A**) Left: Schematic representation of the 3D structures of LC3 proteins, displayed with PyMOL. PDB: LC3A (5CX3), LC3B (2ZJD), LC3C (2NCN) with their N-terminal region highlighted in red, black and green respectively. Right: pI values of the N-terminal region, the remaining sequence, and the full sequence of LC3A, LC3B and LC3C have been computed using the tool "Compute pI/Mw" of Expasy. (**B**) Binding of LC3A, LC3B, and LC3C to liposomes composed of ePC:DOPE:CL (33:33:33 mol ratio) in buffer containing 150 mM NaCl or in buffer containing 300 mM NaCl (+NaCl). Data shown are means ± SD ($n \geq 3$) ***$p < 0.001$, **$p < 0.01$. (**C**) Representative SDS-PAGE Coomassie Brilliant Blue-stained gels of the fractions obtained from LC3A, LC3B, and LC3C vesicle flotation assays, whose quantitative results are summarized in Figure S2B. Bound protein is computed as the proportion retrieved in fractions 3+4 (See Figure 2.8).

Two negatively charged amino acids were observed in LC3B (E14, E18) that were not present in LC3A, the latter protein containing instead one neutral and one positively charged residue (A14, K18) (**Figure 3.11A, B**). To test the involvement of residues 14 and 18 in the differential LC3A and LC3B binding to CL, a series of mutants was designed, expressed and purified. The objective was to "transform" LC3B into LC3A and *vice versa* LC3A into LC3B by mutating the mentioned residues, to elucidate whether the CL-binding affinity was influenced or not. As shown in **Figure 3.11C** and **D**, after changing E14 of LC3B into the corresponding A14 of LC3A, i.e. obtaining the mutant LC3B^{E14A} (LC3B-AE), the percentage of bound protein was higher than with native LC3B. Mutating residue 18, to obtain LC3B^{E18K} (LC3B-EK), also increased binding, to the same extent than for LC3B-AE. The highest proportion of bound protein was found with LC3B^{E14A,E18K} (LC3B-AK), above the value observed for LC3A (**Figure 3.11C, D**).

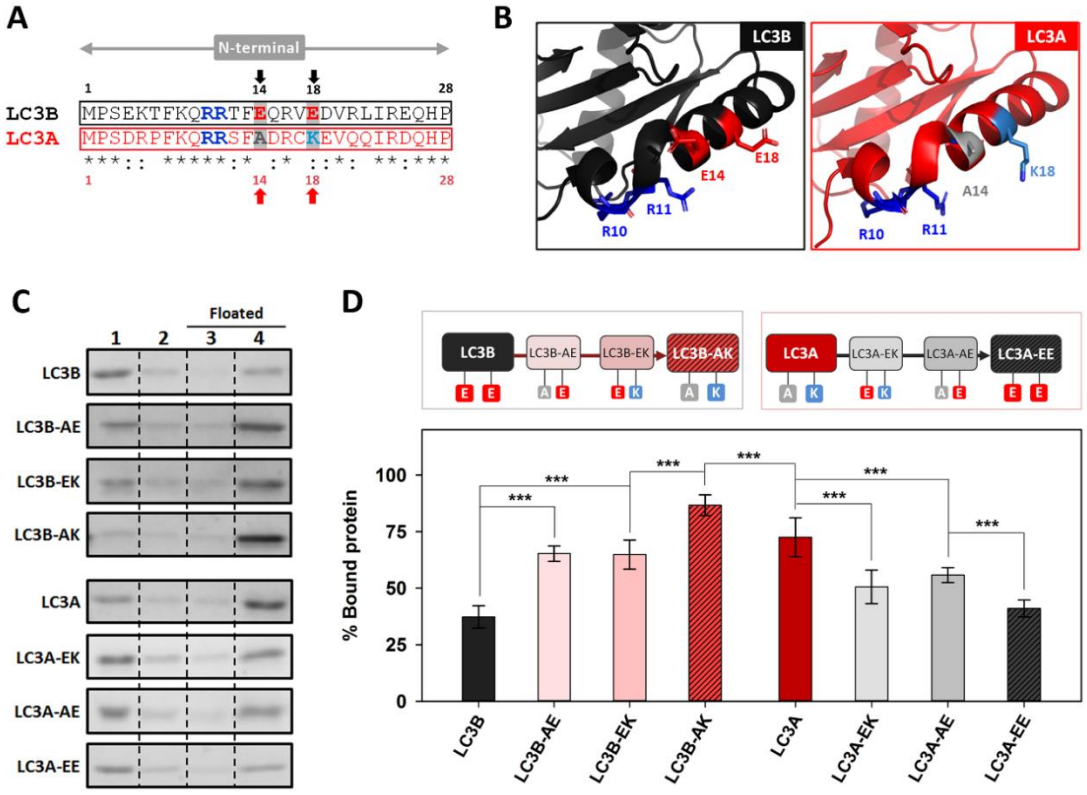

Figure 3.11. A14 and K18 residues in LC3A N-terminal region are key for its higher interaction with CL. (**A**) Comparative analysis of the N-terminal regions of LC3B and LC3A obtained using Clustal W. Amino acids previously proposed to be important in LC3B-CL interaction (R10, R11) and the ones chosen in this study to be mutated (positions 14 and 18) are written in bold and colored; red: negatively charged, blue: positively charged, gray: no charge (**B**) 3D structures of the N-terminal regions of LC3B and LC3A showing the amino acids chosen for this study and the residues already proposed to be involved in the interaction with CL. (**C**) Representative SDS-PAGE/Coomassie Brilliant Blue-stained gels of the fractions obtained from LC3B, LC3B-AE (LC3B^{E14A}), LC3B-EK (LC3B^{E18K}), LC3B-AK (LC3B^{E14A,E18K}), LC3A, LC3A-EK (LC3A^{A14E}), LC3A-AE (LC3A^{K18E}), LC3A-EE (LC3A^{A14E,K18E}) vesicle flotation assays performed with CL-containing liposomes (ePC:DOPE:CL (33:33:33 mol ratio)). Bound protein was computed as the proportion retrieved in fractions 3+4 (see Figure 2.8). (**D**) Binding percentage of LC3B, LC3B-AE (LC3B^{E14A}), LC3B-EK (LC3B^{E18K}), LC3B-AK (LC3B^{E14A,E18K}), LC3A, LC3A-EK (LC3A^{A14E}), LC3A-AE (LC3A^{K18E}), LC3A-EE (LC3A^{A14E,K18E}) to CL-containing liposomes quantified by gel densitometry. Data shown as mean ± SD (n ≥ 5) ANOVA statistical analysis, ***$p < 0.001$.

In the case of LC3A, both single-residue mutants (LC3A^{A14E} [LC3A-EK], LC3A^{K18E} [LC3A-AE]) exhibited a decreased interaction. Furthermore, the LC3A^{A14E,K18E} (LC3A-EE) showed a degree of binding to CL-containing vesicles similar to that of LC3B (**Figure 3.11C, D**). Thus, while mutating the two residues of LC3B almost doubled its interaction, changing the two amino acids of LC3A significantly decreased its interaction with CL, demonstrating the importance of the nature of residues 14 and 18 in the higher CL binding activity of LC3A. In addition, when the equivalent of the LC3B E14 residue (A20) in the N-terminal region of LC3C was mutated, to obtain LC3C^{A20E} (**Figure 3.12A, B**), LC3C binding was not affected (**Figure 3.12C, D**). Thus, the very effective binding of LC3C to CL-containing vesicles should not be interpreted in the same terms described for LC3A and LC3B above, rather indicating that the whole N-terminal region of LC3C was important for its interaction with CL.

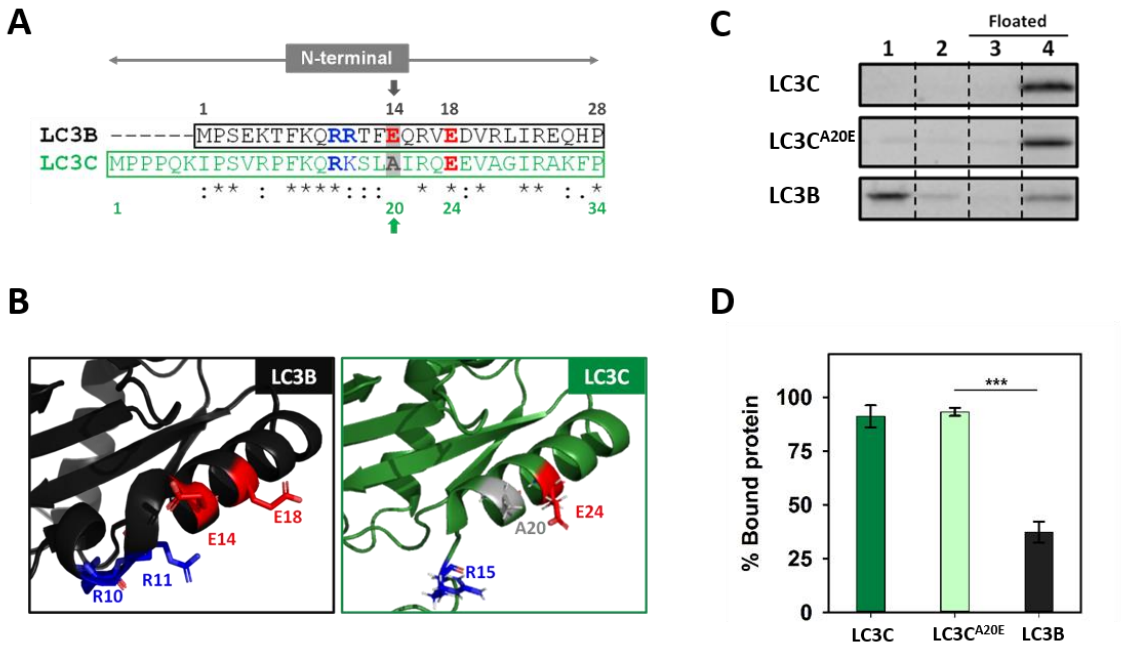

Figure 3.12. Changing a specific LC3C N-terminal residue has no effect on the protein binding to CL. **(A)** Comparative analysis of the N-terminal regions of LC3B and LC3C obtained using Clustal W. Amino acids proposed to be important in LC3B-CL interaction (R10, R11), those residues proposed to make the difference between LC3B and LC3A (E14, E18) and the corresponding ones in LC3C are colored: red, negatively-charged; blue, positively-charged; gray, no charge. The arrows show the amino acid residue designed to be mutated. (**B**) 3D structures of the N-terminal regions of LC3B and LC3C showing the said amino acid residues. (**C**) Representative SDS-PAGE Coomassie Brilliant Blue-stained gels of the fractions obtained from LC3C, LC3C^{A20E} and LC3B vesicle flotation assays performed with CL-containing liposomes (ePC:DOPE:CL (33:33:33 mol ratio)). Bound protein is computed as the proportion retrieved in fractions 3+4 (See Figure 2.8). (**D**) Binding percentage of LC3C, LC3C^{A20E} and LC3B to CL-containing liposomes quantified by gel densitometry. Data shown are means ± SD (n ≥ 3). ***p < 0.001.

3.3.7. LC3A and LC3B puncta per cell and their colocalization with mitochondria increase with rotenone treatment.

CL externalization to the OMM had been shown using treatments with non-lethal doses of rotenone (Chu *et al*., 2013). However, the mechanism controlling CL externalization is not completely understood. CL is a phospholipid mainly found in the inner monolayer of IMM; therefore, three steps are required for it to be fully translocated to the external monolayer of the OMM. Translocation between the monolayers of the same membrane is believed to be catalyzed by PLSCR3 (phospholipid scramblase 3) (Chu *et al*., 2013; Liu *et al.*, 2008). The transfer between the IMM outer monolayer and the inner leaflet of OMM is thought to be carried out by the kinase NME4/NDPK-D/Nm23-H4 (Kagan *et al.*, 2016; Schlattner *et al.*, 2013).

To assess whether the above *in vitro* results were indicative of the behavior of LC3 proteins in cells, the involvement of each LC3 member in CL-mediated mitophagy was tested. Experiments were performed using LC3A, LC3B, LC3C, and GABARAPL2 to test whether this treatment induced an increase in LC3/GABARAP- protein puncta inside the cell (as a signal of autophagy) and whether it increased the number of puncta that colocalized with mitochondria (mitophagy). The experimental conditions were as described in previous studies in which CL externalization had been shown (Chu *et al.*, 2013). SH-SY5Y neuroblastoma cells were transfected with GFP-tagged LC3 proteins and treated with 1 μM rotenone (6 h). GFP-GABARAPL2 was used as a control as this protein was unable to translocate to mitochondria upon rotenone treatment in U87MG cells (Antón *et al.*, 2016).

The formation of puncta, as detected by conventional fluorescence microscopy, has been interpreted in the experiments below as an indicator of soluble LC3 (LC3-I) conversion to the autophagosome-associated form (LC3-II). To ascertain whether the apparent autophagy observed was indeed due to autophagy vesicles and not to protein aggregates, non-conjugatable mutants of the proteins were used. In those mutants the C-terminal Gly had been mutated into an Ala residue, resulting in a non-functional form of the proteins that could not be conjugated to PE, thus they could not be anchored to the phagophore or autophagosomal membrane. The mutant proteins consistently failed to give rise to puncta, indicating that the detected GFP signals did not correspond to non-specific aggregates (**Figure 3.13A, B**).

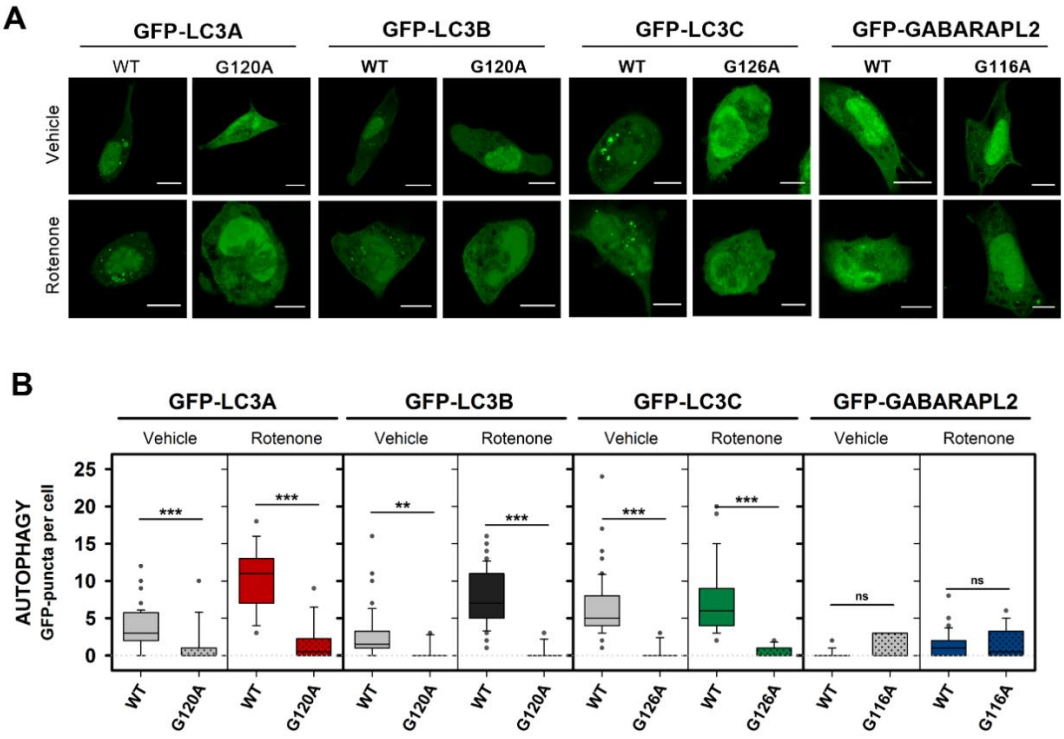

Figure 3.13. Autophagy quantification with native GFP-LC3/GABARAP proteins and with non-conjugatable mutants confirms that most puncta in cells are autophagic vesicles and not aggregates. SH-SY5Y neuroblastoma cells were transfected with different members of the LC3/GABARAP family tagged with GFP (WT) and their respective non-conjugatable mutants (LC3A^{G120A}, LC3B^{G120A}, LC3C^{G126A}, and GABARAPL2^{G116A}). Cells were treated with 1 μM rotenone for 6 h. Vehicle (Veh) controls were treated with DMSO. (**A**) Representative images of each condition. Images were retrieved using a Nikon Eclipse C1 confocal microscope. Scale bar: 10 μm. (**B**) Number of GFP puncta per cell in each condition, an indication of autophagy. At least 30 images were analyzed per condition. ***p < 0.001, **p < 0.01, ns: non-significant.

Six h-rotenone treatment induced an enhanced number of GFP-LC3A and GFP-LC3B puncta, and their colocalization with mitochondria was equally increased (**Figure 3.14A, B and 3.15A, B**). These results, using a CL-externalizing treatment, were consistent with the ability of LC3A and LC3B to interact with CL-containing membranes *in vitro* (**Figure 3.4**). In agreement with previous results (Antón *et al.*, 2016) and with our own *in vitro* studies (**Figure 3.4**), rotenone did not increase GFP-GABARAPL2 colocalization with mitochondria (**Figure 3.14D and 3.15A,B**). However, at variance with the other proteins, a high amount of GFP-LC3C puncta was observed under basal conditions and, despite the remarkable level of interaction displayed by LC3C with CL-containing membranes (**Figure 3.4**), the amount of GFP-LC3C puncta did not increase after rotenone treatment (**Figure 3.14C and 3.15A,B**). These results suggest that LC3A and LC3B are able to recognize CL not only in model membranes but also in damaged mitochondria, while LC3A and LC3B, but not LC3C or GABARAPL2, are involved in cargo recognition during CL-mediated mitophagy.

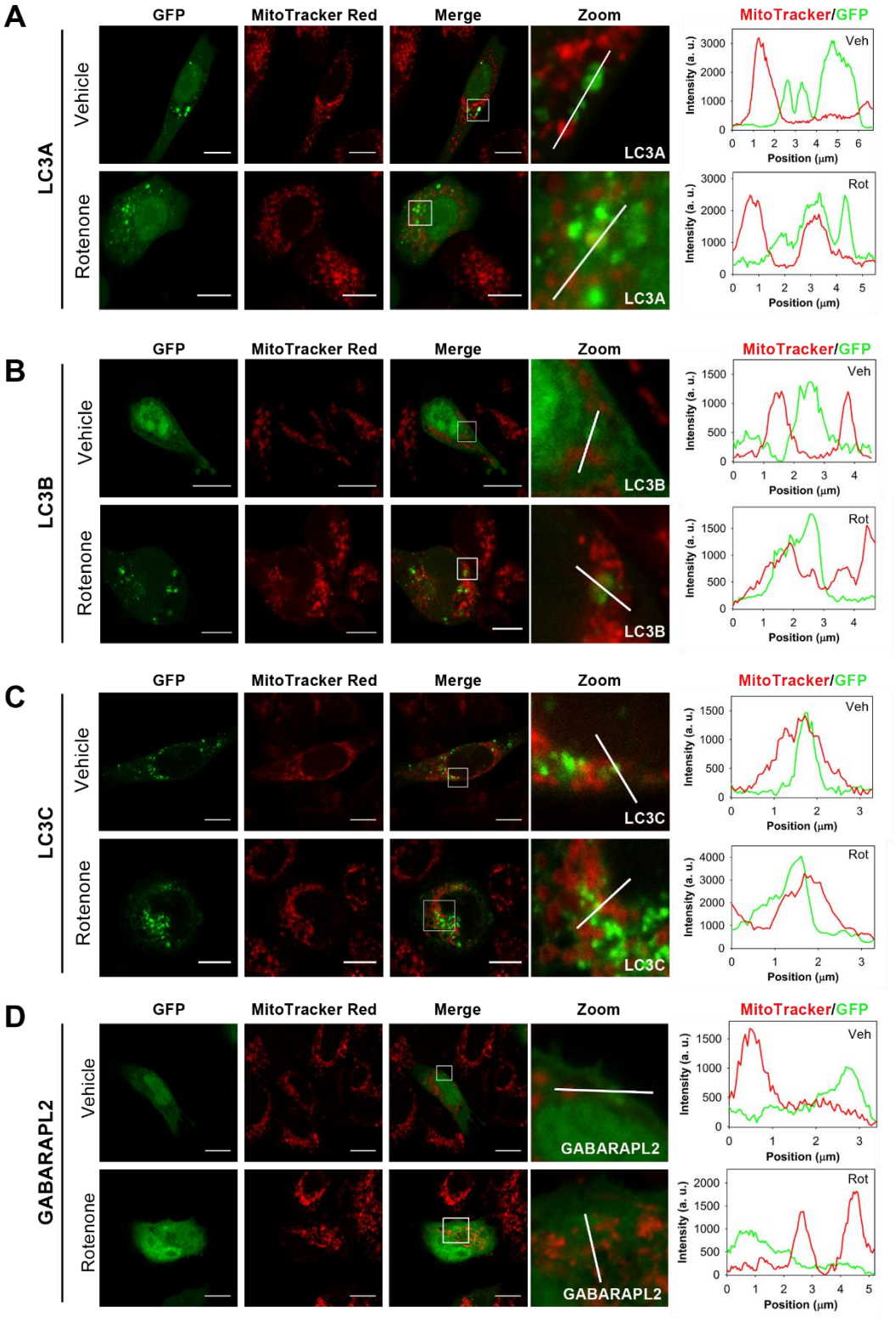

Figure 3.14. LC3A and LC3B puncta and their colocalization with mitochondria increase with rotenone treatment. SH-SY5Y cells were transfected with different members of the LC3/GABARAP family tagged with GFP. Mitochondria were labeled using MitoTracker Red, prior to treatment with 1 μM rotenone for 6 h. Vehicle (Veh) controls were treated with DMSO. Images were retrieved using a Nikon Eclipse C1 confocal microscope. Scale bar: 10 μm. At the right-hand side of each condition, MitoTracker (red) and GFP (green) line-profiles show examples of colocalization and non-colocalization events. Representative images of GFP-LC3A **(A)**, GFP-LC3B **(B)**, GFP-LC3C **(C)** or GFP-GABARAPL2 **(D)** SH-SY5Y transfected cells untreated (vehicle) or treated with rotenone. See Figure 3.15 for details and quantification.

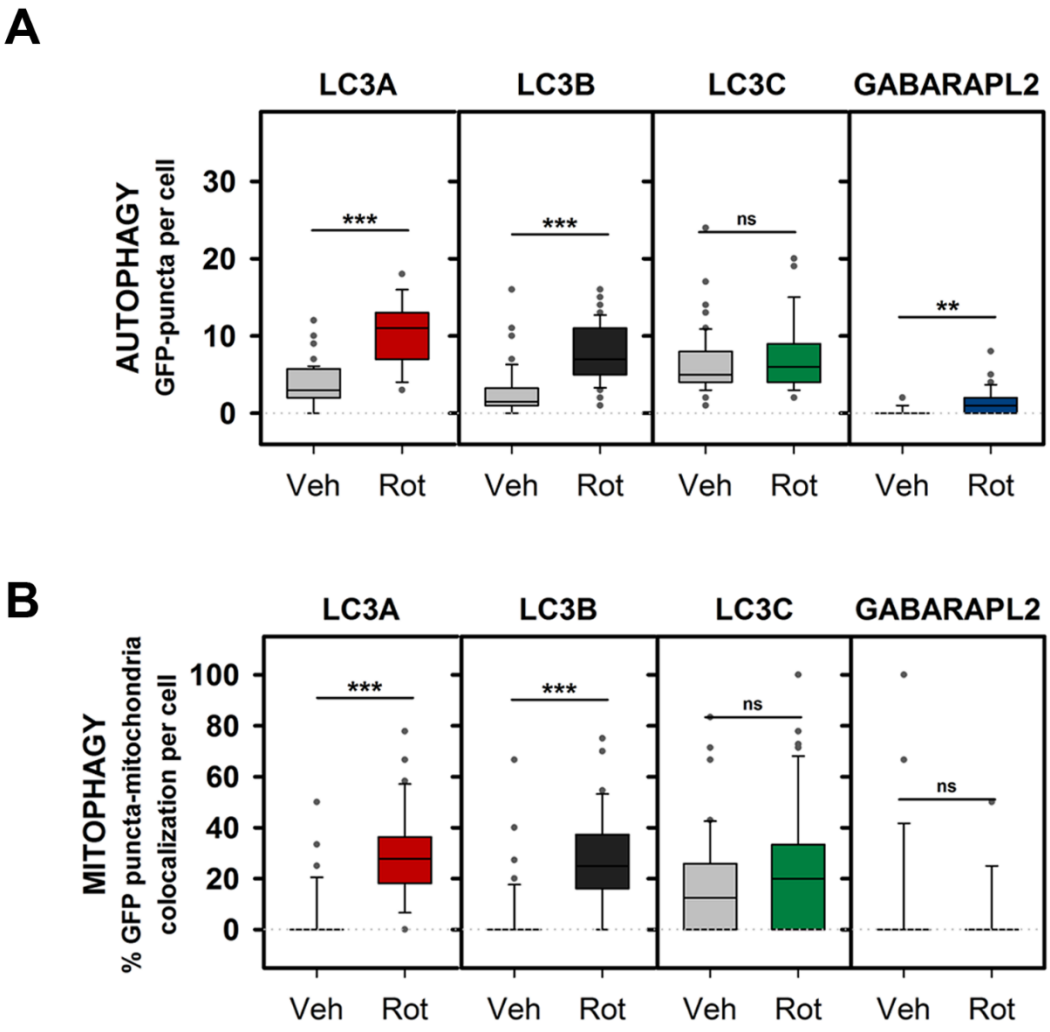

Figure 3.15. LC3A and LC3B puncta and their colocalization with mitochondria increase with rotenone treatment. (**A**) Number of GFP-LC3A, GFP-LC3B, GFP-LC3C and GFP-GABARAPL2 puncta per cell, an indication of autophagy, in SH-SY5Y cells untreated (Veh) and treated with rotenone (Rot). (**B**) Percent GFP-LC3A, GFP-LC3B, GFP-LC3C and GFP-GABARAPL2 puncta that colocalize with mitochondria, a signal of mitophagy, in SH-SY5Y cells untreated (Veh) or treated with rotenone (Rot). To compute the percent colocalization, images were analyzed with JACop plugging of ImageJ. At least 30 images were analyzed per condition. ***p < 0.001, **p < 0.01, ns: non-significant.

In order to confirm the participation of LC3A in CL-mediated mitophagy we treated our cells with a different CL-externalization inductor (Kagan *et al.*, 2016), carbonyl cyanide m-chlorophenyl hydrazone (CCCP). We decided to assess the localization of LC3A after a 1 h treatment in order to study the early stages of the process. We observed an increase in the number of puncta and their colocalization with mitochondria after CCCP treatment (**Figure 3.16A,B**). These results support the conclusion that LC3A, the homolog recognizing CL *in vitro* with a higher specificity and efficiency, can also detect damaged mitochondria during rotenone- or CCCP-induced mitophagy.

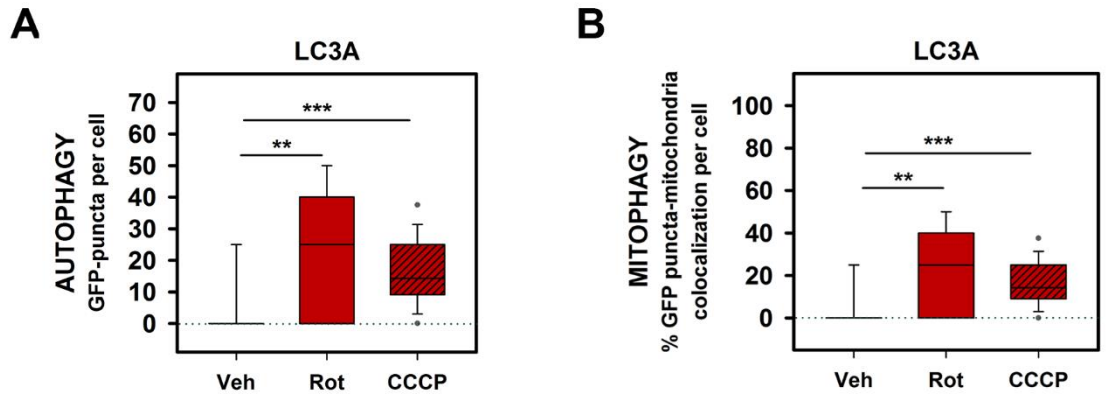

Figure 3.16. LC3A puncta and their colocalization with mitochondria increase with rotenone and CCCP treatment. Cells were co-transfected with DsRed2-Mito7 (DsRed) and with GFP-tagged WT or mutant LC3A. Vehicle (Veh) controls were treated with DMSO. (**A**) Number of GFP puncta per cell, an indication of autophagy, in SH-SY5Y cells treated with 1 μM rotenone for 6 h or with 20 μM CCCP for 1 h. (**B**) Percent GFP puncta that colocalize with mitochondria (DsRed), a signal of mitophagy, in SH-SY5Y cells untreated (Veh), treated with 1 μM rotenone for 6 h (Rot), or with 20 μM CCCP for 1 h (CCCP). Representative images can be found in Figure 3.18B and C.

3.3.8. The double mutation that hampers LC3A binding to CL *in vitro* also decreases its location to mitochondria in rotenone- and CCCP-induced mitophagy.

To determine whether the residues identified as key for the differential *in vitro* interaction of LC3A and LC3B with CL were also important in cells, the ability of the double mutants to recognize damaged mitochondria was tested. SH-SY5Y cells were transfected with the GFP-tagged LC3 WT or mutant proteins and treated with different mitophagy inductors. LC3B-AK, which exerted a significant positive action *in vitro,* did not have a parallel effect in rotenone-treated cells (**Figure 3.17**), suggesting a peculiar mode of LC3B-CL interaction that would not involve residues 14 and 18 of the protein.

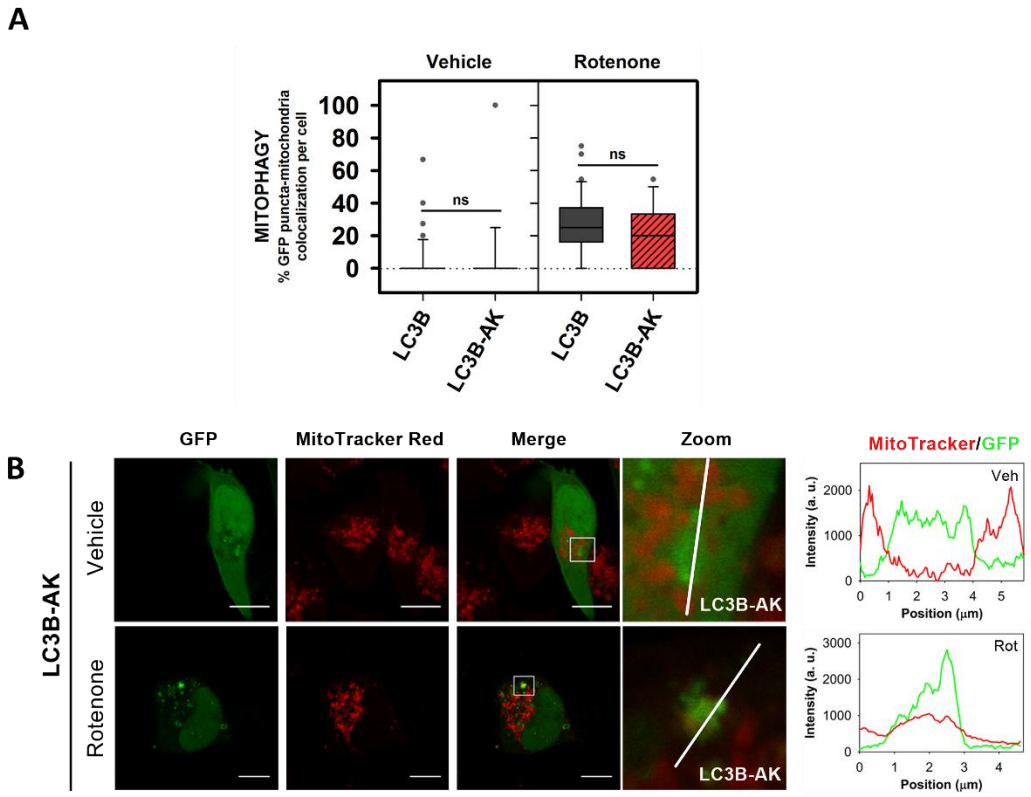

Figure 3.17. The LC3B-AK double mutation that increases LC3B binding to CL *in vitro* does not have a comparable effect in cells. Cells were transfected with GFP-tagged WT or mutant LC3 protein. Mitochondria were labeled using MitoTracker Red, prior to the treatments. Vehicle (Veh) controls were treated with DMSO. (**A**) Percentage of GFP-LC3B or GFP-LC3B-AK puncta that colocalize with mitochondria, a signal of mitophagy, in SH-SY5Y cells untreated (vehicle) or treated with 1 μM rotenone for 6 h. (**B)** Representative images of GFP-LC3B and GFP-LC3B-AK SH-SY5Y transfected cells untreated (vehicle, Veh) or treated with rotenone (Rot). Scale bar: 10 μm. At the right-hand side of each condition, MitoTracker (red) and GFP (green) line profiles show examples of colocalization and non-colocalization events. To compute the percentage of colocalization, images were analyzed with JACop plugging of ImageJ. At least 30 images were analyzed per condition. ***P < 0.001, ns: non-significant.

However, results obtained in cells after substitution of those two amino acids in LC3A pointed to an important role of those residues. The LC3A-EE mutant, which exhibited a much lower binding to CL-containing vesicles than its native counterpart (**Figure 3.11D**), also showed lower colocalization levels with mitochondria in cells treated with rotenone or CCCP, as compared to those transfected with GFP-LC3A (**Figure 3.18**).

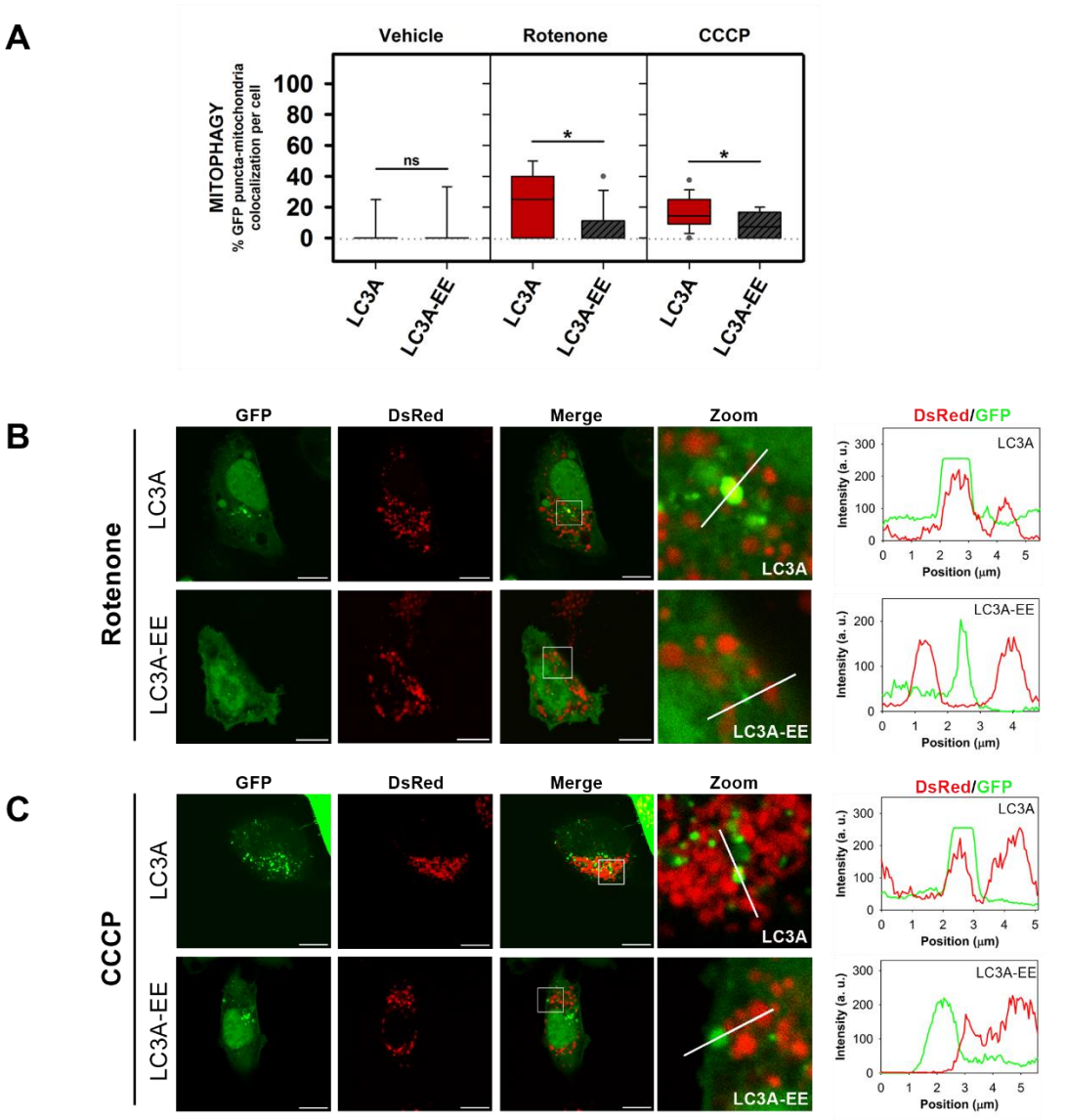

Figure 3.18. The LC3A-EE double mutation that hampers LC3A binding to CL *in vitro* also decreases its location to mitochondria in rotenone- and CCCP-induced mitophagy. SH-SY5Y cells were co-transfected with DsRed2-Mito7 (DsRed) and GFP-tagged WT or mutant LC3A. Vehicle (Veh) controls were treated with DMSO. (**A**) Percent GFP-LC3A or GFP-LC3A-EE puncta that colocalize with mitochondria, a signal of mitophagy, in SH-SY5Y cells untreated (vehicle), or treated with rotenone (1 μM, 6 h) , or CCCP (20 μM, 1 h) or O/A (10/4 μM, 6 h). To compute the percent colocalization, images were analyzed with the JACop plugging of ImageJ. At least 30 images were analyzed per condition. *P < 0.05, ns: non-significant. (**B**) Representative images of GFP-LC3A and GFP-LC3A-EE SH-SY5Y transfected cells treated with 1 μM rotenone for 6 h. (**C**) Representative images of GFP-LC3A and GFP-LC3A-EE SH-SY5Y transfected cells treated with 20 μM CCCP for 1 h. Images were acquired using a Nikon Eclipse C1 confocal microscope. Scale bar: 10 μm. At the right-hand side of each condition, DsRed (red) and GFP (green) line profiles show examples of co-localization and non-colocalization events.

Moreover, in support of the LC3A N-terminal region implication, we used the LC3A^{R10,11A} mutant in which the two Arg, shown by Chu *et al*. to be important for CL recognition in LC3B, were mutated to Ala. The double mutation caused a lower binding to CL-containing vesicles (**Figure 3.19A**) and lower colocalization levels with mitochondria after rotenone treatment (**Figure 3.19B, C**), as compared with the native protein. These results indicate that mutations that reduce the binding of LC3A to CL *in vitro*, also

decrease the ability of LC3A to recognize damaged mitochondria in cells, decreasing or delaying the involvement of this homolog in the mitophagic process.

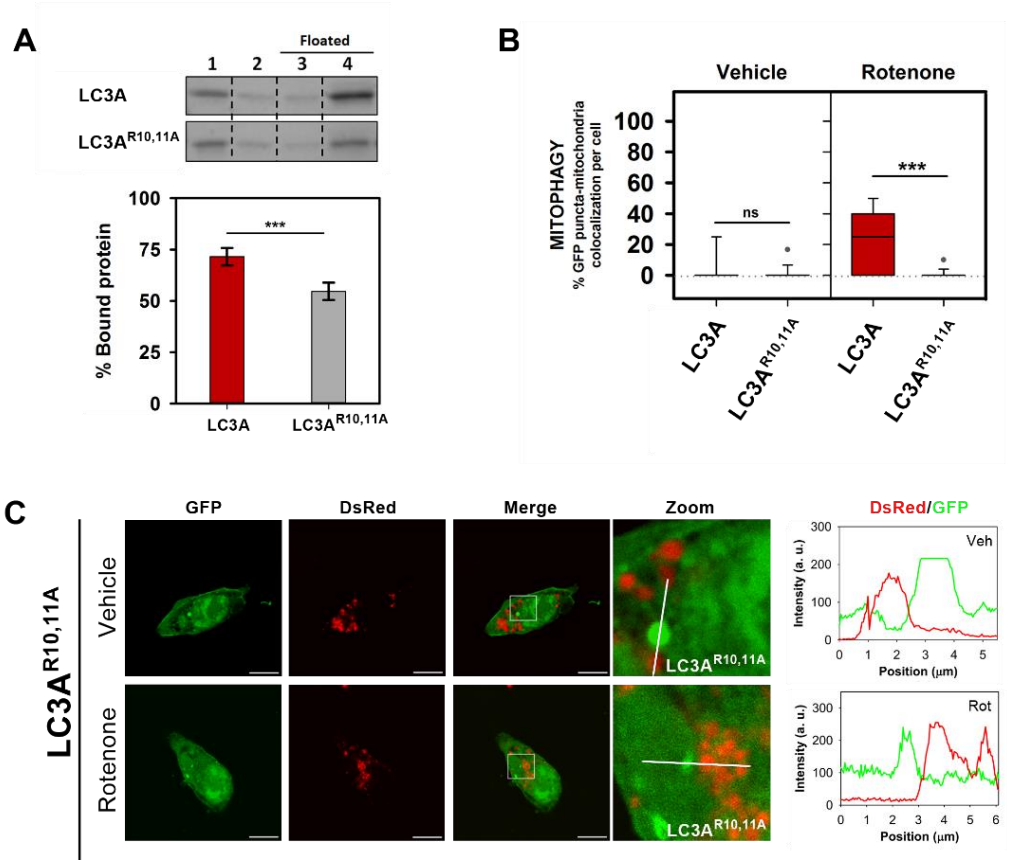

Figure 3.19. The LC3A N-terminal mutation R10,11A decreases its binding to CL-containing vesicles and its location to mitochondria in rotenone-induced mitophagy. (**A)** Top: Representative SDS-PAGE Coomassie Brilliant Blue-stained gels of the fractions obtained from LC3A or LC3A^{R10,11A} vesicle flotation assays performed with liposomes composed of ePC:DOPE:CL (33:33:33 mol ratio). Bound protein is computed as the proportion retrieved in fractions 3+4 (See Figure 2.8). Bottom: Binding of LC3A or LC3A^{R10,11A} to CL-containing liposomes, quantified by gel densitometry. Data shown are means ± SD (n ≥ 3). ***p < 0.001. (**B**) Percentage of GFP-LC3A or GFP-LC3A^{R10,11A} puncta that colocalize with mitochondria, a signal of mitophagy, in SH-SY5Y cells untreated (vehicle), treated with 1 μM rotenone for 6 h. (**C**) Representative images of GFP-LC3A^{R10,11A}-transfected SH-SY5Y cells, untreated (vehicle, Veh), or treated with 1 μM rotenone for 6 h. Images were acquired using a Nikon Eclipse C1 confocal microscope. Scale bar: 10 μm. At the right-hand side of each condition, DsRed (red) and GFP (green) line profiles show examples of colocalization and non-colocalization events. To compute the percentage of colocalization, images were analyzed with JACop plugging of ImageJ. At least 30 images were analyzed per condition. ***p < 0.001, **p < 0.01, ns: non-significant.

The above results were complemented with the use of an additional mitophagy inducer, namely oligomycin A + antimycin A (O/A), shown by Lazarou and co-workers 2015) to induce colocalization of all LC3/GABARAP-family members with mitochondria. As expected, after O/A treatment LC3A gave rise to an increased number of puncta and was found to colocalize with mitochondria (**Figure 3.20**). However, at variance with rotenone or CCCP treatments, neither LC3A-EE nor LC3A^{R10,11A} mutants (**Figure 3.20**) caused a decreased colocalization with mitochondria. These results suggest that in O/A-induced mitophagy, the N terminus is not as important as in rotenone or CCCP treatments.

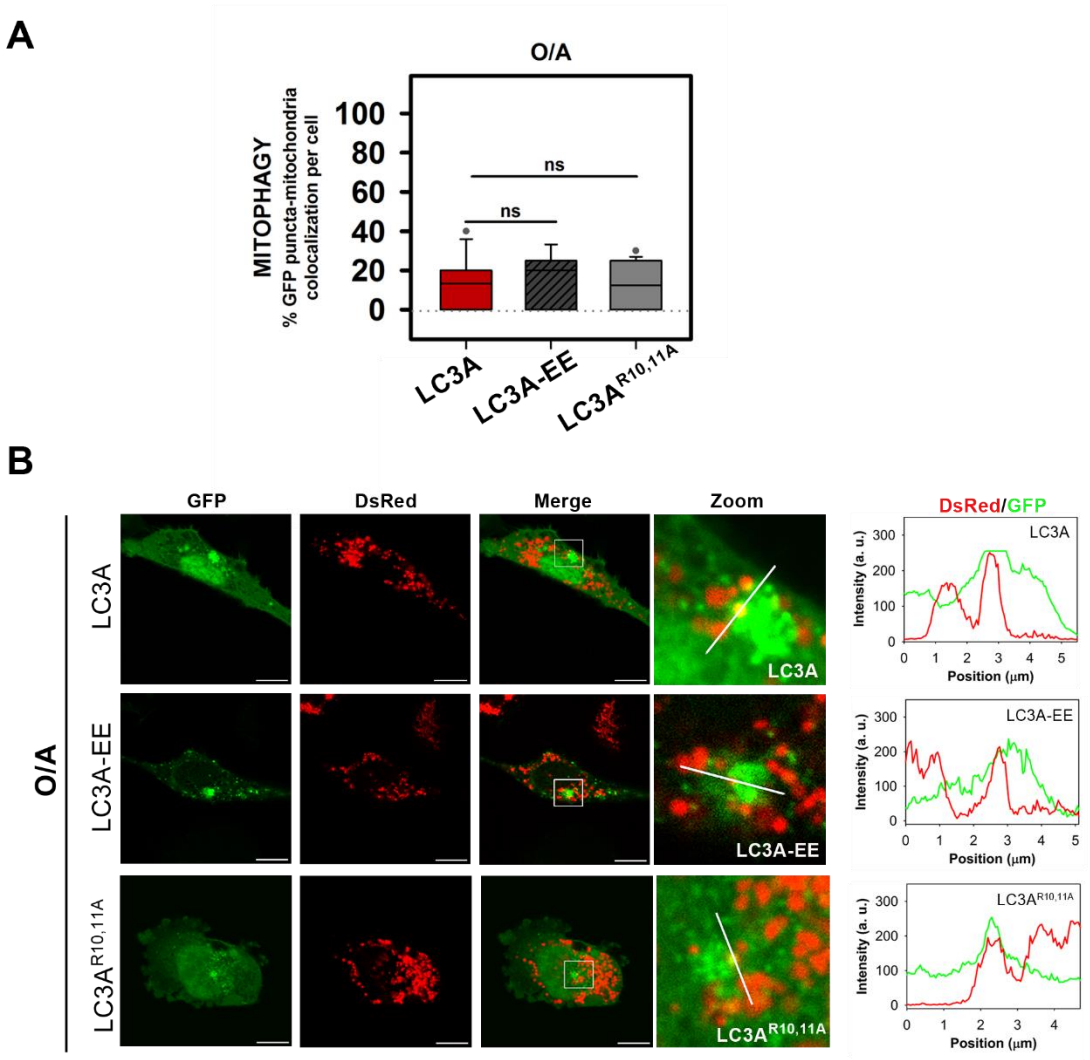

Figure 3.20. Neither the LC3A-EE double mutation nor the LC3A N-terminal mutation R10,11A decrease LC3A location to mitochondria in O/A-induced mitophagy. (**A**) Percentage of GFP-LC3A, GFP-LC3A-EE or GFP-LC3A^{R10,11A} puncta that colocalize with mitochondria, a signal of mitophagy, in SH-SY5Y cells treated with O/A (10/4 μM for 6 h) (**B**) Representative images of GFP-LC3A, GFP-LC3A-EE or GFP-LC3A^{R10,11A}-transfected SH-SY5Y cells, treated with O/A (10/4 μM for 6 h). Images were acquired using a Nikon Eclipse C1 confocal microscope. Scale bar: 10 μm. At the right-hand side of each condition, DsRed (red) and GFP (green) line profiles show examples of colocalization and non-colocalization events. To compute the percentage of colocalization, images were analyzed with JACop plugging of ImageJ. At least 30 images were analyzed per condition. ***p < 0.001, **p < 0.01, ns: non-significant.

3.3.9. Endogenous LC3A and LC3B are involved in CCCP-induced mitophagy.

Several studies have been carried out comparing the role(s) of LC3 proteins in mitophagy (Bhujabal *et al.*, 2017; Lazarou *et al.*, 2015; Le Guerroué *et al.*, 2017; Onishi *et al.*, 2021), but most of them use transfected proteins, which might have an expression level that is not comparable to the endogenous protein levels, overestimating their implication in this process. To determine if SH-SY5Y cells were suitable for the study of endogenous LC3A effects, the protein expression levels of LC3-subfamily members were quantified (**Figure 3.21**). Substantial levels of LC3A protein were detected, indicating that these cells were

an adequate cellular model for the present study. Therefore, in order to confirm the results obtained with the overexpressed protein a direct evaluation of endogenous LC3A activation upon CCCP treatment was performed.

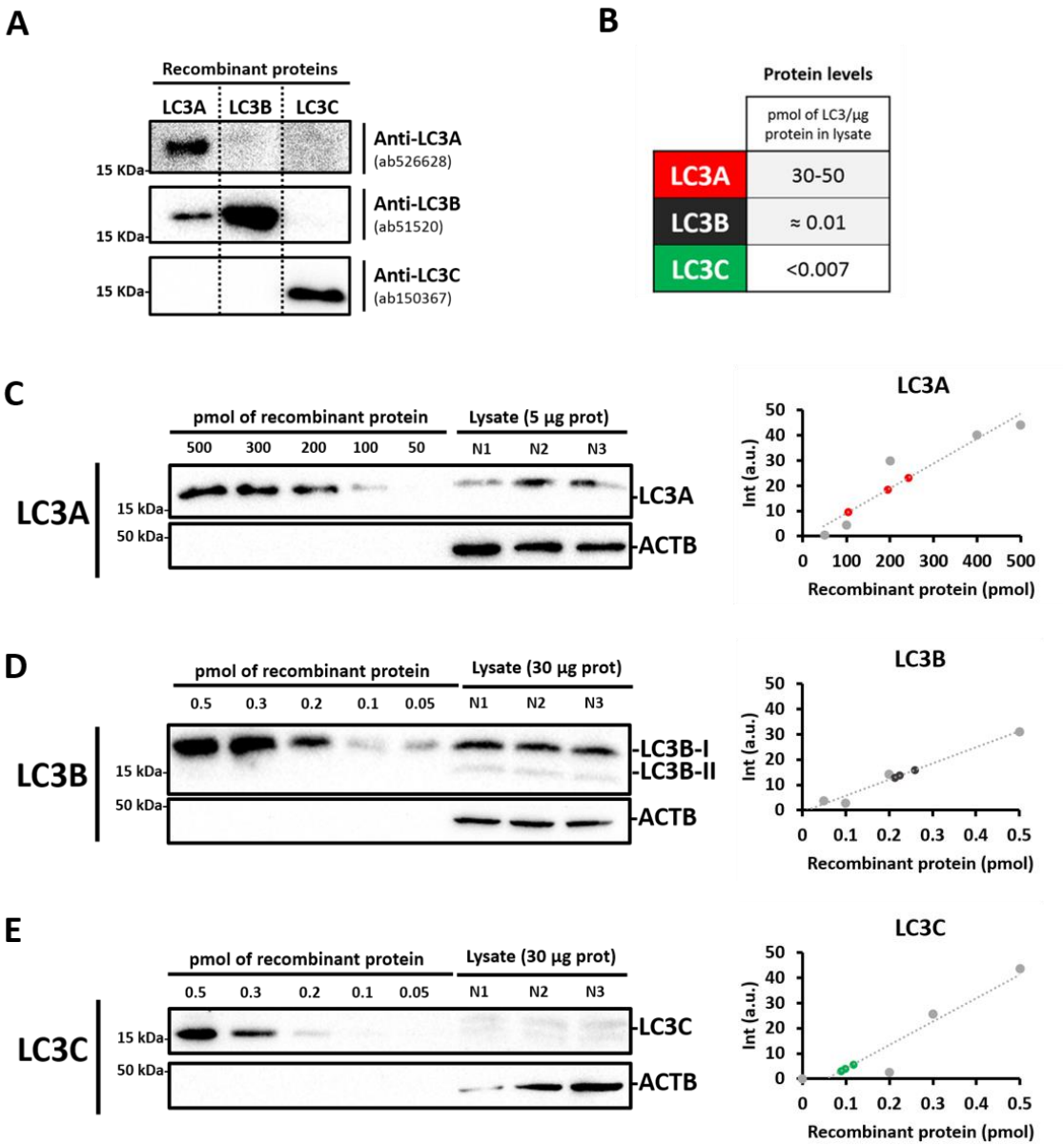

Figure 3.21. Protein expression of LC3A, LC3B and LC3C in SH-SY5Y cells. (**A**) The homolog-specificity of the antibodies used for this work was tested using the same amount (5 pmol) of each LC3 recombinant protein in a western blot. (**B**) LC3A, LC3B and LC3C protein concentration found in SH-SY5Y. A gradient of the recombinant proteins was used as a standard in order to obtain an estimated concentration in the cell lysates. (**C**) Left: representative western blot of SH-SY5Y cell lysate to measure LC3A levels. Right: Estimation of the LC3A protein levels using a calibration curve obtained with recombinant LC3A. (**D**) Left: representative western blot of SH-SY5Y cell lysate to measure LC3B levels. Right: Estimation of the LC3B protein levels using a calibration curve obtained with recombinant LC3B. (**E**) Left: representative western blot of SH-SY5Y cell lysate to measure LC3C levels. Right: Estimation of the LC3C protein levels using a calibration curve obtained with recombinant LC3C.

CCCP (20 µM) treatment for 4 h or 6 h caused a decrease in the inner mitochondrial membrane marker COX4I in SH-SY5Y cells (**Figure 3.22A**) indicating completion of the mitophagy flux. Moreover, an increase in LC3A-II and LC3B-II was already observed within the first hour of treatment (**Figure 3.22B**). This activation also occurred at lower CCCP concentrations, such as 5 µM or 10 µM (**Figure 3.22C**). Consistent with these results, mitochondrial fractionation experiments clearly show that in cells treated with CCCP, LC3A and LC3B were found to a larger extent in the mitochondrial fraction than in the cytosol (**Figure 3.22D**).

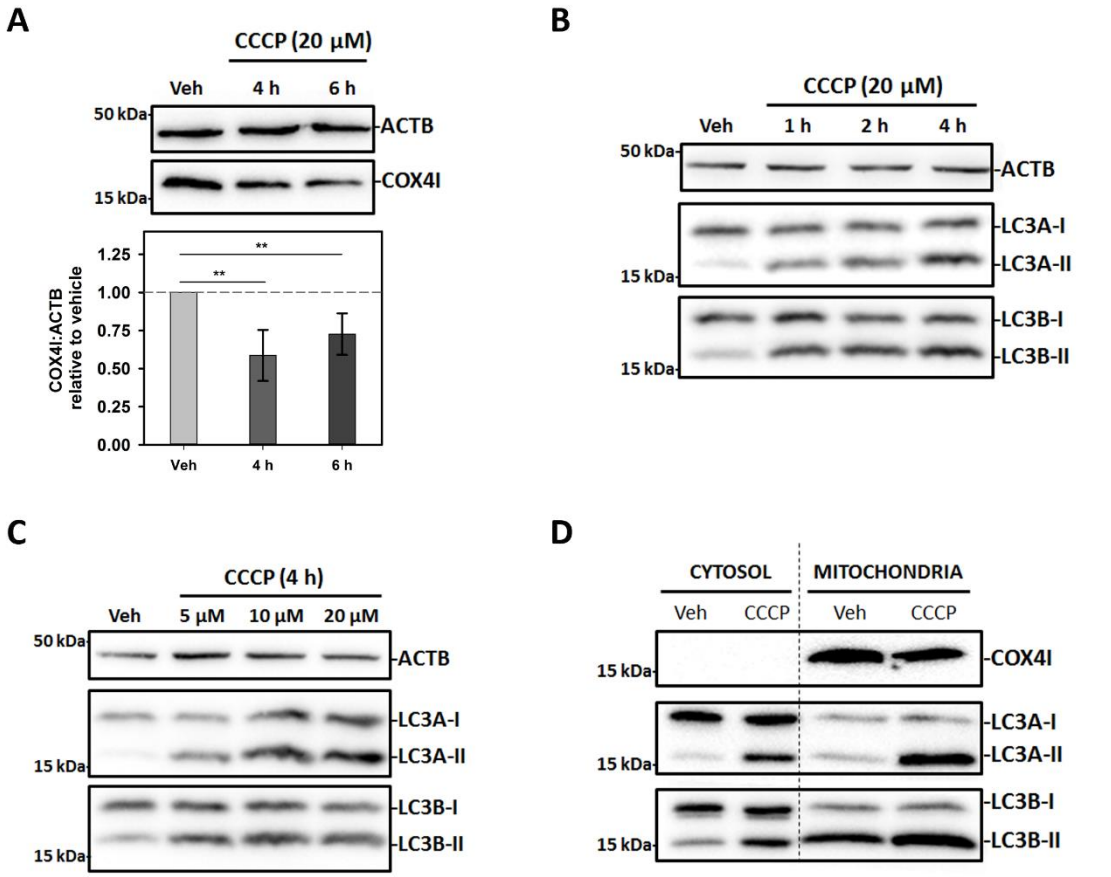

Figure 3.22. Endogenous LC3A and LC3B are involved in CCCP-induced mitophagy in SH-SY5Y cells. SH-SY5Y cells were used to study the activation of endogenous LC3A and LC3B by western blot after CCCP treatment. Vehicle (Veh) controls were treated with DMSO. (**A**) Top: Representative western blot of the degradation of the mitochondrial IMM marker COX4I in cells treated with 20 µM CCCP for 4 h or 6 h. Bottom: COX4I:ACTB ratio in treated cells relative to vehicle quantified by gel densitometry. Data shown are means ± SD **P < 0.01. (**B**) Activation of LC3A and LC3B, shown as an increase of the LC3A-II or LC3B-II corresponding band intensity, in cells treated with 20 µM CCCP for different times (1, 2 and 4 h). (**C**) Activation of LC3A and LC3B, shown as an increase of the LC3A-II or LC3B-II corresponding band intensity, in cells treated for 4 h with different concentrations of CCCP (5, 10 or 20 µM). (**D**) Detection of LC3A and LC3B in the mitochondrial fraction in cells treated with 20 µM CCCP for 4 h, COX4I is used as a marker of efficient mitochondrial fractionation. Data shown are means ± SD *p < 0.05; ns: non-significant.

In order to address the importance of the involvement of these proteins in this type of mitophagy each homolog was independently knocked down. For this purpose, specific siRNAs for each homolog were used (Liu *et al.*, 2017; von Muhlinen *et al*., 2012). Knocking down LC3A or LC3B had no effect on mitochondrial marker reduction, but the double silencing of both homologs was able to reduce mitophagy flux (**Figure 3.23**). These data support the results obtained by confocal microscopy with GFP-tagged proteins, demonstrating the involvement of LC3A and LC3B in cardiolipin-mediated mitophagy induced by CCCP.

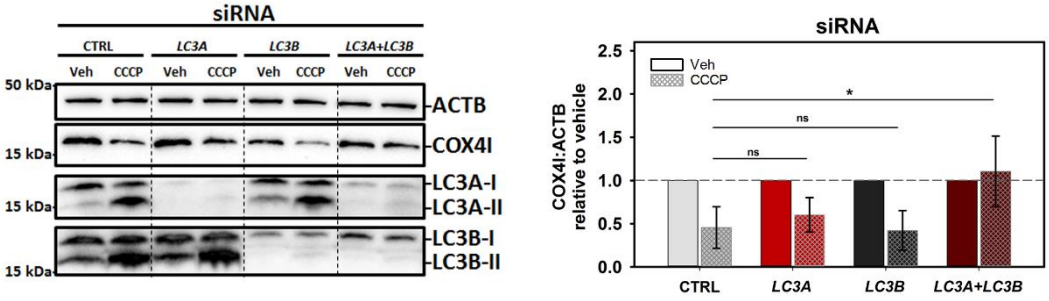

Figure 3.23. Silencing of endogenous LC3A and LC3B in SH-SY5Y cells reduce mitophagy flux. Left: Representative western blot of the degradation of COX4I and the activation of LC3A and LC3B in cells treated with 10 μM CCCP for 4 h in which LC3A and/or LC3B had been silenced compared to control siRNA-transfected cells. Right: Comparison of COX4I:ACTB ratio relative to vehicle in siRNA-transfected cells treated with CCCP, quantified by gel densitometry. Data shown are means ± SD *p < 0.05; ns: non-significant.

3.3.10. LC3A but not LC3B is able to bind oxidized CL.

It has been proposed that, when CL participates in apoptosis, it is previously oxidized due to the peroxidase activity of cytochrome C (Kagan *et al.*, 2005), while the CL fraction that is recognized by the autophagy machinery is not (Chu *et al*., 2013). Taking into account that the interplay between autophagy and apoptosis implies a high level of complexity (Kang *et al.*, 2011), understanding how the role of CL is affected by its oxidation state could help in understanding how these two important processes are regulated.

In order to assess the ability of LC3A and LC3B to recognize oxidized CL, LUV were treated with $CuCl_2$ for 5 h, and the increase in absorbance at 245nm (A_{245}) was measured to quantify lipid oxidation (**Figure 3.24A**). The highly unsaturated CL is the main lipid oxidized under those conditions. Then, protein bound to either control or oxidized vesicles was measured. The results obtained with LC3B and LC3A in these experiments showed that binding of LC3B (**Figure 3.24C**), but not of LC3A (**Figure 3.24B**), decreased with CL oxidation.

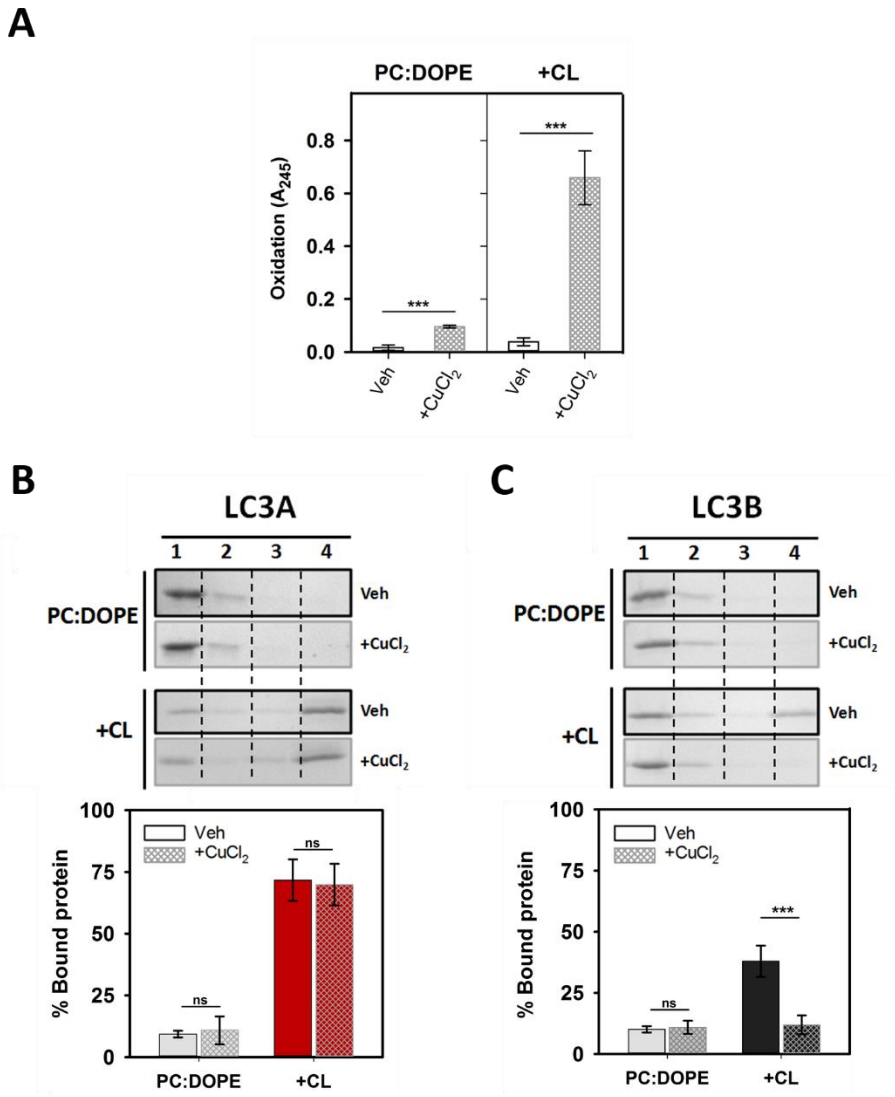

Figure 3.24. LC3A, but not LC3B, binds oxidized CL. Interaction of LC3A or LC3B proteins with oxidized membranes measured by a vesicle flotation assay. (**A**) Lipid oxidation was assessed measuring absorbance at 245 nm (A_{245}) of the ePC:DOPE (50:50) or ePC:DOPE:CL (33:33:33) liposomes (+CL), treated without (Veh) or with $CuCl_2$ (+$CuCl_2$). Data shown as means ± SD (n ≥ 3). ***p < 0.001. (**B and C**) Top: Representative SDS-PAGE/Coomassie Brilliant Blue-stained gels of the fractions obtained from LC3A (B) or LC3B (C) vesicle flotation assays performed with liposomes composed of ePC:DOPE (50:50) or ePC:DOPE:CL (33:33:33) which had been previously treated without (Veh) or with $CuCl_2$. Bound protein is computed as the proportion retrieved in fractions 3+4 (See Figure 2.8). Bottom: Binding of LC3A (B) or LC3B (C) to non-oxidized and oxidized liposomes, quantified by gel densitometry. Data shown are means ± SD (n ≥ 3). ***p < 0.001; ns: non-significant.

At variance with the results observed with wild-type LC3A, the ability of LC3A mutants to bind CL decreased with lipid oxidation (**Figure 3.25A**), showing the importance of residues 14 and 18 for the recognition of oxidized CL. Moreover, LC3B double mutant enhanced the originally low capacity of wild-type LC3B to recognize oxidized CL (**Figure 3.25B**). Therefore, residues 14 and 18, identified as key for the differential interaction of CL with LC3A and LC3B, were shown to be also important for the LC3A-mediated recognition of oxidized CL. These results suggested that LC3A could bind oxidized CL in the OMM, perhaps preventing its recognition by the apoptotic machinery.

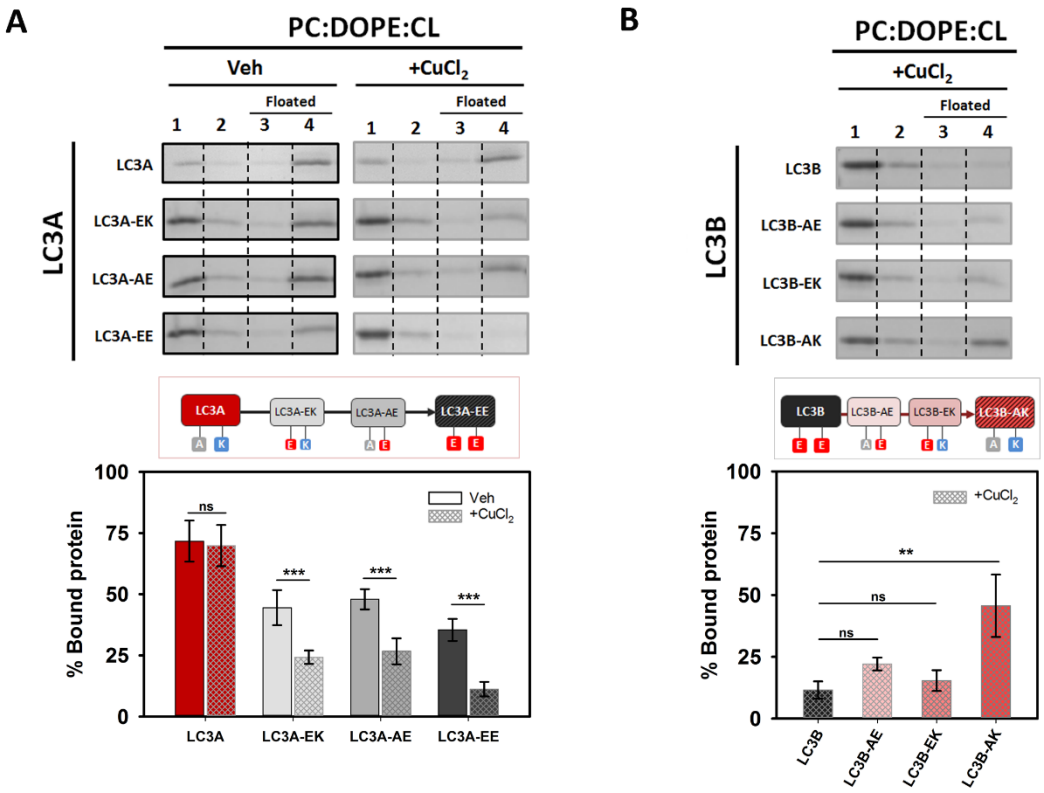

Figure 3.25. LC3A-mutant binding to oxidized CL decreased with the degree of oxidation. (**A**) Top: Representative SDS-PAGE/Coomassie Brilliant Blue-stained gels of the fractions obtained from LC3A, LC3A-EK (LC3A^{A14E}), LC3A-AE (LC3A^{K18E})and LC3A-EE (LC3A^{A14E,K18E}) vesicle flotation assays performed with liposomes composed of ePC:DOPE:CL (33:33:33) that had been previously treated without (Veh) or with $CuCl_2$. Bottom: Binding of LC3A and LC3A mutants to non-oxidized and oxidized liposomes, quantified by gel densitometry. Data shown are means ± SD (n ≥ 3). ***p < 0.001; ns: non-significant. (**B**) Top: Representative SDS-PAGE/Coomassie Brilliant Blue-stained gels of the fractions obtained from LC3B, LC3B-AE (LC3B^{E14A}), LC3B-EK (LC3B^{E18K})and LC3B-AK (LC3B^{E14A,E18K}) vesicle flotation assays performed with liposomes composed of ePC:DOPE:CL (33:33:33) which had been previously treated with $CuCl_2$. Bottom: Binding of LC3B and LC3B mutants to oxidized liposomes, quantified by gel densitometry. Data shown are means ± SD (n ≥ 3). **p < 0.01; ns: non-significant.

3.4. Discussion

Deciphering the different modes of damaged mitochondria signaling, and the role that each of the LC3/GABARAP-family member plays in their recognition is extremely important for understanding mitophagy. Many types of receptors participate in this process, and different studies reinforce the idea that the LC3/GABARAP-family members could play specific roles depending on the particular mechanism involved (Johansen & Lamark, 2020). There are examples of proteins that act as mitophagy receptors by interacting preferentially with one or several of the LC3/GABARAP-family members, for example, BNIP3L recruits GABARAP (Schwarten *et al.*, 2009) and GABARAPL1 (Novak *et al.*, 2010), while FUNDC1, BNIP3 and BCL2L13 are found bound to LC3B (Hanna *et al.*, 2012; L. Liu *et al.*, 2012; Murakawa *et al.*, 2015), and FKBP8 is recognized by LC3A (Bhujabal *et al.*, 2017). In the case of the phospholipid CL acting as a mitophagy receptor, LC3B was shown to be a mediator (Chu *et al*., 2013), and our previous work comparing both Atg8 subfamilies suggested that neither GABARAP nor GABARAPL2 were involved (Antón *et al.*, 2016). However, a comparative study of the different LC3-subfamily member function(s) does not appear to be available.

The specific interaction of LC3A with CL allows its participation in the mechanism of CL-mediated mitophagy.

The interaction of LC3A with membranes was specific for the presence of CL (**Figure 3.7**). LC3A did not show any measurable interaction with other lipids containing the same negative charge of CL, such as PtdIns4P (**Figure 3.6, 3.7**), therefore, this interaction did not seem to be exclusively dependent on the lipid charge. The amino acid sequence of LC3A and LC3B is very similar, and even some residues, demonstrated to be key for the interaction with CL, R10 and R11 (Chu *et al*., 2013), located in the alpha-helix 1, are identical in both proteins (**Figure 3.3B, 3.11A,B**). However, in the above studies with model membranes a clear difference in CL binding was observed between LC3A and LC3B, the former being more active (**Figure 3.4**). Experiments involving the LC3A/B chimera (**Figure 3.9**) and high-salt concentrations (**Figure 3.10**), suggested that the higher binding detected with LC3A could be in part due to the existence of positively charged residues in its N-terminal region, that are not present in LC3B. Comparative binding assays using LC3A and LC3B single and double mutants showed that the key amino acids were located in positions 14 and 18 of helix 2 (**Figure 3.11**). Therefore, the CL binding site of LC3A appears to be composed of two alpha-helices containing positively charged residues, in agreement with previously described binding sites for other soluble proteins that can also bind CL in membranes (Planas-Iglesias *et al.*, 2015). However, the fact that LC3A/B chimera did not reach the same binding levels as LC3A (**Figure 3.10**) suggests the implication of other protein regions apart from the N terminus, as previously proposed for LC3B, in the interaction of LC3A with CL.

To further dissect the differences among these subfamily members, the participation of each LC3-subfamily member in CL-mediated mitophagy was studied by assessing the colocalization of transfected GFP-tagged proteins with mitochondria in SH-SY5Y cells. Even if the effect of the GFP tag in the LC3/GABARAP-protein function has been criticized (Nguyen *et al.*, 2016b), we decided to use this method due to the similar results obtained using anti-LC3 antibodies (Antón *et al.*, 2016; Ryan *et al.*, 2018) and GFP-

tagged LC3B (Chu *et al*., 2013) to study CL-mediated mitophagy in cells. This supports the notion that the GFP-tag does not disturb the recognition of externalized CL in damaged mitochondria. In addition, the results obtained with the non-conjugatable mutants of each homolog (**Figure 3.13**), in which the number of puncta was residual, supported the idea that the GFP puncta were, in fact, autophagic vesicles, and not aggregates. The above observations indicate that the results obtained are reliable.

The experiments performed with cells showed that, apart from LC3B, LC3A was also able to participate in rotenone- or CCCP-induced mitophagy (**Figure 3.14A, 3.15, 3.16**), implying that LC3A could recognize externalized CL in damaged mitochondria in cells. The participation of LC3A in mitophagy has been described previously, LC3A being able to specifically recognize the mitophagy receptor FKBP8 located in the OMM of damaged mitochondria (Bhujabal *et al.*, 2017). LC3A recognition of CL and of FKBP8 are not by necessity mutually excluding events, in fact these two mechanisms might act together in cooperation. It is *e.g.* possible that CL externalization brings LC3A closer to mitochondria to facilitate binding to FKBP8.

Ala 14 and Lys 18 residues, identified *in vitro* as important for LC3A-CL interaction (**Figure 3.11D**), were also shown to be key for CL recognition during rotenone- and CCCP-induced mitophagy in cells, as demonstrated by the behavior of LC3A-EE mutant (**Figure 3.18**). Similar results obtained with the $LC3A^{R10,11A}$ mutant support the notion that the two N-terminal alpha helices of LC3A are also important in CL recognition in cells (**Figure 3.19**). Furthermore, the fact that LC3A mutants are able to participate in O/A-induced mitophagy to the same extent as LC3A WT (**Figure 3.20**) indicates that those mutants are functional, although the importance of CL-recognition is decreased in the case of the O/A treatment. This could be explained taking into account that O/A can activate numerous mitophagy pathways and receptors (Lazarou *et al.*, 2015). It could be possible that, at variance with rotenone and CCCP, in O/A treatment the LDS (LIR docking site) of LC3A becomes more relevant, while the importance of the N terminus residues is diminished.

The differences found *in vitro* between LC3A and LC3B binding to CL-containing vesicles (**Figure 3.4**) were not observed when colocalization with mitochondria was considered (**Figure 3.15**). Moreover, while the exchange of residues 14 and 18 of LC3B for the corresponding ones of LC3A in the LC3B-AK mutant increased significantly its interaction with CL-containing membranes (**Figure 3.11D**), this change did not affect its function in mitophagy: the double mutant did not show a higher level of colocalization with mitochondria when compared to native LC3B (**Figure 3.17**). These results could suggest that the mitophagy level observed with LC3B represents a colocalization threshold for the mitophagy treatment. If that were the case, even if mitochondrial recognition by LC3A or LC3B-AK were better, they would not lead to an observable higher colocalization. This could also indicate that, at variance with the equivalent residues in LC3A, the negatively charged residues present in the LC3B N-terminal region (E14, E18) do not play a role in the interaction with externalized CL in cells (**Figure 3.11B** and **Figure 3.17**). In turn, this would imply that the molecular mechanisms through which LC3A and LC3B interact with CL in the cell might be different, or else that their interaction might be regulated differently.

Analysis of protein levels in SH-SY5Y cells revealed marked differences in the amounts of each form of LC3 (**Figure 3.21B**).Explaining these observations is beyond the scope

of the present work, nevertheless they may be worth mentioning. The possibility that modified forms of LC3 proteins, by *e.g.* acetylation (Huang *et al*., 2015) or phosphorylation (Cherra *et al.*, 2010), could go undetected by the antibodies used in this study, leading to underestimation of the amounts of protein measured, cannot be discarded. The study of endogenous LC3 proteins in SH-SY5Y cells (**Figure 3.22**) supports the conclusions obtained with the transfected GFP-tagged LC3 proteins, demonstrating the participation of LC3A and LC3B in CCCP-induced mitophagy. The results obtained after silencing LC3A and LC3B show the important role of these proteins in CCCP-mediated mitophagy (**Figure 3.23**). Moreover, the need to silence both proteins to detect a reduction in mitophagy suggests some redundancy of function between the two homologs. Perhaps the main conclusion of these experiments is that although the LC3B homolog has been most extensively studied (and most frequently cited) in this context, LC3A does play a role in mitophagy and, in certain cell types such as neuroblastoma cell lines, it may be the most abundant form of LC3.

LC3C does not participate in cargo recognition during CL-mediated mitophagy.

The interaction of LC3C with membranes was not specific for the presence of CL, as this protein could also interact with PA (**Figure 3.7B**). Moreover, despite the higher interaction displayed with CL-containing model membranes when compared with LC3A or LC3B (**Figure 3.4**), LC3C did not appear to play a role in rotenone-mediated mitophagy. These results led to the conclusion that LC3C was less effective than LC3A or LC3B in recognizing damaged mitochondria (**Figure 3.14** and **Figure 3.15**). This LC3C behavior is not surprising, since it has been shown that LC3C has different functions and targets as compared to the other subfamily members (Schaaf *et al.*, 2016), such as its specific function in antibacterial autophagy (von Muhlinen *et al.*, 2012).

While LC3A and LC3B show a high similarity in their sequence (92%), LC3C is the most differentiated homolog (71-72% similarity). Unlike in other LC3/GABARAP-family members, the N-terminal region of LC3C does not form a stable α1-helix but a “sticky arm” (**Figure 3.3A**) consisting of a polyproline motif (Krichel *et al.*, 2019). It has also been shown that the interactome of LC3C differs clearly from that of other members of the LC3 subfamily (Behrends *et al.*, 2010). Another important singularity is that although LC3A and LC3B are ubiquitously expressed in almost all tissues (Bai *et al.*, 2012) LC3C expression is extremely low and/or tissue-specific (lungs and placenta). In the current study the amounts of cellular protein were not sufficient to be detected by the antibodies, thus studying endogenous LC3C in this cell type was not feasible (**Figure 3.21**). The results in this paper show CL-mediated mitophagy as yet another mechanism in which LC3C behaves differently from the other subfamily members.

The assays using SH-SY5Y cells showed that in the basal state GFP-LC3C was already forming puncta (**Figure 3.15A**) and some of these puncta colocalized with mitochondria (**Figure 3.15B**). Moreover, CL externalization by rotenone did not have any further effect on puncta formation/colocalization (**Figure 3.15B**). These unchanged levels of autophagy and mitophagy after rotenone treatment suggest that CL externalization had little or no effect on the participation of LC3C in autophagy or on its mitochondrial localization. These results are in accordance with a previous study that used Saos-2 cells and GFP-LC3C (Bai *et al.*, 2012). In the basal state, they also observed more

puncta per cell than with LC3A or LC3B, but these values did not increase after starvation-induced autophagy.

The observed GFP-LC3C colocalization with mitochondria could be explained by the recently discovered involvement of LC3C in the maintenance of basal mitochondrial network homeostasis (Le Guerroué *et al.*, 2017). In their study, F. Le Guerroue (Le Guerroué *et al.*, 2017) described an LC3C-driven mitophagy mechanism that mediates autophagosome degradation of mitochondrial parts in a piecemeal way. Moreover, the affinity that LC3C shows towards PA-containing membranes could also allow its interaction with healthy mitochondria, which contain PA in their OMM (Basu Ball *et al.*, 2018). In addition, previous results indicated that LC3C does not have a relevant function in PRKN-mediated mitophagy (Nguyen *et al.*, 2016b). Those studies, together with the results in this paper suggest that the main function of LC3C in mitophagy could be related to the maintenance of a healthy mitochondrial network, by regulating degradation of the damaged mitochondrial parts (Le Guerroué *et al.*, 2017).

LC3A could prevent excessive apoptosis activation.

It has been shown that CL could interact with various proteins involved in the regulation of crucial cellular and mitochondrial processes (Planas-Iglesias *et al.*, 2015). Besides LC3A and LC3B interaction with CL studied here, this phospholipid can also interact with BECN1 (Huang *et al.*, 2012), a key component in the autophagic core machinery, with DNM1L/Drp1 (dynamin 1 like), one of the proteins in charge of mitochondrial fission (Stepanyants *et al.*, 2015), or with OPA1, involved in IMM fusion (Ban *et al.*, 2017), among others. Interestingly, CL externalization also occurs during apoptosis (Kagan *et al.*, 2005). Externalized CL can interact with many proteins involved in this process, such as BAK1, BAX, or CASP8 (Gonzalvez *et al.*, 2008; Landeta *et al.*, 2011; Sani *et al.*, 2009), and it also participates in other programmed cellular death pathways such as NLRP3 inflammasome activation (Iyer *et al.*, 2013).

All these studies show that both CL and its location are key for the correct functioning of mitochondria. Among its different roles, it is surprising that CL externalization could promote both a generally “pro-survival” pathway, such as autophagy, and a “pro-death” pathway, such as apoptosis (Li *et al.*, 2015). However, it has been proposed that CL participating in apoptosis is previously oxidized due to the peroxidase activity of cytochrome C (Kagan *et al.*, 2005), while CL recognized by the autophagy machinery is not (Chu *et al.*, 2013). Interestingly, the results obtained with LC3B and LC3A in the experiments with oxidized CL show that while LC3B binding decreases when CL is oxidized (**Figure 3.24C**), CL oxidation does not affect LC3A binding (**Figure 3.24B**). These results together with the ones of LC3A and LC3B single and double mutants (**Figure 3.25**) highlight the importance of the LC3A 14 and 18 residues in oxidized CL-binding. Thus, LC3A would recognize oxidized CL in the OMM, shielding it from the apoptotic machinery, and preventing excessive activation of apoptosis. According to our *in vitro* data, LC3B would not be able to achieve the latter function, as its ability to interact with CL decreases with oxidation.

Concluding remarks.

The importance of CL externalization as a signal to degrade damaged mitochondria via autophagy has been demonstrated *in vitro* and *in vivo* (Antón *et al*., 2016; Chao *et al.*, 2019; Chu *et al*., 2013; Kagan *et al.*, 2016). In this work, LC3A has been identified as an additional LC3-subfamily member involved in mitophagy, and key residues for its interaction with CL have been singled out. This contribution could facilitate the design of precise modulators for this mitophagy mechanism. However, the possibility of this process being cell-, tissue- or organ-specific, or even the possibility of a crosstalk between different types of autophagy cannot be dismissed. Further investigations would be required to improve our understanding of the mechanisms triggering mitophagy, which could in turn be involved in the appearance of important neurodegenerative diseases such as Parkinson or Alzheimer.

CHAPTER 4

EFFECT OF ATG12–ATG5-ATG16L1 AUTOPHAGY E3 COMPLEX ON THE ABILITY OF LC3/GABARAP PROTEINS TO INDUCE VESICLE TETHERING AND FUSION

CHAPTER 4. Effect of E3 complex on the ability of LC3/GABARAP proteins to induce vesicle tethering and fusion

4.1. Introduction

The mode of expansion of the phagophore that will promote AP formation is still unclear. Several authors have approached autophagy, and particularly the fusion processes leading to autophagosomal growth, using model membrane systems consisting of vesicles of defined lipid compositions and purified proteins. One of the most accepted hypothesis is the incorporation of membrane-supplying vesicles to the growing phagophore (Nakatogawa, 2020). Studies with yeast proteins point to the interaction of lipidated Atg8 proteins with different membranes to promote the tethering and hemifusion of vesicles into the growing phagophore (Nakatogawa *et al.* 2007) (**Figure 4.1**).

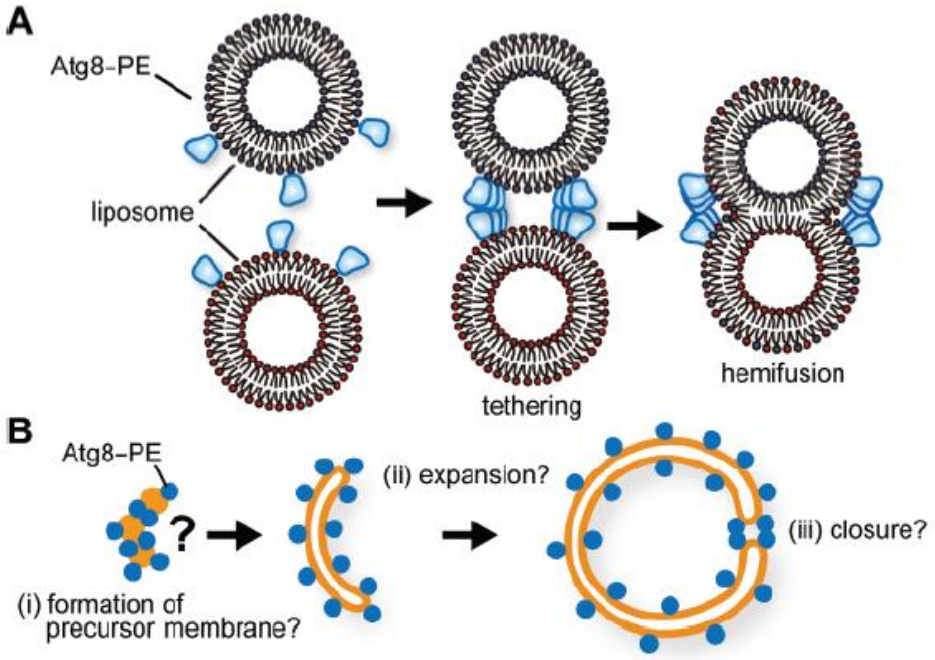

Figure 4.1. Autophagosome expansion model proposed in yeast. (**A**) Atg8–PE oligomerizes and causes tethering and hemifusion of liposomal membranes *in vitro*. (**B**) Possible roles of Atg8–PE during autophagosome formation. Taken from Nakatogawa (2013).

Studies with human proteins are also interesting for discerning the possible different roles of the Atg8 orthologs that constitute the LC3/GABARAP family (Weidberg *et al.*, 2010). In this laboratory, Landajuela *et al*. used two reconstituted liposomal systems to learn more about the molecular mechanisms by which human LC3 and GABARAP

subfamilies trigger AP biogenesis (Landajuela *et al.*, 2016). They studied three of the LC3/GABARAP-family members: LC3B, GABARAP and GABARAPL2. They found that lipidated forms of the GABARAP-subfamily proteins promoted a more extensive membrane tethering and lipid mixing than LC3B. Landajuela *et al.* also showed that negative curvature-inducing lipids (*e.g.*, cardiolipin, diacylglycerol) facilitated the fusion process. Those results strongly supported the hypothesis of a highly bent structural fusion intermediate (stalk) during AP biogenesis and reinforced lipids as key regulators of autophagy (Iriondo *et al.*, 2021; Landajuela *et al.*, 2016).

It is important to take into account that for those functions the Atg8 and LC3/GABARAP proteins need to be bound to membranes. *In vivo*, this lipidation process requires the concerted action of the two ubiquitin-like (UBL) conjugation systems: ATG12 and LC3/GABARAP systems (Section 1.3). In humans, the ATG12 system product, the ATG12–ATG5-ATG16L1 complex (from now on the E3 complex), acts as the E3 ligase enzyme of the second UBL conjugation system (Bento *et al.*, 2016; Gammoh, 2020; Romanov *et al.*, 2012; Walczak & Martens, 2013), catalyzing the conjugation of LC3/GABARAP- family members to phosphatidylethanolamine (PE) (Martens, 2016; Nakatogawa *et al.*, 2007; Tanida *et al.*, 2004). There are some *in vitro* studies with yeast proteins that have investigated the interplay between both ubiquitin-like systems and their interaction with membranes (Hanada *et al.*, 2007; Romanov *et al.*, 2012; Walczak & Martens, 2013). Those works showed that the presence of the E3 complex increased Atg3 activity, boosting the lipid-protein conjugation reaction and specifying the membrane site where Atg8 lipidation occurred (**Figure 4.2**).

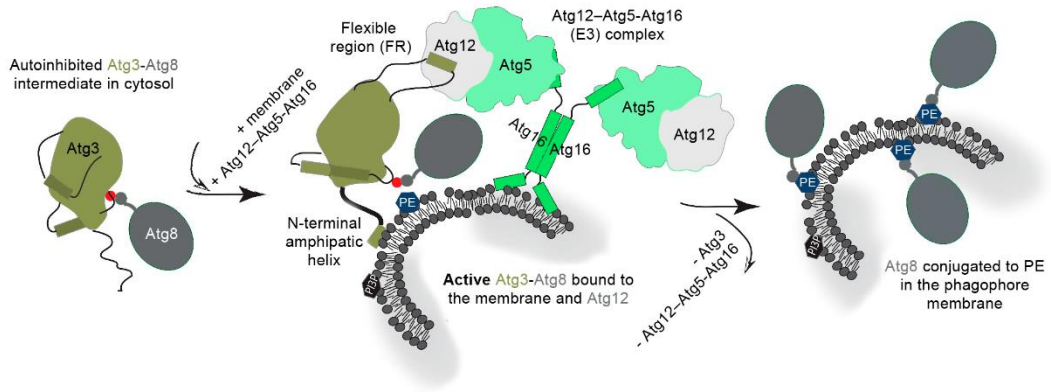

Figure 4.2. Schematic model for yeast Atg3 activation by E3 complex. Membrane binding of Atg3 is either preceded or followed by binding of a short structural element in the flexible region (FR) to Atg12 in the Atg12–Atg5-Atg16 (E3) complex. The Atg3 FR–Atg12 interaction can reposition Cys234 via an allosteric mechanism. Structural changes induced by the membrane and Atg12 near Atg3 Cys234 facilitate the transfer of Atg8 Gly 116 to PE. After Atg3 and Atg12–Atg5-Atg16 disassembly, Atg8 is lipidated on the phagophore membrane. Adapted from Popelka & Klionsky (2021).

However, as the full human E3 complex was only recently available (Fracchiolla *et al.*, 2020; Lystad *et al.*, 2019) and only then was reconstitution of lipidation made possible *in vitro* in the absence of the ATG12 UBL system, studies with the two human reconstitution systems are still scarce. In fact, all the above mentioned studies had been performed in the absence of E3 complex, therefore, its effect on LC3/GABARAP membrane tethering and fusion activities had not been investigated yet.

In the present chapter, first, it was attempted to reconstitute the lipidation of six LC3/GABARAP family members, namely LC3A, LC3B, LC3C, GABARAP, GABARAPL1 and GABARAPL2, by using different *in vitro* approaches in the absence of E3 complex. Once E3 complex purification was implemented in this laboratory, the effect of E3 was tested not only on lipidation of the LC3/GABARAP proteins, but also on their ability to promote membrane tethering and fusion of vesicles.

4.2. Materials and methods

4.2.1. Materials

L-α-phosphatidylcholine from hen egg yolk (ePC, 840051), 1,2-dioleoyl-*sn*-glycero-3-phosphatidylethanolamine (DOPE, 850725), liver phosphatidylinositol (PI, 840042), egg dioleoylglycerol (DOG, 800811), 1,2-dioleoyl-*sn*-glycero-3-phosphoethanolamine-N-[4-(p-maleimidomethyl)cyclohexane-carboxamide] (PEmal, 780201), 1,2-dioleoyl-*sn*-glycero-3-phosphatidylethanolamine-N-lissamine rhodamine B sulfonyl (Rho-PE, 810150) and 1-oleoyl-2-{6-[(7-nitro-2-1,3-benzoxadiazol-4-yl)amino]hexanoyl}-*sn*-glycero-3-phosphoethanolamine (NBDtail-PE, 810145) were purchased from Avanti Polar Lipids, Inc. (Alabaster, AL). N-(7-nitrobenz-2-oxa-1,3-diazol-4-yl)-1,2-dihexadecanoyl-*sn*-glycero-3-phosphatidylethanolamine (NBD-PE, N360), p-xylene-bis-pyridinium bromide (DPX, X-1525) and 8-aminonaphthalene-1,3,6-trisulfonic acid, disodium salt (ANTS, A350) were purchased from Thermo Fisher Scientific (Waltham, MA).

4.2.2. DNA constructs and mutagenesis

The details of the constructs are shown in Chapter 2 (**Table 2.1**). The pGEX4T-1 plasmids for expression of several of the various Gly-exposed LC3/GABARAP subfamily members tagged with glutathione S-transferase (GST) were obtained by mutagenesis (see Materials and Methods Chapter 3). The mutated version of LC3/GABARAP proteins to have a C-terminal Cys instead of a Gly: LC3A^{C17S,G120C} (LC3A^{G120C} for simplicity), LC3B^{G120C}, LC3C^{G126C}, GABARAP^{G116C}, GABARAP^{G116C} and GABARAPL2^{C15S,G116C} (GABARAPL2^{G116C} for simplicity), were obtained by site-directed mutagenesis (synthesized by GenScript) The pGEX6P-1 plasmid for expression of human ATG3 was kindly provided by Dr. Isei Tanida (National Institute of Infectious Diseases, Tokyo, Japan). Plasmids for expression of mouse ATG7 and E3 complex were kindly provided by Prof. S. Martens (Max Perutz Labs, Vienna, Austria).

4.2.3. Recombinant protein expression and purification

LC3/GABARAP proteins, their mutants and ATG3 were purified (**Protocol 3**) from soluble fractions of bacterial extracts obtained in the absence of detergents, and they were >90% pure as evaluated by Coomassie Brilliant Blue-stained SDS-PAGE. *E. coli* BL21 (λDE3) cells were transformed with the appropriate plasmids. They were grown to A_{600}= 0.8 and protein expression was induced with 0.5 mM IPTG for 16 h at 20°C. Following centrifugation at 4,500 x g for 15 min, the pellet was resuspended and sonicated in Breaking buffer (PBS 1x, 20 mM Tris-HCl pH 7, 150 mM NaCl, 1mM DTT supplemented with lysozyme, protease inhibitors and DNase) (See also **Table 2.4**). After removal of cellular debris by centrifugation at 30,000 x g for 30 min at 4°C, the sample supernatant was incubated with 1 ml Glutathione Sepharose 4B (GE Healthcare, 17-0756-01) for 3 h at 4°C to bind GST-tagged proteins. LC3/GABARAP proteins were cleaved with Thrombin Protease (GE Healthcare, 27-0846-01) overnight at room temperature in Thrombin Buffer (140 mM NaCl, 2.7 mM KCl, 10 mM Na_2HPO_4, 1.8 mM

KH_2PO_4 (pH 7.3), with freshly added 1 mM DTT). ATG3 protein was cleaved with PreScission Protease (GE Healthcare, 27-0843-01) for 4h at 4ºC in PreScission Buffer (50 mM Tris-HCl pH 7.5, 150 mM NaCl, 1 mM EDTA, with freshly added 1 mM DTT) (See also **Table 2.5**). After cleavage, they were eluted in Elution Buffer (50 mM Tris-HCl pH 7.5, 150 mM NaCl, 1 mM EDTA, with freshly added 1 mM DTT), then concentrated to 500 µl using Amicon Ultra-4 (4 mL, 3 kDa cut-off) (Millipore, UFC800324), and loaded onto a Superdex-75 10/300 GL size exclusion column (GE Healthcare, GE17-5174-01) equilibrated in Elution Buffer. Proteins were distributed in aliquots, flash-frozen and stored in 20% glycerol at -80°C until further use.

ATG12–ATG5-ATG16L1 (E3) complex was purified (**Protocol 7**) from soluble fractions of insect cell extracts obtained in the absence of detergents, and it was >90% pure as evaluated by Coomassie Brilliant Blue-stained SDS-PAGE. For E3 complex expression the Bac-to-Bac Baculovirus expression system was used. The pGEBdest vector containing a poly-cistronic construct (**Table 2.1**) with the ATG12-system necessary proteins for E3 complex formation (Fracchiolla *et al.*, 2020) was transformed into DH10Bac *E. coli* cells. Blue/white colony selection was used to identify colonies containing the recombinant bacmid. The recombinant bacmid was isolated (**Protocol 5**) and 2.5 µg were used to transfect 10^6 Sf9 insect cells using FuGENE transfection reagent (Promega, E2311). When the transfected cells demonstrated signs of late stage infection (typically around 72 h) the medium containing the free virus was harvested (V0) and used to produce a stock virus (V1) solution (**Protocol 6**). V1 was used to further infect a 1-liter culture of Sf9 cells at 0.8–1x10^6/ml in SF921 medium containing penicillin-streptomycin. Cultures were harvested when cells reduced their viability to a maximum of 95-98%. They were pelleted down and further washed in PBS at 3,315 x g for 10 min at 4°C. Pellets were flash frozen in liquid nitrogen and stored at −80°C until purification. Then, cell pellets were thawed and resuspended in ice-cold buffer containing 50 mM Hepes, pH 7.5, 300 mM NaCl, 2 mM $MgCl_2$, 1 mM DTT, complete protease inhibitors, Protease Inhibitor Cocktail, and Benzonase Nuclease. Cells were lysed on ice by extrusion in a tissue homogenizer, and lysates were cleared by centrifugation at 48,398 x g for 1 hour at 4°C. Supernatant was applied to a 5-ml StrepTactin column (GE Healthcare) to bind Strep-tagged proteins. Bound proteins were eluted with 2.5 mM desthiobiotin in 25 mM Hepes, pH 7.5, 150 mM NaCl, and 1 mM DTT. Fractions containing the E3 complex were pooled, concentrated down to 500 µl using Amicon Ultra-15 (15 mL, 30 kDa cut-off), applied onto a Superdex 6 column (Increase 10/ 300; GE Healthcare), and eluted in a buffer containing 25 mM Hepes, pH 7.5, 300 mM NaCl, and 1 mM DTT. Fractions containing pure E3 complex were pooled, distributed in aliquots, flash-frozen, and stored at -80°C until further use.

Mouse ATG7 (mATG7) was purified (See **Section 2.4.4**) from soluble fractions of insect cell extracts obtained in the absence of detergents, and it was >90% pure as evaluated by Coomassie Brilliant Blue-stained SDS-PAGE. It was also expressed in Sf9 insect cells and harvested following the same procedure described above for the E3 complex. See **Table 2.1** for construct details. For purification, pellets were thawed and resuspended in ice cold buffer containing 50 mM Hepes, pH 7.5, 300 mM NaCl, 10 mM imidazole, 2 mM $MgCl_2$, 2 mM β-mercaptoethanol, complete protease inhibitors (Roche), Protease Inhibitor Cocktail (Sigma), and Benzonase Nuclease (Sigma). Cells were lysed on ice by extrusion in a tissue homogenizer, and lysates were cleared by centrifugation at 48,398 x g for 1 hour at 4°C. Supernatant was applied to a 5-ml nickel-nitrilotriacetic acid (Ni-

NTA) column (GE Healthcare) and eluted via a stepwise imidazole gradient (50, 75, 100, 150, 200, and 300 mM). Protein eluted in fractions containing 150 mM imidazole. These fractions were pooled, concentrated, applied onto a Superdex 200 10/300 GL (GE Healthcare), and eluted in a buffer containing 25 mM Hepes, pH 7.5, 150 mM NaCl, and 1 mM DTT. Fractions containing pure mATG7 were pooled, concentrated, flash-frozen in liquid nitrogen, and stored at −80°C.

4.2.4. Liposome preparation.

The appropriate lipids (ePC:DOPE:PI:DOG, 33:55:10:2 mol ratio or ePC:DOPE:PEmal: PI, 35:25:30:10) were mixed in organic solution and the solvent was evaporated to dryness under a N_2 stream. Then the sample was kept under vacuum for 1 h to remove solvent traces. The lipids were swollen in System Buffer (150 mM NaCl, 50 mM Tris, pH 7.5) in order to obtain multilamellar vesicles (MLV) (**Protocol 12**). Large unilamellar vesicles (LUV) were produced from MLV according to the extrusion method described by Mayer *et al*. (1986) (**Protocol 13**). They were subjected to 10 freeze/thaw cycles, and then extruded through a LIPEX Liposome Extrusion System (Transferra Nanosciences, Burnaby, CA) using 0.05-µm pore size Nuclepore filters (Whatman, 110605). Vesicle size was checked by quasi-elastic light scattering using a Malvern Zeta-Sizer 4 spectrometer (Malvern Instruments, Malvern, UK). LUV had an average diameter of ≈80 nm. Phospholipid concentration was determined by phosphate analysis (Böttcher *et al.*, 1961) (**Protocol 11**).

4.2.5. *In vitro* chemical lipidation assays

To reconstitute LC3/GABARAP-PE conjugation *in vitro* without the use of ATG7, ATG3, or E3, the pertinent LC3/GABARAP-family member with the Gly C-terminal exposed mutated to Cys (5 µM) was mixed with PEmal-containing liposomes (0.4 mM total lipid) in System Buffer (50 mM Tris pH 7.5, 150 mM NaCl) to a final volume of 100 µl (see **Figure 4.3** and **Figure 4.4** legends for details). Reactions were performed at 37°C and initiated by addition of the protein. 15 µl of the reaction mixture were sampled at each time point (0, 5, 10, 30 and 60 min), mixed with 3 µl of 6x Protein Loading dye and heated at 100°C for 5 min to stop the reaction. Lipidation was analyzed in SDS-PAGE gels using Coomassie Brilliant Blue staining. The gels were quantified using ImageJ. The amounts of LC3/GABARAP and LC3C/GABARAP–PEmal at each time point were measured as the area below the corresponding absorption peak. The percent LC3/GABARAP–PEmal relative to total protein (% lipidation) was calculated at each time point and plotted as a function of time.

4.2.6. *In vitro* enzymatic lipidation assays

Purified ATG7 (0.5 µM), ATG3 (1 µM), $MgCl_2$ (1 mM), E3 complex (0.1 µM) (when indicated) and the pertinent member of the LC3/GABARAP-family with an exposed Gly C-terminal (5 µM) were mixed with liposomes (0.4 mM total lipid) in System Buffer (50 mM Tris pH 7.5, 150 mM NaCl) to a final volume of 100 µl (see **Figure 4.5**, **Figure 4.6**, **Figure 4.10**, **Figure 4.11**, **Figure 4.12** and **Figure 4.13** legends for details). Reactions were performed at 37°C and initiated by ATP addition (5 mM). 15 µl of the reaction

mixture were sampled at each time point (0, 5, 10, 15, 30 and 60 min), mixed with 3 µl of 6x Protein Loading dye and heated at 60°C for 10 min to stop the reaction. Lipidation was analyzed in SDS-PAGE gels by using Coomassie Brilliant Blue staining. Lipidation reactions as performed in **Figure 4.12** were also analyzed using a VersaDoc MP 4000 Imaging System to detect NBD fluorescence. The gels of three independent experiments were quantified using ImageJ. The amounts of LC3/GABARAP and LC3C/GABARAP–PE at each time point were measured as the area below the corresponding absorption peak. The percent LC3/GABARAP–PE relative to total protein (% lipidation) was calculated at each time point and plotted as a function of time.

4.2.7. Vesicle flotation assay

Protein interaction with membranes was assessed using flotation in sucrose gradients (**Protocol 16**). All the liposome and protein concentrations used were increased (by 5-fold) with respect to the other assays, all proportions being otherwise kept, to allow detection of the E3 complex in the gels (see **Figure 4.18** legend for details). Liposomes were incubated with the indicated proteins for 30 min at 37°C in System Buffer. The protein/lipid mix was adjusted to 1.4 M sucrose concentration in 300 µl and transferred to a centrifuge tube. This first (bottom) layer was overlaid with successive solutions containing 0.8 M (400 µl) and 0.5 M (300 µl) sucrose. The three-layer gradients were centrifuged in a TLA-120.2 rotor (Beckman Coulter, Brea, CA, US) at 355,040 x g for 50 min at 4°C. After centrifugation, four 250-µl fractions were collected, starting from the bottom. Proteins were detected in SDS-PAGE gels using Coomassie Brilliant Blue staining. Densitometry of the protein bands was performed using ImageJ software, and the percent liposome-bound protein was estimated from the band intensities measured in the third + fourth fractions (floating vesicle fractions), relative to the total sum of intensities measured in all fractions.

4.2.8. Tethering assays

Liposome tethering/aggregation was monitored in a Varian Cary 300 (Agilent Technologies, Santa Clara, CA) spectrophotometer as an increase in turbidity (absorbance at 400 nm) of the sample (See also **Protocol 17**). All assays were carried out at 37°C with continuous stirring (Landajuela *et al.*, 2016). See **Figure 4.19** legend for protein and lipid concentration details.

4.2.9. Total and inner Lipid mixing assay

A fluorescence resonance energy transfer (FRET) assay (**Protocol 18**) was used to monitor inter-vesicular membrane lipid mixing (Alonso *et al.*, 1982). The appropriate LUV containing 1.5 mol % NBD-PE and 1.5 mol % Rho-PE (labeled in the head group) were mixed with a 9-fold excess of unlabeled LUV (see **Figure 4.25** and **Figure 4.31** legend for protein and lipid concentration details). NBD-PE emission was monitored in a Fluorolog®-3 (Horiba Jobin Yvon, Edison, NJ) spectrofluorometer with constant stirring at 37°C. NBD emission was monitored at 530 nm with the excitation wavelength set at 465 nm (slits at 4 nm). A 515 nm cut-off filter was placed between the sample and the

emission monochromator to avoid scattering interference. Inner monolayer lipid mixing was measured using asymmetrically labeled membrane vesicles produced by the quenching of the outer leaflet NBD-PE fluorescence upon addition of sodium dithionite (Xu *et al.*, 2005). Excess dithionite was removed by gel filtration in Sephadex G-25M, using System Buffer for elution. 100% inter-vesicular membrane lipid mixing and 100% inner-monolayer lipid mixing were established by adding 10 µL 10% (v/v) Triton X-100. The extent of lipid mixing was quantified on a percentage basis according to the equation: $(F_t-F_0/F_{100}-F_0)$ x 100 where F_t is the measured NBD fluorescence of protein-treated LUV at time t, F_0 is the initial NBD fluorescence of the LUV suspension before ATP addition, and F_{100} is the NBD fluorescence value after complete disruption of LUV by addition of Triton X-100. Details for the inter-vesicular lipid mixing assay can be found in Goñi *et al.* (2003).

4.2.10. Leakage assay

Leakage of vesicle contents was monitored by the ANTS/DPX leakage assay (Ellens *et al.*, 1985) (**Protocol 19**). Liposomes were swollen in ANTS/DPX buffer (20 mM ANTS, 70 mM DPX, 50 mM Tris, 40 mM NaCl, pH 7.5). Non-encapsulated ANTS and DPX were removed by gel filtration in Sephadex G-25M, using System Buffer for elution (see **Figure 4.32** legend for protein and lipid concentration details). ANTS emission was monitored at 520 nm with the excitation wavelength set at 355 nm (slits at 4 nm). To establish the 100% leakage signal, 10 µL of 10% (v/v) Triton X-100 were added. Details for the vesicle contents leakage assay can be found in Goñi *et al.* (2003).

4.2.11. Aqueous content mixing assay

Inter-vesicular aqueous contents mixing was monitored by the ANTS/DPX mixing assay (Ellens *et al.*, 1985) (**Protocol 20**). Three types of liposomes were prepared. Liposomes were swollen in either ANTS buffer (39 mM ANTS, 50 mM Tris, 72 mM NaCl, pH 7.5), in DPX buffer (140 mM DPX, 50 mM Tris, 10 mM NaCl, pH 7.5), or in ANTS/DPX buffer (20 mM ANTS, 70 mM DPX, 50 mM Tris, 40 mM NaCl, pH 7.5). Non-encapsulated ANTS and/or DPX were removed by gel filtration in Sephadex G-25M, using System Buffer for elution. All buffers had the same osmolarity (see **Figure 4.33** legend for protein and lipid concentration details). ANTS emission was monitored at 520 nm with the excitation wavelength set at 355 nm (slits, 1 nm). 0% vesicle content mixing was set by using a 1:1 mixture of ANTS- and DPX-containing liposomes. 100% contents mixing corresponded to the fluorescence of the vesicles containing co-encapsulated ANTS and DPX. The extent of aqueous contents mixing was quantified on a percentage basis according to the equation: $(-(F_t-F_0/F_{100}-F_0))$ x 100 where F_t is the measured ANTS fluorescence of protein-treated LUV at time t, F_0 is the initial ANTS fluorescence of the LUV suspension before protein addition, and F_{100} is the ANTS fluorescence value of the vesicles containing co-encapsulated ANTS/DPX. Details for the aqueous contents mixing assay can be found in Goñi *et al.* (2003).

4.3. Results

4.3.1. LC3/GABARAP protein *in vitro* lipidation in the absence of E3 complex.

In order to study the possible implication of LC3/GABARAP proteins in phagophore expansion, we should first reconstitute their covalent anchoring to the membrane. This covalent lipid-protein binding, named lipidation can be detected by the appearance of a faster migrating band in a SDS-PAGE gel. *In vivo* this process requires the concerted action of both UBL-systems (**Section 1.3**, **Figure 1.15**), but different *in vitro* assays can be used to reconstitute the lipidation of some of the LC3/GABARAP proteins. Based on previous studies from this laboratory (Landajuela *et al.*, 2016), lipidation of the six members of the LC3/GABARAP family was attempted using two different approaches: chemical and enzymatic. These approaches do not require the participation of E3 complex, and in order to favor lipidation in the absence of E3 complex, a composition with a relatively high PE concentration (55% PE) was used.

4.3.1.1. Chemical lipidation

The chemical approach is the simplest. It consists of the attachment of LC3/GABARAP proteins to the membrane through a chemical reaction between a protein Cys residue and a maleimide group. For that purpose, the six LC3/GABARAP proteins, whose exposed C-terminal glycine had been mutated to cysteine, were designed and purified. This would allow their conjugation to a chemically modified PE containing a reactive maleimide in its head group (PEmal) (**Figure 4.3A**).

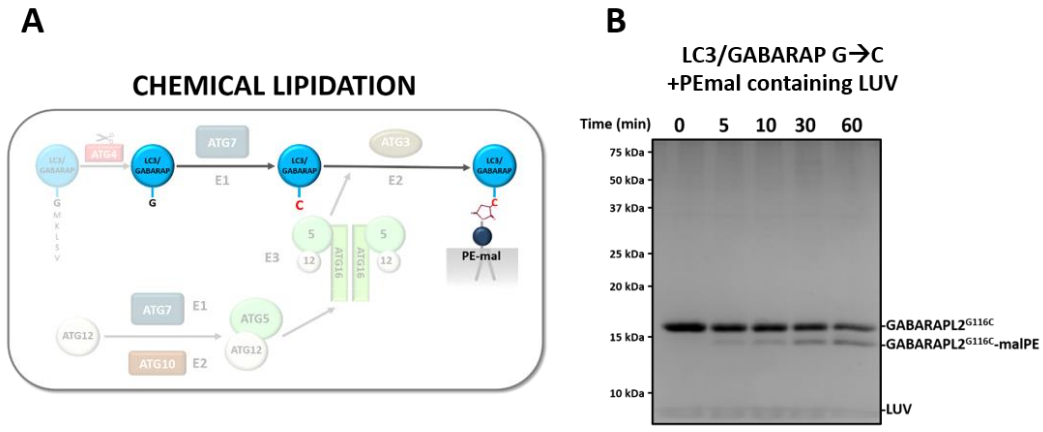

Figure 4.3. LC3/GABARAP chemical lipidation system. (A) Schematic representation of the chemical lipidation system. LC3/GABARAP proteins had their Gly C-terminal exposed mutated to Cys in order to allow their chemical conjugation to PEmal in the membrane. **(B)** Representative gel of a chemical lipidation assay. 5 µM GABARAPL2^{G116C} were mixed with 0.4 mM of PE-mal-containing LUV (ePC:DOPE:PEmal:PI (35:25:30:10: mol ratio)) and incubated at 37°C in System Buffer. Aliquots were retrieved at 0, 5, 10, 30 and 60 min after protein addition, and loaded on a 15% SDS-polyacrylamide gel.

The various LC3/GABARAP proteins with the C-terminal Gly mutated to Cys were added to PEmal-containing LUV. Aliquots were collected at pre-fixed times after protein addition, up to 60 min. The chemically lipidated (faster migrating band) and non-lipidated forms were resolved by SDS-PAGE (**Figure 4.3B**). Chemical lipidation of the six LC3/GABARAP family members (**Figure 4.4A**) differed in their kinetics and extent (**Figure 4.4B, C**).

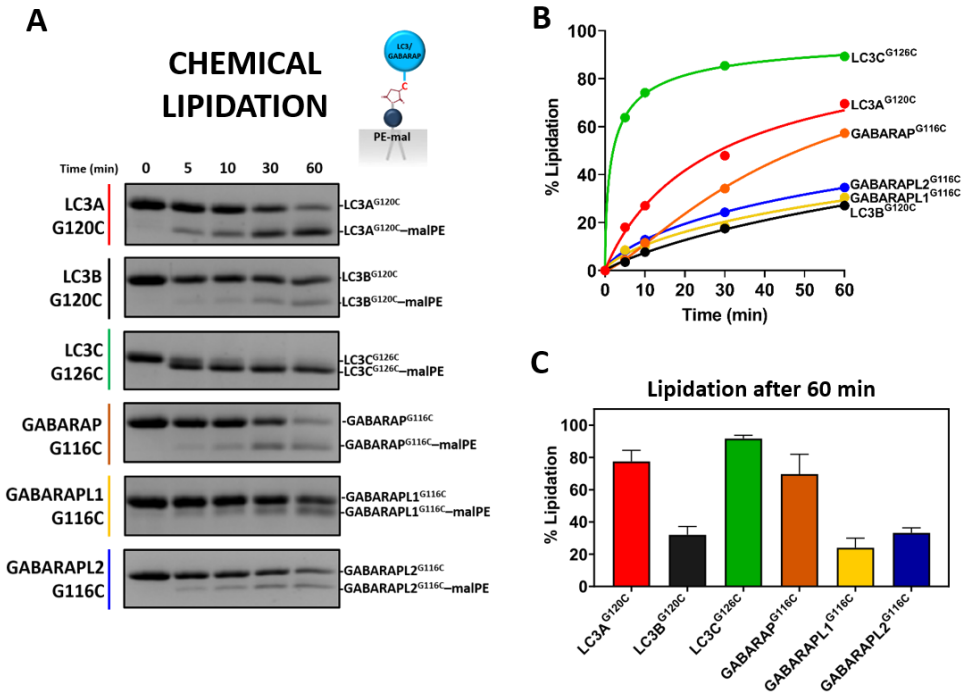

Figure 4.4. LC3/GABARAP proteins were lipidated to a different extent with the chemical approach. The indicated LC3/GABARAP G→C (5 µM) were mixed with 0.4 mM PE-mal containing LUV [PC:DOPE:PEmal:PI (35:25:30:10: mol ratio)] and incubated at 37°C in System Buffer. Aliquots were retrieved at 0, 5, 10, 30 and 60 min after protein addition, and loaded onto a 15% SDS-polyacrylamide gel. **(A)** Cropped lipidation gels corresponding to the LC3/GABARAP protein region (an example of a full gel can be seen in Figure 4.3B). **(B)** Lipidation time-course data from gels shown in (A). **(C)** Percent lipidated LC3/GABARAP 60 min after protein addition. Data are means ± SD (n = 3).

These results suggest that the chemical approach could be very interesting and helpful for reconstituting the lipidation of each family member in the absence of any other protein. For comparative purposes, the enzymatic approach was used next.

4.3.1.2. Enzymatic lipidation in the absence of E3 complex

The enzymatic approach is somewhat more complex, as it is closer to the *in vivo* system. To reduce complexity and avoid the use of ATG4 protein, the LC3/GABARAP recombinant proteins used had their C-terminal Gly already exposed. Therefore, ATG7 and ATG3 proteins could act upon ATP addition to promote LC3/GABARAP lipidation in PE-containing membranes (**Figure 4.5A**).

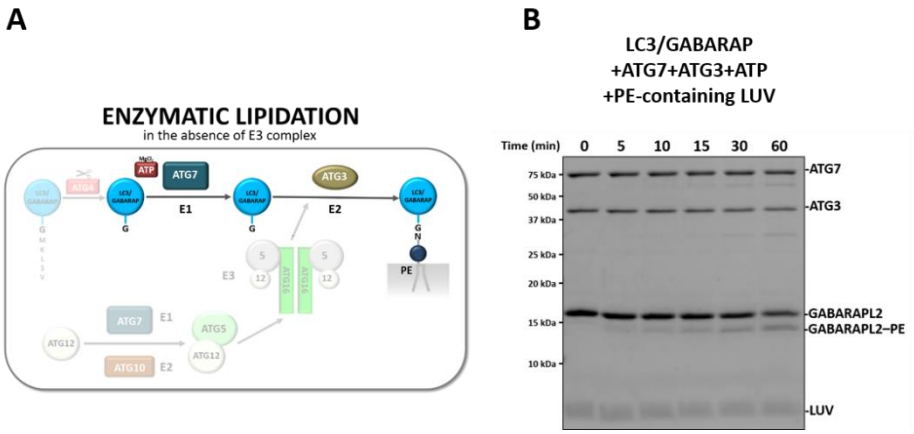

Figure 4.5. LC3/GABARAP enzymatic lipidation system in the absence of E3 complex. (A) Outline of the system. ATP promoted ATG7 (E1-like), ATG3 (E2-like) actions triggering LC3/GABARAP conjugation to PE in PE-containing liposomes. LC3/GABARAP proteins had their C-terminal Gly exposed to avoid the requirement of ATG4 participation. **(B)** Representative gel of an enzymatic lipidation assay. 0.5 µM ATG7, 1 µM ATG3, and 5 µM GABARAPL2 were mixed with 0.4 mM LUV [ePC:DOPE:PI:DOG (33:55:10:2 mol ratio)], and incubated at 37°C in System Buffer containing $MgCl_2$. After ATP addition, aliquots retrieved at 0, 5, 10, 15, 30 and 60 min were loaded on a 15% SDS-polyacrylamide gel.

The various LC3/GABARAP proteins with the exposed C-terminal Gly were added to a mix of ATG7, ATG3 and PE-containing LUV. Aliquots were collected at pre-fixed times after ATP addition and the lipidated (faster migrating band) and non-lipidated forms were resolved by SDS-PAGE (**Figure 4.5B**). Again, lipidation of the six LC3/GABARAP family members (**Figure 4.6A**) differed in their time courses and extents (**Figure 4.6B, C**).

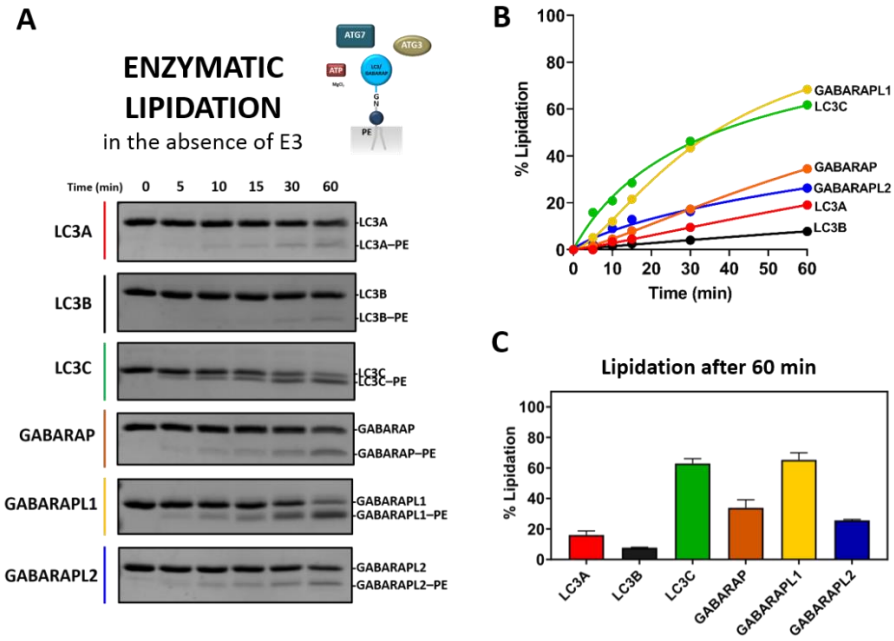

Figure 4.6. Different proportions of lipidated LC3/GABARAP proteins were obtained with the enzymatic approach. 0.5 µM ATG7, 1 µM ATG3, and 5 µM of the indicated LC3/GABARAP protein were mixed with 0.4 mM LUV [ePC:DOPE:PI:DOG (33:55:10:2 mol ratio)], and incubated at 37°C in System Buffer containing $MgCl_2$. After ATP addition, aliquots retrieved at 0, 5, 10, 15, 30 and 60 min were loaded on a 15% SDS-polyacrylamide gel. **(A)** Cropped lipidation gels corresponding to the LC3/GABARAP protein region (An example of a full gel can be seen in Figure 4.5). **(B)** Time-course of the protein percent lipidation corresponding to gels shown in (A) **(C)** Percent lipidated LC3/GABARAP 60 min after ATP addition. Data are means ± SD (n = 3).

The observed different lipidation levels of the various LC3/GABARAP members could provide hints of what happens under physiological conditions. One hypothesis is that they reflect different affinities of the LC3/GABARAP family members towards ATG7 and/or ATG3. In further experiments, the enzymatic approach was used to compare LC3/GABARAP lipidation, tethering and lipid mixing abilities in the presence and absence of E3 complex.

4.3.2. E3 complex expression and purification

Only recently was the full E3 complex obtained in eukaryotic cells (Fracchiolla *et al.*, 2020; Lystad *et al.*, 2019). After the author's international stay in Prof. S. Martens' laboratory, the expression and purification of the full human E3 complex was set up and optimized in Alonso's lab. Plasmid pGBdest obtained via the Golden Gate approach (Fracchiolla *et al.*, 2020) contained the five proteins needed for ATG12–ATG5-ATG16L1 (E3) complex formation, namely ATG7, ATG10, ATG12, ATG5 and ATG16L1 (**Figure 4.7A**). This poly-cistronic gene was the gene of interest (GOI) and was 10640 bp long. It was inserted by transposition in a bacmid. The insertion was checked by PCR (**Figure 4.7B**) and the recombinant bacmid was extracted.

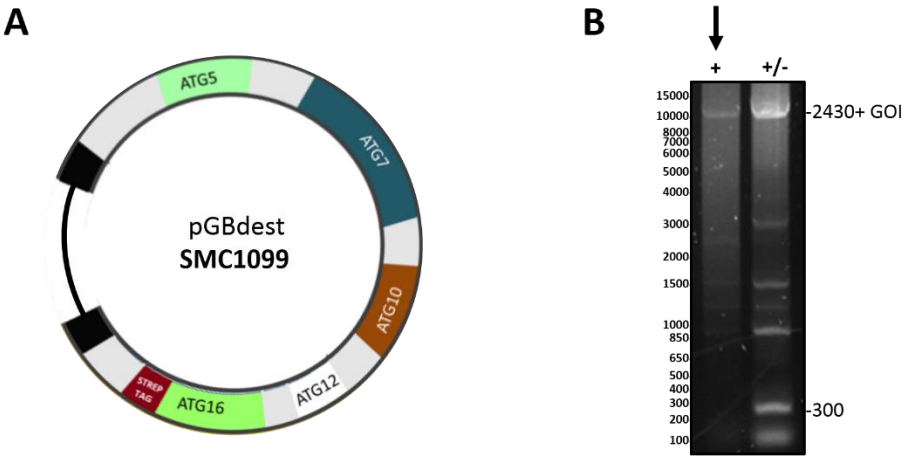

Figure 4.7. E3 construct for expression and transposition into the bacmid. (A) pGBdest poly-cistronic gene construct cloned via Golden Gate approach by the Vienna BioCenter Core Facilities (Fracchiolla *et al.*, 2020) (Table 2.1). **(B)** Analysis by PCR of a positive (white) and a mixed colony. The band corresponded to 2430 + length of the GOI (10640bp).

Transfection of Sf9 insect cells with the bacmid was supposed to promote expression of the five components of the ATG12 conjugation system and therefore production of the E3 complex (**Figure 4.8A**). YFP protein expression together with the observation of larger insect cells confirmed the efficient transfection and subsequent baculovirus production (**Figure 4.8B**). Expression and production of the E3 complex were checked. Two bands corresponding to ATG16L1 and ATG12–ATG5 conjugate were observed (**Figure 4.8C**).

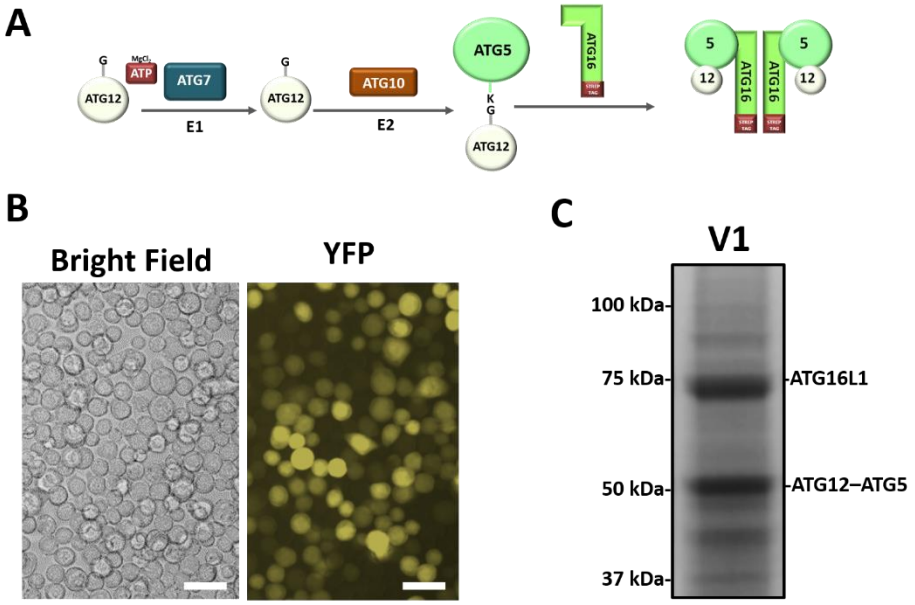

Figure 4.8. E3 was efficiently expressed in insect cells. (A) Scheme of the ATG12 UBL-system. **(B)** Sf9 insect cells transfected with the bacmid containing the GOI for E3 expression. Bar = 50µm **(C)** SDS-PAGE analysis of cells infected by the rBV (V1).

The Strep-tag included in ATG16L1 allowed affinity purification of the E3 complex. It was further purified using size exclusion chromatography (**Figure 4.9**).

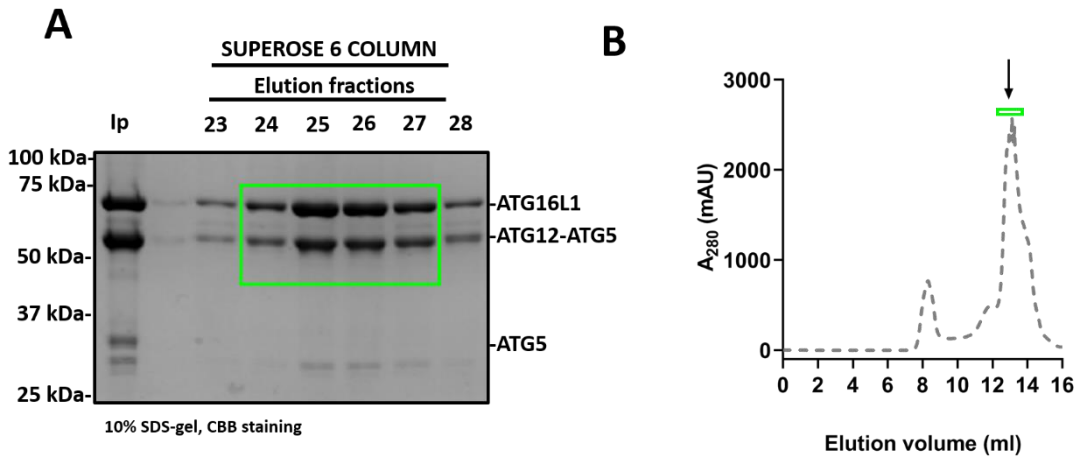

Figure 4.9. E3 purification. (A) SDS-PAGE of the size exclusion chromatography step using Superose 6 Increase column (Inp: Input). 0.5 ml fractions. **(B)** Size exclusion E3 chromatogram. 2.3 ml at 12 µM concentration were obtained. The protein is indicated by a green rectangle in both A and B.

4.3.3. LC3/GABARAP *in vitro* lipidation in the presence of E3 complex.

The functionality of the purified E3 was assayed next. Each member of the family was mixed with PE-containing liposomes, ATG7, ATG3, E3 complex and ATP (**Figure 4.10A**). Since relatively high amounts of PE were used, low levels of E3 complex were required in our reconstitution system. As seen in a representative gel (**Figure 4.10B**), when E3 was present a higher proportion of the faster migrating band was observed upon addition of ATP, in comparison with the same experiment in the absence of E3 (compare Figs. 4.10B and 4.6A).

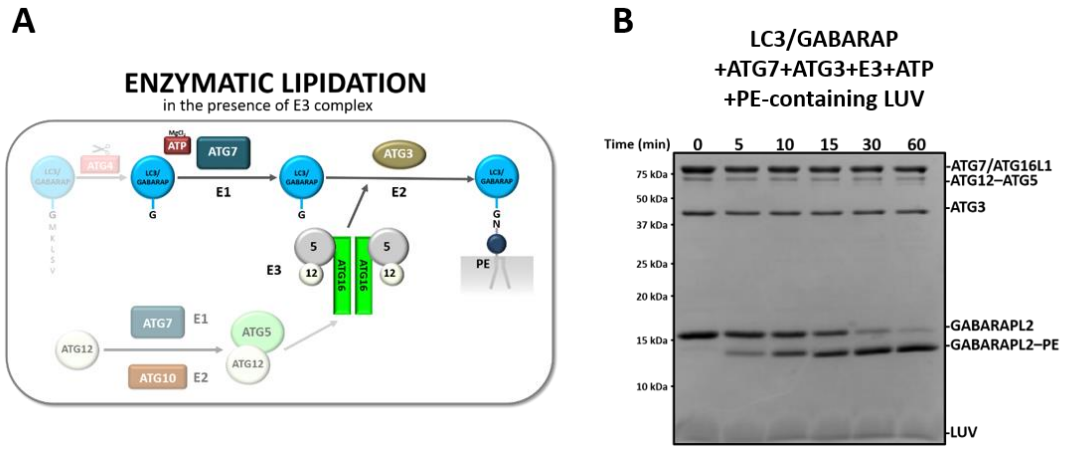

Figure 4.10. LC3/GABARAP enzymatic lipidation in the presence of E3 complex. (A) Outline of the system. ATP promoted ATG7 (E1-like), ATG3 (E2-like) and ATG12-ATG5-ATG16 (E3-like) actions triggering LC3/GABARAP conjugation to PE in PE-containing liposomes. LC3/GABARAP proteins had their C-terminal Gly exposed to avoid the requirement of ATG4. The full-length ATG12-ATG5-ATG16 (E3) complex was expressed in insect cells (See section 4.3.2). **(B)** Representative gel of an enzymatic lipidation assay. 0.5 µM ATG7, 1 µM ATG3, 0.1 µM E3 complex and 5 µM GABARAPL2 protein were mixed with 0.4 mM LUV [PC:DOPE:PI:DOG (33:55:10:2 mol ratio)], and incubated at 37°C in System Buffer containing $MgCl_2$. After ATP addition, aliquots retrieved at 0, 5, 10, 15, 30 and 60 min were loaded onto a 15% SDS-polyacrylamide gel.

0.1 µM E3 complex was enough for achieving over 80% lipidation after 1 hour for the six members of LC3/GABARAP family (**Figure 4.11A,C**). These results confirmed that our purified E3 complex was functional. At variance with the previous approaches, in the presence of E3, a similar time course (**Figure 4.11B**) and extent of lipidation (**Figure 4.11C**) was observed for all the protein family members. Thus, the enzymatic reconstitution system in the presence of E3 allowed similar high levels of lipidation for all six LC3/GABARAP proteins.

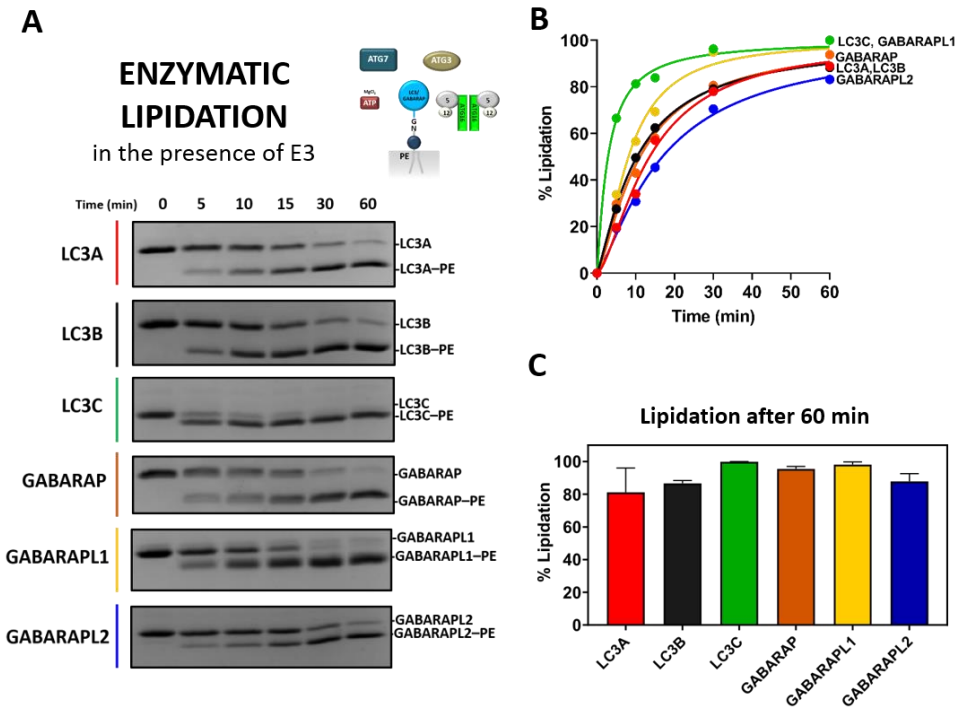

Figure 4.11. All six LC3/GABARAP proteins were similarly lipidated with the enzymatic approach in the presence of E3 complex. 0.5 µM ATG7, 1 µM ATG3, and 5 µM of the indicated LC3/GABARAP protein were mixed with 0.4 mM LUV [ePC:DOPE:PI:DOG (33:55:10:2 mol ratio)], and incubated at 37°C in System Buffer containing $MgCl_2$. After ATP addition, aliquots retrieved at 0, 5, 10, 15, 30 and 60 min were loaded onto a 15% SDS-polyacrylamide gel. **(A)** Cropped lipidation gels corresponding to the LC3/GABARAP protein region (an example of a full gel can be seen in Figure 4.10B). **(B)** Time-course of protein lipidation computed from gels as shown in Figure (A) **(C)** Percent lipidated LC3/GABARAP 60 min after ATP addition. Data are means ± SD (n = 3).

Next, it was checked if the faster migrating band was, in fact, the lipidated version of the protein. This was confirmed by the appearance of a fluorescent faster migrating band when liposomes containing NBDtail-PE were used (**Figure 4.12**).

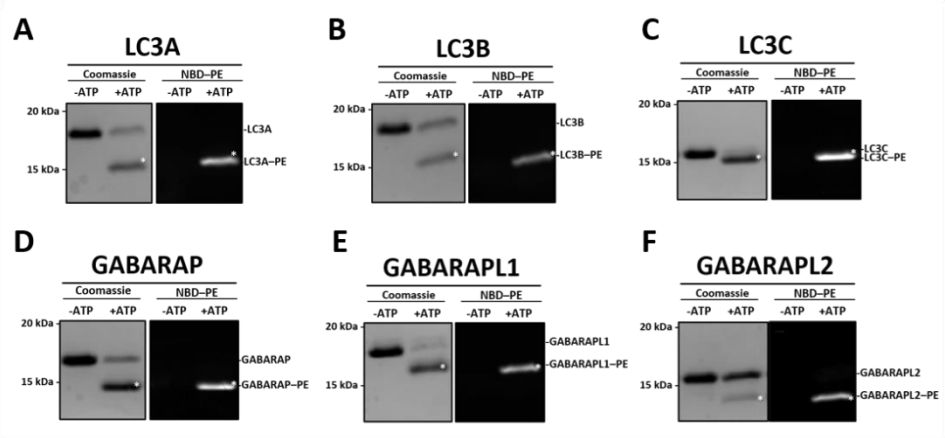

Figure 4.12. The faster migrating band observed in the presence of E3 after ATP addition represents the lipidated LC3/GABARAP protein. (A-F) *In vitro* LC3/GABARAP lipidation assay: 0.5 µM ATG7, 1 µM ATG3, 0.1 µM E3 and 5 µM of the indicated LC3/GABARAP-protein member were mixed with 0.4 mM LUV [ePC:DOPE:PI:DOG:NBDtail-PE (33:45:10:2:10 mol ratio)]. Each reaction mixture was incubated at 37°C for 30 min, run on 15% SDS-PAGE gels, and visualized by Coomassie Brilliant Blue staining (left-hand panels) or using a VersaDoc MP 4000 Imaging System to detect NBD-PE fluorescence (right-hand panels). Only the faster migrating band (*) showed fluorescence.

4.3.4. E3 complex increases and accelerates LC3/GABARAP lipidation.

The effect of E3 on the capacity of LC3/GABARAP proteins to covalently bind vesicles, and to promote vesicle tethering and inter-vesicle lipid mixing was examined next. For an analysis of E3 complex effects on lipidation, the various LC3/GABARAP proteins were added to a mix of ATG7, ATG3, PE-containing LUV and, when indicated, E3. Aliquots were collected in parallel (-E3, +E3) at pre-fixed times after ATP addition (0, 5, 10, 15, 30 and 60 minutes), and the lipidated and non-lipidated forms were resolved by SDS-PAGE. The results from Figs. 4.6 and 4.11 are redrawn on Figure 4.13 for convenience. When results obtained in the absence or presence of E3 complex were compared, a clear E3-dependent increase in the lipidation rates and extents was observed for all the LC3/GABARAP proteins (**Figure 4.13**).

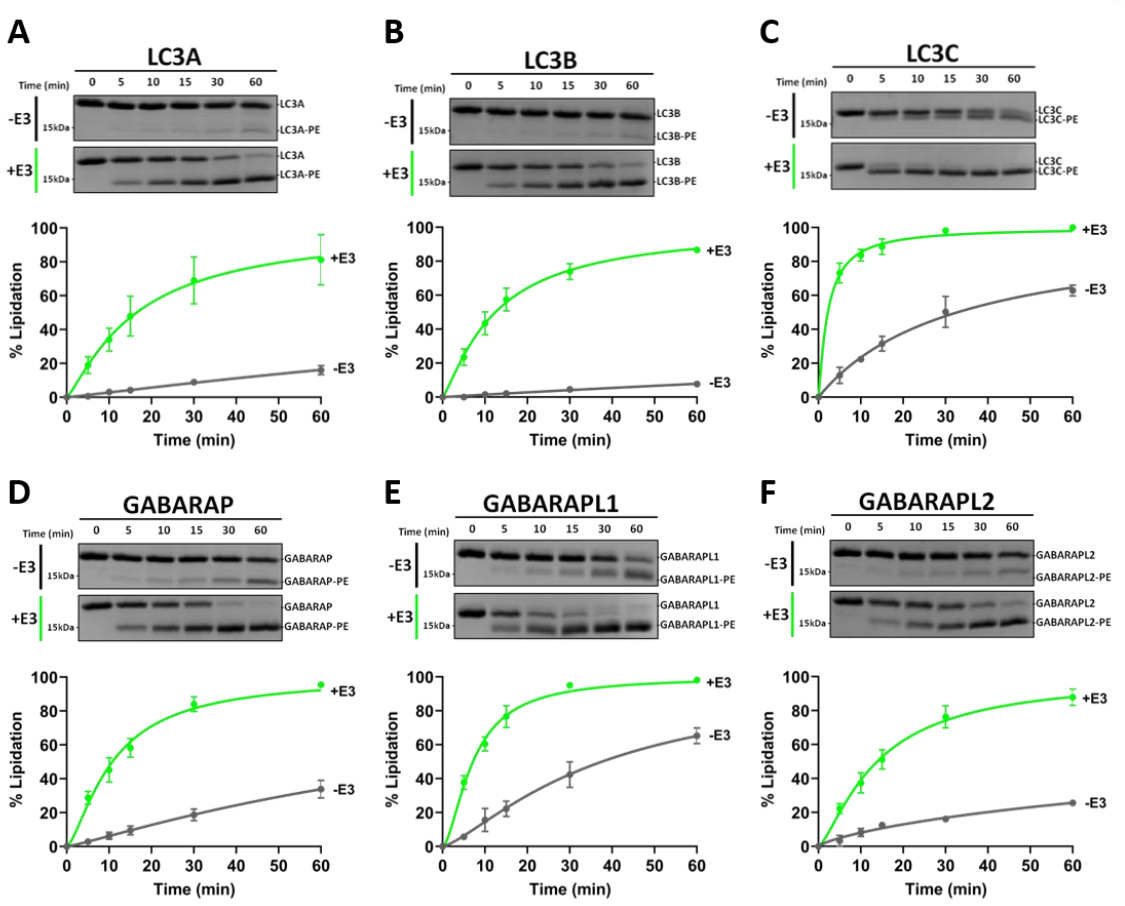

Figure 4.13. E3 complex increases and accelerates LC3/GABARAP lipidation. **(A-F)** *In vitro* LC3/GABARAP lipidation assay: 0.5 µM ATG7, 1 µM ATG3, and 5 µM of the indicated LC3/GABARAP protein were mixed with 0.4 mM LUV [ePC:DOPE:PI:DOG (33:55:10:2 mol ratio)], in the absence (-E3, grey) or presence (+E3, green) of 0.1 µM E3 complex and incubated at 37°C. After ATP addition, aliquots retrieved at pre-fixed time points were loaded on 15% SDS-polyacrylamide gels. Upper panel: Cropped lipidation gels corresponding to the LC3/GABARAP protein region Lower panel: Time-course of protein lipidation.

In the absence of E3 complex, the extents of lipidation after 30 min (**Figure 4.14**, -E3 panel) were highest for LC3C and GABARAPL1 (>30%), followed by GABARAP, GABARAPL2 (>10%), LC3A and LC3B (>5%). However, when E3 complex was present (**Figure 4.14**, +E3 panel), all the proteins were >70% lipidated, with small differences between the various homologs.

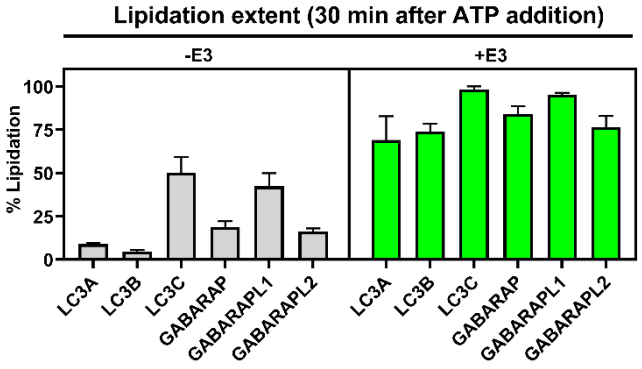

Figure 4.14. Lipidation extent in the absence and presence of E3 complex. Percent lipidated LC3/GABARAP 30 min after ATP addition in the absence (left) or presence (right) of E3 complex. Data are means ± SD (n = 3). See also Figure 4.13.

When comparing lipidation rates (**Figure 4.15**) LC3C and GABARAPL1 exhibited the fastest lipidation in the absence of E3 (**Figure 4.15**, -E3 panel). When E3 was present, all lipidation reactions went faster and LC3C exhibited the highest rate, up to 15% lipidated protein/min, followed by GABARAPL1 with a 7% (**Figure 4.15**, +E3 panel).

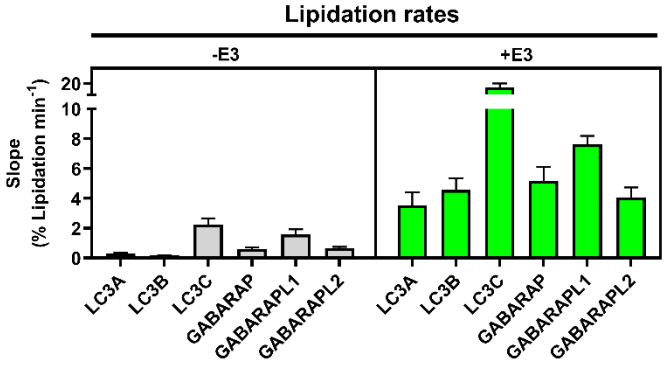

Figure 4.15. Lipidation rates in the absence and presence of E3 complex. Initial lipidation rates of the various LC3/GABARAP in the absence (left) or presence (right) of E3 complex. Data are means ± SD (n = 3). See also Figure 4.13.

These results confirmed the ability of the E3 complex to increase and accelerate LC3/GABARAP protein lipidation. The E3-complex effect was particularly visible in LC3A and LC3B lipidation, since lipidation of those proteins in the absence of the complex was quite low.

4.3.5. In the presence of ATG3, low concentrations of E3 complex allow vesicle tethering.

The tethering ability of E3 complex had been previously described in yeast (Romanov *et al.*, 2012). In the present investigation, the capacity of low concentrations (0.1 µM) of human E3 complex to cause vesicle tethering was tested. Liposome tethering/aggregation is usually assessed as an increase in suspension turbidity. When E3 alone was added to liposomes, no change in turbidity (ΔA_{400}) was detected (**Figure 4.16**, orange line). However, when added to a mixture composed of liposomes, GABARAPL1, ATG7 and ATG3, a fast increase in A_{400} was observed. Vesicle tethering started as soon as E3 was added, and reached a plateau in about 3 min (**Figure 4.16**, green line). The role of the various components in the observed tethering effect was dissected next.

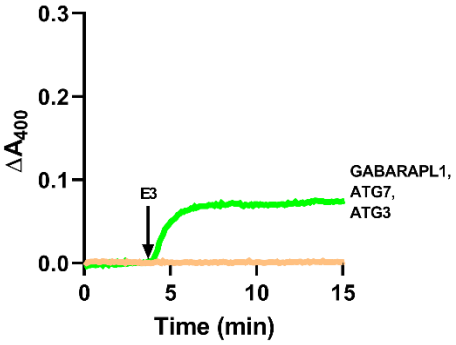

Figure 4.16. E3 addition to a mix containing GABARAPL1, ATG7 and ATG3 promotes vesicle tethering. Changes in turbidity (ΔA_{400}), as a signal of vesicle tethering, were measured after E3 addition. Tethering of 0.4 mM LUV [ePC:DOPE:PI:DOG (33:55:10:2 mol ratio)] caused by 0.1 µM E3 alone (orange line) or in the presence of 5 µM GABARAPL1, 0.5 µM ATG7 and 1 µM ATG3 (green line).

When, in addition to liposomes, only GABARAPL1 was present, E3 addition did not cause any increase in turbidity (**Figure 4.17**, blue line). Thus, the E3 tethering effect would require either ATG3 or ATG7, or a combination of both. Experiments performed with each of them separately showed that ATG3 was the main agent co-operating with E3 in the tethering effect (**Figure 4.17**).

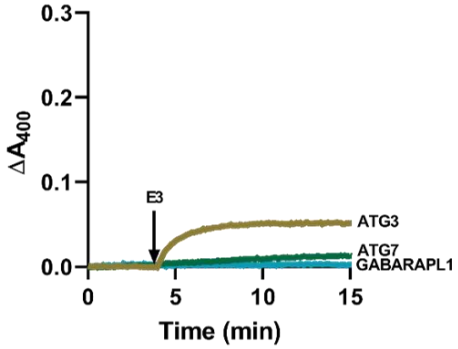

Figure 4.17. In the presence of ATG3, low concentrations of E3 complex allow vesicle tethering. Changes in turbidity (ΔA_{400}), as a signal of vesicle tethering, were measured after E3 addition. Tethering of 0.4 mM LUV [PC:DOPE:PI:DOG (33:55:10:2 mol ratio)] caused by addition of 0.1 µM E3 in the presence of 5 µM GABARAPL1 (blue line), 0.5 µM ATG7 (dark green line) or 1 µM ATG3 (ochre line).

To further understand why E3 was able to promote vesicle tethering when ATG3 was present, a liposome flotation assay was performed comparing the E3 ability to interact with membranes in the absence or presence of ATG3. All of the E3 complex was vesicle-bound when ATG3 was present (**Figure 4.18**). Thus, ATG3 enhanced E3 complex interaction with the membrane, allowing an initial stage of liposome tethering.

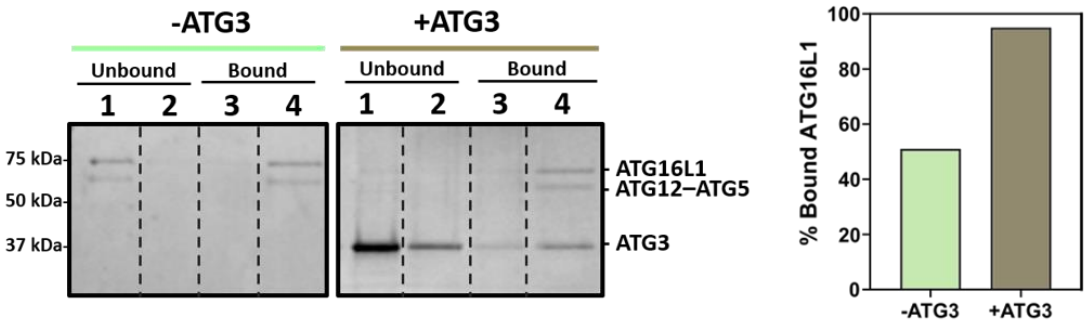

Figure 4.18. ATG3 promotes E3 interaction with membranes. Interaction of E3 complex with membranes in the absence and in the presence of ATG3 measured by a vesicle flotation assay. Protein and liposome concentrations were increased by 5-fold to allow detection of E3 complex in the gels. 0.5 µM E3 was incubated with 2 mM LUV [ePC:DOPE:PI:DOG (33:55:10:2 mol ratio)] in the absence or presence of 2.5 µM ATG3. Left: SDS-PAGE/Coomassie Brilliant Blue stained gels of the fractions obtained from E3 vesicle flotation assays in the absence (-ATG3 panel) or presence of ATG3 (+ATG3 panel). Protein found in fractions 3+4 was taken as bound protein. Right: Percent ATG16L1 bound to liposomes in the absence or presence of ATG3, quantified by gel densitometry.

4.3.6. E3 complex enhances and accelerates LC3/GABARAP-promoted vesicle tethering.

The capacity of the different lipidated LC3/GABARAP to induce vesicle tethering was comparatively tested (**Figure 4.19**). To this aim, PE-containing LUV, ATG3, ATG7, and the pertinent LC3/GABARAP-family member were mixed. After 4 min either E3 complex (+E3, green lines) or buffer (-E3, grey lines) were added, and 10 min later, ATP (+ATP, solid lines) or buffer (-ATP, dashed lines) were equally added.

When proteins could not be lipidated (in the absence of ATP) and E3 complex was not present (**Figure 4.19A-F**, -E3-ATP, grey dashed lines), no change in turbidity (A_{400}) was observed. However, as described in the previous section for GABARAPL1 (**Figure 4.19**), E3 addition caused an initial tethering activity for all LC3/GABARAP proteins (**Figure 4.19A-F**, +E3, green lines).

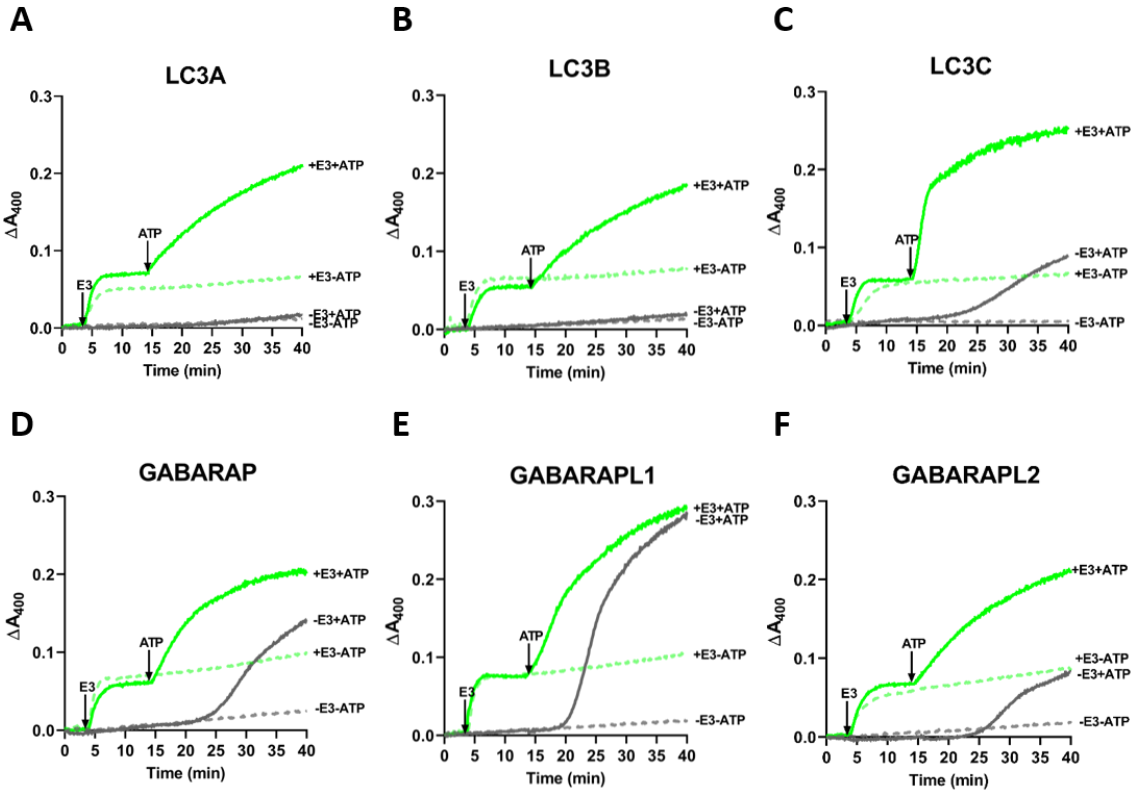

Figure 4.19. E3 complex enhances and accelerates LC3/GABARAP-promoted vesicle tethering. Membrane tethering activities by lipidated LC3/GABARAP proteins in the absence or presence of E3 complex. 0.4 mM LUV [ePC:DOPE:PI:DOG (33:55:10:2 mol ratio)], 0.5 μM ATG7, 1 μM ATG3, and 5 μM of the pertinent LC3/GABARAP-family member were mixed. After 4 min either 0.1 μM E3 complex (+E3, green lines) or buffer (-E3, grey lines) were added, and 10 min later ATP (+ATP, solid lines) or buffer (-ATP, dashed lines) were added. Changes in absorbance at 400 nm (ΔA_{400}), as an indication of vesicle tethering, were recorded. **(A-F)** Representative curves of the indicated LC3/GABARAP member under the four analyzed conditions: -E3 -ATP (grey dashed lines), -E3 +ATP (grey solid lines), +E3 -ATP (green dashed lines), +E3 +ATP (green solid lines).

After ATP addition, which would allow protein lipidation, tethering was observed in almost all cases (**Figure 4.19A-F**, solid lines). In the absence of E3 (**Figure 4.19A-F**, -E3, +ATP, grey solid lines), the protein eliciting the fastest and most extensive tethering was GABARAPL1, followed by GABARAP, GABARAPL2 and LC3C. LC3A and LC3B had no measurable effect (**Figure 4.20**, -E3 panel). However, if E3 was present (**Figure 4.19A-F**, +E3, +ATP, green solid lines), all the proteins, including LC3A and LC3B, were able to induce some tethering, LC3C achieving by far the fastest rates (**Figure 4.20**, +E3 panel).

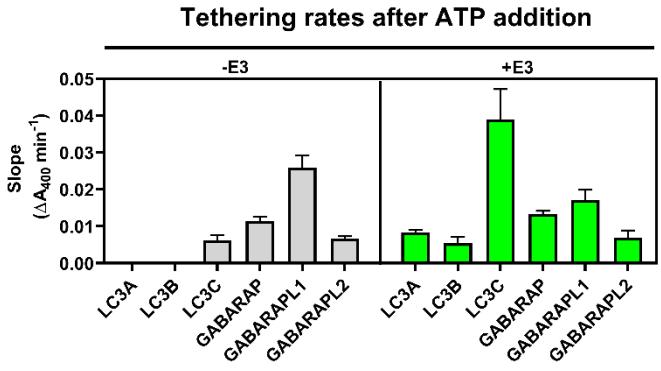

Figure 4.20. Tethering rates after ATP addition. Experiments performed in the absence (left) or in the presence (right) of E3 complex. LC3A or LC3B did not cause any measurable activity in the absence of E3. Data are means ± SD (n = 3).

All four LC3/GABARAP proteins that induced a measurable extent of tethering in the absence of E3 (LC3C, GABARAP, GABARAPL1, and GABARAPL2) also showed a considerable lag phase (**Figure 4.21**). A negative correlation appeared to exist between rate (maximum slope) and lag time (**Figure 4.20 and Figure 4.21**, -E3 panel). However, when E3 was present, no lag phase was detected implying that vesicle tethering started immediately after adding ATP (**Figure 4.21**). This could indicate that a minimum degree of lipidation, achieved faster when E3 was present, would be required for tethering to start.

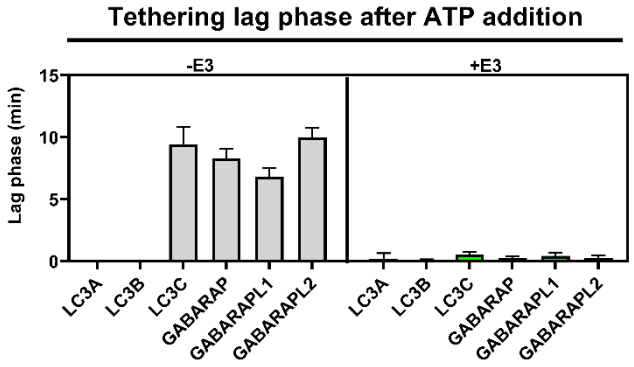

Figure 4.21. Lag phase of tethering activity after ATP addition. Experiments performed in the absence (left) or presence (right) of E3 complex. Data are means ± SD (n = 3).

There was in general a good parallelism between the time courses of LC3/GABARAP protein lipidation and LC3/GABARAP-induced vesicle tethering when E3 was present (**Figure 4.22**) In Figure 4.22 the curves were normalized by subtracting the effect of E3 and setting the 0 time at the moment of ATP addition. This allows an easier perception of the effect of the lipidated protein. **Figure 4.23** compares the effects of E3 on each protein. In all cases, the ATP-dependent change in tethering is considered. In that way, the initial E3 effect is suppressed and a better comparison of the LC3/GABARAP effects in the presence or absence of E3 is made feasible.

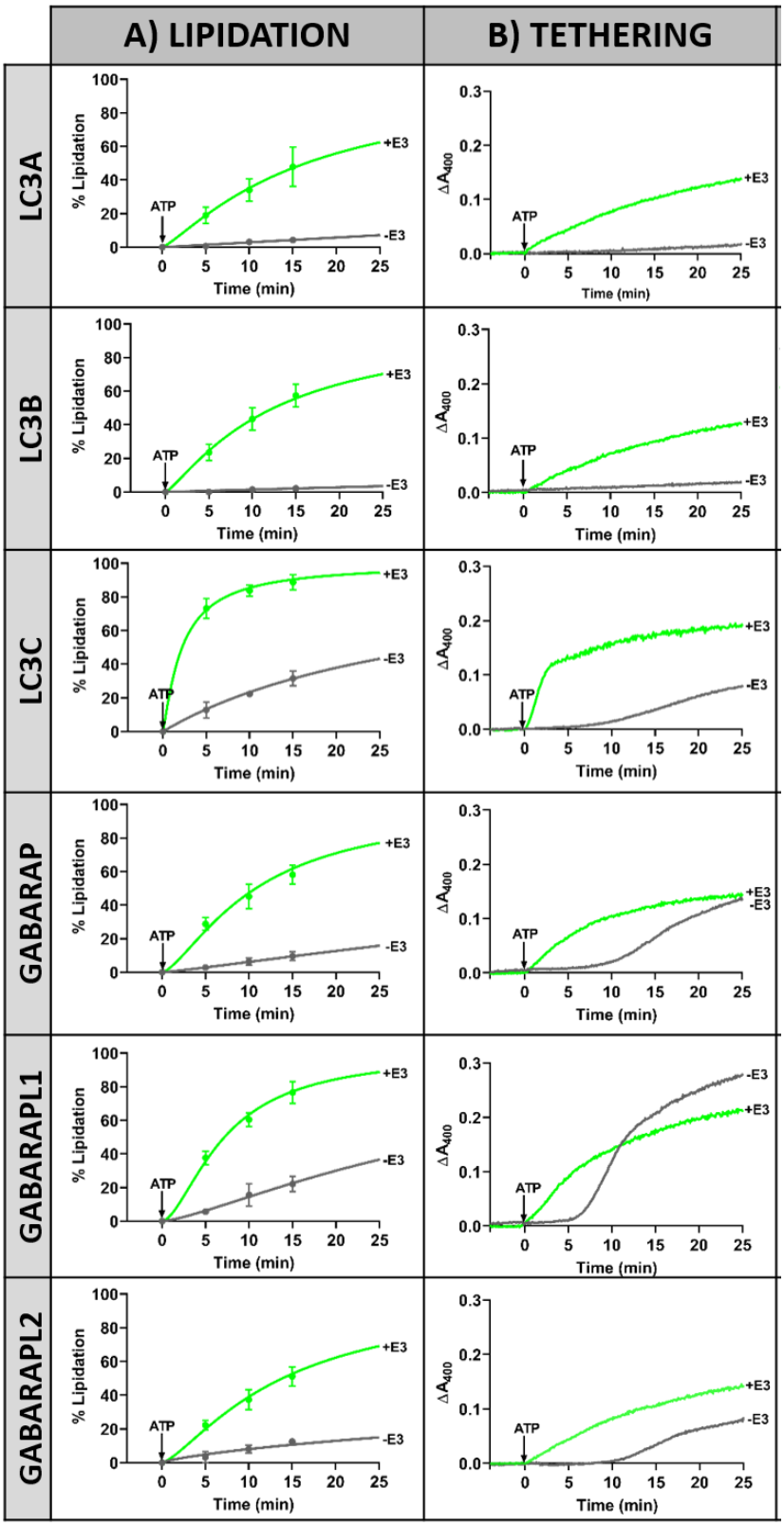

Figure 4.22. Comparative summary of LC3/GABARAP-protein lipidation and tethering time courses in the absence and presence of E3 complex. Data from Figure 4.13 and Figure4.19 were redrawn in order to allow an easier comparison of the results in this study. **(A)** Lipidation time course of LC3/GABARAP proteins after ATP addition in the absence (grey) and in the presence (green) of E3 complex. **(B)** Tethering time course of each LC3/GABARAP-family member after ATP addition in the absence (grey) and in the presence (green) of E3 complex.

However, some peculiarities should be considered. (a) When E3 was not present, even if LC3C lipidation level was similar to that of GABARAPL1, both the extent and rate of vesicle tethering were lower (**Figure 4.22, Figure 4.23**, grey). (b) LC3A and LC3B, in the absence of E3, did not induce vesicle tethering, probably because of the low lipidation level (<10%) achieved. However, GABARAP or GABARAPL2, with a slightly higher lipidation level were able to cause a markedly higher extent of liposome tethering (**Figure 4.18**, grey bars). (c) E3 increased lipidation levels in all cases, however, at variance with the LC3 subfamily, the extent of tethering was similar with and without E3 for GABARAP and GABARAPL2 and lower in the presence of E3 for GABARAPL1 (**Figure 4.23**).

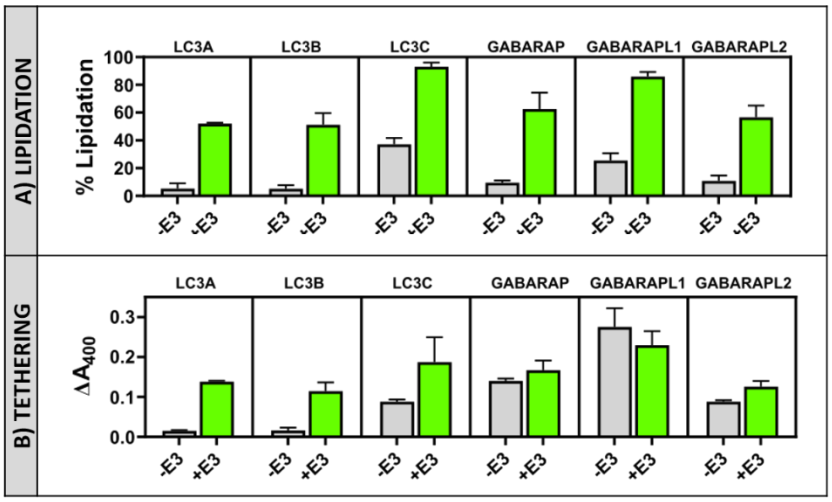

Figure 4.23. Effect of E3 complex on LC3/GABARAP-protein lipidation and the subsequent vesicle tethering 25 min after ATP addition. (A) Final lipidation levels in the absence (grey) and presence (green) of E3 complex. **(B)** Extent of vesicle tethering induced by LC3/GABARAP proteins in the absence (grey) and presence (green) of E3 complex. Data are means ± SD (n = 3).

When the ratio between the extent of vesicle tethering and the percent lipidated protein at a given time (25 min after ATP addition was chosen for convenience) was computed (**Figure 4.24**), a clear difference between both subfamilies was observed in the absence of E3 (**Figure 4.24**, -E3 panel). However, in the presence of E3, when all homologs were lipidated by ≥50%, and their ability to induce vesicle tethering was quite similar (**Figure 4.24**, green bars), the tethering/lipidation ratio was also similar for all proteins (**Figure 4.24**, +E3 panel). This could suggest a different lipidation threshold for each LC3/GABARAP-family member, above which each of them would be able to induce vesicle tethering. This lipidation threshold would be lower for the GABARAP subfamily.

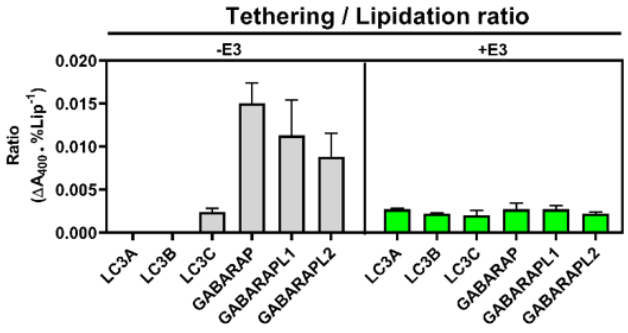

Figure 4.24. Tethering/lipidation ratios. Ratios final tethering levels caused by lipidated LC3/GABARAP proteins over percent lipidated protein', in the absence (left) or presence (right) of E3 complex. Data are means ± SD (n = 3).

4.3.7. E3 complex hampers LC3/GABARAP-protein capacity to induce inter-vesicular lipid mixing.

Previous studies (Landajuela *et al.*, 2016; Nakatogawa *et al.*, 2007; Weidberg *et al.*, 2010) had shown that at least some of the LC3/GABARAP proteins were able to induce inter-vesicular lipid mixing. The present study has found that the lipidated LC3/GABARAP proteins were able to induce vesicle tethering, and that this process was enhanced and accelerated by E3. A further step in our study consisted of checking the LC3/GABARAP protein ability to induce inter-vesicular lipid mixing and liposome fusion, and analyzing how E3 affected the process. First, we examined whether the small extent of tethering caused by E3 addition to the lipidation machinery also caused lipid mixing. In fact, a small lipid mixing effect was observed prior to ATP addition in all cases (**Figure 4.25**, +E3, green lines, first 14 min).

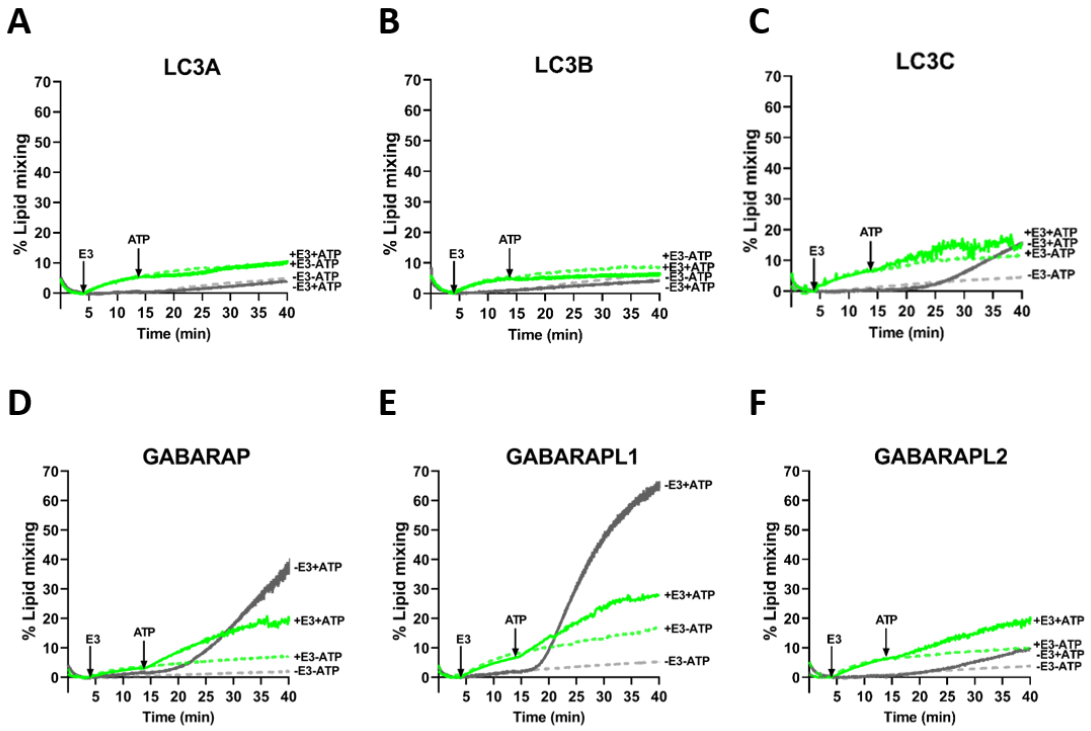

Figure 4.25. E3 complex hampers LC3/GABARAP capacity to induce inter-vesicular lipid mixing. Membrane lipid mixing activities by lipidated LC3/GABARAP proteins in the absence and in the presence of E3 complex were monitored with the NBD-PE/Rho-PE lipid dilution assay. 0.4 mM unlabeled and (NBD-PE + Rho-PE)-labeled liposomes (9:1) were mixed with 0.5 µM ATG7, 1 µM ATG3, and 5 µM of the pertinent LC3/GABARAP-family member. After 4 min either 0.1 µM E3 complex (+E3, green lines) or buffer (-E3, grey lines) were added, followed 10 min later by ATP (+ATP, solid lines) or buffer (-ATP, dashed lines). Increases in NBD fluorescence detection, as a signal of lipid mixing of labelled and unlabeled vesicles, were measured and the percentage of lipid mixing was computed. See Methods for details. **(A-F)** Representative curves of the indicated LC3/GABARAP member under the four analyzed conditions: -E3 -ATP (grey dashed lines), -E3 +ATP (grey solid lines), +E3 -ATP (green dashed lines), +E3 +ATP (green solid lines).

With the whole set of proteins, except E3, the results were in agreement with the lipidation and vesicle tethering observations (**Figure 4.25 A-F** and **Figure 4.26**, grey solid lines). LC3A and LC3B were unable to induce lipid mixing. GABARAPL1 was the fastest and most effective inducer of inter-vesicular lipid mixing, followed by GABARAP (**Figure 4.26**, -E3 panel). Although LC3C lipidation levels were similar to those of GABARAPL1 (**Figure 4.30A**, grey bars), its effect on lipid mixing was low, and similar to that of GABARAPL2 (**Figure 4.30C**, grey bars).

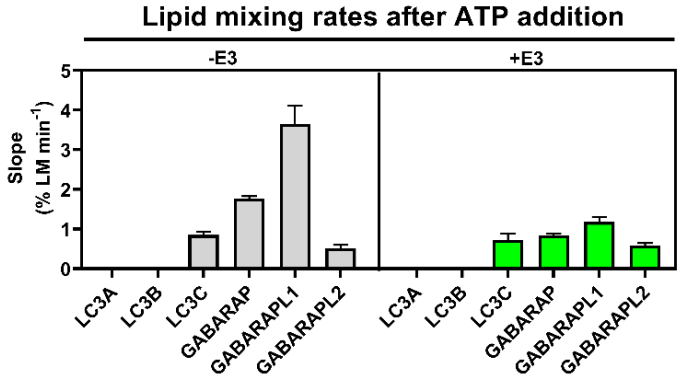

Figure 4.26. Lipid mixing rates after ATP addition. Experiments performed in the absence (left) or in the presence (right) of E3 complex. LC3A or LC3B did not cause any measurable activity. Data are means ± SD (n = 3).

The four LC3/GABARAP proteins that induced a measurable extent of lipid mixing (LC3C, GABARAP, GABARAPL1, GABARAPL2), showed a lag phase before activity started, pointing again to a required threshold of protein lipidation before lipid mixing became detectable (**Figure 4.27**, -E3 panel). There also seemed to be a negative correlation between rate (maximum slope) and lag time (**Figure 4.26 and Figure 4.27**, -E3 panel).

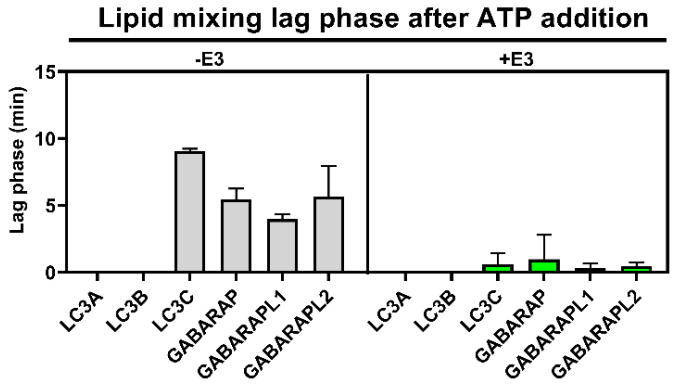

Figure 4.27. Lag phase of lipid mixing activity after ATP addition. Experiments performed in the absence (left) or in the presence (right) of E3 complex. Data are means ± SD (n = 3).

Moreover, the 'lipid mixing/lipidation ratio' revealed a clear difference between the two subfamilies (**Figure 4.28**, -E3 panel), as previously observed for vesicle tethering (**Figure 4.24**, -E3 panel). This could indicate, again, that the lipidation threshold would be lower for the GABARAP-subfamily members.

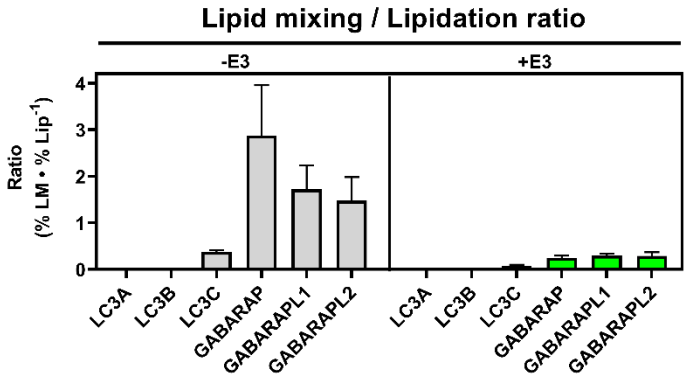

Figure 4.28. Lipid mixing / lipidation ratio. Final lipid mixing levels caused by lipidated LC3/GABARAP proteins related to the percent lipidated protein present, in the absence (left) or in the presence (right) of E3 complex. Data are means ± SD (n = 3).

However, at variance with the lipidation and tethering observations, E3 complex did not increase the LC3/GABARAP protein capacity to promote lipid mixing (**Figure 4.25A-F** and **Figure 4.26**). **Figure 4.29** summarizes the above results. The curves have been normalized as in Figure 4.22. **Figure 4.30** compares the effects of E3 on each protein. In all cases, the variation of tethering and lipid mixing once ATP is added is shown. In this way, the initial E3 effect is compensated and a comparison of each LC3/GABARAP protein effect in the presence and in the absence of E3 is more easily achieved. In the case of LC3A and LC3B, the amount of protein that was able to cause vesicle tethering in the presence of E3 did not induce lipid mixing. For LC3C, the fast and extensive tethering observed in presence of E3 did not imply a comparable degree of lipid mixing. GABARAPL2 exhibited a similar behavior in the presence and absence of E3. For GABARAP and GABARAPL1 both the extents and rates of lipid mixing were decreased in the presence of E3.

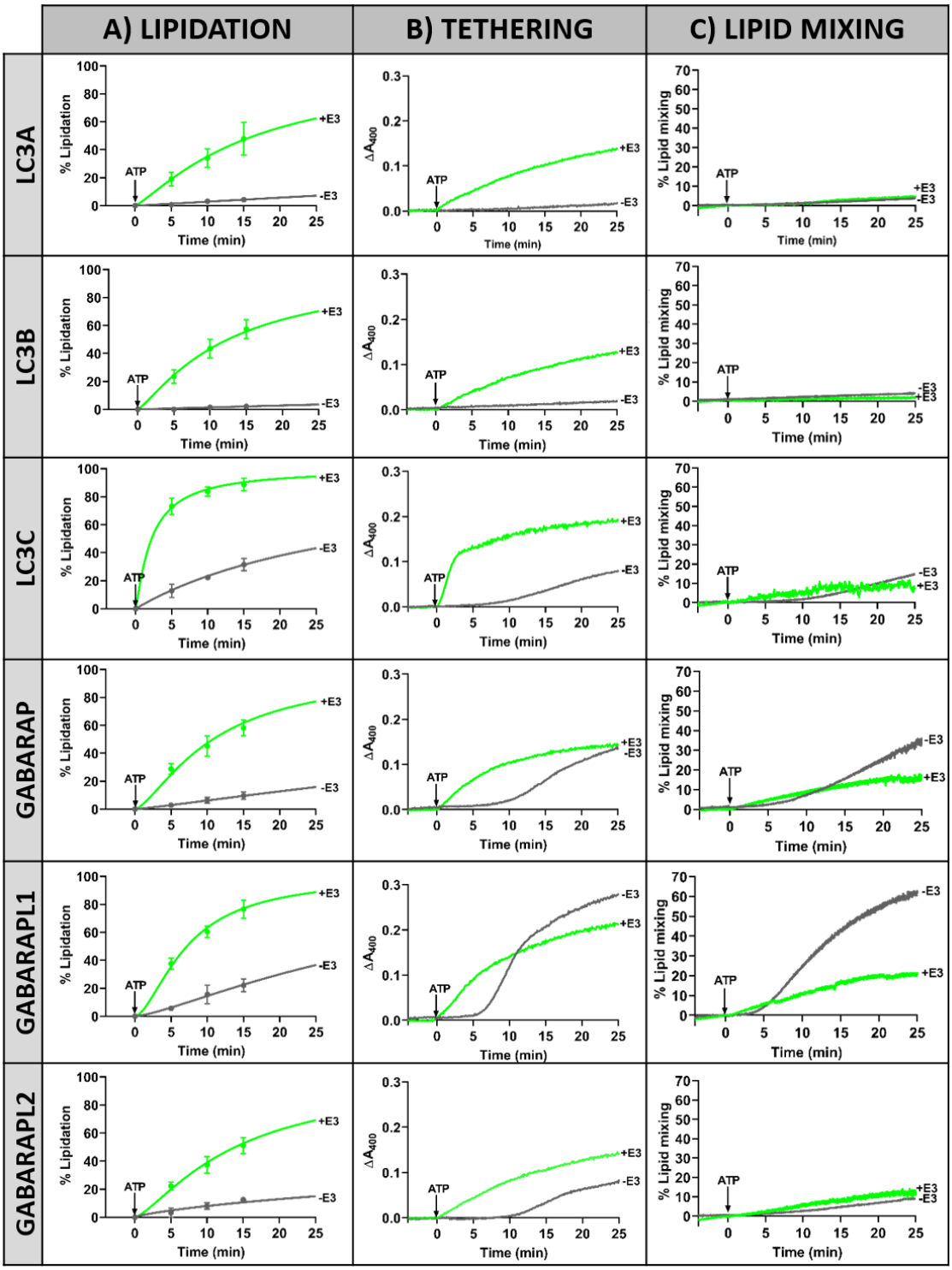

Figure 4.29. Comparative summary of LC3/GABARAP-protein lipidation, tethering and lipid mixing time courses in the absence and presence of E3 complex. Data from Figure 4.13, Figure 4.19 and Figure 4.25 were redrawn in order to allow an easier comparison of the results in this study. **(A)** Lipidation time courses of LC3/GABARAP proteins after ATP addition in the absence (grey) and in the presence (green) of E3 complex. **(B)** Tethering time courses of each LC3/GABARAP-family member after ATP addition in the absence (grey) and in the presence (green) of E3 complex. **(C)** Lipid mixing kinetics of LC3/GABARAP proteins after ATP addition in the absence (grey) and in the presence (green) of E3 complex.

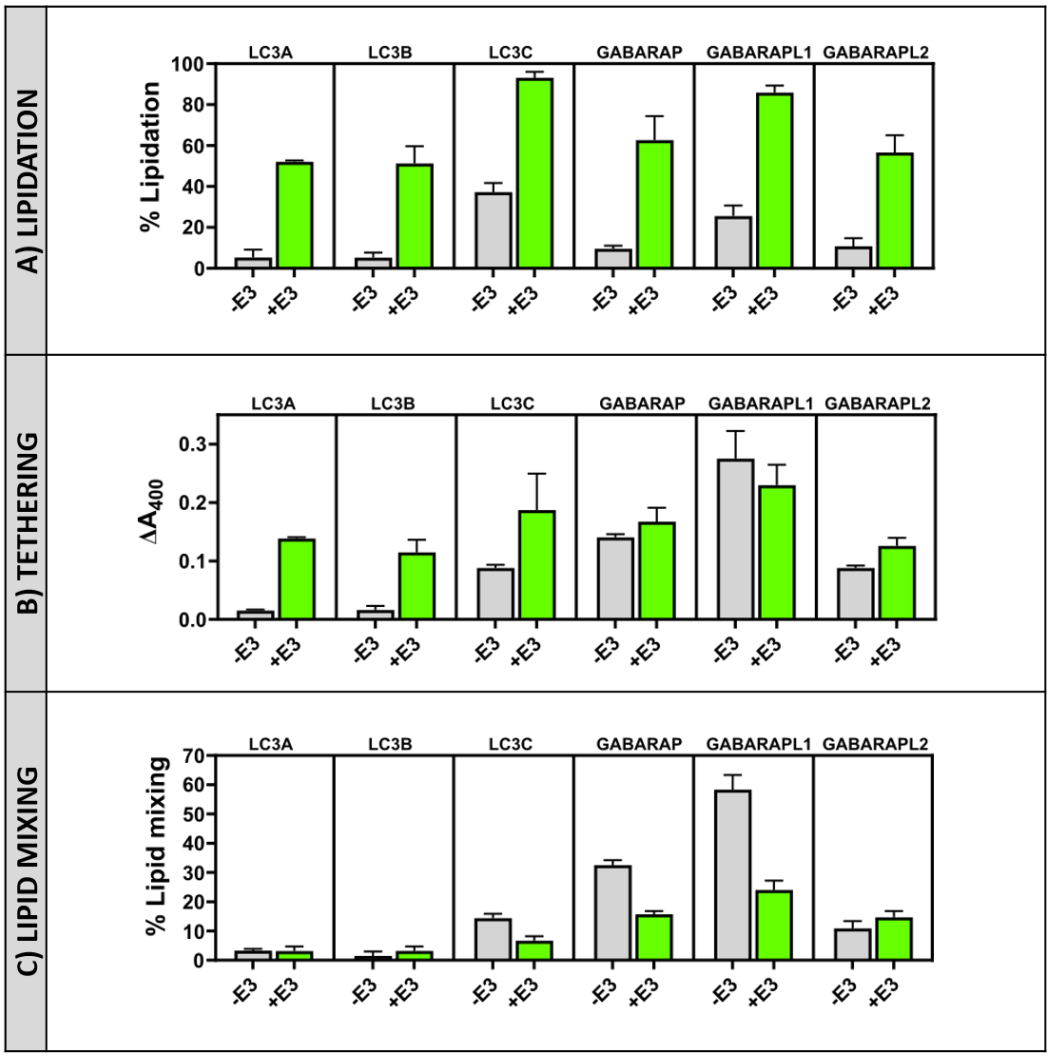

Figure 4.30. Effect of E3 complex on LC3/GABARAP-protein lipidation and the subsequent vesicle tethering and lipid mixing 25 min after ATP addition. (A) Final lipidation levels in the absence (grey) and presence (green) of E3 complex. **(B)** Extent of vesicle tethering induced by LC3/GABARAP proteins in the absence (grey) and presence (green) of E3 complex. **(C)** Extent of lipid mixing induced by LC3/GABARAP proteins in the absence (grey) and presence (green) of E3 complex. Data are means ± SD (n = 3).

These results indicate that the presence of E3, which enhanced protein lipidation and vesicle tethering, reduced, by contrast, vesicle lipid mixing.

4.3.8. GABARAP and GABARAPL1 cause membrane hemifusion but are poor inducers of vesicle-vesicle fusion.

The demonstration of vesicle-vesicle fusion requires the independent observation of vesicle tethering, total lipid mixing, inner-monolayer lipid mixing, and, in the absence of leakage, mixing of inter-vesicular aqueous contents (Landajuela *et al.*, 2016; Nieva *et al.*, 1989). Since GABARAP and GABARAPL1 were the proteins showing a higher ability to induce total lipid mixing (**Figure 4.31**), their capacity to induce lipid mixing of the vesicle inner monolayers was explored, to determine whether the observed process was one of membrane hemifusion or of full fusion. The results indicated that, even if some inner lipid monolayer mixing occurred (**Figure 4.31**), the extent reached remained well below the 50% of the total lipid mixing required for an extensive fusion event.

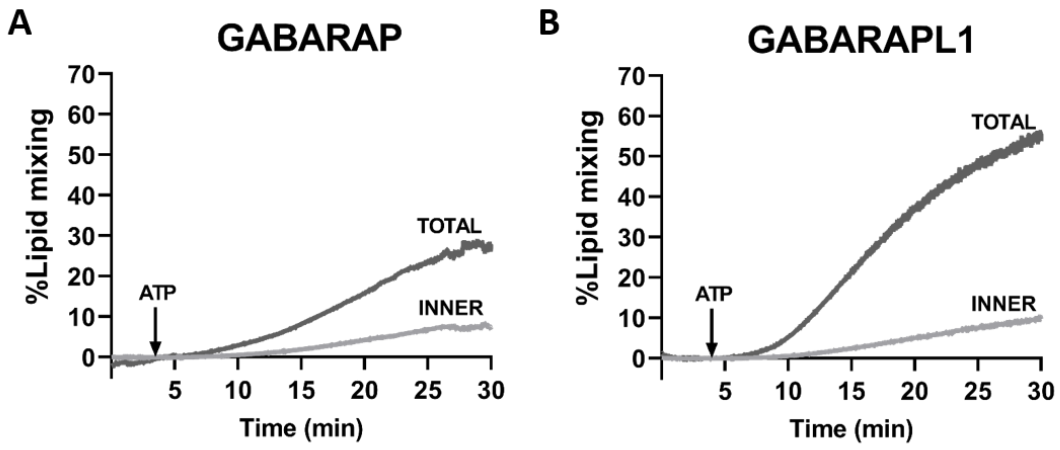

Figure 4.31. GABARAPL1 and GABARAP cause membrane hemifusion but are poor inducers of vesicle-vesicle fusion. (A-B) Representative curves of total (grey) and inner (light grey) lipid mixing activities by lipidated GABARAP (A) and GABARAPL1 (B) in the absence of the E3 complex, monitored with the NBD-PE/Rho-PE lipid dilution assay. For inner monolayer lipid mixing NBD/Rho-liposomes were pretreated with the appropriate amounts of sodium dithionite to quench NBD fluorescence of the outer leaflet. 0.4 mM of unlabeled and (NBD-PE + Rho-PE)-labeled liposomes (9:1) were mixed with 0.5 µM ATG7, 1 µM ATG3, and 5 µM of the pertinent LC3/GABARAP-family member. After 4 min incubation, ATP was added.

To confirm these results, we next measured the ability of GABARAP and GABARAPL1 to promote vesicle fusion using an aqueous contents mixing assay. A preliminary check had to be performed to determine whether, once lipidated, LC3/GABARAP proteins induced the release of vesicular aqueous contents (leakage) or not (**Figure 4.32**). No leakage was observed under our conditions, neither in the presence nor in the absence of E3, therefore the aqueous contents mixing assay could be performed, providing meaningful results.

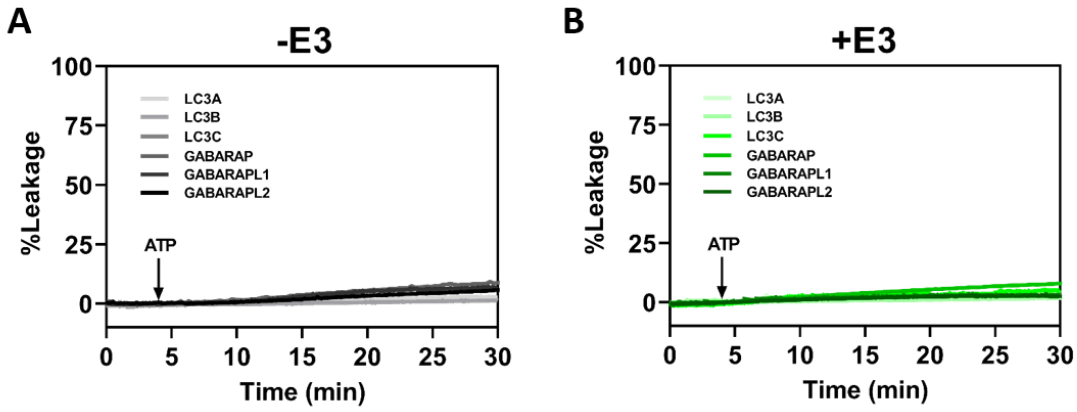

Figure 4.32. Lipidated LC3/GABARAP proteins did not induce vesicle permeabilization neither in the absence nor in the presence of E3 complex. Membrane vesicle content leakage analysis induced by lipidated LC3/GABARAP proteins in the absence and presence of the E3 complex was monitored by the ANTS/DPX leakage assay. 0.4 mM LUV containing co-encapsulated ANTS and DPX were mixed with 0.5 µM ATG7, 1 µM ATG3, and 5 µM of the pertinent LC3/GABARAP-family member and ATP was added after 4 min. 100% leakage signal was obtained by adding Triton X-100. Contents leakage in the absence **(A)** or in the presence **(B)** of E3 complex.

As expected from the low levels of inner-monolayer lipid mixing, a low capacity of GABARAP or GABARAPL1 to produce aqueous contents mixing was recorded **(Figure 4.33)**. Furthermore, in accordance with the E3 effect on GABARAP and GABARAPL1 lipid mixing ability, the small amount of aqueous contents mixing was totally abolished when E3 was present **(Figure. 4.33)**

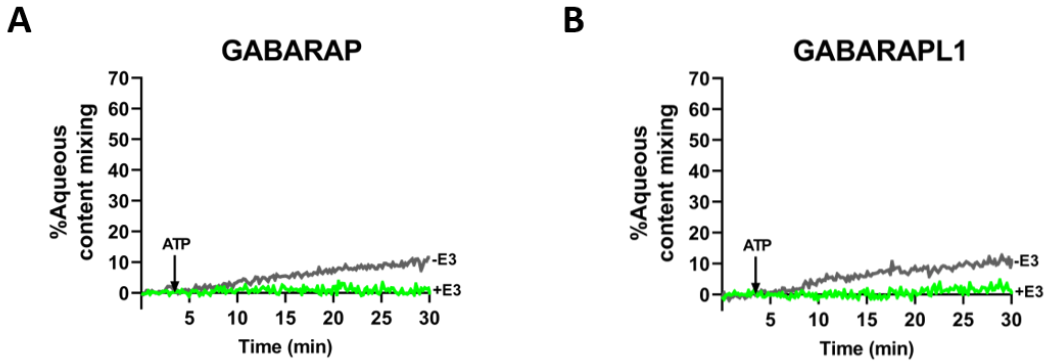

Figure 4.33. E3 further decreases the low aqueous content mixing activity of GABARAP and GABARAPL1. Representative curves of aqueous content mixing activities induced by lipidated GABARAP **(A)** and GABARAPL1 **(B)** in the absence (-E3, grey) and presence (+E3, green) of the E3 complex was monitored by the ANTS/DPX mixing assay. 0.4 mM ANTS and DPX liposomes (1:1) were mixed with 0.5 µM ATG7, 1 µM ATG3, and 5 µM of the pertinent LC3/GABARAP-family member, ATP was added after 4 min. 100% mixing was determined using LUV containing co-encapsulated ANTS and DPX.

Thus, the overall results obtained suggest a mode of action of lipidated GABARAP and GABARAPL1 in the absence of E3 compatible with a large fraction of the vesicles undergoing close apposition, or hemifusion, and a minor fraction carrying out full fusion.

4.4. Discussion

Advantages and downsides of the enzymatic and the chemical approaches

In vitro reconstitution systems allow a higher control of the experimental conditions compared to cellular approaches. Independent roles of the different components, sometimes hidden due to the complexity of the cellular context, can be revealed by simplified model systems (Brier *et al.*, 2016). In this chapter, three approaches of increasing complexity have been used to achieve the *in vitro* reconstitution of LC3/GABARAP lipidation. Each one showed advantages and disadvantages.

Structurally, the chemical linkage differs from the native coupling in the addition of the maleimide ring; however, these maleimide-anchored conjugates have been reported to be functionally active and are generally considered as useful mimetic analogs to the naturally coupled proteins (Ballesteros *et al.*, 2022; Landajuela *et al.*, 2016). Therefore, when studying the function of LC3/GABARAP–PE, the chemical approach (**Figure 4.3**) could have been useful if similar lipidation levels had been obtained with the different family members, but this was not the case. (**Figure 4.4**). There could be two possible explanations (1) each protein shows for different intrinsic affinities for membranes (as showed in Chapter 3) or (2) the Cys C-terminal exposure of each protein to the medium is different. Recent results by Maruyama *et al.* indicate that the chemically modified PEmal actually changes the bilayer curvature in a different way than native PE. This would constitute an additional caveat for the studies based on the chemical method of Atg8 lipidation (Maruyama *et al.*,2021).

Enzymatic approaches (**Figure 4.5 and 4.10**) add more complexity to the system, but they are closer to the *in vivo* situation. For that reason, the differences found between homologs using the enzymatic approach in the absence of E3 (**Figure 4.6)** were of interest, as they could be related to the different interaction between them and ATG7 or ATG3. Therefore, that situation could be more representative of the *in vivo* process. This observation was supported by the fact that in the presence of E3 (**Figure 4.11)**, although considerably decreased, those tendencies were maintained.

Differences in LC3/GABARAP-protein activities suggest the existence of a lipidation threshold, lower for the GABARAP subfamily.

Our lipidation results pointed to two relevant observations, one was that, under otherwise similar conditions, E3-independent lipidation appeared to differ for each subfamily (**Figure 4.6 and 4.13**). GABARAP-subfamily members were the most easily lipidated homologs. In turn, LC3A and LC3B reached low lipidation levels, but LC3C was the exception to the rule, see below (**Figure 4.14 and 4.15**, -E3 panel). These results agree with those by Lystad *et al.* (2019), who showed that E3 was essential for LC3B lipidation, while the GABARAP subfamily was less E3-dependent, since it could be lipidated in the absence of E3 in liposomes under certain conditions. However, the inclusion of six family members in our study revealed that E3 effects did not strictly depend on the subfamilies. In particular, while LC3A behaved similarly to LC3B, LC3C could be lipidated to a large extent in the absence of E3 (**Figure 4.13C and 4.14**), thus parting with the rest of the

LC3 subfamily. LC3C equally failed to follow the general trends of the LC3 subfamily in previous studies on cardiolipin-mediated mitophagy (Iriondo *et al*., 2022)(Chapter 3).

The second observation worthy of comment is the existence of a lag phase in the absence of E3 (**Figure 4.21 and Figure 4.27**, -E3 panel), suggesting the need to reach a lipidation threshold before proceeding to deeper levels of interaction with the host lipid bilayer. The situation is reminiscent of the lag phase required by phospholipase C before inducing vesicle aggregation (Basáñez *et al.*, 1996a). This behavior could indicate that reaching a similar level of lipidation was not as important as reaching the lipidation threshold for each of the proteins. Taking into account that the growing edge of the phagophore should be a narrow area, with a high concentration of lipids with negative curvature but leaving little space for proteins, a protein that could induce membrane fusion with the minimum number of molecules per area would be needed. The tethering/lipidation or lipid mixing/lipidation ratios (**Figure 4.22 and Figure 4.28**, -E3 panel) pointed to a lower lipidation threshold for all the GABARAP proteins as compared to the LC3 subfamily, suggesting that members of the GABARAP subfamily would be excellent candidates to perform this function.

E3 increases and accelerates vesicle tethering by LC3/GABARAP proteins but hampers their ability to induce lipid mixing.

The interaction of E3 with membranes of different composition and curvature has been recently described, showing that ATG16L1 is the main protein responsible for E3 interaction with membranes, both in human (Dudley *et al.*, 2019; Lystad *et al.*, 2019) and yeast proteins (Popelka *et al.*, 2021). However, these studies did not consider the effect of E3 on vesicle tethering, detected in yeast by Romanov *et al.* (2012). Under our experimental conditions, with lower protein concentration and smaller curvature, E3 caused no aggregation on its own (**Figure 4.16**). However, the presence of ATG3 elicited membrane tethering, albeit to a low extent. (**Figure 4.17**). This positive effect could be explained by the well-known interaction between ATG12 and ATG3 (Metlagel *et al.*, 2013; Ye *et al.*, 2021; Zheng *et al.*, 2019). Such interaction could increase E3 affinity towards the membrane (**Figure 4.18**), thus the activation of E3-dependent tethering activity. This effect could also be a combination of both proteins, as an ATG3-dependent tethering activity sensitive to lipid composition was already shown (Hervás *et al.*, 2017). The E3-promoted conformational changes in ATG3 (Popelka & Klionsky, 2021) could also activate its tethering activity and make ATG3 act in combination with E3, however further studies would be needed to understand this behavior. In any case, this initial aggregation of vesicles could be partially responsible for the faster lipidation and tethering effects seen once ATP was added (**Figure 4.19**).

Including E3 in our *in vitro* system was aimed at getting the six members of the family lipidated to >50% and to about the same extent in all cases. This made possible the comparison of LC3/GABARAP proteins, at similar levels of lipidation, in their ability to induce tethering and fusion of membranes. Such lipidation levels were achieved with low amounts of E3 (0.1μM). The presence of E3 accelerated and increased lipidation, reaching levels of at least 70% in 30 min under our conditions (**Figure 4.14**, +E3 panel). Note that, when E3-enhanced lipidation rates are compared, LC3C and GABARAPL1

continue to be the fastest ones in being lipidated (**Figure 4.15**, +E3 panel), just as they were in the absence of E3.

When E3 was present, lipidation levels of LC3/GABARAP proteins were also related to their tethering ability. Their increased lipidation allowed the participation of any of the LC3/GABARAP members in aggregation events (**Figure 4.19**). The absence of a lag phase when E3 was present (**Figure 4.20**) suggested that under those conditions all the proteins were able to reach their lipidation threshold earlier. E3 interaction with membranes and the subsequent vesicle aggregation (**Figure 4.16**), together with the positive effect of ATG3, could explain the acceleration. Moreover, comparing the lipidated LC3/GABARAP-protein tethering activities and relating them to the protein lipidation levels reached during those experiments, no differences among the different family members were observed when E3 was present (**Figure 4.21**). Thus, E3 could equalize the various LC3/GABARAP-family members in their capacities to cause membrane tethering. However, E3 had not the same effect on all proteins when it came to inducing inter-vesicular lipid mixing. E3 clearly lowered the lipid mixing activity of the two proteins, GABARAP and particularly GABARAPL1, which were most active in this respect (**Figure 4.25D, E**). The outstanding questions are why E3 decreases their ability to produce inter-vesicular lipid mixing, and why proteins with similar lipidation levels induce similar tethering but different levels of inter-vesicular lipid mixing. Further experiments regarding this topic will be discussed in Chapter 5.

The role of GABARAP and GABARAPL1 in the phagophore expansion process: an evolutionary discussion.

LC3/GABARAP proteins play different roles in autophagy. Their binding to autophagic receptors containing LIR motifs (Johansen & Lamark, 2020) is well known. Moreover, the LC3/GABARAP-protein family is deemed very important in phagophore expansion (Weidberg *et al.*, 2010). Studies with knockouts of all six members of the family found that the autophagy mechanism could work in the absence of LC3/GABARAP proteins, although autophagosomes were formed at a much slower rate, they were smaller, and often had trouble fusing with lysosomes (Nguyen *et al.* 2016b). This points to an important, if not essential, role of LC3/GABARAP family in phagophore expansion.

Under our conditions GABARAP and GABARAPL1 were the LC3/GABARAP-family members promoting the most extensive vesicle tethering (**Figure 4.19D, E**) and inter-vesicular lipid mixing (**Figure 4.25D, E**). For these two proteins lipid mixing included some degree of inner monolayer mixing (**Figure 4.31**) and a low amount of aqueous content mixing (**Figure 4.33**). The scenario is one of vesicle hemifusion with occasional fusion events. A more extensive fusion would require the localized presence (perhaps in nanodomains) of lipids with an intrinsic negative lipid curvature such as diacilgycerol or cardiolipin (Iriondo *et al.*, 2021; Landajuela *et al.*, 2016) or the action of additional proteins in the growing areas of the phagophore. Moreover, in order to make phagophore expansion possible, the recently described lipid transfer ability of the protein ATG2, suggests that this protein could work in conjunction with the LC3/GABARAP mediated fusion of vesicles (Sawa-Makarska *et al.*, 2020).

In general, the above results show that the GABARAP subfamily is clearly more active than its LC3 homologs in the induction of membrane fusion. Since Atg8 in yeast has the ability to cause vesicle hemifusion (Nakatogawa *et al.*, 2007), LC3s appear to have lost this function during evolution. This is consistent with GABARAPs being more evolutionarily related to Atg8 than LC3. The LC3 subfamily may have become more specialized in the recognition of autophagic receptors and adapters (Johansen & Lamark, 2020), losing functions related to vesicle-fusion induction in the process. This hypothesis is consistent with the study performed with the Atg8 orthologs in *C. elegans* LGG-1 and LGG-2 (Wu *et al.*, 2015). Those authors found that the LGG-1 homolog, more similar to GABARAP, had the ability to tether and fuse vesicles, while LGG-2 (more similar to LC3) had only a limited capacity to induce tethering and none to fuse vesicles.

The hypothesis of the LC3 loss of fusogenic function along evolution can also help understand the results obtained in different studies with knockouts of the entire human LC3/GABARAP family. In the latter, expressing GABARAP in ATG8-depleted cells leads to the recovery of autophagy, while LC3 expression does not (Nguyen *et al*., 2016b), and the expression of LC3s can actually have a negative effect on autophagy (Grunwald *et al.*, 2020). It is possible that LC3, lacking the vesicle fusion activity, cannot replace the absence of GABARAP, while the latter, possessing a fusogenic activity and with the ability to recognize LIR sequences, can almost fully replace the LC3 functions. LC3C is an exception to this model but as this homolog is evolutionarily more distant (Jatana *et al.*, 2020) it could follow a different regulation pattern.

Concluding remarks.

Assaying protein lipidation, vesicle tethering and inter-vesicular lipid mixing activities of all members of the LC3/GABARAP family under the same experimental conditions allows a number of conclusions to be drawn. (i) While the large differences between GABARAPL1/GABARAP and LC3A/LC3B resemble the ‘canonical’ differences between the two subfamilies shown in other studies, LC3C appears as an unusual case within the LC3 subfamily, with a tethering activity akin to the one of the GABARAP subfamily. (ii) GABARAP and GABARAPL1 appear to be the most efficient homologs in the entire family for vesicle tethering and lipid mixing. However, as they are able to produce but a low level of full fusion, other proteins or the presence of other lipids that promote fusion could be needed in the *in vivo* situation. (iii) The results suggest a model in which the growing regions of the phagophore would be areas possessing a high curvature and/or with high levels of PE, compatible with points of membrane fusion. In those regions, some of the LC3/GABARAP proteins could be lipidated without E3, or in the case that E3 helped lipidation, a regulation should exist to allow fusion of vesicles in those regions in order to permit phagophore expansion. (iv) The fact that LC3A or LC3B showed more difficulties to be lipidated even in the presence of E3 points to other functions for these homologs during autophagy, such as cargo receptors, in accordance to results obtained in Chapter 3.

CHAPTER 5

A PROTEIN COAT INCLUDING GABARAPL1 AND E3 COMPLEX IS FORMED ON THE SURFACE OF VESICLES DURING LIPIDATION

CHAPTER 5. A protein coat including GABARAPL1 and E3 complex is formed on the surface of vesicles during lipidation

5.1. Introduction

GABARAPL1 or GABARAP-like protein 1 shares a high identity with GABARAP and was first described to play a role in intracellular $GABA_A$ receptor trafficking (Mansuy *et al.*, 2004), which would explain its high expression in brain (Le Grand *et al.*, 2013). In 2010, Chakrama *et al.* demonstrated that this protein was associated with autophagic vesicles (Chakrama *et al.*, 2010), and it was also shown that cells with decreased expression levels of GABARAPL1 had a reduced autophagy flux and lower levels of lysosomes (Boyer-Guittaut *et al.*, 2014). GABARAPL1 has been shown to be the LC3/GABARAP-subfamily member promoting the most extensive tethering and lipid mixing of vesicles (Iriondo *et al.*, in preparation, Chapter 4). A lipidation threshold for LC3/GABARAP-protein family to start their activities has been suggested. E3 complex presence promoted a faster lipidation, however, this not led to higher activities of GABARAPL1, on the contrary, it caused a decrease in its lipid mixing ability (Iriondo *et al.*, in preparation, Chapter 4).Therefore, the outstanding question was why E3 decreases GABARAPL1 ability to induce inter-vesicular lipid mixing.

Apart from growing in size, the phagophore membrane should bend while growing to allow the engulfment of the material to be degraded. Thus, a membrane shaping system is needed during AP biogenesis (Nakatogawa, 2020). Different mechanisms have been suggested for this process, involving physical properties of lipid bilayers (Knorr *et al.*, 2012), membrane curvature generators or sensors (Nguyen *et al.*, 2017), or actin (Mi *et al.*, 2015), among others. In this context, Kaufmann *et al.* (2014) observed that, once the yeast Atg8 had been lipidated, it was able to associate with E3 thanks to an Atg8-interacting motif (AIM) in Atg12, and to become organized into a membrane scaffold with the help of Atg16 (**Figure 5.1A**). They suggested that E3 complex-Atg8–PE assemblies affected the shaping of the phagophore. This is in agreement with the fact that in yeast, the E3 complex had been detected on the convex face (the outer part) of the growing phagophore, together with Atg8, while in the concave face (facing the cargo) only some Atg8–PE remained (Abdollahzadeh *et al.*, 2017; Mizushima *et al.*, 2001; Xie *et al.*, 2008) (**Figure 5.1B**).

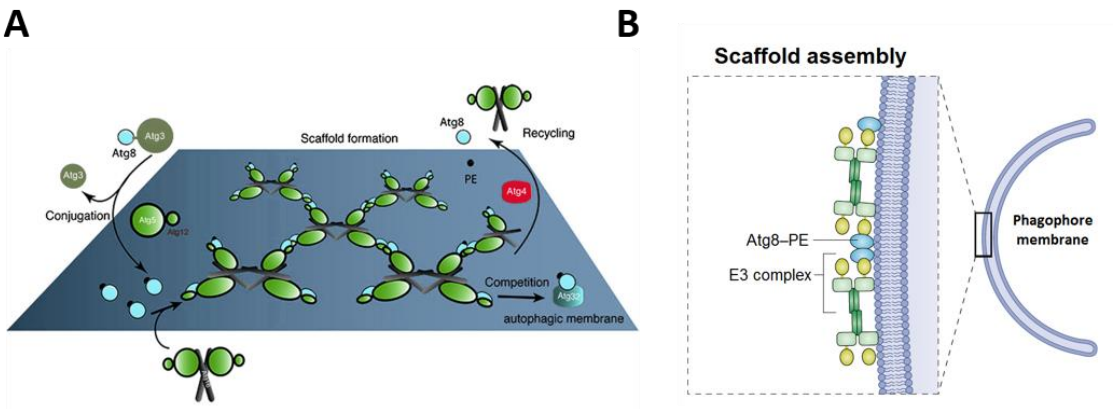

Figure 5.1. The autophagic membrane scaffold formed by E3 and Atg8–PE in yeast. **(A)** Model proposed by Kaufmann *et al.*, (2014). **(B)** Formation of a membrane scaffold by E3 in association with lipidated Atg8–PE on the convex surface of the phagophore may help its bending. Taken from Nakatogawa (2020).

Some differences in the structure (**Figure 5.2**) and mechanism of action between the yeast and mammalian E3 complex can be found (Gammoh, 2020; Martens & Fracchiolla, 2020). In yeast, the Atg16 subunit is not required for the *in vitro* E3 activity (Hanada *et al.*, 2007; Romanov *et al.*, 2012). However, ATG16L1 appears to be important for the mammalian system (Fracchiolla *et al.*, 2020; Lystad *et al.*, 2019). In yeast, the E3 interaction with membranes was shown to be mediated by Atg5 subunit (Romanov *et al.*, 2012), however in mammalians the main determinant for its membrane recruitment is the ATG16L1 subunit (Dudley *et al.*, 2019; Lystad *et al.*, 2019). A similar scaffold formation with human proteins could explain why GABARAPL1 had a lower lipid mixing ability when E3 was present. Therefore, the study of the potential formation of a membrane scaffold with human proteins will be of interest.

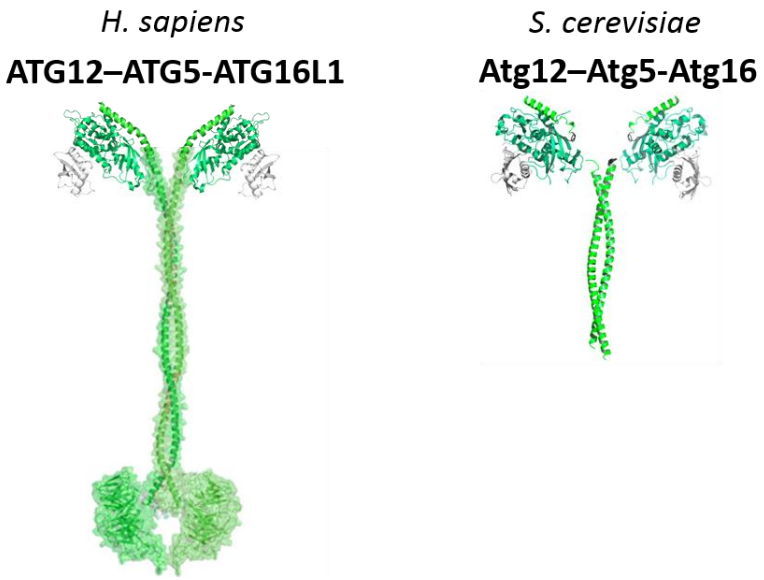

Figure 5.2. Comparison between human and yeast E3 complex. Model of human E3 adapted from Wilson *et al.*, (2014) and model of yeast E3 adapted from Fujioka *et al.*, (2010). Atg12/ATG12 (grey), Atg5/ATG5 (green) and Atg16/ATG16L1 (light green).

In the present chapter, previous results with GABARAPL1 in the absence of E3 were reviewed and confirmed by Cryo-EM, and some experiments were performed to study the GABARAPL1 oligomeric state when the protein is lipidated. Then, the results obtained in the presence of E3 were confirmed by Cryo-EM, and the reason why E3 had an inhibitory effect on LC3/GABARAP lipid mixing ability was explored. With this aim, the effect of different concentrations of E3 on lipid mixing, the localization of the ULB-system proteins during conjugation, together with the potential interaction between GABARAPL1 and E3 complex were studied. Moreover, using a GUV reconstitution system, the colocalization of GABARAPL1 and E3 in the membrane upon ATP addition was assessed, and AFM experiments suggested the possible formation of a protein coat (reminiscent of the yeast scaffold) on the vesicle surface.

5.2. Materials and methods

5.2.1. Materials

L-α-phosphatidylcholine from hen egg yolk (ePC, 840051), 1,2-dioleoyl-sn-glycero-3-phosphatidylethanolamine (DOPE, 850725), liver phosphatidylinositol (PI, 840042), egg dioleoylglycerol (DOG, 800811) 1,2-dioleoyl-sn-glycero-3-phosphoethanolamine-N-[4-(p-maleimidomethyl)cyclohexane-carboxamide] (PEmal, 780201) and 1,2-dioleoyl-sn-glycero-3-phosphatidylethanolamine-N-lissamine rhodamine B sulfonyl (Rho-PE, 810150) were purchased from Avanti Polar Lipids, Inc. (Alabaster, AL). Alexa Fluor™ 633 carboxylic acid, succinimidyl ester (A20005) and N-(7-nitrobenz-2-oxa-1,3-diazol-4-yl)-1,2-dihexadecanoyl-sn-glycero-3-phosphatidylethanolamine (NBD-PE, N360) were purchased from Thermo Fisher Scientific (Waltham, MA).

5.2.2. Protein expression and purification

GABARAPL1, mATG7, ATG3, E3 complex (without and with GFP) were purified as described in Materials and Methods section in Chapter 4.

GST and GST-LC3/GABARAP proteins were purified (**Protocol 3**) from soluble fractions of bacterial extracts obtained in the absence of detergents, and they were >90% pure as evaluated by Coomassie Brilliant Blue-stained SDS-PAGE. *E. coli* BL21 (λDE3) cells were transformed with the appropriate plasmids. They were grown to A_{600}= 0.8 and protein expression was induced with 0.5 mM IPTG for 16 h at 20°C. Following centrifugation at 4,500 x g for 15 min, the pellet was resuspended and sonicated in Breaking buffer (PBS 1x, 20 mM Tris-HCl pH 7, 150 mM NaCl, 1mM DTT supplemented with lysozyme, protease inhibitors and DNase) (See also **Table 2.4**). After removal of cellular debris by centrifugation at 30,000 x g for 30 min at 4°C, the sample supernatant was incubated with 1 ml Glutathione Sepharose 4B (GE Healthcare, 17-0756-01) for 3 h at 4°C to bind GST-tagged proteins. After two washing steps, GST and GST-LC3/GABARAP proteins were incubated for 1h at RT with GST-protein elution Buffer (50 mM Hepes pH 7.5, 300mM NaCl, 1mM DTT, 20mM Gluthatione red) and then 4 fractions of 4 ml were eluted. They were concentrated to 500 µl using Amicon Ultra-4 (4 mL, 3 kDa cut-off) (Millipore, UFC800324), and loaded onto a Superdex-75 10/300 GL size exclusion column (GE Healthcare, GE17-5174-01) equilibrated in Buffer SEC (25mM Hepes pH 7.5, 150mM NaCl, 1mM DTT). Proteins were distributed in aliquots, flash-frozen and stored at -80°C until further use.

GFP was purified (**Protocol 4**) from soluble fractions of bacterial extracts obtained in the absence of detergents, and it was >90% pure as evaluated by Coomassie Brilliant Blue-stained SDS-PAGE. E. coli BL21 (λDE3) cells were transformed with the appropriate plasmids. They were grown to A_{600}= 0.8 and protein expression was induced with 0.5 mM IPTG for 16 h at 20°C. Following centrifugation at 4,500 x g for 15 min, the pellet was resuspended and sonicated in Breaking buffer (50 mM Hepes pH 7.5, 300 mM NaCl, 1mM TCEP supplemented with lysozyme, protease inhibitors and DNase). After removal of cellular debris by centrifugation at 30,000 x g for 30 min at 4°C, the sample supernatant was applied to a 5-ml nickel-nitrilotriacetic acid (Ni-NTA) column (GE Healthcare) and

eluted via a stepwise imidazole gradient (50, 75, 100, 150, 200, and 300 mM). Protein eluted in fractions containing 300 mM imidazole. These fractions were pooled, concentrated, applied onto a Superdex 75 10/300 GL (GE Healthcare), and eluted in a buffer containing 25 mM Hepes, pH 7.5, 150 mM NaCl, and 1 mM DTT. Fractions containing pure GFP were pooled, concentrated, flash-frozen in liquid nitrogen, and stored at −80°C.

5.2.3. Preparation of LUV and SUV

The appropriate lipids were mixed in organic solution and the solvent was evaporated to dryness under a N_2 stream. Then the sample was kept under vacuum for 1 h to remove solvent traces. The lipids were swollen in Assay Buffer in order to obtain multilamellar vesicles (MLV). Large unilamellar vesicles (LUV) were produced from MLV according to the extrusion method described by Mayer *et al.* (1986). See also **Protocol 13**. They were subjected to 10 freeze/thaw cycles, and then extruded using a LIPEX Liposome Extrusion System (Evonik Health Care, Essen, Germany) with a 0.05-µm pore size Nuclepore filters (Whatman, 110605). Small unilamellar vesicles (SUV) for supported lipid bilayer (SLB) formation were obtained by sonicating MLV with a probe tip sonicator (MSE Soniprep 150, MSE, UK) for 20 min (10 sec on, 10 sec off) on ice. See also **Section 2.6.3**. Vesicle size was checked by quasi-elastic light scattering using a Malvern Zeta-Sizer 4 spectrometer (Malvern Instruments, Malvern, UK). LUV had an average diameter of ≈80 nm and SUV average diameter was ≈50 nm. Phospholipid concentration was determined by phosphate analysis (Böttcher *et al.*, 1961) (**Protocol 11**).

5.2.4. Size exclusion chromatography assays of GABARAPL1 oligomerization

In order to assess the oligomerization state of GABARAPL1 an analytical size exclusion chromatography (SEC) was performed (**Protocol 9**). SEC was performed in an AKTA system using a Superdex 75 10/300 column from Amersham Biosciences equilibrated in System Buffer (50 mM Tris pH 7.5, 150 mM NaCl) supplemented with 0.75% (v/v) CHAPS. Proteins and liposomes were mixed and incubated for 30 min at 37ºC (See **Figure 5.5** legend for details). The sample was solubilized by adding 2% CHAPS (Landeta *et al.*, 2011) and applied to the column in a total volume of 250 µl. The column was eluted at a flow rate of 0.35 ml/min. 0.5-ml fractions were collected and analyzed by Coomassie Brilliant Blue-stained SDS-PAGE.

5.2.5. Cryo-EM sample preparation and image collection

Conjugation reactions (See **Figure 5.4, 5.7 and 5.8** legend for protein and lipid concentration details) were performed at 37°C for 90 min with continuous stirring and the reaction mixtures loaded on freshly glow-discharged 300-mesh R2/2 Quantifoil holey carbon grids (Quantifoil Micro Tools GmbH). Vitrification was performed on a LEICA GP2 automatic plunge freezer (LEICA microsystems) maintained at 8°C at a relative humidity close to saturation (90% rH). Grids were loaded with 4 µL sample solutions for 30 s,

blotted with absorbent standard filter paper, and plunged into a liquid ethane bath. The vitrified grids were removed from the plunger and stored under liquid nitrogen.
Imaging of cryo-EM samples was performed on a JEM-2200FS/CR (JEOL Europe, CIC bioGUNE, Spain) transmission electron microscope operated at 200 kV and images were recorded under low-dose conditions, with a total dose of the order of 30-40 electrons/Å^2 per exposure, at defocus values ranging from −1.5 to −4.0 µm. The in-column Omega energy filter of the microscope helps to record images with improved signal-to-noise ratio (SNR) by zero-loss filtering, using an energy selecting slit width of 20 eV centered at the zero-loss peak of the energy spectra. Digital images were recorded on a GATAN K2 summit direct detection camera 4K × 4K (5 µm pixels) (Gatan Inc., Pleasanton, CA) using Digital Micrograph (Gatan Inc.) software, at a nominal magnification of 30,000×, resulting in final sampling of 1.3 Å/pixel (See also **Protocol 21**).

5.2.6. Total Lipid mixing assay

A fluorescence resonance energy transfer (FRET) assay (**Protocol 18**) was used to monitor inter-vesicular membrane lipid mixing in the presence of different concentrations of E3 (Alonso *et al.*, 1982). The appropriate LUV containing 1.5 mol % NBD-PE and 1.5 mol % Rho-PE were mixed with a 9-fold excess of unlabeled LUV (see **Figure 5.10** legend for protein and lipid concentration details). NBD-PE emission was monitored in a Fluorolog®-3 (Horiba Jobin Yvon, Edison, NJ) spectrofluorometer with constant stirring at 37°C. NBD emission was monitored at 530 nm with the excitation wavelength set at 465 nm (slits at 4 nm). A 515 nm cut-off filter was placed between the sample and the emission monochromator to avoid scattering interference. 100% inter-vesicular membrane lipid mixing were established by adding 10 µL of 10% (v/v) Triton X-100. The extent of lipid mixing was quantified on a percentage basis according to the equation: $(F_t-F_0/F_{100}-F_0) \times 100$ where F_t is the measured NBD fluorescence of protein-treated LUV at time t, F_0 is the initial NBD fluorescence of the LUV suspension before ATP addition, and F_{100} is the NBD fluorescence value after complete disruption of LUV by addition of Triton X-100. Details for the inter-vesicular lipid mixing assay can be found in Goñi *et al*. (2003)

5.2.7. Vesicle flotation assay

Protein interaction with membranes was assessed using flotation in sucrose gradients (**Protocol 16**). All the liposome and protein concentrations used were increased (by 5-fold) with respect to the other assays, all proportions being otherwise kept, to allow detection of the E3 complex in the gels (See **Figure 5.11** and **Figure 5.12** legends for protein and lipid concentration details). Liposomes were incubated with the indicated proteins for 30 min at 37°C in System Buffer. The protein/lipid mix was adjusted to 1.4 M sucrose concentration in 300 µl and transferred to a centrifuge tube. This first (bottom) layer was overlaid with successive solutions containing 0.8 M (400 µl) and 0.5 M (300 µl) sucrose. The three-layer gradients were centrifuged in a TLA-120.2 rotor (Beckman Coulter, Brea, CA, US) at 355,040 x g for 50 min at 4°C. After centrifugation, four 250-µl fractions were collected, starting from the bottom. Proteins were detected in SDS-PAGE gels using Coomassie Brilliant Blue staining. Densitometry of the protein bands was performed using ImageJ software, and the percent liposome-bound protein was

estimated from the band intensities measured in the third + fourth fractions (floating vesicle fractions), relative to the total sum of intensities measured in all fractions.

5.2.8. Microscopy-based bead protein–protein interaction assay

For interaction between E3 (prey) and LC3/GABARAP proteins (bait) a microscopy-based bead protein-protein interaction assay was used (**Protocol 10**). A mixture of 25 µl GST-tagged LC3/GABARAPs or GST at 10 µM was incubated with 25 µl Glutathione Sepharose 4B beads (GE Healthcare, 17-0756-01) at 4ºC for 30 min on a rotating wheel (final concentration: 5 µM). Then the beads were washed three times with System Buffer to remove unbound proteins. Later, 100 µl GFP or GFP-E3 at 1 µM were transferred to the observation chamber precoated with a 5 mg/ml BSA solution, and 5 µl beads were added. It was incubated at RT for 30 min without shaking. Finally, images were acquired on a Leica SP5 confocal microscope with a 63× Plan Apochromat 1.4 NA objective. The excitation and emission wavelengths used for GFP-E3 detection were 488 nm and 515 nm respectively.

5.2.9. Alexa Fluor 633 GABARAPL1 labelling

For GABARAPL1 labelling (**Protocol 8**), an Alexa Fluor™ 633 NHS Ester (A20005, Thermo Fisher) stock was prepared at 20 mM in DMSO. GABARAPL1 purified using a SEC buffer containing Hepes 25 mM, NaCl 150 mM (pH 7.5) buffer was adjusted to 25 µM, then 5 µl of the reactive dye solution Alexa 633 was slowly added to the protein solution. The reaction was incubated for 90 min at 37ºC with continuous stirring. A Sephadex G-25 chromatography column (GE Healthcare) was used to separate the conjugate from unreacted labeling reagent with buffer 25 mM Hepes, 150 mM NaCl (pH 7.5). The degree of labeling was determined measuring the absorbance of the protein-dye conjugate at 280 nm, and at 633 nm that of the dye. Labeled samples were subjected to SDS-PAGE and visualized using a VersaDoc MP 4000 Imaging System (Bio-Rad).

5.2.10. Preparation of GUV

Giant unilamellar vesicles (GUV) in solution were prepared by electroformation (Estes & Mayer, 2005) using two different surfaces.

Platinum wire method (**Protocol 14**). A lipid stock of the desired GUV composition (0.2 mM total lipid containing 0.5 mol % Rho-PE) was prepared in chloroform:diethylether:methanol (4:5:1, v/v). GUV were formed in a PRETGUV 4 chamber supplied by Industrias Técnicas ITC (Bilbao, Spain). 3 µl of the lipid stocks were added onto the surface of platinum (Pt) electrodes and solvent traces were removed by drying the chamber under high vacuum for at least 1 h. The Pt electrodes were covered with 500 µl of a 300 mM sucrose solution, previously equilibrated at 37°C. The Pt electrodes were connected to a generator (TG330 function generator, Thurlby Thandar Instruments) under AC field conditions (10 Hz, 1 VRMS for 90 min, followed by 2.5 Hz, 1 VRMS, 60 min) at 37°C. Finally, the AC field was turned off and the vesicles (in 300 mM sucrose) were collected from the PRETGUV 4 chamber. This method was used in experiments shown in **Figure 5.17** and **Figure 5.18**.

ITO method (**Protocol 15**). A lipid stock of the desired GUV composition (1 mM total lipid containing 0.5 mol % Rho-PE) was prepared in chloroform:diethylether:methanol (4:5:1, v/v). 20 µl of the stock were placed on indium tin oxide (ITO)-coated glass electrodes (10 µl on each conducting surface) and solvent traces were removed by drying the chamber under high vacuum for at least 1 h. Then, sucrose (300 mM) was added between the ITO coated glass electrodes and they were connected to a generator (TG330 function generator, Thurlby Thandar Instruments) under AC field conditions (10 Hz, 1 VRMS for 90 min) at 37 °C. Finally, the AC field was turned off and the vesicles (in 300 mM sucrose) were collected. This method was used in experiments shown in **Figure 5.19**, **Figure 5.20**, **Figure 5.21**, **Figure 5.22**, **Figure 5.23** and **Figure 5.24**.

5.2.11. *In vitro* reconstitution of GABARAPL1 lipidation on GUV

80 µl GUV (in 300 mM sucrose) were added to 8-well chambered coverslips (Ibidi, 80826) pre-treated with bovine serum albumin (BSA) (2 mg/ml) containing an equiosmolar buffer solution and the adequate protein mix (See **Figure 5.17-5.24** for details). The chamber was incubated for 30 min at 37ºC. Due to the different density of the two solutions, the vesicles sedimented at the bottom of the chamber, and this facilitated observation under the microscope. The excitation and emission wavelengths used for GFP were 458 nm and 467-538nm, for Rho- PE they were 543 nm and 578-617 nm, and for Alexa 633, 633 nm and 659-770 nm respectively. Images were acquired on a Leica SP5 confocal microscope with a 63x Water Planar Apochromat 1.2 NA objective.

5.2.12. AFM measurements

Supported lipid bilayers (SPB) were prepared by the vesicle adsorption method (Jass *et al.*, 2000). 120 µl assay buffer containing 3 mM $CaCl_2$ were added onto a previously prepared 1.2 cm^2 freshly cleaved mica substrate mounted onto a JPK coverslip-based liquid cell for atomic force microscopy (AFM) measurements (JPK Instruments, Berlin, Germany). 80 µl SUV (ePC:DOPE:PI, 70:20:10 mol ratio) were then added on top of the mica. Vesicles were left to adsorb and extend for 20 min keeping the sample temperature at 37 ºC. The non-adsorbed vesicles were discarded by washing the samples 10 times with assay buffer without $CaCl_2$, in order to remove remaining Ca^{2+} cations from the solution (See also **Protocol 22**).

Topographical images of the SLBs and proteins were taken using an UltraSpeed AFM (JPK Instruments) under QI mode AFM scanning. Two different approaches were used. The first one allowed the visualization of the final structure formed. First, the SBL was scanned, then the protein mix (see **Figure 5.25, 5.26 and 5.27** for details) was added and incubated for 20 min at 37ºC, and the resulting structure was imaged. The second approach allowed the analysis of the time course of the process as the mix was added to SLB and the scans were performed in the same zone every 5 min at room temperature.

5.3. Results

5.3.1. GABARAPL1 vesicle tethering, lipid mixing and oligomerization ability in the absence of E3

GABARAPL1 was shown to be the LC3/GABARAP family member with the highest lipid mixing ability (Chapter 4). The results obtained in the absence of E3 are summarized in **Figure 5.3.** First, GABARAPL1 is anchored to the membrane, through the ATP-dependent action of the UBL-conjugation system (**Figure 5.3A**). Its lipidation allows the GABARAPL1-promoted tethering of these vesicles (**Figure 5.3B**). In turn, this gives rise to mixing of their membrane lipids, and cause inter-vesicle hemifusion/fusion (**Figure 5.3C**). Relatively low levels of protein lipidation are needed, only 10% lipidated GABARAPL1 is required to start the tethering/lipid mixing action. Tethering and lipid mixing assay results correlate well, the inner lipid and aqueous contents mixing assays suggest that only part of the vesicles can undergo full fusion (**Figure 5.3**, bottom panels).

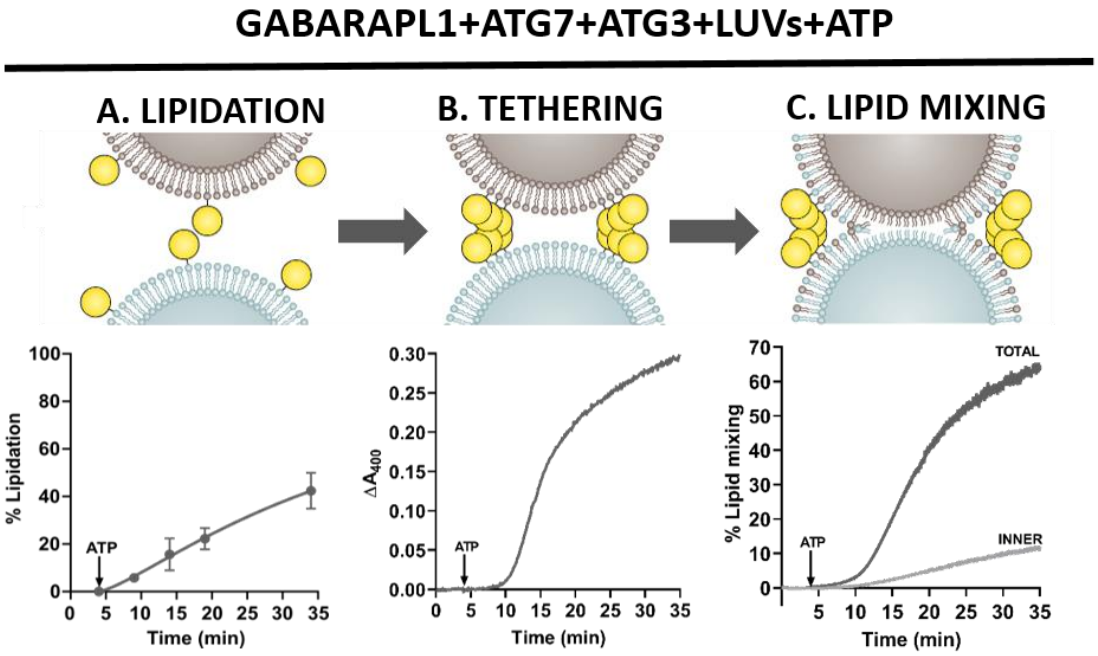

Figure 5.3. Comparative summary of GABARAPL1 lipidation, tethering and lipid mixing time courses in the absence of E3. Top: A model of Atg8 tethering and hemifusion ability, as proposed by Nakatogawa *et al.*, (2007), adapted for GABARAPL1 and based on its ability to get lipidated **(A)**, tether **(B)**, and cause lipid mixing **(C)** of vesicles. Bottom: Time courses of lipidation **(A)**, tethering **(B)**, and lipid mixing **(C)** produced when GABARAPL1, ATG7, ATG3 and ATP are mixed with PE-containing liposomes (See Chapter 4 for details).

To explore this effect in further detail, the ability of GABARAPL1 to cause vesicle tethering and fusion was also analyzed using cryo-electron microscopy (cryo-EM). We observed extensive vesicle tethering, with membrane contacts and some extended sheet-like structures, 300-400 nm long, all of them compatible with a degree of membrane fusion. **Figure 5.4** displays several examples of structures evocative of aggregation and hemifusion (triple parallel lines and inter-vesicular discontinuous lines) and fusion (sheets). Thus, cryo-EM data confirm the previous results and suggest a

mode of action of lipidated GABARAPL1 in the absence of E3, compatible with a large fraction of the vesicles undergoing close apposition, or hemifusion, and a minor fraction carrying out full fusion.

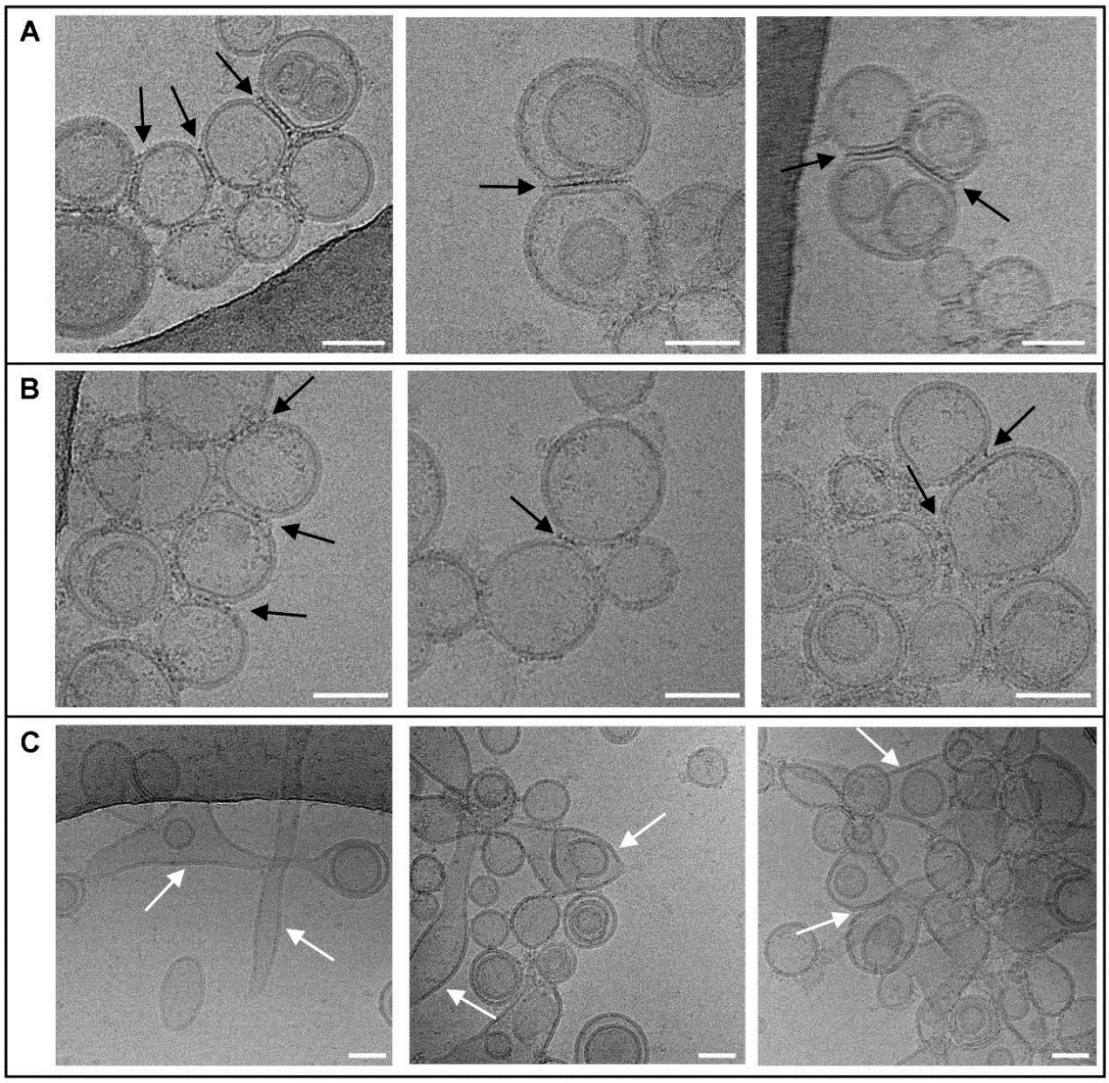

Figure 5.4. GABARAPL1 ability to tether and fuse vesicles in the absence of E3 complex, analyzed by cryo-EM. A gallery of cryo-EM images obtained under the condition "-E3, +ATP". 0.5 μM ATG7, 1 μM ATG3, and 5 μM GABARAPL1 were mixed with 0.4 mM LUV [ePC:DOPE:PI:DOG (33:55:10:2 mol)] and, after ATP addition, were incubated at 37°C for 90 min. Arrows point to the specific structures observed. **(A)** Examples of structures evocative of aggregation or hemifusion ("triple parallel lines"). **(B)** Examples of structures evocative of hemifusion (inter-vesicular discontinuous lines). **(C)** Examples of structures evocative of fusion (sheets). Bar = 50 nm.

The mechanism of autophagosome expansion proposed by Nakatogawa *et al.* (2007) for yeast Atg8 (**Figure 5.3**, top panels) was based on the hypothesis that oligomerization of Atg8s attached to different vesicles could be responsible for vesicle tethering and hemifusion. In order to test if this hypothesis could be also true for GABARAPL1, its oligomeric state was studied by size exclusion chromatography. All samples were treated with 2% (w/v) CHAPS to allow membrane solubilization. In this experimental approach using chemical (**Figure 5.5A**) and enzymatic lipidation (**Figure 5.5B**), GABARAPL1 eluted close to its calculated monomeric mass when PEmal or ATP were not present.

However, if PEmal or ATP were in the mix and the protein was able to be anchored to the membrane, a further peak corresponding to higher molecular weight fractions appeared, suggesting that GABARAPL1 could form dimeric complexes under these conditions. Therefore, this preliminary oligomerization results support the hypothesis that GABARAPL1 could interact with other GABARAPL1 molecules to promote the tethering and lipid mixing of vesicles.

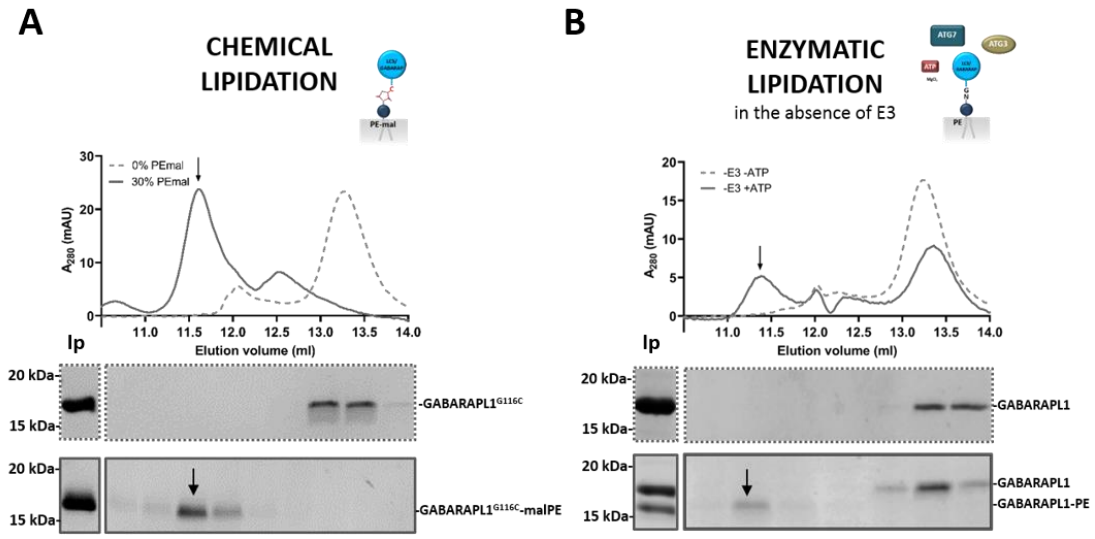

Figure 5.5. Preliminary GABARAPL1 oligomerization studies. (A) Size exclusion chromatography analysis of GABARAPL1 oligomerization using chemical lipidation. GABARAPL1^{G116C} was incubated with non PEmal-containing liposomes [ePC:DOPE:PI (35:55:10 mol)] (dashed lines) or with PEmal-containing LUV [ePC:DOPE:PEmal:PI (35:25:30:10 mol)] (solid lines) for 30 min at 37ºC. Samples were then treated with 2% CHAPS (w/v) and injected in a Superdex 75 10/300 column. Top: Elution profile of GABARAPL1^{G116C}. Note that, according to Superdex 75 10/300 instruction manual, 43 kDa and 14 kDa correspond to elution volumes of 10.5/13.5 ml respectively. Bottom: Fraction analysis by SDS-PAGE, upper panel: non PEmal-containing LUV and, lower panel, PEmal-containing LUV. Input (Ip) **(B)** Size exclusion chromatography analysis of GABARAPL1 oligomerization using enzymatic lipidation in the absence of E3. PE-containing liposomes [ePC:DOPE:PI (35:55:10 mol)], GABARAPL1, ATG7 and ATG3 were incubated without ATP (dashed lines) or with ATP (solid lines) for 30 min at 37ºC. Samples were then treated with 2% CHAPS (w/v) and injected in a Superdex 75 10/300. Top: Elution profile of GABARAPL1. According to Superdex 75 10/300 instruction manual, 43 kDa and 14 kDa correspond to elution volumes of 10.5/13.5 ml respectively. Bottom: Fraction analysis by SDS-PAGE, upper panel: without ATP, lower panel: with ATP. Input (Ip).

5.3.2. Effect of E3 on GABARAPL1 tethering and lipid mixing ability

The effect of E3 complex on LC3/GABARAP-induced tethering and lipid mixing ability was described in the previous Chapter. E3 effects on the capacity of GABARAPL1 to aggregate/fuse vesicles are summarized in **Figure 5.6**, in which all the results obtained with GABARAPL1 are compared. **Figure 5.6A** shows an outline of the E3 effect on GABARAPL1 lipidation, tethering and lipid mixing. Although E3 increased lipidation rates and levels (**Figure 5.6B**), the rates and extent of tethering were similar in both cases, even if tethering started later in the absence of E3 (**Figure 5.6C**). Moreover, lipid mixing also took longer to start when E3 was not present, but its rates and extent were much higher than when E3 was present (**Figure 5.6D**).

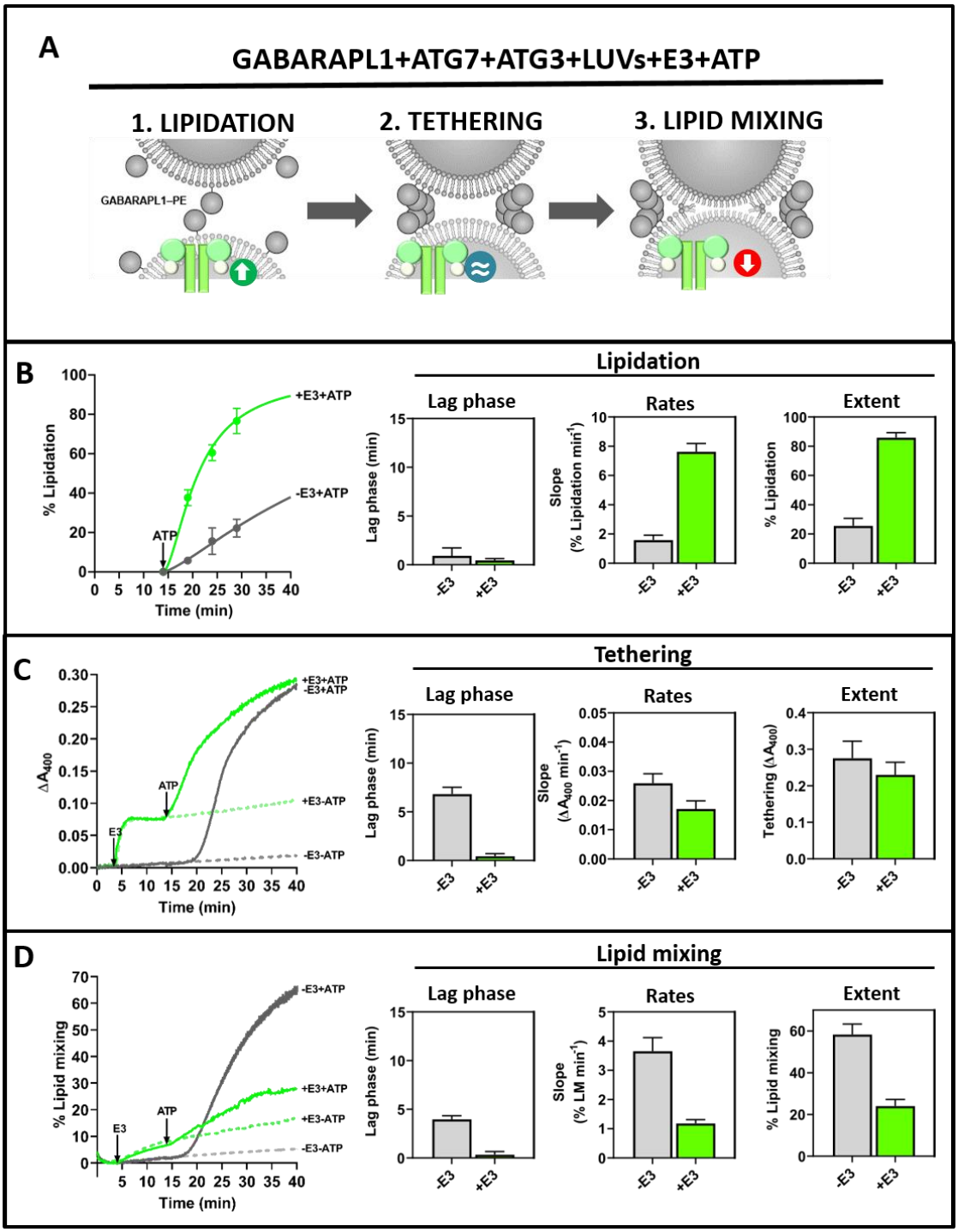

Figure 5.6. Comparative summary of GABARAPL1 lipidation, tethering and lipid mixing levels and time courses in the absence and presence of E3. (A) An outline of the effect of E3 on GABARAPL1 lipidation, tethering and lipid mixing ability. **(B)** Comparative time course, lag phase, rates and extent of lipidation in the absence (grey) or in the presence (green) **(C)** Comparative time course, lag phase, rates and extent of tethering in the absence (grey) or presence (green) of E3. **(D)** Comparative time course, lag phase, rates and extent of lipid mixing in the absence (grey) or presence (green) of E3. (See Chapter 4 for details).

When cryo-EM was used to compare GABARAPL1 ability to cause vesicle tethering and hemifusion in the absence or presence of E3, the results were similar to the above. In the absence of E3 and ATP (**Figure 5.7A**), the vesicles appeared well differentiated, mostly unilamellar, and with a diameter close to 80 nm. Addition of ATP, which induced GABARAPL1 lipidation, caused extensive vesicle tethering, with membrane contacts and some extended sheet-like structures, 300-400-nm long, (**Figure 5.7B**) all of them compatible with a degree of membrane fusion. Cryo-EM of vesicles treated with E3, but not ATP, indicate only some vesicle tethering/aggregation (**Figure 5.7C**), as expected from the turbidity data in **Figure 5.6C** (green dashed line). Finally, vesicles in the presence of both ATP and E3 did show triple parallel lines as a signal of aggregation and a few inter-vesicular discontinuous lines, but without extended structures suggestive of fusion (**Figure 5.7D**), again as expected from the fluorescence data (**Figure 5.6D**, green solid line).

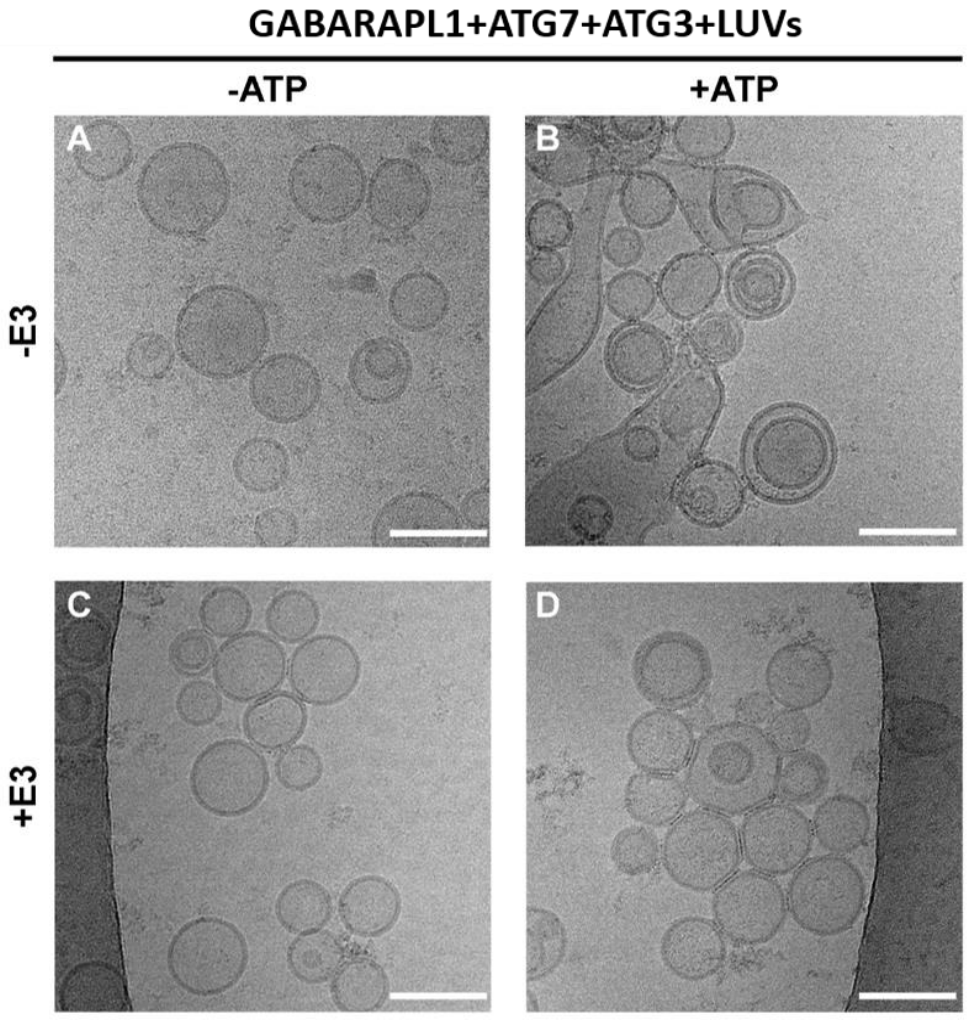

Figure 5.7. GABARAPL1 ability to tether and fuse vesicles in the absence or presence of E3 complex analyzed by cryo-EM. Cryo-EM images of the four conditions analyzed in Chapter 4 (-E3 –ATP, -E3+ATP, +E3-ATP, +E3+ATP) 0.5 µM ATG7, 1 µM ATG3, and 5 µM GABARAPL1 were mixed with 0.4 mM LUV [ePC:DOPE:PI:DOG (33:55:10:2 mol ratio)], in the absence (-E3) or in the presence (+E3) of 0.1 µM E3 complex. After addition of buffer (-ATP) or ATP (+ATP) the mixture was incubated at 37°C for 90 min. **(A-D)** Cryo-EM images of liposomes after reconstituting GABARAPL1 conjugation reaction: **(A)** in the absence of E3 and ATP. **(B)** In the absence of E3 but in the presence of ATP. **(C)** In the presence of E3 but in the absence of ATP. **(D)** In the presence of both E3 and ATP. Bar = 100 nm.

Galleries of images obtained under the conditions in **Figure 5.7** can be found in **Figure 5.8.**

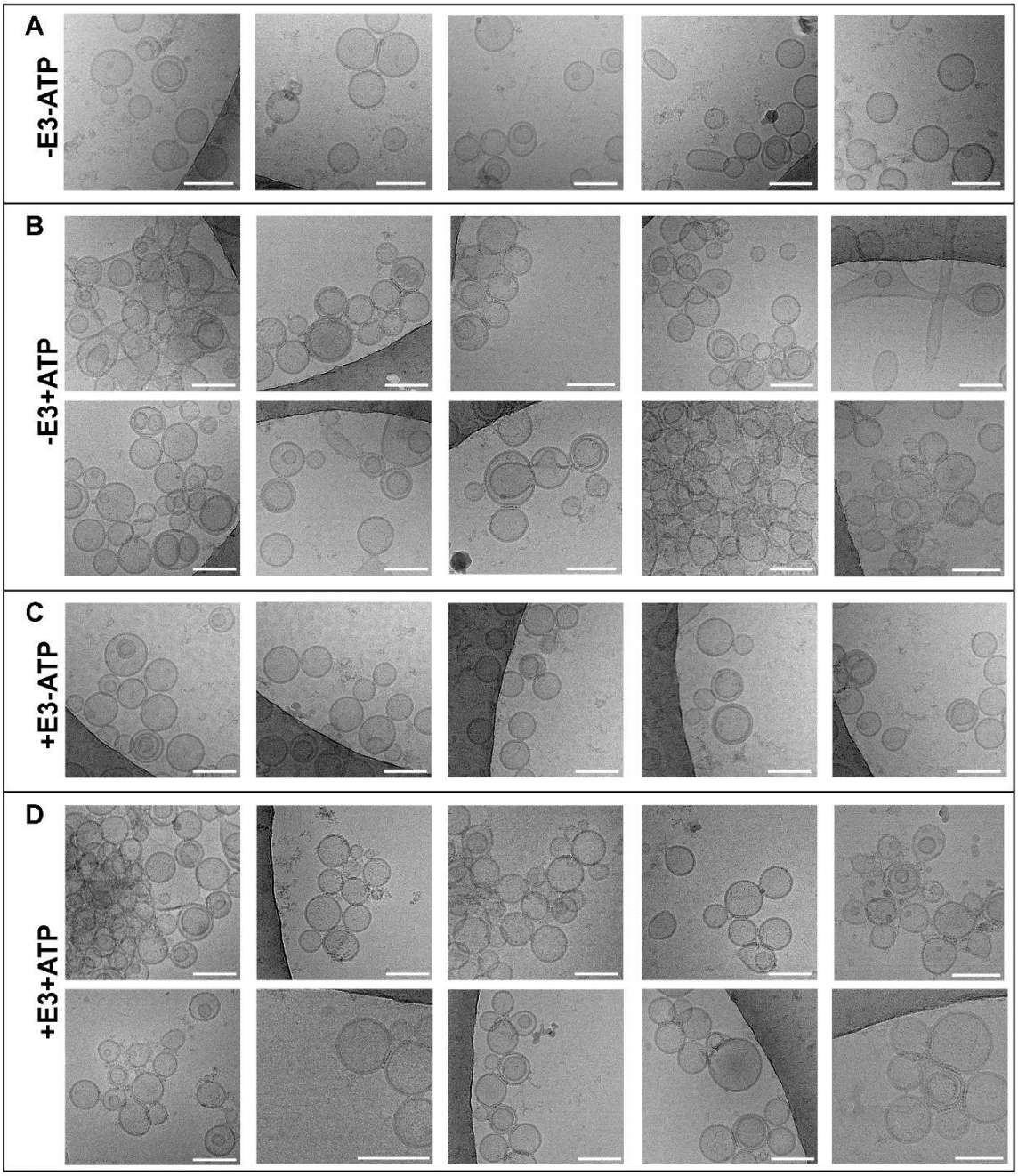

Figure 5.8. Gallery of images of GABARAPL1 ability to tether and fuse vesicles in the absence or presence of E3 complex analyzed by cryo-EM. Additional cryo-EM images of the four conditions analyzed in Figure 5.5. Details as in Figure 5.5. Bar = 100 nm.

Therefore, cryo-EM data supports the results obtained in Chapter 4 in the presence of E3, in which E3-induced inhibition of lipid and aqueous contents mixing was shown. The next step was to further investigate the reason why E3 was able to cause this effect.

5.3.3. Effect of E3 concentration on GABARAPL1 lipidation and lipid mixing ability

To assess whether the E3 effect was concentration dependent, a lipidation reaction was performed with different E3 concentrations: 0.00, 0.02, 0.10 and 0.20 µM. A clear increase in lipidation levels could be seen from 0.00 to 0.02 to 0.10 µM E3 (**Figure 5.9),** however, amounts above 0.10 µM did not cause any further protein lipidation.

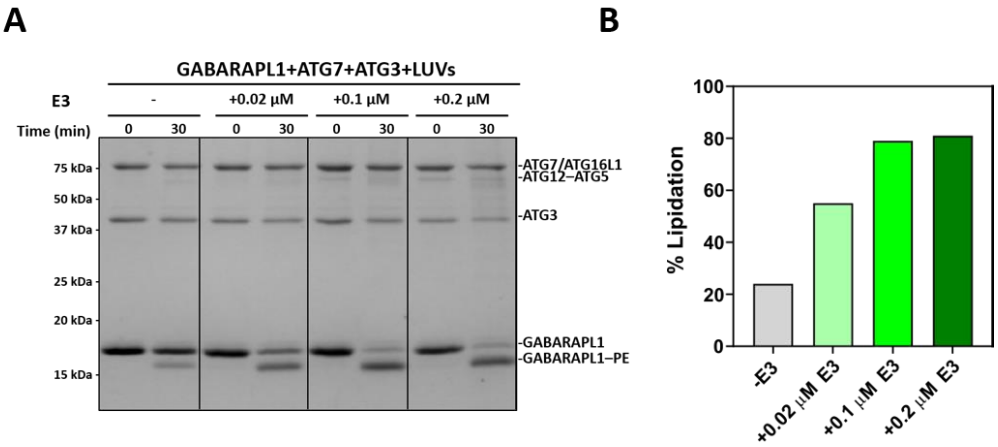

Figure 5.9. E3 concentration effect on lipidation. *In vitro* GABARAPL1 lipidation assay in the presence of increasing E3 concentrations. (A) 0.5 µM ATG7, 1 µM ATG3, and 5 µM GABARAPL1 were mixed with 0.4 mM LUV [ePC:DOPE:PI:DOG (33:55:10:2 mol ratio)], in the absence (-) or in the presence of different E3 complex concentrations (0.02, 0.1, 0.2 µM), and incubated at 37°C in System Buffer containing $MgCl_2$ and ATP. Aliquots were retrieved 0 and 30 min after ATP addition, and loaded on a 15% SDS-polyacrylamide gel. **(B)** Percent lipidated protein, quantified as described under *In vitro* enzymatic lipidation assay (Materials and Methods Chapter 4).

Moreover, when the effect of the different E3 concentrations on GABARAPL1 lipid mixing ability was considered, an inverse correlation could be seen (**Figure 5.10)**. When E3 concentration increased, GABARAPL1 lipid mixing ability decreased.

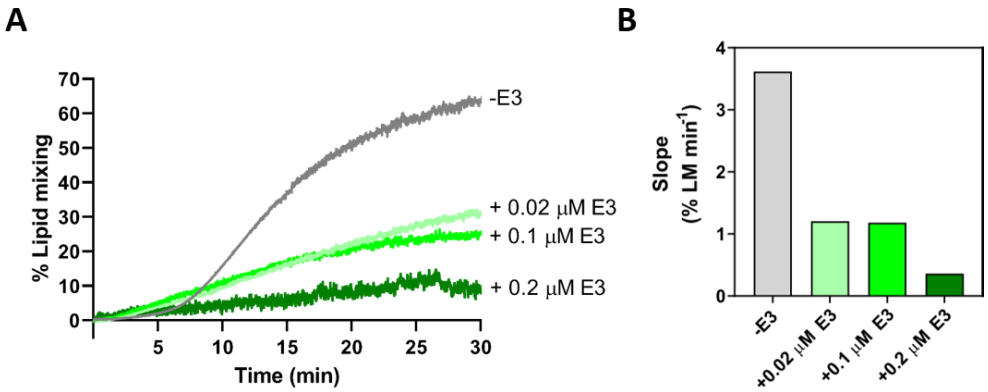

Figure 5.10. E3 concentration effect on lipid mixing. GABARAPL1 lipid mixing assay in the presence of increasing E3 concentrations. (A) 0.5 µM ATG7, 1 µM ATG3, and 5 µM GABARAPL1 were mixed with 0.4 mM LUV [ePC:DOPE:PI:DOG (33:55:10:2 mol ratio)], in the absence (-) or in the presence of different E3 complex concentrations (0.02, 0.1, 0.2 µM), and incubated at 37°C in System Buffer containing $MgCl_2$ and ATP. **(B)** Tethering rates after ATP addition.

The overall results showed that higher levels of lipidated protein and E3 promote a larger decrease in GABARAPL1 lipid mixing ability, supporting the idea of a protein structure being formed in the presence of E3, that could impede lipid mixing.

5.3.4. The interaction of lipidation machinery proteins with membranes

To determine the interaction with membranes of the various proteins involved in GABARAPL1 lipidation and explore the possible formation of a protein coat or scaffold, protein-liposome flotation assays were performed. Specifically, membrane interaction of the lipidation machinery proteins under the four conditions described above (-E3-ATP, -E3+ATP, +E3-ATP, +E3+ATP) was checked. To allow detection of the E3 complex in the SDS-PAGE gel after the flotation assay, concentrations of all the reagents in the assay had to be increased by 5-fold. This increased concentration originated that, even in the absence of E3, all GABARAPL1 was lipidated.

In the absence of E3 (**Figure 5.11**) an ATP-dependent increased interaction of all the proteins was observed. Before ATP addition (**Figure 5.11,** -ATP, left panel), part of ATG3 and ATG7 appeared in the bound fraction together with a small percentage of GABARAPL1. As expected, upon ATP addition (**Figure 5.11,** +ATP, right panel) the band corresponding to the lipidated form of GABARAPL1 only appeared in the bound fraction, together with ATG3, and part of ATG7. This suggests that ATP addition did not only allow lipidation, but it also enhanced ATG7 and ATG3 binding to vesicles.

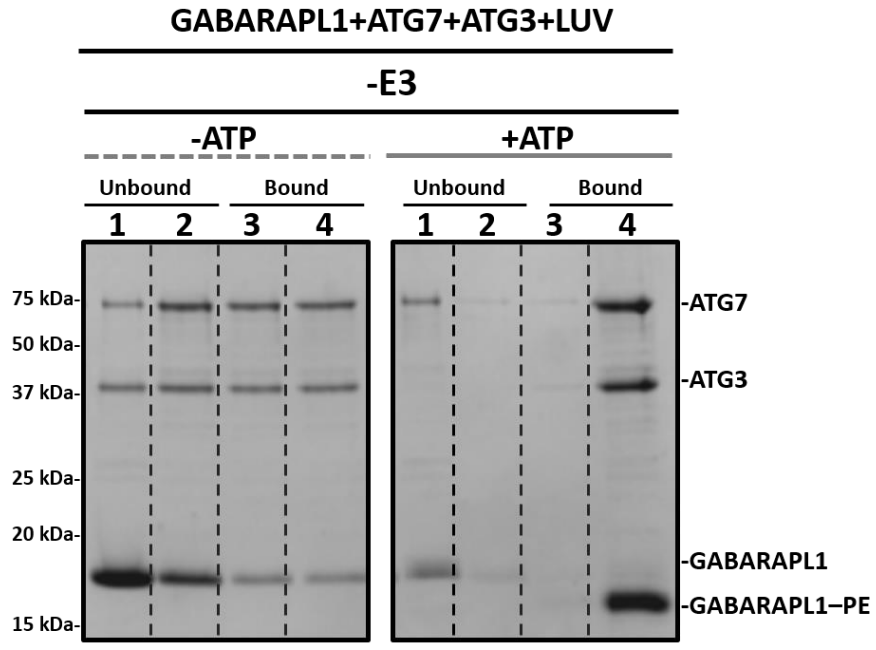

Figure 5.11. Membrane interaction of the lipidation machinery in the absence of E3 increases in the presence of ATP. SDS-PAGE/Coomassie Brilliant Blue-stained gels of the fractions obtained from a vesicle flotation assay of the proteins that form the lipidation machinery in the absence (left) or presence (right) of ATP. Protein found in fractions 3+4 was taken as bound protein. Protein and lipid concentrations were increased by 5-fold. 2.5 µM ATG7, 5 µM ATG3, 0.5 µM E3 and 25 µM of GABARAPL1 were incubated with 2 mM LUV [ePC:DOPE:PI:DOG (33:55:10:2 mol ratio)] at 37°C for 30 min in the absence or presence of ATP.

In the presence of E3 (**Figure 5.12**), an ATP-dependent increased interaction for ATG3, ATG7 and GABARAPL1 was also observed, including lipidation of the latter. However, all E3 was already in the bound fraction in the absence of ATP (**Figure 5.12,** -ATP, left panel). This is in agreement with the results obtained in Chapter 4 (**Figure 4. 16**, showing full E3 binding to membranes when ATG3 was present. Upon ATP addition, E3 remained in the membrane-bound fraction (**Figure 5.12,** +ATP, left panel).

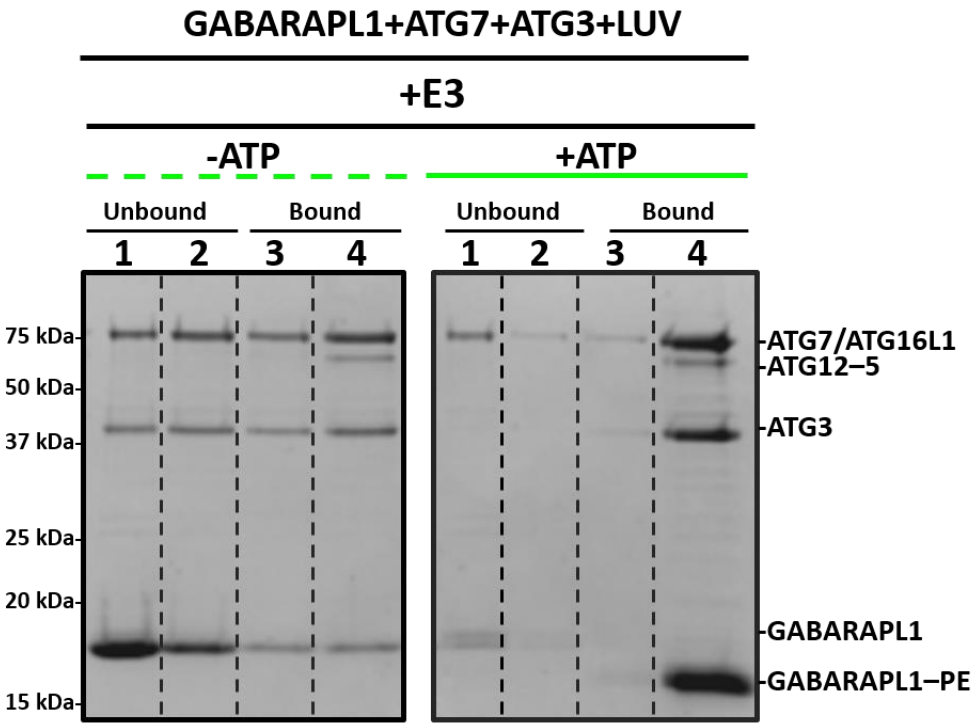

Figure 5.12. Membrane interaction of the lipidation machinery in the presence of E3 increases in the presence of ATP. SDS-PAGE/Coomassie Brilliant Blue-stained gels of the fractions obtained from a vesicle flotation assay of the proteins that form the lipidation machinery in the absence (left) or presence (right) of ATP. Protein found in fractions 3+4 was taken as bound protein. Protein and lipid concentrations were increased by 5-fold. 2.5 μM ATG7, 5 μM ATG3, 0.5 μM E3 and 25 μM of GABARAPL1 were incubated with 2 mM LUV [ePC:DOPE:PI:DOG (33:55:10:2 mol ratio)] at 37°C for 30 min in the absence or presence of ATP.

The overall results demonstrate that GABARAPL1 lipidation facilitates membrane binding of the other system components. However, as the flotation assay does not provide details about the nature of the interaction, the question remains on whether ATP addition caused a reorganization that made E3 complex change its mode of interaction with the membrane/and or proteins, and whether this could affect GABARAPL1 lipid mixing ability.

5.3.5. Direct interaction of GABARAPL1 with E3 complex.

Based on the previously described interaction of Atg8 with E3 complex in yeast (Kaufmann *et al.*, 2014), experiments were addressed to test a putative direct interaction between GABARAPL1 and E3 in the absence of the remaining elements in the lipidation machinery, ATG7 and ATG3.

A microscopy-based glutathione sepharose-bead interaction assay was used to assess GABARAPL1 ability to interact with the E3 complex. An E3 complex containing a GFP tag in ATG16L1 was used. GFP-E3 complex was recruited to beads coated with GST-GABARAPL1 **(Figure 5.13)**. The result supported a direct interaction between GABARAPL1 and E3.

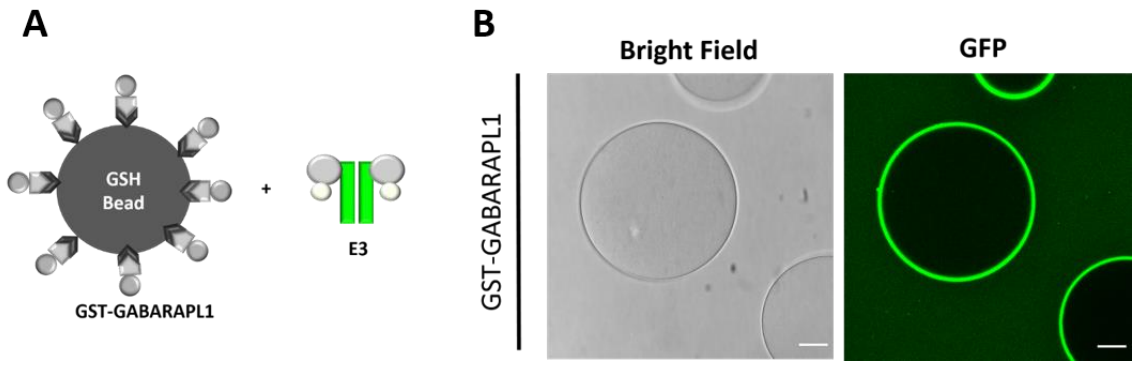

Figure 5.13. GFP-E3 complex was recruited to beads coated with GABARAPL1. (A) An outline of the microscopy-based Glutathione (GSH) sepharose-bead interaction assay. **(B)** Representative images of GSH beads coated with GST-GABARAPL1 incubated with GFP-E3. Images were acquired on a Leica SP5 confocal microscope. Bar = 25 µm.

In a time course assay **(Figure 5.14)** the interaction between GABARAPL1 and E3 was seen to occur in a matter of seconds, and to require the presence of GABARAPL1.

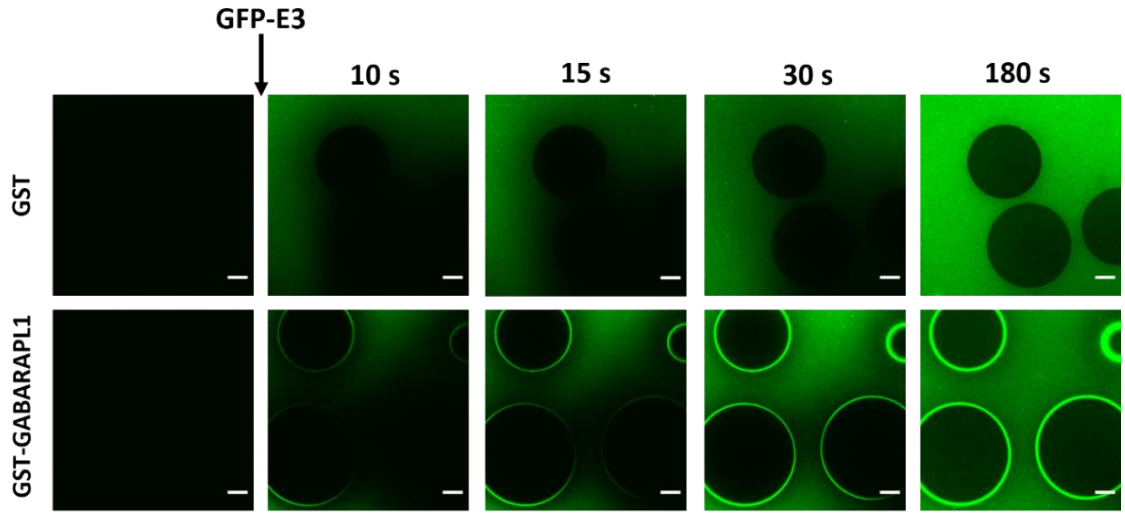

Figure 5.14. Time course of GFP-E3 binding to GST- and GST-GABARAPL1-coated beads. GFP-E3 was added to GSH Beads coated with GST (upper panel) or GST-GABARAPL1 (lower panel). Images were acquired on a Leica SP5 confocal microscope every second. Images at time 0, 10, 15, 30 and 180 s are shown. Bar = 25 µm.

To confirm that the interaction was specific for GFP-E3, it was tested whether the GFP tag (not bound to E3) would interact with GST- **(Figure 5.15A)** or GST-GABARAPL1- **(Figure 5.15C)** coated beads**.** The green halo around the beads was only observed when both GABARAPL1 and E3 were present (**Figure 5.15D).**

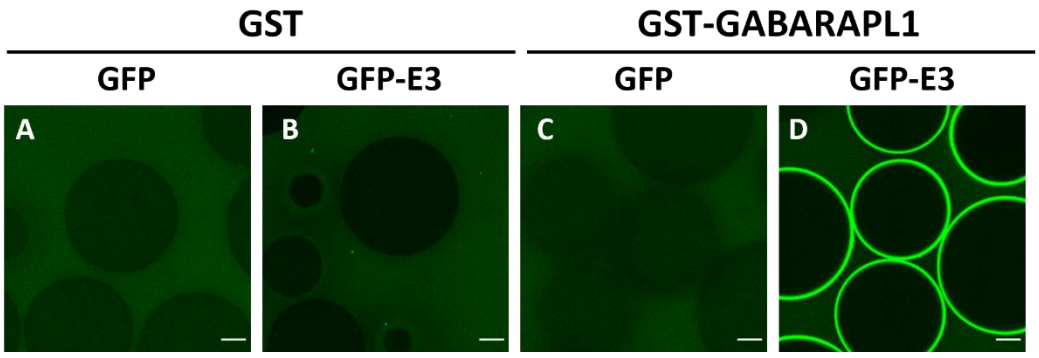

Figure 5.15. GFP-E3 complex was specifically recruited to beads coated with GABARAPL1. (A) Representative images of GSH Beads coated with GST incubated with GFP. **(B)** Representative images of GSH Beads coated with GST incubated with GFP-E3. **(C)** Representative images of GSH Beads coated with GST-GABARAPL1 incubated with GFP. **(D)** Representative images of GSH Beads coated with GST-GABARAPL1 incubated with GFP-E3. Images were acquired on a Leica SP5 confocal microscope. Bar = 25 µm.

In the same way, the interaction of E3 with other LC3/GABARAP family members was tested (**Figure 5.16**). GFP-E3, but not GFP, was able to interact with any of the LC3/GABARAP proteins in beads. A semi-quantitative appraisal indicated a weaker interaction of LC3B and GABARAPL2 with E3. In general, the results confirmed a direct interaction between LC3/GABARAP proteins and E3.

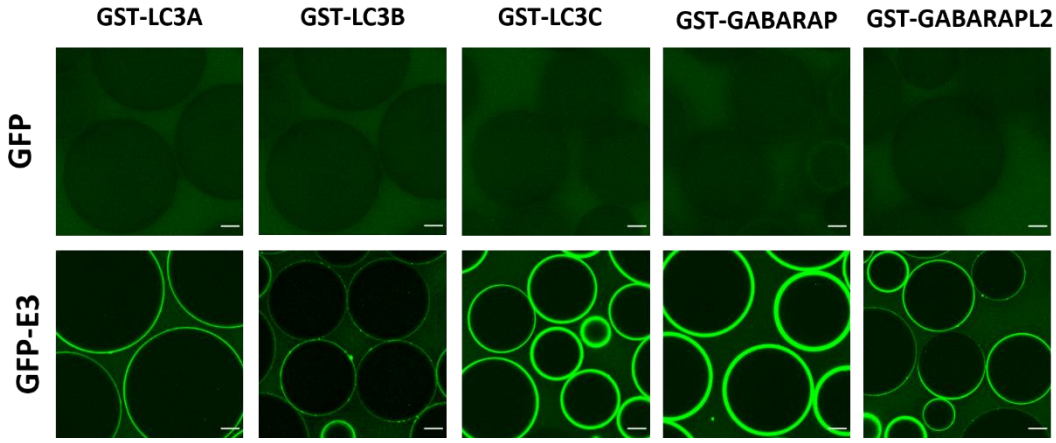

Figure 5.16. GFP-E3 complex was recruited to beads coated with LC3/GABARAP-family members. Top panels: Representative images of GSH Beads coated with GST-LC3A, GST-LC3B, GST-LC3C, GST-GABARAP and GST-GABARAPL2 incubated with GFP. Bottom panels: Representative images of GSH Beads coated with GST-LC3A, GST-LC3B, GST-LC3C, GST-GABARAP and GST-GABARAPL2 incubated with GFP-E3. Images were acquired on a Leica SP5 confocal microscope. Bar = 25 µm.

5.3.6. Reconstitution of GABARAPL1 lipidation in GUV

Giant unilamellar vesicles (GUV) constitute a cell-sized model membrane system that allows direct visualization of particular membrane-related phenomena, such as domain protein interaction, at the single-vesicle level, using fluorescence microscopy-related techniques. This method was used to test whether or not GABARAPL1 was able to interact with PE-containing GUV and whether this interaction was or not dependent on

E3 or ATP. In addition, this technique helped to shed more light on the potential protein coat/scaffold formation, since it could allow observation of putative GABARAPL1 and E3 coexistence, and detect whether a homogeneous structure was formed.

5.3.6.1. GABARAPL1 and E3 complex colocalize on GUV membranes in the presence of ATP.

Following previous work that used GUV for Atg8 or LC3B lipidation reconstitution (Fracchiolla *et al.*, 2020; Kaufmann *et al.*, 2014) the concentrations of GABARAPL1, ATG7 and ATG3 used in our tethering and lipid mixing assays were reduced by 5-fold. The E3 concentration was maintained at 0.1 µM, already a low concentration as discussed in Chapter 4. GABARAPL1 was labelled with Alexa Fluor 633 and GFP-E3 was used (**Figure 5.17A**).

GABARAPL1 lipidation in the presence of E3 was reconstituted in GUV (**Figure 5.17A**). A recruitment of E3 (green) and GABARAPL1 (blue) to GUV membranes (red) was observed (**Figure 5.17B**). Moreover, a Z-axis projection showed a homogeneous distribution of the proteins around the GUV (**Figure 5.17B**, lower panels).

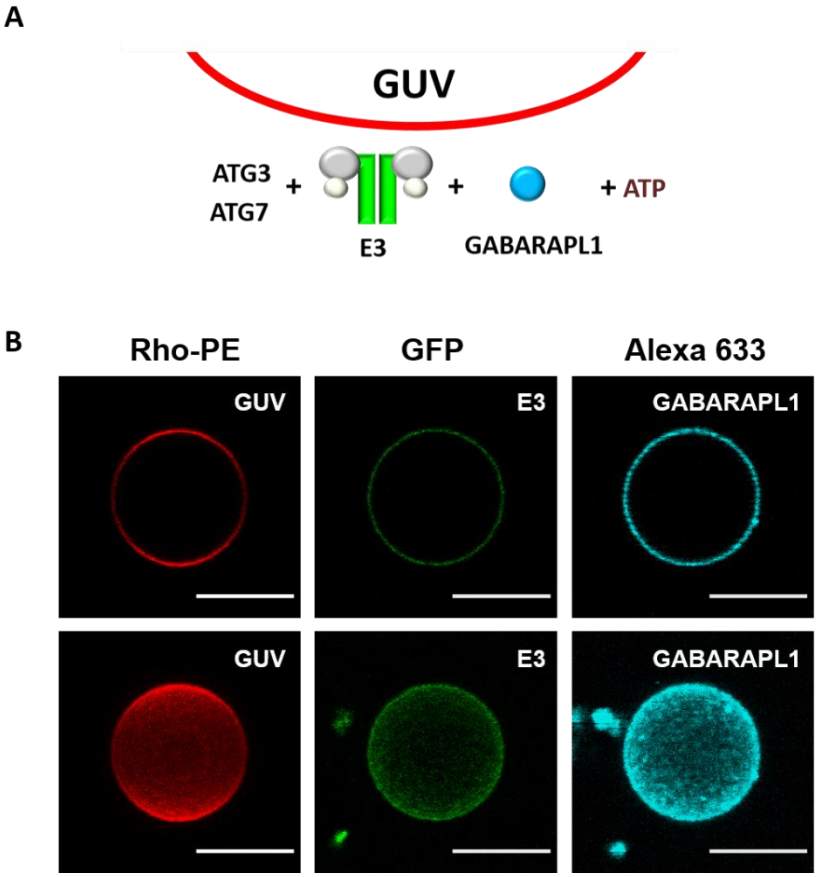

Figure 5.17. GABARAPL1 and E3 complex colocalize on GUV membranes in the presence of ATP. (A) Schematic representation of the approach used. 0.1 µM mATG7, 0.2 µM ATG3, 1 µM Alexa 633 labelled GABARAPL1, 0.1 µM GFP-E3 and ATP were mixed with Rho-PE containing GUV prepared with the "platinum wire method" (3µl of a 0.2 mM Stock; [ePC:DOPE:PI:DOG (33:55:10:2 mol ratio)]. The mixture was incubated for 30 min at 37ºC. **(B)** Top: Representative confocal images. Bottom: Z projection of the images. Images were acquired on a Leica SP5 confocal microscope. Bar = 10 µm.

In order to confirm that E3 and GABARAPL1 localization in GUV was ATP dependent, the reconstitution system was tested under the same four conditions described in Chapter 4 (-E3-ATP, -E3+ATP, +E3-ATP, +E3+ATP) (**Figure 5.18**). No GABARAPL1 recruitment was observed when ATP was not present (**Figure 5.18, -ATP**). Moreover, when E3 was not present just a faint halo of GABARAPL1 could be seen on some of the GUV after ATP addition (**Figure 5.18, -E3, +ATP**). In agreement with the previous experiment, a clear GABARAPL1 signal was detected when both E3 and ATP were present (**Figure 5.18, +E3, +ATP**). E3 was found in the GUV only after ATP addition, colocalizing with GABARAPL1. Those results support the possibility of a GABARAPL1-E3 coat formation, dependent on ATP presence, or on GABARAPL1 lipidation.

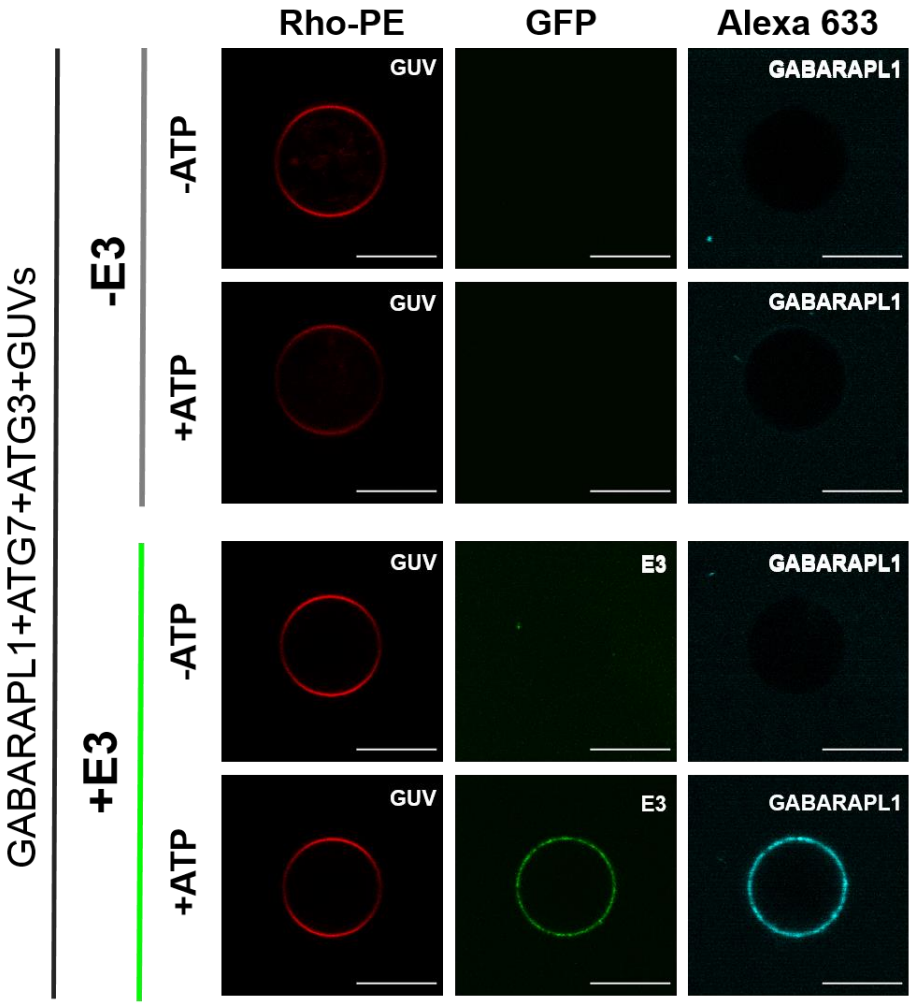

Figure 5.18. GABARAPL1 and E3 complex colocalization on GUV membranes is ATP dependent. Representative confocal images of -E3-ATP, -E3+ATP, +E3-ATP, +E3+ATP conditions. 0.1 µM mATG7, 0.2 µM ATG3, 1 µM Alexa 633 labelled GABARAPL1 and when indicated 0.1 µM GFP-E3 and ATP were mixed with Rho-PE containing GUV prepared with the "platinum wire method" (3µl of a 0.2 mM stock; [ePC:DOPE:PI:DOG (33:55:10:2 mol ratio)]. The mixture was incubated for 30 min at 37ºC. Images were acquired on a Leica SP5 confocal microscope. Bar = 10 µm.

In order to reproduce lipid mixing experiments in GUV, a different GUV production method (ITO, see methods for details) was used. This method allows the simultaneous observation of increased numbers of GUV. This increase permitted the use of protein concentrations as used in LUV experiments, i.e. 5-fold lower than in **Figure 5.16**, which

allowed a closer approach to the tethering and fusion experimental conditions in GUV and LUV. Under these conditions (**Figure 5.19**), in the absence of E3 and of ATP, no GABARAPL1 was seen on the GUV membranes **(Figure 5.19**, -E3-ATP**)**. However, when ATP was in the mixture, and therefore GABARAPL1 lipidation could happen, a faint GABARAPL1 signal could be observed in the contact regions between GUV **(Figure 5.19,** -E3+ATP, arrows**)**.

In the presence of E3 but not ATP, the E3 complex was detected in the contact regions of the GUV and little amounts of GABARAPL1 could be observed colocalizing with E3. **(Figure 5.19,** +E3-ATP, arrows**)**. When both E3 and ATP were present, thus GABARAPL1 lipidation could happen, 30 min incubation were enough for GABARAPL1 to be detected around the GUV, colocalizing with E3 **(Figure 5.19,** +E3+ATP**)**. However, while GABARAPL1 signal was maintained in the contact zones, E3 was no longer present in most of them **(Figure 5.19,** +E3+ATP, arrows**)**.

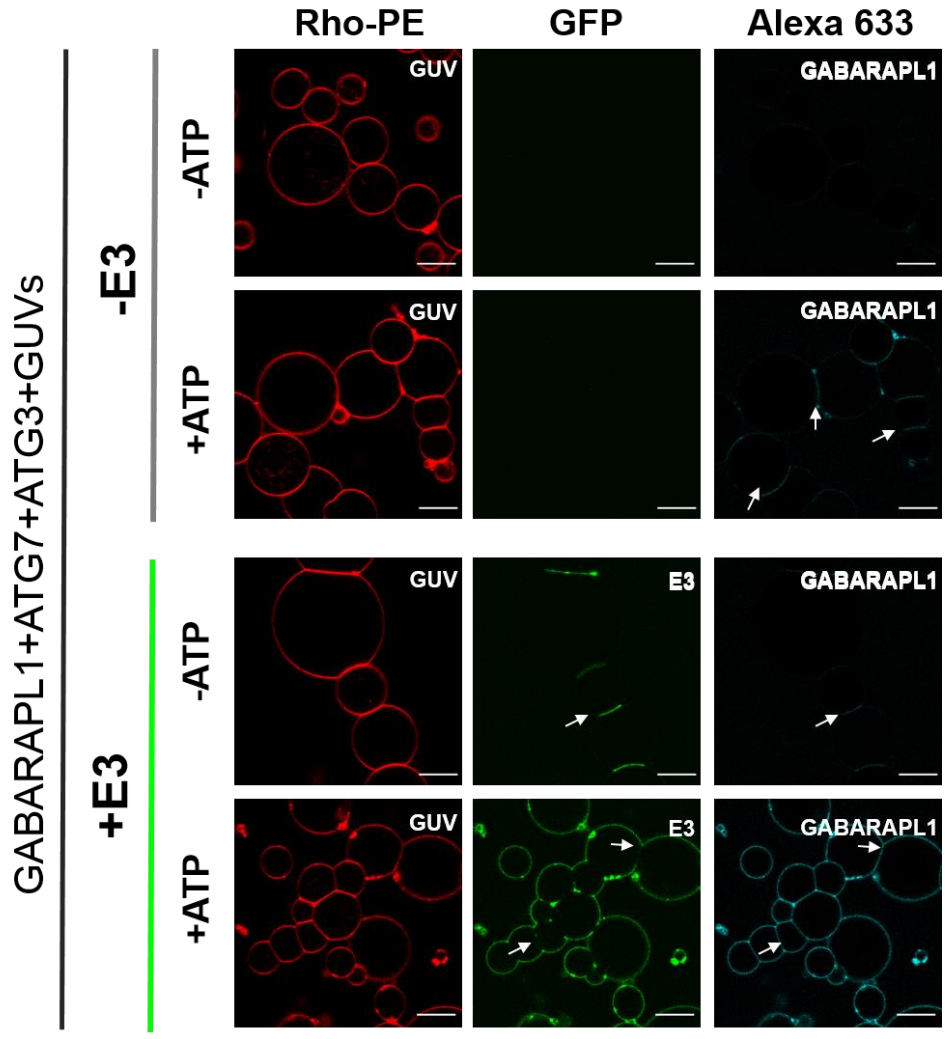

Figure 5.19. GABARAPL1 and E3 complex localization on GUV prepared by the ITO method. Representative confocal images of -E3-ATP, -E3+ATP, +E3-ATP, +E3+ATP conditions. 0.5 µM mATG7, 1 µM ATG3, 5 µM Alexa 633 labelled GABARAPL1 and when indicated 0.1 µM GFP-E3 and ATP were mixed with Rho-PE containing GUV prepared with the "ITO" method (20 µl of a 1 mM Stock; [ePC:DOPE:PI:DOG (33:55:10:2 mol ratio)]. The mixture was incubated for 30 min at 37ºC. Images were acquired on a Leica SP5 confocal microscope. Bar = 10 µm.

The results obtained with the ITO GUV support the possibility of a GABARAPL1-E3 coat formation dependent on ATP presence/lipidation. However, GABARAPL1 behavior in the absence of E3 and E3 behavior in the absence and presence of ATP should be studied in more detail.

5.3.6.2.GABARAPL1 behavior in the absence of E3

30 min after GABARAPL1 incubation with ATG7, ATG3, ATP and GUV, a GABARAPL1 signal was observed in the GUV contact zones that was not seen in the absence of ATP (**Figure 5.19,** -E3**)**. Based on previous results summarized in **Figure 5.6B,** in which it was shown that GABARAPL1 lipidation was slower in the absence of E3, the system was examined for a longer time, namely 120 min (**Figure 5.20**). Some effects were observed that were not evident after 30 min (**Figure 5.19, -E3)**. In particular, some signal of GABARAPL1 binding was detected in the condition without ATP (**Figure 5.20,** -ATP, GABARAPL1), however the differences between GABARAP intensity in the absence and presence of ATP were still clear. When ATP was present and lipidation could occur, GABARAPL1 was located around the GUV but with a higher intensity in the contact zones (**Figure 5.20,** +ATP, GABARAPL1). In addition, although the high production of GUV obtained by the ITO method caused the appearance of GUV closer to each other even in the absence of ATP (**Figure 5.20,** -ATP, GUV), a higher amount of tethering and some structures suggestive of inter-GUV lipid mixing (flatter and larger contact zones) could be seen 120 min after ATP addition (**Figure 5.20,** +ATP, GUV).

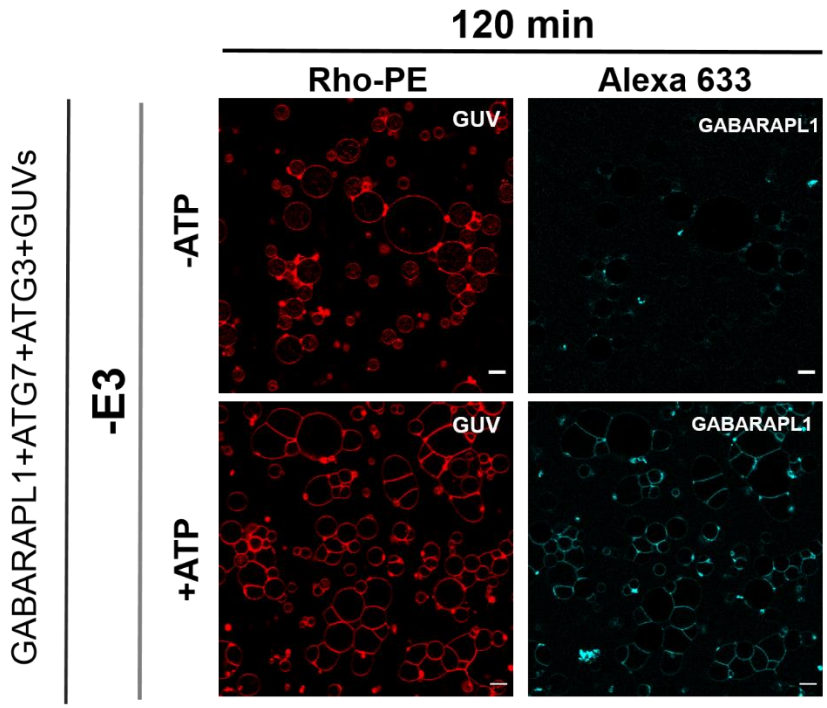

Figure 5.20. GABARAPL1 behavior in the absence of E3 120 min after ATP addition. Representative confocal images of -E3-ATP, -E3+ATP conditions. 0.5 µM mATG7, 1 µM ATG3, 5 µM Alexa 633 labelled GABARAPL1 and when indicated ATP were mixed with Rho-PE containing GUV prepared with the "ITO" method (20 µl of a 1 mM Stock; [ePC:DOPE:PI:DOG (33:55:10:2 mol ratio)]. The mixture was incubated for 120 min at 37ºC. Images were acquired on a Leica SP5 confocal microscope. Bar = 10 µm.

Therefore, these results showed a different behavior of GABARAPL1 when ATP was present. ATP addition promoted higher levels of GUV tethering that would correspond to a higher localization of GABARAPL1 in GUV membranes, particularly in their contact zones, even if the lack of E3 required longer incubation periods.

5.3.6.3.E3 and GABARAPL1 behavior after ATP addition

In the presence of E3, 30 min GABARAPL1 incubation with the lipidation machinery were enough to detect GABARAPL1 and E3 interaction with GUV membranes (**Figure 5.18 and Figure 5.19**, **+E3 +ATP)**. The process may be better understood when lipidation is observed in a wider microscopic field in the absence or presence of ATP (**Figure 5.20**). In the absence of ATP, E3 appeared at the contact zones of some tethered GUV but also surrounding some of them (**Figure 5.21, -ATP**). However, when ATP was present and GABARAPL1 lipidation could happen, E3 had disappeared from many of the contact zones, GABARAPL1 was located all over the GUV and a tighter tethering of GUV was observed (**Figure 5.21, +ATP**).

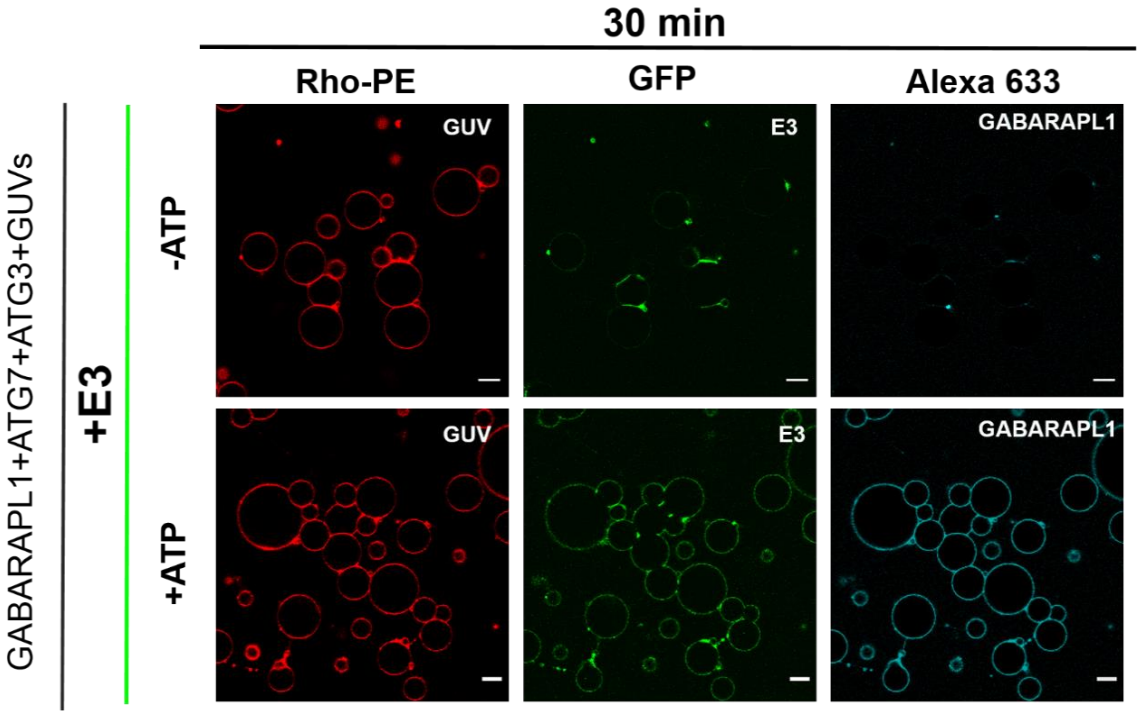

Figure 5.21. GABARAPL1 and E3 behavior before and after ATP addition. Representative confocal images of +E3-ATP, +E3+ATP conditions. 0.5 µM mATG7, 1 µM ATG3, 5 µM Alexa 633-labelled GABARAPL1, 0.1 µM E3 and, when indicated, ATP, were mixed with Rho-PE containing GUV prepared with the ITO method (20 µl of a 1 mM Stock; [ePC:DOPE:PI:DOG (33:55:10:2 mol ratio)]. The mixture was incubated for 30 min at 37ºC. Images were acquired on a Leica SP5 confocal microscope. Bar = 10 µm.

As seen in **Figure 5.22,** when ATP was present, E3 disappearance from contact zones was a generalized behavior. A faint E3 signal in some of the contact zones (**Figure 5.22)** suggests, as expected from the observation of E3 location in the absence of ATP (**Figure 5.21, -ATP**), that E3 would go first to these zones, and then relocate to other GUV

regions. Moreover, the slightly polyhedral or flat surfaces in the E3-free zones could indicate that some inter-vesicular lipid mixing could happen in those areas (**Figure 5.22).**

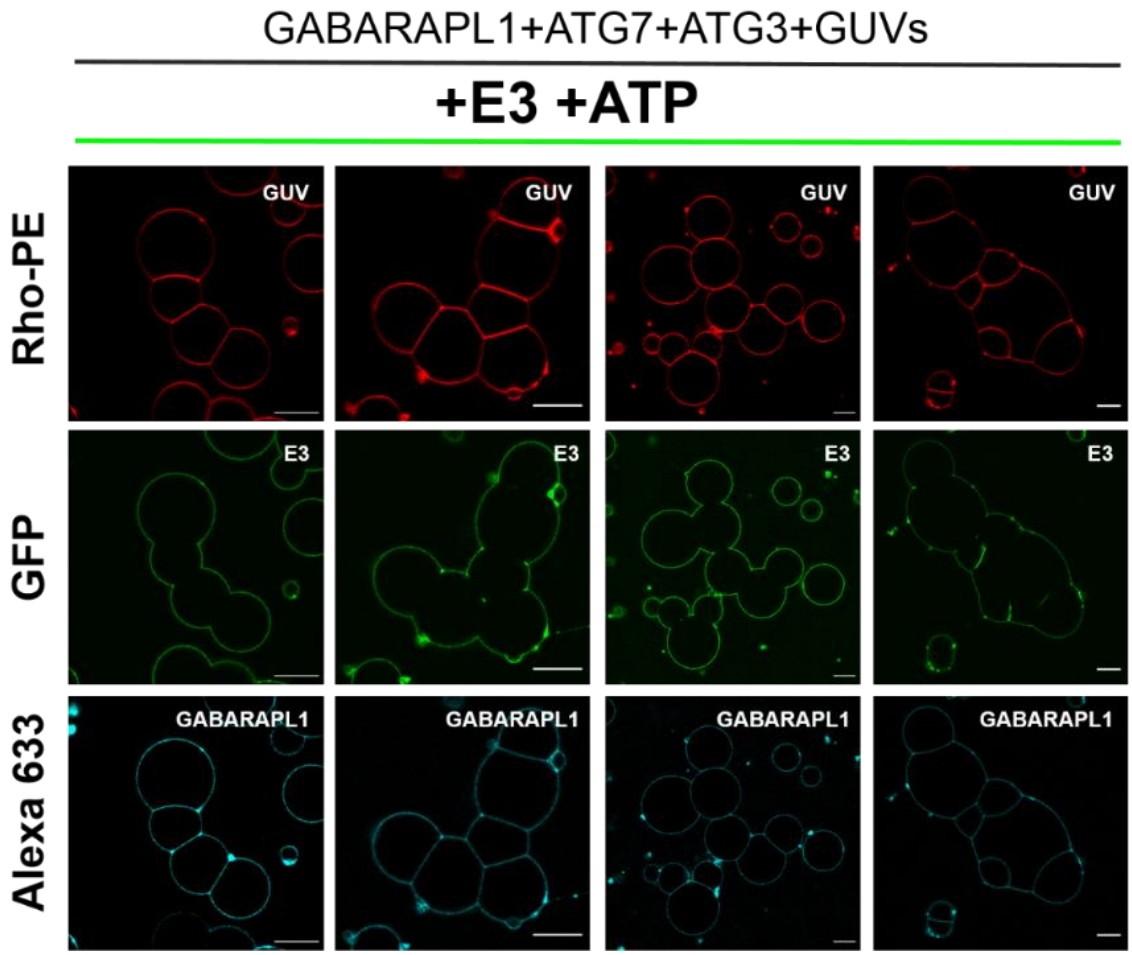

Figure 5.22. E3 disappeared from GUV contact zones after ATP addition. Representative confocal images of +E3+ATP conditions. 0.5 µM mATG7, 1 µM ATG3, 5 µM Alexa 633 labelled GABARAPL1, 0.1 µM E3 and ATP were mixed with Rho-PE containing GUV prepared with the ITO method (20 µl of a 1 mM stock; [ePC:DOPE:PI:DOG (33:55:10:2 mol ratio)]. The mixture was incubated for 30 min at 37ºC. Images were acquired on a Leica SP5 confocal microscope. Bar = 10 µm.

Z-axis and 3D projections confirm that, while GABARAPL1 is interacting with the contact surfaces between GUV, E3 is absent from those zones. E3 rather stays bound to the membrane areas not in contact with other vesicles (**Figure 5.23**).

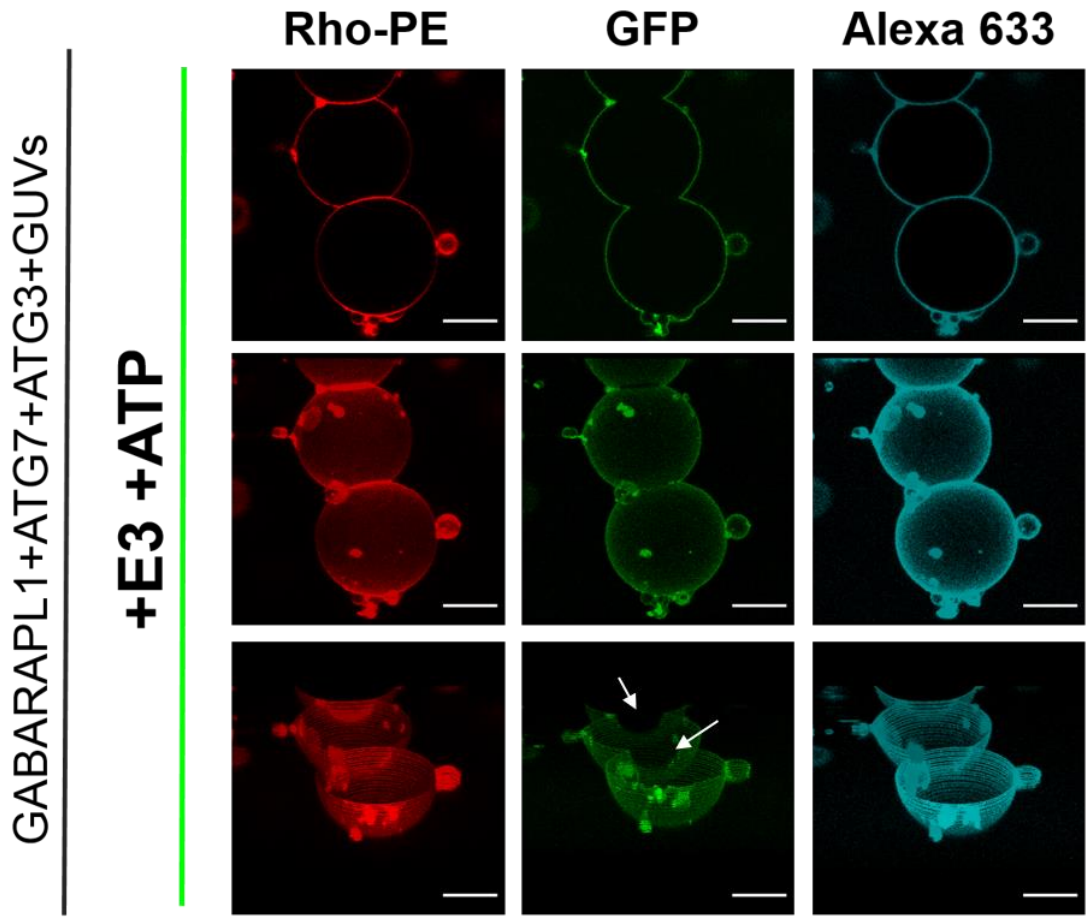

Figure 5.23. Z-axis and 3D projections of GUV, E3 and GABARAP signal 30 min after ATP addition. Representative confocal image of +E3+ATP condition. 0.5 µM mATG7, 1 µM ATG3, 5 µM Alexa 633 labelled GABARAPL1, 0.1 µM E3 and when indicated ATP were mixed with Rho-PE containing GUV prepared with the ITO method (20 µl of a 1 mM stock; [ePC:DOPE:PI:DOG (33:55:10:2 mol ratio)]. The mixture was incubated for 30 min at 37ºC. Top: Confocal image. Middle: Z-axis, Bottom: 3D projection. Images were acquired on a Leica SP5 confocal microscope. Bar = 10 µm.

A time-resolved assay was performed to further understand the process. After identifying GUV in close apposition (**Figure 5.24**, 5 min), E3 was first located at a higher concentration in the contact regions, according to the GFP signal. Then, E3 concentration increased all over the GUV, as GABARAPL1 began to interact with the lipids, with E3, or both (**Figure 5.24**, 15 min). As this happened, the curved shape of the GUV contact zones gradually became flat (**Figure 5.24**, 35 min, GUV panel). By the end of the observation time lapse, E3 left the contact zone, while GABARAPL1 stayed (**Figure 5.24**, 45 min, E3 panel). Thus, it appears that, under our conditions, E3 and GABARAPL1 could cooperate in inducing the tethering and possible lipid mixing between vesicles, even with low-curvature structures such as GUV. Moreover, the coexistence of GABARAPL1 and E3 surrounding the GUV outer surface support the idea of the formation of a scaffold or protein coat being formed in those zones.

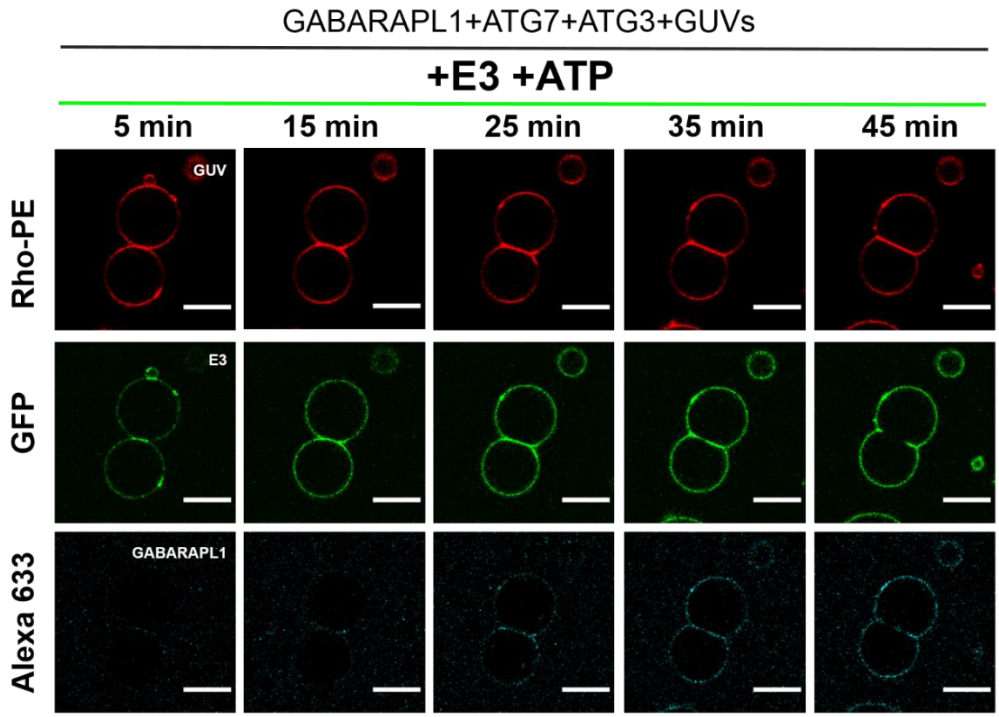

Figure 5.24. Time course assay of GABARAPL1 lipidation reconstitution in GUV in the presence of E3 complex. Representative confocal images of +E3+ATP condition. 0.5 µM mATG7, 1 µM ATG3, 5 µM Alexa 633 labelled GABARAPL1, 0.1 µM E3 and ATP were mixed with Rho-PE containing GUV prepared with the ITO method (20 µl of a 1 mM stock; [ePC:DOPE:PI:DOG (33:55:10:2 mol ratio)]. Images were acquired on a Leica SP5 confocal microscope every minute. Images at time 5, 15, 25, 35 and 45 min are shown. Bar = 10 µm.

5.3.7. AFM preliminary studies: A protein coat/scaffold could be formed over the membrane

5.3.7.1. An homogeneous structure is formed on top of the bilayer

A combination of GUV and AFM studies allowed Kaufman *et al.* (2014) to propose that Atg8–PE assembles with Atg12–Atg5-Atg16 into an immobile membrane scaffold, Atg16 the element driving the ordered assembly of the scaffold by crosslinking Atg8–PE/Atg12–Atg5 complexes into a two-dimensional meshwork. Preliminary AFM studies were used to determine whether a mesh or a scaffold like structure is formed when GABARAPL1 lipidation system is present. To asses this objective, SLB containing PE were formed. Before protein addition, the SLB were scanned **(Figure 5.25B, 0 min)** and their extension was checked. Only some lipid aggregates were detected. After incubation for 20 min at 37ºC with a mixture that contained GABARAPL1, mATG7, ATG3, E3 and ATP (**Figure 5.25A**) the sample was scanned again **(Figure 5.25B, 20 min).** A higher structure was observed on top of the bilayer suggesting the possible formation of a protein scaffold similar to what was seen for Atg8.

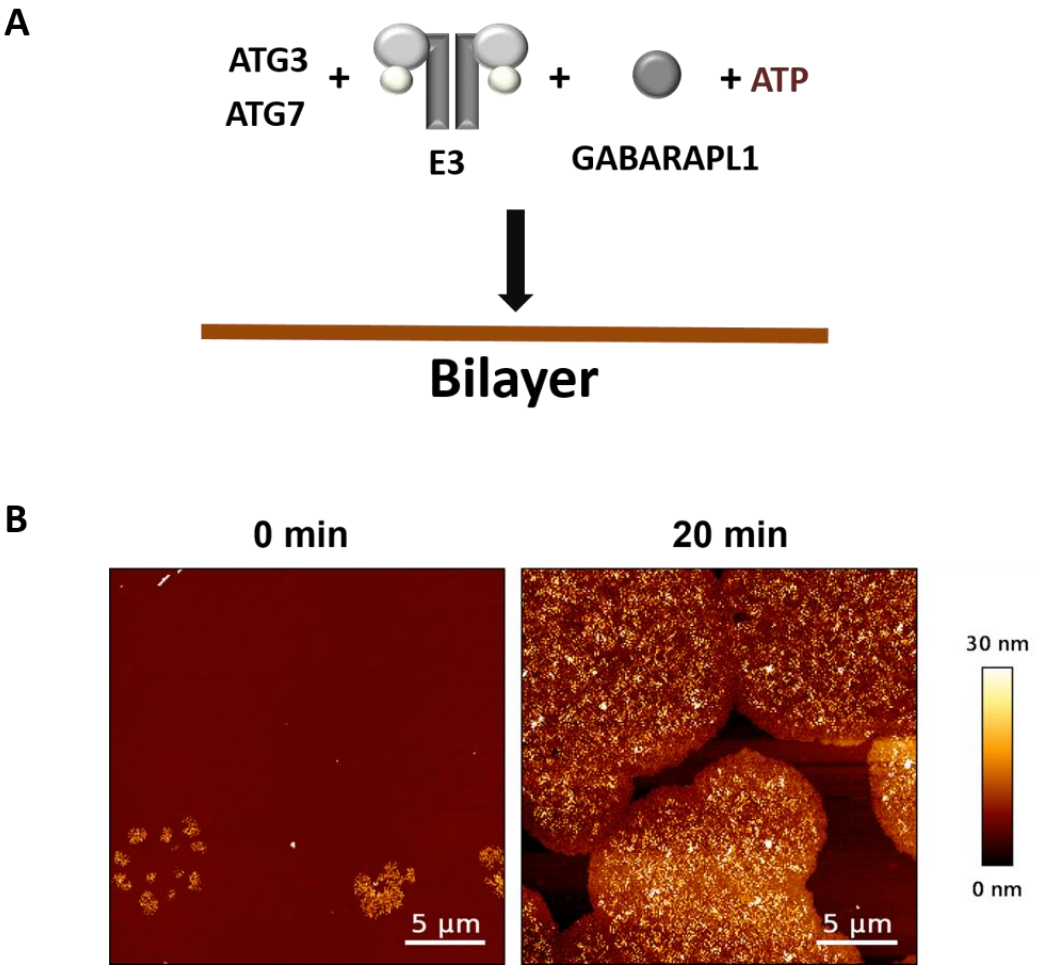

Figure 5.25. A structure is formed on top of the bilayer when GABARAPL1 lipidation system is present. (A) Outline of the approach. 0.5 µM mATG7, 1 µM ATG3, 5 µM GABARAPL1, 0.1 µM GFP-E3 and ATP were added to a SLB containing PE [ePC:DOPE:PI (70:20:10 mol ratio)]. The mixture was incubated for 20 min at 37ºC. (B) Line-fitted raw height images of SLBs before protein addition (left, t = 0 min) and 20 min after GABARAPL1, ATG7, ATG3, E3 and ATP addition (right t = 20 min).

If the sample was washed before scanning to avoid lipid and protein aggregates deposition and a smaller area was scanned (around 5 µm), a better topography image was obtained (**Figure 5.26A**). A cross section of a zone including bilayer and protein structures revealed that the structure was 6 nm higher than the bilayer (**Figure 5.26B**). The histogram of the full image supports the notion of a homogeneous structure around 6nm height. These characteristics rule out the possibility that the observation corresponds simply to a protein aggregate. The constant height and the homogeneity of the protein layer indicate that it is a specific structure.

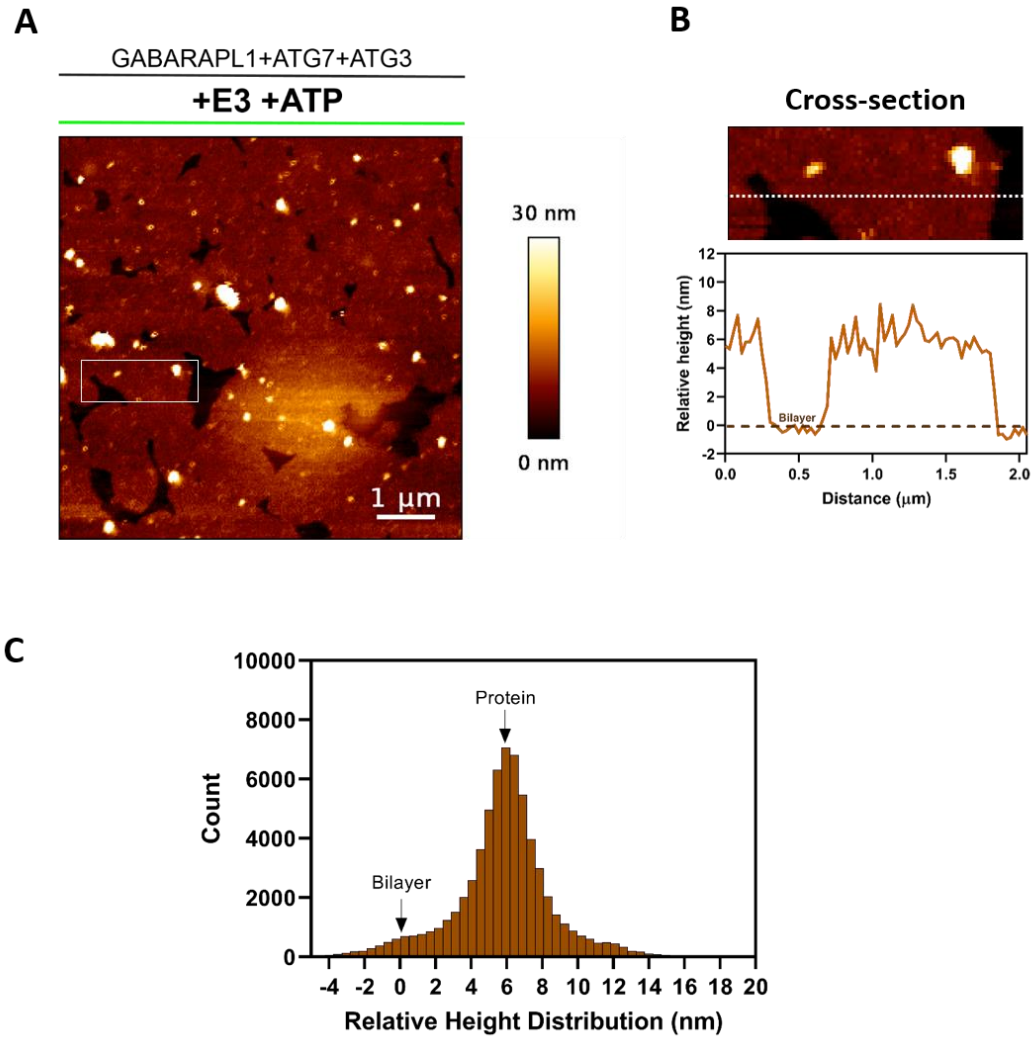

Figure 5.26. A homogeneous structure is formed on top of the bilayer when the GABARAPL1 lipidation system is present. (A) Line-fitted raw height images of SLBs 20 min after GABARAPL1, ATG7, ATG3, E3 and ATP addition. The sample was washed before scanning. The brightest area in the image was due to a deformation in the mica, which seemed not to be totally flat. **(B)** Cross-section of the zone in the rectangle in (A). Membrane height was set to zero. **(C)** Histogram of the relative height distribution of the zone in the rectangle in (A). Membrane height was set to zero.

5.3.7.2. Structure formation is dependent of ATP presence

To determine whether the structure resulting from the interaction between GABARAPL1, ATG7, ATG3, E3 and a PE-containing membrane was dependent on ATP a comparative time-course assay in the absence or presence of ATP was performed. These studies were performed at room temperature.

As seen in **Figure 5.27A** (lower panel), when ATP was present, just a few minutes were needed to make this structure detectable, seemingly "attached" to the lipid bilayer. However when ATP was not present **Figure 5.27A** (upper panel), only small changes in topography could be observed, probably due to protein interactions with the bilayer. The histogram of the full image supports the notion of a new structure beingformed when ATP is present (**Figure 5.27B)**. The lower height of the new structure could be explained by

the difference in temperature between assays that did not allow reaching the final point obtained in the previous experiments (**Figure 5.25** and **Figure 5.26**).

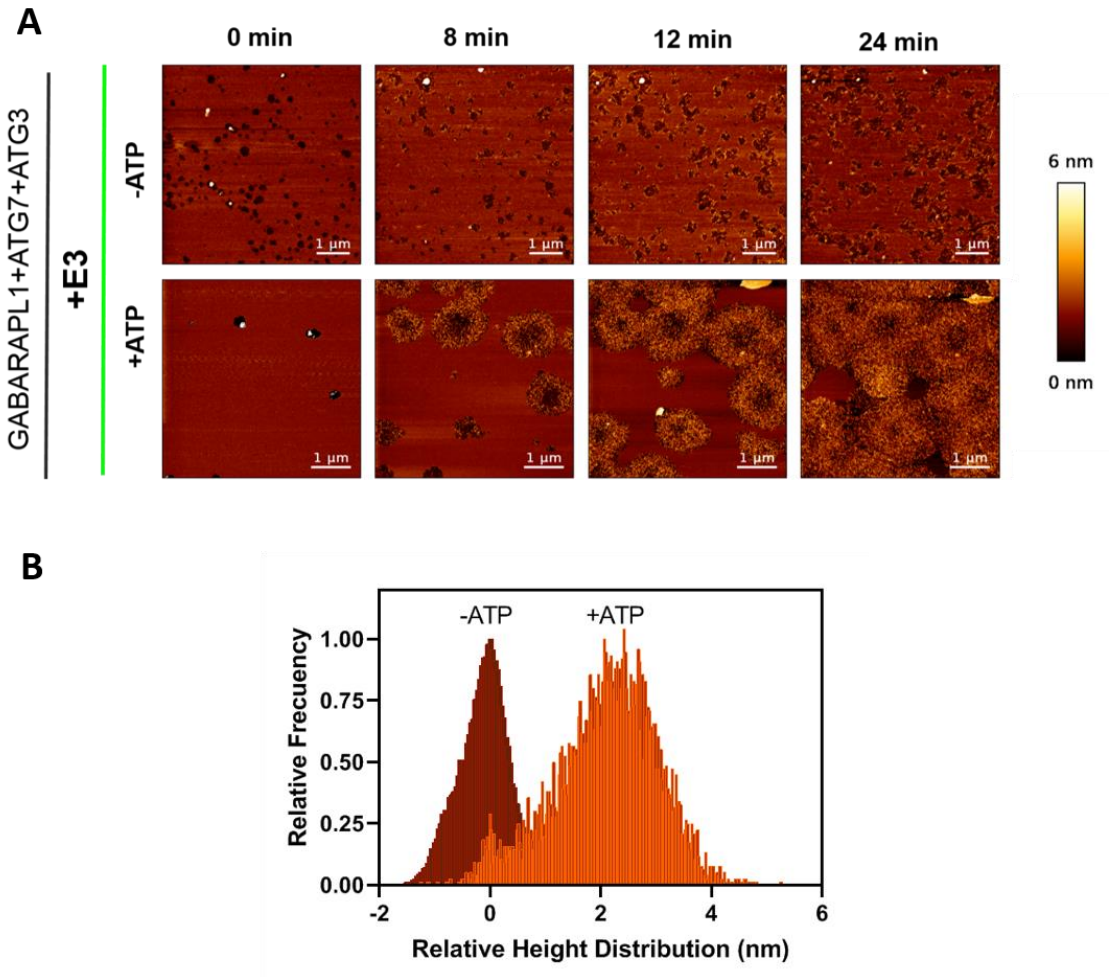

Figure 5.27. Time course of structure formation in the absence or in the presence of ATP. (A) Line-fitted raw height images of SLBs at different time points after ATP addition (0, 8, 12 and 24 min). Top: in the absence of ATP. Bottom: in the presence of ATP. GABARAPL1, ATG7, ATG3, E3 and ATP addition. **(B)** Histogram of the relative height distribution of the image at time 24 min in (A). Membrane height was set to zero.

Further experiments would be needed to characterize the observed structure, but our preliminary results suggest that GABARAPL1, ATG7, ATG3, E3 complex could form a homogenous structure over the lipid bilayer if ATP were present.

5.4 Discussion

GABARAPL1 oligomerization after lipidation could be responsible for its tethering and lipid mixing ability

The results on the potential ability of GABARAPL1 to oligomerize showed the appearance of a peak corresponding to a two-fold molecular weight once lipidation had been induced (**Figure 5.5**). This suggests the possibility of the tethering and lipid mixing ability being related to the interaction between two GABARAPL1 molecules, each bound to a different vesicle. Further experiments using more quantitative techniques such as native gels, cross-linking, or fluorescence correlation spectroscopy (FCS) could help understand whether dimers were being formed.

In addition, GABARAPL1 localization in GUV in the presence of ATP but in the absence of E3 (**Figure 5.20, +ATP**) suggested that lipidation in GUV could occur in the absence of E3, although at a slower rate. Results obtained with GUV in the absence of E3 after 120 min (**Figure 5.20, +ATP**) indicated that there was an ATP-dependent tethering and possible inter-vesicle lipid mixing together with an increased localization of GABARAPL1 in the contact zones of these GUV. These observations would be compatible with an interaction of a GABARAPL1 lipidated protein on one GUV with a GABARAPL1 on the adjacent GUV. Moreover, in Cryo-EM images, the presence of vesicles in close apposition and of structures suggestive of hemifusion and fusion only when ATP was present (**Figure 5.4**) supports the previous conclusions obtained by spectroscopic measurements (**Figure 5.3 and Chapter 4**), that pointed again to a role of this protein in phagophore expansion. However, as stated in the previous chapter, this effect would be concurrent with other factors and mechanisms such as ATG2 lipid transfer (Valverde *et al.*, 2019).

Protein coat formation in E3 presence could be responsible for the hampering of lipid mixing in the presence of E3

Kaufman *et al.* (2014) studied the reason why yeast Atg12-Atg5 were retained in the convex face of the autophagosome during phagophore expansion, and what was the function of yeast Atg16. Their results suggested that, after catalyzing Atg8 conjugation to PE, Atg12–5 was recruited by Atg8-PE, and that antiparallel arrangements of Atg16 coiled-coil domains were in charge of the Atg8–PE/Atg12–Atg5 oligomer organization to form a continuous protein layer with a meshwork-like architecture on the membranes. Taking into account these results, it is conceivable that in the human *in vitro* reconstitution system in the presence of E3, discussed in this thesis, once GABARAPL1 had reached a certain lipidation level (**Figure 5.6B**), this kind of scaffold could also be formed on our liposomes. That could explain why E3 hampered GABARAPL1 lipid mixing ability. A protein scaffold would facilitate vesicle tethering but it would also inhibit inter-vesicular lipid mixing, for which vesicle hemi-fusion or close apposition of membranes would be required (Chernomordik *et al.*, 1995; Martens & McMahon, 2008; Viguera *et al.*, 1993).

Our objective was to determine whether scaffold formation (Kaufmann *et al.*, 2014), as described in yeast (Atg8–PE assemblies with Atg12–Atg5-Atg16) and related to phagophore shaping, could also be formed with human proteins (GABARAPL1–PE and

ATG12–ATG5-ATG16L1). Taking into account the results obtained with other LC3/GABARAP family members (Chapter 4, Iriondo *et al.*, in preparation), the fact that the decrease was more marked for GABARAPL1 could indicate that more lipidated protein meant a larger scaffold formation, and therefore a less favorable situation for lipid mixing. Moreover, the results obtained with different E3 concentrations could support this hypothesis, as they showed that higher E3 concentrations promote higher lipidation levels (**Figure 5.9)** but also lower lipid mixing ability (**Figure 5.10).**

The analysis of UBL-protein localization in membranes provided valuable information. Upon ATP addition, a dense protein concentration was observed in the membranes, not only in the presence of E3 (**Figure 5.12**) but also in its absence (**Figure 5.11**). However, ATG3 and ATG7 presence in membranes were not enough to inhibit GABARAPL1 lipid mixing ability (**Figure 5.3)**, only when E3 was present among the membrane-localized proteins a hampering of lipid mixing was observed (**Figure 5.6).**

The co-localization of E3 and GABARAPL1 assessed by the liposome flotation assay after lipidation (**Figure 5.12**) supported the possibility of an interaction between E3 and GABARAPL1-PE compatible with the formation of a scaffold similar to the one formed by yeast proteins. The direct interaction seen between E3 and GABARAPL1 (**Figure 5.13**) could be similar to the one proposed by Kaufman *et al*. between Atg12 and Atg8, and therefore be responsible for scaffold formation. However, further studies are needed in order to determine whether the interacting regions of these proteins are similar to the ones described by Kaufman *et al.* An interesting experiment would be to study whether mutations in the putative interaction regions of GABARAPL1 or ATG12 could hamper the interaction and also reduce E3 lipid mixing inhibition.

Results obtained after lipidation reconstitution in GUV supported the coexistence of E3 and GABARAPL1 in their membranes (**Figure 5.18, 5.19**). Localization of GABARAPL1 all over the GUV membrane when E3 and ATP were present, suggested that GABARAPL1 had been anchored to the GUV membrane through the concerted action of the two UBL-systems, although mass spectrometry studies would be needed to confirm this hypothesis.

E3 disappearance from the contact zones (**Figure 5.22**) could have different interpretations. Scaffold formation could be inhibited in those zones due to steric hindrance, or to a stronger affinity of GABARAPL1 for another GABARAPL1 molecule than for E3 (as Kaufman *et al.* showed with the competition between scaffold formation and cargo receptor binding). These impediments could promote that, once E3 had achieved its enzymatic function, it would leave the contact zones (**Figure 5.24**).

It thus seems that, in GUV, E3 has the opportunity to reorganize and leave the contact zones although in the remaining regions both proteins coexist (**Figure 5.23, 5.24**). This is in agreement with the proposed model, according to which, in the growing zones of the autophagosome, GABARAPL1 would be lipidated in the absence of E3. Alternatively, a regulatory mechanism would exist to promote its action but not its permanence in those zones (Chapter 4). In our *in vitro* reconstitution system using LUV the lipidation reaction in the presence of E3 was easier and therefore, the potential scaffold formation would have been faster. Then, protein reorganization would not have time to happen, or would be undetectable with the available methods.

AFM results support the formation of a homogenous structure on the SLB surface upon ATP addition (**Figure 5.25, 5.26**). Its structure appeared to share formal characteristics with the one proposed by Kaufman *et al*. However, more experiments are needed to confirm these results. An important aspect to be ascertained is whether the observed structure constitutes an immobile scaffold along the plane of the membrane. It would be possible that lipid mixing inhibition did not necessarily require an immobile scaffold, perhaps formation of a dense protein structure could be enough. Irrespective of its lateral mobility, and according to flotation assays (**Figure 5.12**), it would include ATG7 or ATG3 together with E3 and GABARAPL1.

CHAPTER 6

OVERVIEW AND CONCLUSIONS

CHAPTER 6: OVERVIEW AND CONCLUSIONS

Autophagy is a highly conserved degradation pathway that is essential for eukaryotic cell homeostasis (Cable *et al.*, 2022) (**Section 1.1.2**). Among the various types of autophagy (**Section 1.1.3**) (Okamoto, 2014), macroautophagy (hereafter autophagy) is the best characterized one. Its activation is followed by the formation of a nascent double membrane structure, the phagophore, which develops into the so-called autophagosome (AP). The AP is capable of engulfing portions of the cytoplasm, then fusing with lysosomes/vacuoles, where the sequestered cargo is degraded and recycled (Noda & Inagaki, 2015) (**Section 1.1.4**). When autophagy is activated under starvation conditions, it ensures cell survival by providing nutrients (non-selective autophagy). Moreover, it can also play a housekeeping role, selectively removing misfolded or aggregated proteins, damaged and/or superfluous organelles, as well as intracellular pathogens (selective autophagy) (**Section 1.1.3**) (Anding & Baehrecke, 2017). Altered autophagy mechanisms can give rise to a whole range of diseases (**Section 1.1.2**), including cancer and neurodegeneration (Klionsky *et al.*, 2021).

To date, more than 20 ATG proteins (**Table 1.1**) involved in AP biogenesis have been reported (Nakatogawa, 2020), including two ubiquitin-like (UBL) conjugation systems: the ATG12 and the LC3/GABARAP systems (**Section 1.3**). Both are interconnected and need to act together for a proper AP assembly *in vivo* as the product of the ATG12 system, the ATG12-ATG5-ATG16L1(E3) complex, acts as a E3 enzyme for the LC3/GABARAP system (Geng & Klionsky, 2008; Martens & Fracchiolla, 2020; Nakatogawa, 2013). The concerted action of both systems results in the covalent anchoring of LC3/GABARAP proteins (**Section 1.4**) to autophagic membranes (Martens, 2016; Nakatogawa *et al.*, 2007; Tanida *et al.*, 2004). Once attached to the membrane, LC3/GABARAP proteins are involved in autophagosomal membrane expansion, closure, and fusion with lysosomes (Behrends *et al.*, 2010; Noda *et al.*, 2010; Tsuboyama *et al.*, 2016; Weidberg *et al.*, 2010; Wild *et al.*, 2014). They are also able to interact with receptors for the selective recognition of the cargo to be degraded (Johansen & Lamark, 2020; Stolz *et al.*, 2014) (**Section 1.4.3**).

A large number of studies has been devoted to the genetics, cell biology, and biochemistry of the process, particularly in what refers to the proteins. The role of lipids (**Section 1.2**) has been relatively less well studied. An even more scant attention has been paid to the biophysical aspects of AP generation and fate, although events such as the generation of a double-bilayer organelle, and its interaction with the other membranous systems in the cytosol pose interesting (and difficult) physical-chemical problems (Iriondo *et al.*, 2021). This thesis intends to shed some light onto the autophagic process by analyzing the implications of two instances of lipid-protein interactions (**Section 1.2.6**) taking part in the autophagic process, namely the interaction of LC3/GABARAP family member with CL, and with PE. The interaction with CL has been related to cargo recognition during selective degradation of mitochondria (mitophagy) (**Chapter 3**). Their interaction with PE (or lipidation) is the mode of anchoring

to the phagophore membrane and it has also been shown to lead to membrane tethering and fusion (**Chapter 4 and 5**).

The human LC3/GABARAP family can be divided into two subfamilies (**Section 1.4**): LC3A, LC3B and LC3C form the LC3 subfamily, while GABARAP, GABARAPL1 and GABARAPL2 constitute the GABARAP subfamily (Jatana *et al.*, 2020). The existence of at least six members of the LC3/GABARAP family in humans while only one, Atg8, is known in yeast (**Section 1.4.2**), suggests that each of them could play a different role. For this reason, the main aim of this thesis was to contribute to a better understanding of the differences among the six LC3/GABARAP family members during cargo recognition in selective autophagy and during phagophore expansion to form the autophagosome. To this aim, biophysical techniques, model membranes and cell lines had been used to (i) study the ability of LC3 subfamily members to recognize CL and participate in CL-mediated mitophagy, (ii) achieve the *in vitro* reconstitution of LC3/GABARAP protein lipidation in the presence and absence of E3 complex, and (iii) compare under the same conditions vesicle tethering and inter-vesicular lipid mixing promoted by LC3/GABARAP proteins.

Mitochondrial recruitment of LC3A and LC3B subfamily members upon CL externalization participates in damaged-mitochondria recognition during mitophagy.

Mitophagy is a selective autophagy pathway in which cells turn over mitochondria for quality control and adjustment to changing metabolic requirements (Pickles *et al.*, 2018). For a better understanding of the process, it is important to decipher the different modes of mitochondria signaling (Nguyen *et al.*, 2016a; Villa *et al.*, 2018) and the role of LC3/GABARAP-family members in their recognition (Johansen & Lamark, 2020) (**Section 3.1**). The importance of CL externalization to the outer mitochondrial membrane (OMM) as a signal to degrade damaged mitochondria via autophagy had been demonstrated *in vitro* and *in vivo* (Antón *et al.*, 2016; Chao *et al.*, 2019; Chu *et al.*, 2013; Kagan *et al.*, 2016) but a comparative study of the possible different roles of LC3-subfamily members was not available.

The quantitative data on LC3-CL interaction showed that LC3A and LC3C, as well as LC3B, interacted with CL-containing model membranes (**Figure 3.4**). LC3C interaction with membranes was not specific for the presence of CL, as this protein could also interact with PA (**Figure 3.7**). Moreover, despite the higher interaction displayed with CL-containing model membranes when compared with LC3A or LC3B (**Figure 3.4**), LC3C did not appear to play a role in rotenone-mediated mitophagy. These results led to the conclusion that LC3C was less effective than LC3A or LC3B in recognizing damaged mitochondria (**Figure 3.14 and 3.15**). This LC3C behavior is not surprising, since it has been shown that LC3C has different functions and targets as compared to the other subfamily members (Schaaf *et al.*, 2016), such as its specific function in antibacterial autophagy (von Muhlinen *et al.*, 2012).

The interaction of LC3A and LC3B with membranes was specific for the presence of CL (**Figure 3.7**). Examining the participation of each LC3-subfamily member in CL-mediated mitophagy showed that, apart from LC3B, LC3A was also able to participate in rotenone- or CCCP-induced mitophagy (**Figure 3.14A, 3.15, 3.16**). This would imply that LC3A

could recognize externalized CL in damaged mitochondria in cells. LC3A or LC3B recognition of CL does not by necessity exclude other similar events in mitophagy, but it could also act in cooperation with other signals and receptors (Bhujabal *et al.*, 2017). The study of endogenous LC3 proteins in SH-SY5Y cells (**Figure 3.21**) supports the conclusions obtained with the transfected GFP-tagged LC3 proteins, demonstrating the participation of LC3A and LC3B in CCCP-induced mitophagy. Moreover, the results obtained after silencing LC3A and LC3B show the important role of these proteins in CCCP-mediated mitophagy (**Figure 3.22**).

The residues in the first alpha-helix N-terminus of the protein were known to be important for LC3B recognition of CL (Chu *et al.*, 2013). Comparative binding assays using LC3A and LC3B single and double mutants showed that the key amino acids responsible for the stronger interaction of LC3A were located in positions 14 and 18 of its helix 2 (**Figure 3.11**). Moreover, Ala 14 and Lys 18 also showed to be key residues for CL recognition by LC3A during rotenone- and CCCP- induced mitophagy in cells (**Figure 3.18** and **Figure 3.19**). Results obtained with O/A, an inductor that activates numerous mitophagy pathways and receptors (Lazarou *et al.*, 2015) (**Figure 3.20**), suggested that, at variance with rotenone or CCCP, in O/A treatment the LDS (LIR docking site) of LC3A could become more relevant, while the importance of the N- terminal residues would be diminished. Moreover, the results obtained with LC3B and LC3A in the experiments with oxidized CL show that while LC3B binding decreases when CL is oxidized (**Figure 3.24C**), CL oxidation does not affect LC3A binding (**Figure 3.24B**). Thus, LC3A would recognize oxidized CL in the OMM, shielding it from the apoptotic machinery, and preventing excessive activation of apoptosis.

Therefore, in this thesis, LC3A has been identified as an additional LC3-subfamily member involved in mitophagy, and key residues for its interaction with CL have been singled out. This contribution could facilitate the design of precise modulators for this mitophagy mechanism. However, the possibility of this process being cell-, tissue- or organ-specific, or even the possibility of a crosstalk between different types of autophagy cannot be dismissed. Further investigations would be required to improve our understanding of the mechanisms triggering mitophagy, which could in turn be involved in the appearance of important neurodegenerative diseases such as Parkinson or Alzheimer.

GABARAP and GABARAPL1 are the most efficient in promoting vesicle tethering and inter-vesicular lipid mixing: Their possible participation in phagophore expansion.

Although the mode of expansion of the phagophore is still unclear (**Section 4.1**), one of the most accepted hypotheses proposes that LC3/GABARAP proteins, once they are lipidated, participate in the process, helping small vesicles to reach the nascent organelle and fuse to it, thus promoting its growth (Nakatogawa *et al.*, 2007; Weidberg *et al.*, 2010). Their participation was supported by studies with knockouts of all six family members, where they found that under those conditions autophagosomes were formed at a much slower rate, they were smaller, and often had trouble fusing with lysosomes (Nguyen *et al.*, 2016b).

Experiments reconstituting *in vitro* LC3/GABARAP lipidation in the absence of E3 complex showed that GABARAP-subfamily members were the most easily lipidated homologs. In turn, LC3A and LC3B reached low lipidation levels, but LC3C was the exception to the rule (**Figure 4.12**). In particular, while LC3A behaved similarly to LC3B, LC3C could be lipidated to a large extent in the absence of E3 (**Figure 4.13**), thus parting with the rest of the LC3 subfamily. LC3C equally failed to follow the general trends of the LC3 subfamily in cardiolipin-mediated mitophagy (Iriondo *et al.*, 2022) (**Chapter 3**).

The most extensive vesicle tethering (**Figure 4.17**) and inter-vesicular lipid mixing (**Figure 4.23**) was observed with GABARAP and GABARAPL1. The need of a lipidation threshold before proceeding to deeper levels of interaction with the host lipid bilayer was suggested by the lag phase observed in the absence of E3 (**Figure 4.19** and **Figure 4.25**). The tethering/lipidation or lipid mixing/lipidation ratios (**Figure 4.22** and **Figure 4.26**) pointed to a lower lipidation threshold for all the GABARAP proteins as compared to the LC3 subfamily, suggesting that members of the GABARAP family would be excellent candidates to assist in phagophore expansion. GABARAP and GABARAPL1 lipid mixing included some degree of inner monolayer mixing and a low amount of aqueous content mixing (**Figure 4.29** and **Figure 4.31**). The scenario is one of vesicle hemifusion with occasional fusion events, confirmed by Cryo-EM (**Figure 5.4**). A more extensive fusion would require the localized presence (perhaps in nanodomains) of lipids with an intrinsic negative lipid curvature such as diacylglycerol or cardiolipin (Iriondo *et al.*, 2021; Landajuela *et al.*, 2016) or the action of additional proteins in the growing areas of the phagophore.

In general, the results obtained in this thesis (**Figure 4.27**) show that the GABARAP subfamily is clearly more active than its LC3 homologs in the induction of membrane fusion. Since Atg8 in yeast has the ability to cause vesicle hemifusion (Nakatogawa *et al.*, 2007), LC3 proteins appear to have lost this function during evolution. This is consistent with GABARAP being more closely related to Atg8 than LC3 in evolution (**Section 1.4**). The LC3 subfamily may have become more specialized in the recognition of autophagic receptors and adapters (Johansen & Lamark, 2020), losing functions related to vesicle-fusion induction in the process (Wu *et al.*, 2015).

To sum up, the study of protein lipidation, vesicle tethering and inter-vesicular lipid mixing activities of each member of the LC3/GABARAP family under the same experimental conditions allowed a number of conclusions to be drawn (**Chapter 4**). While the large differences between GABARAPL1/GABARAP and LC3A/LC3B resemble the 'canonical' differences between the two subfamilies shown in other studies, LC3C appears as an unusual case within the LC3 subfamily, with a tethering activity akin to the one of the GABARAP subfamily. GABARAP and GABARAPL1 appear to be the most efficient homologs in the entire family for vesicle tethering and lipid mixing. However, as they are able to produce but a low level of full fusion, other proteins or the presence of other lipids that promote fusion could be needed in the *in vivo* situation. The results suggest a model in which the growing regions of the phagophore would be areas possessing a high curvature and/or with high levels of PE, compatible with points of membrane fusion.

E3 hampers lipid mixing ability of LC3/GABARAP proteins, probably due to the formation of a protein coat on top of the vesicle membrane.

The ability of human LC3/GABARAP proteins to mediate tethering and fusion in a reconstituted system including E3 complex had never been assessed, to the author's knowledge. E3 complex presence in the reconstitution system allowed a lipidation higher than 50% and similar for all the six family members tested (**Figure 4.12**). This made possible the comparison of LC3/GABARAP proteins, at similar levels of lipidation, with respect to their ability to induce tethering and fusion of membranes.

When E3 was present, lipidation levels of LC3/GABARAP proteins ran in parallel with their tethering ability. Their increased lipidation allowed the participation of any of the LC3/GABARAP members in tethering events (**Figure 4.17**). The absence of a lag phase when E3 was present (**Figure 4.19** and **Figure 4.25**) suggested that under those conditions all the proteins were able to reach their lipidation threshold earlier. E3 could equalize the various LC3/GABARAP-family members in their capacities to cause membrane tethering (**Figure 4.22**). However, E3 had not the same effect on all proteins when it came to inducing inter-vesicular lipid mixing. E3 clearly lowered the lipid mixing activity of two of the proteins, GABARAP and particularly GABARAPL1, which were most active in this respect (**Figure 4.24**). The outstanding questions were why proteins with similar lipidation levels induced similar tethering but different levels of inter-vesicular lipid mixing, and why E3 decreased their ability to produce inter-vesicular lipid mixing (**Figure 5.6**) (**Chapter 5**).

The observations by Kaufmann *et al.* with yeast proteins could provide an explanation since they observed that, once the yeast Atg8 had been lipidated, it was able to associate with E3 into a membrane scaffold (Kaufmann *et al.*, 2014). A series of experiments were performed with GABARAPL1, to test this hypothesis. Higher E3 concentrations promoted higher lipidation levels (**Figure 5.9),** but also lower lipid mixing ability (**Figure 5.10).** This could indicate that more lipidated protein meant a larger scaffold formation, and therefore a less favorable situation for lipid mixing. The joint localization of E3 and GABARAPL1 assessed by the liposome flotation assay after lipidation (**Figure 5.12**) suggested the presence of a dense protein coat on the liposomes that could be compatible with the possibility of this scaffold being built in the cellular situation. Results obtained after lipidation reconstitution in GUV supported the coexistence of E3 and GABARAPL1 in their membranes (**Figure 5.18** and **Figure 5.19**). AFM results support the formation of a homogenous structure on the vesicles upon lipidation induction (**Figure 5.25, 5.26**). Its structure appeared to share formal characteristics with the one proposed by Kaufman *et al.* (2014). However, further experiments are needed to confirm these results. An important aspect to be ascertained is whether the observed structure constitutes an immobile scaffold along the plane of the membrane. It would be also possible that lipid mixing inhibition did not necessarily require an immobile scaffold, perhaps the formation of a dense protein structure could be enough. Irrespective of its lateral mobility, and according to the flotation assays (**Figure 5.12**), it would include ATG7 or ATG3 together with E3 and GABARAPL1. Therefore, the results would be also compatible with the hypothesis that the protein coat would only be formed during the lipidation reaction. In addition, according to previous results (Kaufmann *et al.*, 2014; Nakatogawa, 2020), E3 could only form an immobile scaffold on the convex face of the growing AP as its

formation on the concave face or on the edges of the nascent AP would not allow cargo recognition, nor successive rounds of vesicle fusion and therefore phagophore growth (**Figure 6.1**).

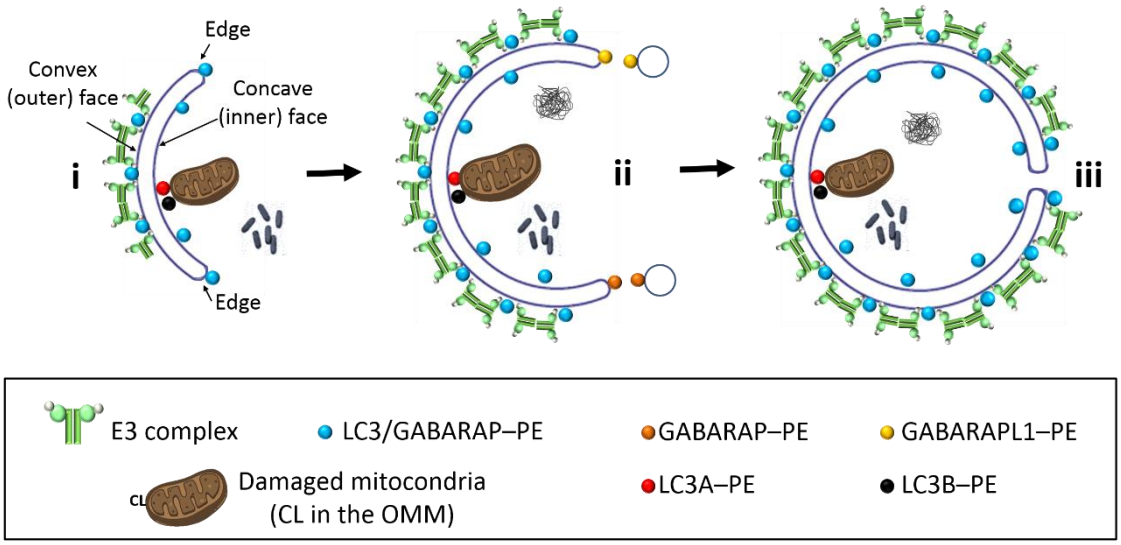

Figure 6.1. Different roles of the LC3/GABARAP proteins: a hypothetical model based on the results in this thesis. (i) LC3/GABARAP–PE is distributed along the whole phagophore surface. E3 complex could form an scaffold with lipidated LC3/GABARAP proteins on the convex side of the outer bilayer (Kaufmann *et al.*, 2014) but not on the edges and growing zones of the phagophore. The concave zone is reserved to cargo recognition and upon CL-externalization in damaged mitochondria, LC3A and LC3B could participate in their degradation (ii) GABARAP and GABARAPL1 are the main candidates to promote the phagophore expansion, particularly on the highly curved edges, as these proteins reach faster the necessary lipidation levels to trigger vesicle tethering and inter-vesicular lipid mixing. (iii) The subsequent vesicle fusion mediated by the tethering and lipid mixing ability of these proteins (with the concerted action of other factors and proteins) will cause the expansion of the phagophore.

CONCLUSIONS

1. LC3A was identified as a novel stakeholder in CL-mediated mitophagy. Ala 14 and Lys 18 residues located in its N-terminal region were shown to be important for CL recognition in model membranes and during mitophagy.
2. GABARAPL1 and GABARAP were the LC3/GABARAP family members exhibiting highest capacity to promote membrane tethering and inter-vesicular lipid mixing, which suggests a role of these proteins in the phagophore expansion process.
3. E3 promotes LC3/GABARAP lipidation, and vesicle tethering, but hampers inter-vesicular lipid mixing induced by LC3/GABARAP. The E3 inhibitory effect could be due to formation of a protein coat on vesicle membranes, which would hinder close contact between vesicles.

REFERENCES

REFERENCES

Abdollahzadeh, I., Schwarten, M., Gensch, T., Willbold, D., & Weiergräber, O. H. (2017). The Atg8 Family of Proteins-Modulating Shape and Functionality of Autophagic Membranes. *Frontiers in Genetics*, *8*(AUG). https://doi.org/10.3389/FGENE.2017.00109

Aeffner, S., Reusch, T., Weinhausen, B., & Salditt, T. (2009). Membrane fusion intermediates and the effect of cholesterol: An in-house X-ray scattering study. *The European Physical Journal E*, *30*(2), 205–214. https://doi.org/10.1140/EPJE/I2009-10466-X

Alessandrini, A., & Facci, P. (2005). AFM: a versatile tool in biophysics. *Measurement Science and Technology*, *16*(6), R65. https://doi.org/10.1088/0957-0233/16/6/R01

Alonso, A., Sáez, R., Villena, A., & Goñi, F. M. (1982). Increase in size of sonicated phospholipid vesicles in the presence of detergents. *The Journal of Membrane Biology*, *67*(1), 55–62. https://doi.org/10.1007/BF01868647

Anding, A. L., & Baehrecke, E. H. (2017). Cleaning House: Selective Autophagy of Organelles. *Developmental Cell*, *41*(1), 10–22. https://doi.org/10.1016/J.DEVCEL.2017.02.016

Angelova, M. I., & Dimitrov, D. S. (1986). Liposome electroformation. *Faraday Discussions of the Chemical Society*, *81*(0), 303–311. https://doi.org/10.1039/DC9868100303

Angelova, M. I., Soléau, S., Méléard, P., Faucon, F., & Bothorel, P. (1992). Preparation of giant vesicles by external AC electric fields. Kinetics and applications. *Trends in Colloid and Interface Science VI*, 127–131. https://doi.org/10.1007/BFB0116295

Antón, Z., Landajuela, A., Hervás, J. H., Montes, L. R., Hernández-Tiedra, S., Velasco, G., Goñi, F. M., & Alonso, A. (2016). Human Atg8-cardiolipin interactions in mitophagy: Specific properties of LC3B, GABARAPL2 and GABARAP. *Autophagy*, *12*(12), 2386–2403. https://doi.org/10.1080/15548627.2016.1240856

Antonny, B. (2011). Mechanisms of membrane curvature sensing. *Annual Review of Biochemistry*, *80*, 101–123. https://doi.org/10.1146/ANNUREV-BIOCHEM-052809-155121

Bach, M., Larance, M., James, D. E., & Ramm, G. (2011). The serine/threonine kinase ULK1 is a target of multiple phosphorylation events. *Biochemical Journal*, *440*(2), 283–291. https://doi.org/10.1042/BJ20101894

Bagatolli, L. A. (2003). Thermotropic behavior of lipid mixtures studied at the level of single vesicles: giant unilamellar vesicles and two-photon excitation fluorescence microscopy. *Methods in Enzymology*, *367*, 233–253. https://doi.org/10.1016/S0076-6879(03)67015-1

Bai, H., Inoue, J., Kawano, T., & Inazawa, J. (2012). A transcriptional variant of the LC3A gene is involved in autophagy and frequently inactivated in human cancers. *Oncogene 2012 31:40*, *31*(40), 4397–4408. https://doi.org/10.1038/onc.2011.613

Ballesteros, U., Etxaniz, A., Iriondo, M. N., Varela, Y. R., Lázaro, M., Viguera, A. R., Montes, L. R., Valle, M., Goñi, F. M., & Alonso, A. (2022). Autophagy protein LC3C binding to phospholipid and interaction with lipid membranes. *International Journal of Biological Macromolecules*, *212*, 432–441. https://doi.org/10.1016/J.IJBIOMAC.2022.05.129

Ban, T., Ishihara, T., Kohno, H., Saita, S., Ichimura, A., Maenaka, K., Oka, T., Mihara, K., & Ishihara, N. (2017). Molecular basis of selective mitochondrial fusion by heterotypic action between OPA1 and cardiolipin. *Nature Cell Biology*, *19*(7), 856–863. https://doi.org/10.1038/ncb3560

Bartlett, G. R. (1959). Phosphorus Assay in Column Chromatography. *Journal of Biological Chemistry*, *234*(3), 466–468. https://doi.org/10.1016/S0021-9258(18)70226-3

Basáñez, G., Nieva, J. L., Goñi, F. M., & Alonso, A. (1996a). Origin of the lag period in the phospholipase C cleavage of phospholipids in membranes. Concomitant vesicle aggregation and enzyme activation. *Biochemistry*, *35*(48), 15183–15187. https://doi.org/10.1021/BI9616561

Basáñez, G., Nieva, J. L., Rivas, E., Alonso, A., & Goñi, F. M. (1996b). Diacylglycerol and the promotion of lamellar-hexagonal and lamellar-isotropic phase transitions in lipids: implications for membrane fusion. *Biophysical Journal*, *70*(5), 2299–2306. https://doi.org/10.1016/S0006-3495(96)79795-3

Bassereau, P., Jin, R., Baumgart, T., Deserno, M., Dimova, R., Frolov, V. A., Bashkirov, P. V., Grubmüller, H., Jahn, R., Risselada, H. J., Johannes, L., Kozlov, M. M., Lipowsky, R., Pucadyil, T. J., Zeno, W. F., Stachowiak, J. C., Stamou, D., Breuer, A., Lauritsen, L., … Weikl, T. R. (2018). The 2018 biomembrane curvature and remodeling roadmap. *Journal of Physics D: Applied Physics*, *51*(34), 343001. https://doi.org/10.1088/1361-6463/AACB98

Basu Ball, W., Neff, J. K., & Gohil, V. M. (2018). The role of nonbilayer phospholipids in mitochondrial structure and function. *FEBS Letters*, *592*(8), 1273–1290. https://doi.org/10.1002/1873-3468.12887

Behrends, C., Sowa, M. E., Gygi, S. P., & Harper, J. W. (2010). Network organization of the human autophagy system. *Nature*, *466*(7302), 68–76. https://doi.org/10.1038/nature09204

Bento, C. F., Renna, M., Ghislat, G., Puri, C., Ashkenazi, A., Vicinanza, M., Menzies, F. M., & Rubinsztein, D. C. (2016). Mammalian Autophagy: How Does It Work? *Annual Review of Biochemistry*, *85*, 685–713. https://doi.org/10.1146/ANNUREV-BIOCHEM-060815-014556

Bhujabal, Z., Birgisdottir, Å. B., Sjøttem, E., Brenne, H. B., Øvervatn, A., Habisov, S., Kirkin, V., Lamark, T., & Johansen, T. (2017). FKBP8 recruits LC3A to mediate Parkin- independent mitophagy. *EMBO Reports*, *18*(6), 947–961. https://doi.org/10.15252/embr.201643147

Bigay, J., & Antonny, B. (2012). Curvature, Lipid Packing, and Electrostatics of Membrane Organelles: Defining Cellular Territories in Determining Specificity. *Developmental Cell*, *23*(5), 886–895. https://doi.org/10.1016/J.DEVCEL.2012.10.009

Bolte, S., & Cordelières, F. P. (2006). A guided tour into subcellular colocalization analysis in light microscopy. *Journal of Microscopy*, *224*(3), 213–232. https://doi.org/10.1111/j.1365-2818.2006.01706.x

Böttcher, C. J. F., Van gent, C. M., & Pries, C. (1961). A rapid and sensitive sub-micro phosphorus determination. *Analytica Chimica Acta*, *24*, 203–204. https://doi.org/10.1016/0003-2670(61)80041-X

Boyer-Guittaut, M., Poillet, L., Liang, Q., Bôle-Richard, E., Ouyang, X., Benavides, G. A., Chakrama, F. Z., Fraichard, A., Darley-Usmar, V. M., Despouy, G., Jouvenot, M., Delage-Mourroux, R., & Zhang, J. (2014). The role of GABARAPL1/GEC1 in autophagic flux and mitochondrial quality control in MDA-MB-436 breast cancer cells. *Autophagy*, *10*(6), 986–1003. https://doi.org/10.4161/AUTO.28390

Cable, J., Weber-Ban, E., Clausen, T., Walters, K. J., Sharon, M., Finley, D. J., Gu, Y., Hanna, J., Feng, Y., Martens, S., Simonsen, A., Hansen, M., Zhang, H., Goodwin, J. M., Reggio, A., Chang, C., Ge, L., Schulman, B. A., Deshaies, R. J., … Carra, S. (2022). Targeted protein degradation: from small molecules to complex organelles—a Keystone Symposia report. *Annals of the New York Academy of Sciences*, *1510*(1), 79–99. https://doi.org/10.1111/NYAS.14745

Cappadocia, L., & Lima, C. D. (2018). Ubiquitin-like Protein Conjugation: Structures, Chemistry, and Mechanism. *Chemical Reviews*, *118*(3), 889–918. https://doi.org/10.1021/ACS.CHEMREV.6B00737

Chabanon, M., Stachowiak, J. C., & Rangamani, P. (2017). Systems biology of cellular membranes: a convergence with biophysics. *Wiley Interdisciplinary Reviews: Systems Biology and Medicine*, *9*(5), e1386. https://doi.org/10.1002/WSBM.1386

Chakrama, F. Z., Seguin-Py, S., Le Grand, J. N., Fraichard, A., Delage-Mourroux, R., Despouy, G., Perez, V., Jouvenot, M., & Boyer-Guittaut, M. (2010). GABARAPL1 (GEC1) associates with autophagic vesicles. *Autophagy*, *6*(4), 495–505. https://doi.org/10.4161/AUTO.6.4.11819

Chao, H., Lin, C., Zuo, Q., Liu, Y., Xiao, M., Xu, X., Li, Z., Bao, Z., Chen, H., You, Y., Kochanek, P. M., Yin, H., Liu, N., Kagan, V. E., Bayır, H., & Ji, J. (2019). Cardiolipin-Dependent Mitophagy Guides Outcome after Traumatic Brain Injury. *The Journal of Neuroscience*, *39*(10), 1930–1943. https://doi.org/10.1523/JNEUROSCI.3415-17.2018

Chen, C., Li, J. G., Chen, Y., Huang, P., Wang, Y., & Liu-Chen, L. Y. (2006). GEC1 Interacts with the κ Opioid Receptor and Enhances Expression of the Receptor *. *Journal of Biological Chemistry*, *281*(12), 7983–7993. https://doi.org/10.1074/JBC.M509805200

Cheng, J., Fujita, A., Yamamoto, H., Tatematsu, T., Kakuta, S., Obara, K., Ohsumi, Y., & Fujimoto, T. (2014). Yeast and mammalian autophagosomes exhibit distinct phosphatidylinositol 3-phosphate asymmetries. *Nature Communications 2014 5:1*, *5*(1), 1–12. https://doi.org/10.1038/ncomms4207

Chernomordik, L., Chanturiya, A., Green, J., & Zimmerberg, J. (1995). The hemifusion intermediate and its conversion to complete fusion: regulation by membrane composition. *Biophysical Journal*, *69*(3), 922–929. https://doi.org/10.1016/S0006-3495(95)79966-0

Cherra, S. J., Kulich, S. M., Uechi, G., Balasubramani, M., Mountzouris, J., Day, B. W., & Chu, C. T. (2010). Regulation of the autophagy protein LC3 by phosphorylation. *Journal of Cell Biology*, *190*(4), 533–539. https://doi.org/10.1083/jcb.201002108

Chu, C. T. (2019). Mechanisms of selective autophagy and mitophagy: Implications for neurodegenerative diseases. *Neurobiology of Disease*, *122*, 23–34. https://doi.org/10.1016/j.nbd.2018.07.015

Chu, C. T., Ji, J., Dagda, R. K., Jiang, J. F., Tyurina, Y. Y., Kapralov, A. A., Tyurin, V. A., Yanamala, N., Shrivastava, I. H., Mohammadyani, D., Qiang Wang, K. Z., Zhu, J., Klein-Seetharaman, J., Balasubramanian, K., Amoscato, A. A., Borisenko, G., Huang, Z., Gusdon, A. M., Cheikhi, A., … Kagan, V. E. (2013). Cardiolipin externalization to the outer mitochondrial membrane acts as an elimination signal for mitophagy in neuronal cells. *Nature Cell Biology*, *15*(10), 1197–1205. https://doi.org/10.1038/ncb2837

Corona Velazquez, A. F., & Jackson, W. T. (2018). So Many Roads: the Multifaceted Regulation of Autophagy Induction. *Molecular and Cellular Biology*, *38*(21). https://doi.org/10.1128/MCB.00303-18

Cuervo, A. M., Bergamini, E., Brunk, U. T., Dröge, W., Ffrench, M., & Terman, A. (2005). Autophagy and aging: the importance of maintaining “clean” cells. *Autophagy*, *1*(3), 131–140. https://doi.org/10.4161/AUTO.1.3.2017

Cullis, P. R., de Kruijff, B., Verkleij, A. J., & Hope, M. J. (1986a). Lipid polymorphism and membrane fusion. *Biochemical Society Transactions*, *14*(2), 242–245. https://doi.org/10.1042/BST0140242

Cullis, P. R., Hope, M. J., & Tilcock, C. P. S. (1986b). Lipid polymorphism and the roles of lipids in membranes. *Chemistry and Physics of Lipids*, *40*(2–4), 127–144. https://doi.org/10.1016/0009-3084(86)90067-8

De Duve, C. (1963). The lysosome. *Scientific American*, *208*, 64–72. https://doi.org/10.1038/SCIENTIFICAMERICAN0563-64

de la Ballina, L. R., Munson, M. J., & Simonsen, A. (2020). Lipids and Lipid-Binding Proteins in Selective Autophagy. *Journal of Molecular Biology*, *432*(1), 135–159. https://doi.org/10.1016/J.JMB.2019.05.051

Deretic, V. (2011). Autophagy in immunity and cell-autonomous defense against intracellular microbes. *Immunological Reviews*, *240*(1), 92–104. https://doi.org/10.1111/J.1600-065X.2010.00995.X

Dooley, H. C., Razi, M., Polson, H. E. J., Girardin, S. E., Wilson, M. I., & Tooze, S. A. (2014). WIPI2 links LC3 conjugation with PI3P, autophagosome formation, and pathogen clearance by recruiting Atg12-5-16L1. *Molecular Cell*, *55*(2), 238–252. https://doi.org/10.1016/J.MOLCEL.2014.05.021

Dudek, J. (2017). Role of Cardiolipin in Mitochondrial Signaling Pathways. *Frontiers in Cell and Developmental Biology*, *5*. https://doi.org/10.3389/fcell.2017.00090

Dudley, L. J., Cabodevilla, A. G., Makar, A. N., Sztacho, M., Michelberger, T., Marsh, J. A., Houston, D. R., Martens, S., Jiang, X., & Gammoh, N. (2019). Intrinsic lipid binding activity of ATG16L1 supports efficient membrane anchoring and autophagy. *The EMBO Journal*, *38*(9). https://doi.org/10.15252/EMBJ.2018100554

Ellens, H., Bentz, J., & Szoka, F. C. (1985). H+- and Ca2+-induced fusion and destabilization of liposomes. *Biochemistry*, *24*(13), 3099–3106. https://doi.org/10.1021/BI00334A005

Engelman, D. M. (2005). Membranes are more mosaic than fluid. *Nature*, *438*(7068), 578–580. https://doi.org/10.1038/NATURE04394

Epand, R. M. (1998). Lipid polymorphism and protein–lipid interactions. *Biochimica et Biophysica Acta (BBA) - Reviews on Biomembranes*, *1376*(3), 353–368. https://doi.org/10.1016/S0304-4157(98)00015-X

Estes, D. J., & Mayer, M. (2005). Electroformation of giant liposomes from spin-coated films of lipids. *Colloids and Surfaces B: Biointerfaces*, *42*(2), 115–123. https://doi.org/10.1016/J.COLSURFB.2005.01.016

Fiske, C. H., & Subbarow, Y. (1925). The colorimetric determination of phosphorus. *Journal of Biological Chemistry*, *66*(2), 375–400. https://doi.org/10.1016/S0021-9258(18)84756-1

Fracchiolla, D., Chang, C., Hurley, J. H., & Martens, S. (2020). A PI3K-WIPI2 positive feedback loop allosterically activates LC3 lipidation in autophagy. *The Journal of Cell Biology*, *219*(7). https://doi.org/10.1083/JCB.201912098

Frezza, C., Cipolat, S., & Scorrano, L. (2007). Organelle isolation: functional mitochondria from mouse liver, muscle and cultured filroblasts. *Nature Protocols 2007 2:2*, *2*(2), 287–295. https://doi.org/10.1038/nprot.2006.478

Fujioka, Y., Noda, N. N., Nakatogawa, H., Ohsumi, Y., & Inagaki, F. (2010). Dimeric coiled-coil structure of saccharomyces cerevisiae Atg16 and its functional significance in autophagy. *Journal of Biological Chemistry*, *285*(2), 1508–1515. https://doi.org/10.1074/JBC.M109.053520

Galluzzi, L., Baehrecke, E. H., Ballabio, A., Boya, P., Pedro, J. M. B.-S., Cecconi, F., Choi, A. M., Chu, C. T., Codogno, P., Colombo, M. I., Cuervo, A. M., Debnath, J., Deretic, V., Dikic, I., Eskelinen, E.-L., Fimia, G. M., Fulda, S., Gewirtz, D. A., Green, D. R., … Kroemer, G. (2017). Molecular definitions of autophagy and related processes. *The EMBO Journal*, *36*(13), 1811–1836. https://doi.org/10.15252/EMBJ.201796697

Galluzzi, L., Pietrocola, F., Pedro, J. M. B.-S., Amaravadi, R. K., Baehrecke, E. H., Cecconi, F., Codogno, P., Debnath, J., Gewirtz, D. A., Karantza, V., Kimmelman, A., Kumar, S., Levine, B., Maiuri, M. C., Martin, S. J., Penninger, J., Piacentini, M., Rubinsztein, D. C., Simon, H.-U., … Kroemer, G. (2015). Autophagy in malignant transformation and cancer progression. *The EMBO Journal*, *34*(7), 856–880. https://doi.org/10.15252/EMBJ.201490784

Gammoh, N. (2020). The multifaceted functions of ATG16L1 in autophagy and related processes. *Journal of Cell Science*, *133*(20). https://doi.org/10.1242/JCS.249227

Geng, J., & Klionsky, D. J. (2008). The Atg8 and Atg12 ubiquitin-like conjugation systems in macroautophagy. *EMBO Reports*, *9*(9), 859–864. https://doi.org/10.1038/EMBOR.2008.163

Gennis, R. B. (1989). *Biomembranes*. https://doi.org/10.1007/978-1-4757-2065-5

Gilbert, R. J. C. (2016). Protein–lipid interactions and non-lamellar lipidic structures in membrane pore formation and membrane fusion. *Biochimica et Biophysica Acta (BBA) - Biomembranes*, *1858*(3), 487–499. https://doi.org/10.1016/J.BBAMEM.2015.11.026

Goñi, F. M. (2002). Non-permanent proteins in membranes: when proteins come as visitors (Review). *Molecular Membrane Biology*, *19*(4), 237–245. https://doi.org/10.1080/0968768021000035078

Goñi, F. M. (2014). The basic structure and dynamics of cell membranes: An update of the Singer–Nicolson model. *Biochimica et Biophysica Acta (BBA) - Biomembranes*, *1838*(6), 1467–1476. https://doi.org/10.1016/J.BBAMEM.2014.01.006

Goñi, F. M., Villar, A. V., Nieva, J. L., & Alonso, A. (2003). Interaction of phospholipases C and sphingomyelinase with liposomes. *Methods in Enzymology*, *372*, 3–19. https://doi.org/10.1016/S0076-6879(03)72001-1

Gonzalvez, F., Schug, Z. T., Houtkooper, R. H., MacKenzie, E. D., Brooks, D. G., Wanders, R. J. A., Petit, P. X., Vaz, F. M., & Gottlieb, E. (2008). Cardiolipin provides an essential activating platform for caspase-8 on mitochondria. *Journal of Cell Biology*, *183*(4), 681–696. https://doi.org/10.1083/jcb.200803129

Green M. R.; Sambrook J. (2012). *Molecular Cloning: A Laboratory Manual* (Fourth Edi). Cold Spring Harbor Laboratory Press.

Grunwald, D. S., Otto, N. M., Park, J. M., Song, D., & Kim, D. H. (2020). GABARAPs and LC3s have opposite roles in regulating ULK1 for autophagy induction. *Autophagy*, *16*(4), 600–614. https://doi.org/10.1080/15548627.2019.1632620

Hamasaki, M., Furuta, N., Matsuda, A., Nezu, A., Yamamoto, A., Fujita, N., Oomori, H., Noda, T., Haraguchi, T., Hiraoka, Y., Amano, A., & Yoshimori, T. (2013). Autophagosomes form at ER–mitochondria contact sites. *Nature 2013 495:7441*, *495*(7441), 389–393. https://doi.org/10.1038/nature11910

Hanada, T., Noda, N. N., Satomi, Y., Ichimura, Y., Fujioka, Y., Takao, T., Inagaki, F., & Ohsumi, Y. (2007). The Atg12-Atg5 conjugate has a novel E3-like activity for protein lipidation in autophagy. *The Journal of Biological Chemistry*, *282*(52), 37298–37302. https://doi.org/10.1074/JBC.C700195200

Hanna, R. A., Quinsay, M. N., Orogo, A. M., Giang, K., Rikka, S., & Gustafsson, Å. B. (2012). Microtubule-associated Protein 1 Light Chain 3 (LC3) Interacts with Bnip3 Protein to Selectively Remove Endoplasmic Reticulum and Mitochondria via Autophagy. *Journal of Biological Chemistry*, *287*(23), 19094–19104. https://doi.org/10.1074/jbc.M111.322933

He, C., & Klionsky, D. J. (2009). Regulation mechanisms and signaling pathways of autophagy. *Annual Review of Genetics*, *43*, 67–93. https://doi.org/10.1146/ANNUREV-GENET-102808-114910

He, H., Dang, Y., Dai, F., Guo, Z., Wu, J., She, X., Pei, Y., Chen, Y., Ling, W., Wu, C., Zhao, S., Liu, J. O., & Yu, L. (2003). Post-translational modifications of three members of the human MAP1LC3 family and detection of a novel type of modification for MAP1LC3B. *Journal of Biological Chemistry*, *278*(31), 29278–29287. https://doi.org/10.1074/JBC.M303800200

Hervás, J. H., Landajuela, A., Antón, Z., Shnyrova, A. V., Goñi, F. M., & Alonso, A. (2017). Human ATG3 binding to lipid bilayers: role of lipid geometry, and electric charge. *Scientific Reports*, *7*(1), 15614. https://doi.org/10.1038/s41598-017-15057-6

Hsu, P., Liu, X., Zhang, J., Wang, H.-G., Ye, J.-M., & Shi, Y. (2015). Cardiolipin remodeling by TAZ/tafazzin is selectively required for the initiation of mitophagy. *Autophagy*, *11*(4), 643–652. https://doi.org/10.1080/15548627.2015.1023984

Huang, R., Xu, Y., Wan, W., Shou, X., Qian, J., You, Z., Liu, B., Chang, C., Zhou, T., Lippincott-Schwartz, J., & Liu, W. (2015). Deacetylation of nuclear LC3 drives autophagy initiation under starvation. *Molecular Cell*, *57*(3), 456–466. https://doi.org/10.1016/j.molcel.2014.12.013

Huang, W., Choi, W., Hu, W., Mi, N., Guo, Q., Ma, M., Liu, M., Tian, Y., Lu, P., Wang, F.-L., Deng, H., Liu, L., Gao, N., Yu, L., & Shi, Y. (2012). Crystal structure and biochemical analyses reveal Beclin 1 as a novel membrane binding protein. *Cell Research*, *22*(3), 473–489. https://doi.org/10.1038/cr.2012.24

Hurley, J. H. (2006). Membrane binding domains. *Biochimica et Biophysica Acta (BBA) - Molecular and Cell Biology of Lipids*, *1761*(8), 805–811. https://doi.org/10.1016/J.BBALIP.2006.02.020

Ichimura, Y., Kirisako, T., Takao, T., Satomi, Y., Shimonishi, Y., Ishihara, N., Mizushima, N., Tanida, I., Kominami, E., Ohsumi, M., Noda, T., & Ohsumi, Y. (2000). A ubiquitin-like system mediates protein lipidation. *Nature*, *408*(6811), 488–492. https://doi.org/10.1038/35044114

Iriondo, M. N., Etxaniz, A., Antón, Z., Montes, L. R., & Alonso, A. (2021). Molecular and mesoscopic geometries in autophagosome generation. A review. *Biochimica et Biophysica Acta - Biomembranes*, *1863*(12). https://doi.org/10.1016/j.bbamem.2021.183731

Iriondo, M. N., Etxaniz, A., Varela, Y. R., Ballesteros, U., Hervás, J. H., Montes, L. R., Goñi, F. M., & Alonso, A. (2022). LC3 subfamily in cardiolipin-mediated mitophagy: a comparison of the LC3A, LC3B and LC3C homologs. *Autophagy*, 1–19. https://doi.org/10.1080/15548627.2022.2062111

Israelachvili, J. N., Marcelja, S., Horn, R. G., & Israelachvili, J. N. (1980). Physical principles of membrane organization. *Quarterly Reviews of Biophysics*, *13*(2), 121–200. https://doi.org/10.1017/S0033583500001645

Itakura, E., Kishi-Itakura, C., & Mizushima, N. (2012). The hairpin-type tail-anchored SNARE syntaxin 17 targets to autophagosomes for fusion with endosomes/lysosomes. *Cell*, *151*(6), 1256–1269. https://doi.org/10.1016/J.CELL.2012.11.001

Iyer, S. S., He, Q., Janczy, J. R., Elliott, E. I., Zhong, Z., Olivier, A. K., Sadler, J. J., Knepper-Adrian, V., Han, R., Qiao, L., Eisenbarth, S. C., Nauseef, W. M., Cassel, S. L., & Sutterwala, F. S. (2013). Mitochondrial Cardiolipin Is Required for Nlrp3 Inflammasome Activation. *Immunity*, *39*(2), 311–323. https://doi.org/10.1016/j.immuni.2013.08.001

Jass, J., Tjärnhage, T., & Puu, G. (2000). From liposomes to supported, planar bilayer structures on hydrophilic and hydrophobic surfaces: an atomic force microscopy study. *Biophysical Journal*, *79*(6), 3153. https://doi.org/10.1016/S0006-3495(00)76549-0

Jatana, N., Ascher, D. B., Pires, D. E. V., Gokhale, R. S., & Thukral, L. (2020). Human LC3 and GABARAP subfamily members achieve functional specificity via specific structural modulations. *Autophagy*, *16*(2), 239–255. https://doi.org/10.1080/15548627.2019.1606636

Johansen, T., & Lamark, T. (2020). Selective Autophagy: ATG8 Family Proteins, LIR Motifs and Cargo Receptors. *Journal of Molecular Biology*, *432*(1), 80–103. https://doi.org/10.1016/J.JMB.2019.07.016

Kagan, V. E., Jiang, J., Huang, Z., Tyurina, Y. Y., Desbourdes, C., Cottet-Rousselle, C., Dar, H. H., Verma, M., Tyurin, V. A., Kapralov, A. A., Cheikhi, A., Mao, G., Stolz, D., St. Croix, C. M., Watkins, S., Shen, Z., Li, Y., Greenberg, M. L., Tokarska-Schlattner, M., … Schlattner, U. (2016). NDPK-D (NM23-H4)-mediated externalization of cardiolipin enables elimination of depolarized mitochondria by mitophagy. *Cell Death & Differentiation*, *23*(7), 1140–1151. https://doi.org/10.1038/cdd.2015.160

Kagan, V. E., Tyurin, V. A., Jiang, J., Tyurina, Y. Y., Ritov, V. B., Amoscato, A. A., Osipov, A. N., Belikova, N. A., Kapralov, A. A., Kini, V., Vlasova, I. I., Zhao, Q., Zou, M., Di, P., Svistunenko, D. A., Kurnikov, I. V, & Borisenko, G. G. (2005). Cytochrome c acts as a cardiolipin oxygenase required for release of proapoptotic factors. *Nature Chemical Biology*, *1*(4), 223–232. https://doi.org/10.1038/nchembio727

Kaiser, S. E., Mao, K., Taherbhoy, A. M., Yu, S., Olszewski, J. L., Duda, D. M., Kurinov, I., Deng, A., Fenn, T. D., Klionsky, D. J., & Schulman, B. A. (2012). Noncanonical E2 recruitment by the autophagy E1 revealed by Atg7–Atg3 and Atg7–Atg10 structures. *Nature Structural & Molecular Biology*, *19*(12), 1242–1249. https://doi.org/10.1038/nsmb.2415

Kakuta, S., Yamaguchi, J., Suzuki, C., Sasaki, M., Kazuno, S., & Uchiyama, Y. (2017). Small GTPase Rab1B is associated with ATG9A vesicles and regulates autophagosome formation. *The FASEB Journal*, *31*(9), 3757–3773. https://doi.org/10.1096/FJ.201601052R

Kang, R., Zeh, H. J., Lotze, M. T., & Tang, D. (2011). The Beclin 1 network regulates autophagy and apoptosis. *Cell Death & Differentiation*, *18*(4), 571–580. https://doi.org/10.1038/cdd.2010.191

Kates, M., Syz, J.-Y., Gosser, D., & Haines, T. H. (1993). pH-dissociation characteristics of cardiolipin and its 2′-deoxy analogue. *Lipids*, *28*(10), 877–882. https://doi.org/10.1007/BF02537494

Kauffman, K. J., Yu, S., Jin, J., Mugo, B., Nguyen, N., O'Brien, A., Nag, S., Lystad, A. H., & Melia, T. J. (2018). Delipidation of mammalian Atg8-family proteins by each of the four ATG4 proteases. *Autophagy*, *14*(6), 992–1010. https://doi.org/10.1080/15548627.2018.1437341

Kaufmann, A., Beier, V., Franquelim, H. G., & Wollert, T. (2014). Molecular mechanism of autophagic membrane-scaffold assembly and disassembly. *Cell*, *156*(3), 469–481. https://doi.org/10.1016/J.CELL.2013.12.022

Kirisako, T., Ichimura, Y., Okada, H., Kabeya, Y., Mizushima, N., Yoshimori, T., Ohsumi, M., Takao, T., Noda, T., & Ohsumi, Y. (2000). The reversible modification regulates the membrane-binding state of Apg8/Aut7 essential for autophagy and the cytoplasm to vacuole targeting pathway. *The Journal of Cell Biology*, *151*(2), 263–275. https://doi.org/10.1083/JCB.151.2.263

Kirkin, V., Lamark, T., Sou, Y. S., Bjørkøy, G., Nunn, J. L., Bruun, J. A., Shvets, E., McEwan, D. G., Clausen, T. H., Wild, P., Bilusic, I., Theurillat, J. P., Øvervatn, A., Ishii, T., Elazar, Z., Komatsu, M., Dikic, I., & Johansen, T. (2009). A Role for NBR1 in Autophagosomal Degradation of Ubiquitinated Substrates. *Molecular Cell*, *33*(4), 505–516. https://doi.org/10.1016/J.MOLCEL.2009.01.020

Klionsky, D. J. (2008). Autophagy revisited: a conversation with Christian de Duve. *Autophagy*, *4*(6), 740–743. https://doi.org/10.4161/AUTO.6398

Klionsky, D. J., Petroni, G., Amaravadi, R. K., Baehrecke, E. H., Ballabio, A., Boya, P., Pedro, J. M. B.-S., Cadwell, K., Cecconi, F., Choi, A. M. K., Choi, M. E., Chu, C. T., Codogno, P., Colombo, M. I., Cuervo, A. M., Deretic, V., Dikic, I., Elazar, Z., Eskelinen, E.-L., … Pietrocola, F. (2021). Autophagy in major human diseases. *The EMBO Journal*, *40*(19), e108863. https://doi.org/10.15252/EMBJ.2021108863

Knorr, R. L., Dimova, R., & Lipowsky, R. (2012). Curvature of Double-Membrane Organelles Generated by Changes in Membrane Size and Composition. *PLOS ONE*, *7*(3), e32753. https://doi.org/10.1371/JOURNAL.PONE.0032753

Knorr, R. L., Lipowsky, R., & Dimova, R. (2015). Autophagosome closure requires membrane scission. *Autophagy*, *11*(11), 2134–2137. https://doi.org/10.1080/15548627.2015.1091552

Knorr, R. L., Mizushima, N., & Dimova, R. (2017). Fusion and scission of membranes: Ubiquitous topological transformations in cells. *Traffic*, *18*(11), 758–761. https://doi.org/10.1111/TRA.12509

Kost, T. A., Condreay, J. P., & Jarvis, D. L. (2005). Baculovirus as versatile vectors for protein expression in insect and mammalian cells. *Nature Biotechnology*, *23*(5), 567–575. https://doi.org/10.1038/nbt1095

Koyama-Honda, I., Itakura, E., Fujiwara, T. K., & Mizushima, N. (2013). Temporal analysis of recruitment of mammalian ATG proteins to the autophagosome formation site. *Autophagy*, *9*(10), 1491–1499. https://doi.org/10.4161/AUTO.25529

Kozlov, M. M., & Chernomordik, L. V. (2015). Membrane tension and membrane fusion. *Current Opinion in Structural Biology*, *33*, 61–67. https://doi.org/10.1016/J.SBI.2015.07.010

Kozlovsky, Y., Chernomordik, L. V., & Kozlov, M. M. (2002). Lipid Intermediates in Membrane Fusion: Formation, Structure, and Decay of Hemifusion Diaphragm. *Biophysical Journal*, *83*(5), 2634–2651. https://doi.org/10.1016/S0006-3495(02)75274-0

Krichel, C., Möckel, C., Schillinger, O., Huesgen, P. F., Sticht, H., Strodel, B., Weiergräber, O. H., Willbold, D., & Neudecker, P. (2019). Solution structure of the autophagy-related protein LC3C reveals a polyproline II motif on a mobile tether with phosphorylation site. *Scientific Reports*, *9*(1), 14167. https://doi.org/10.1038/s41598-019-48155-8

Ktistakis, N. T., & Tooze, S. A. (2016). Digesting the Expanding Mechanisms of Autophagy. *Trends in Cell Biology*, *26*(8), 624–635. https://doi.org/10.1016/J.TCB.2016.03.006

Kuma, A., Hatano, M., Matsui, M., Yamamoto, A., Nakaya, H., Yoshimori, T., Ohsumi, Y., Tokuhisa, T., & Mizushima, N. (2004). The role of autophagy during the early neonatal starvation period. *Nature*, *432*(7020), 1032–1036. https://doi.org/10.1038/NATURE03029

Kuma, A., Mizushima, N., Ishihara, N., & Ohsumi, Y. (2002). Formation of the approximately 350-kDa Apg12-Apg5.Apg16 multimeric complex, mediated by Apg16 oligomerization, is essential for autophagy in yeast. *The Journal of Biological Chemistry*, *277*(21), 18619–18625. https://doi.org/10.1074/JBC.M111889200

Landajuela, A., Hervás, J. H., Antón, Z., Montes, L. R., Gil, D., Valle, M., Rodriguez, J. F., Goñi, F. M., & Alonso, A. (2016). Lipid Geometry and Bilayer Curvature Modulate LC3/GABARAP-Mediated Model Autophagosomal Elongation. *Biophysical Journal*, *110*(2), 411–422. https://doi.org/10.1016/j.bpj.2015.11.3524

Landeta, O., Landajuela, A., Gil, D., Taneva, S., DiPrimo, C., Sot, B., Valle, M., Frolov, V. A., & Basañez, G. (2011). Reconstitution of Proapoptotic BAK Function in Liposomes Reveals a Dual Role for Mitochondrial Lipids in the BAK-driven Membrane Permeabilization Process. *Journal of Biological Chemistry*, *286*(10), 8213–8230. https://doi.org/10.1074/jbc.M110.165852

Lazarou, M., Sliter, D. A., Kane, L. A., Sarraf, S. A., Wang, C., Burman, J. L., Sideris, D. P., Fogel, A. I., & Youle, R. J. (2015). The ubiquitin kinase PINK1 recruits autophagy receptors to induce mitophagy. *Nature*, *524*(7565), 309–314. https://doi.org/10.1038/nature14893

Le Grand, J. N., Bon, K., Fraichard, A., Zhang, J., Jouvenot, M., Risold, P. Y., Boyer-Guittaut, M., & Delage-Mourroux, R. (2013). Specific Distribution of the Autophagic Protein GABARAPL1/GEC1 in the Developing and Adult Mouse Brain and Identification of Neuronal Populations Expressing GABARAPL1/GEC1. *PLOS ONE*, *8*(5), e63133. https://doi.org/10.1371/JOURNAL.PONE.0063133

Le Guerroué, F., Eck, F., Jung, J., Starzetz, T., Mittelbronn, M., Kaulich, M., & Behrends, C. (2017). Autophagosomal Content Profiling Reveals an LC3C-Dependent Piecemeal Mitophagy Pathway. *Molecular Cell*, *68*(4), 786-796.e6. https://doi.org/10.1016/j.molcel.2017.10.029

Lee, Y. K., & Lee, J. A. (2016). Role of the mammalian ATG8/LC3 family in autophagy: differential and compensatory roles in the spatiotemporal regulation of autophagy. *BMB Reports*, *49*(8), 424–430. https://doi.org/10.5483/BMBRep.2016.49.8.081

Leikin, S. L., Kozlov, M. M., Chernomordik, L. V., Markin, V. S., & Chizmadzhev, Y. A. (1987). Membrane fusion: Overcoming of the hydration barrier and local restructuring. *Journal of Theoretical Biology*, *129*(4), 411–425. https://doi.org/10.1016/S0022-5193(87)80021-8

Leil, T. A., Chen, Z. W., Chang, C. S. S., & Olsen, R. W. (2004). GABAA Receptor-Associated Protein Traffics GABAA Receptors to the Plasma Membrane in Neurons. *Journal of Neuroscience*, *24*(50), 11429–11438. https://doi.org/10.1523/JNEUROSCI.3355-04.2004

Levine, B., & Kroemer, G. (2019). Leading Edge Review Biological Functions of Autophagy Genes: A Disease Perspective. *Cell*, *176*, 11–42. https://doi.org/10.1016/j.cell.2018.09.048

Li, S. S., & Giometti, C. S. (2007). A combinatorial approach to studying protein complex composition by employing size-exclusion chromatography and proteome analysis. *Journal of Separation Science*, *30*(10), 1549–1555. https://doi.org/10.1002/JSSC.200700011

Li, X. X., Tsoi, B., Li, Y. F., Kurihara, H., & He, R. R. (2015). Cardiolipin and Its Different Properties in Mitophagy and Apoptosis. *Journal of Histochemistry & Cytochemistry*, *63*(5), 301–311. https://doi.org/10.1369/0022155415574818

Liu, J., Epand, R. F., Durrant, D., Grossman, D., Chi, N., Epand, R. M., & Lee, R. M. (2008). Role of Phospholipid Scramblase 3 in the Regulation of Tumor Necrosis Factor-α-Induced Apoptosis †. *Biochemistry*, *47*(15), 4518–4529. https://doi.org/10.1021/bi701962c

Liu, L., Feng, D., Chen, G., Chen, M., Zheng, Q., Song, P., Ma, Q., Zhu, C., Wang, R., Qi, W., Huang, L., Xue, P., Li, B., Wang, X., Jin, H., Wang, J., Yang, F., Liu, P., Zhu, Y., … Chen, Q. (2012). Mitochondrial outer-membrane protein FUNDC1 mediates hypoxia-induced mitophagy in mammalian cells. *Nature Cell Biology*, *14*(2), 177–185. https://doi.org/10.1038/ncb2422

Liu, X., Li, Y., Wang, X., Xing, R., Liu, K., Gan, Q., Tang, C., Gao, Z., Jian, Y., Luo, S., Guo, W., & Yang, C. (2017). The BEACH-containing protein WDR81 coordinates p62 and LC3C to promote aggrephagy. *Journal of Cell Biology*, *216*(5), 1301–1320. https://doi.org/10.1083/jcb.201608039

Lizama, B. N., & Chu, C. T. (2021). Neuronal autophagy and mitophagy in Parkinson's disease. *Molecular Aspects of Medicine*, *82*. https://doi.org/10.1016/J.MAM.2021.100972

Luckow, V. A., Lee, S. C., Barry, G. F., & Olins, P. O. (1993). Efficient generation of infectious recombinant baculoviruses by site-specific transposon-mediated insertion of foreign genes into a baculovirus genome propagated in Escherichia coli. *Journal of Virology*, *67*(8), 4566. https://doi.org/10.1128/JVI.67.8.4566-4579.1993

Lynch-Day, M. A., Mao, K., Wang, K., Zhao, M., & Klionsky, D. J. (2012). The Role of Autophagy in Parkinson's Disease. *Cold Spring Harbor Perspectives in Medicine*, *2*(4), a009357. https://doi.org/10.1101/CSHPERSPECT.A009357

Lystad, A. H., Carlsson, S. R., de la Ballina, L. R., Kauffman, K. J., Nag, S., Yoshimori, T., Melia, T. J., & Simonsen, A. (2019). Distinct functions of ATG16L1 isoforms in membrane binding and LC3B lipidation in autophagy-related processes. *Nature Cell Biology*, *21*(3), 372–383. https://doi.org/10.1038/S41556-019-0274-9

Maeda, S., Otomo, C., & Otomo, T. (2019). The autophagic membrane tether ATG2A transfers lipids between membranes. *ELife*, *8*. https://doi.org/10.7554/ELIFE.45777

Mann, S. S., & Hammarback, J. A. (1994). Molecular characterization of light chain 3. A microtubule binding subunit of MAP1A and MAP1B. *Journal of Biological Chemistry*, *269*(15), 11492–11497. https://doi.org/10.1016/S0021-9258(19)78150-2

Mansuy, V., Boireau, W., Fraichard, A., Schlick, J. L., Jouvenot, M., & Delage-Mourroux, R. (2004). GEC1, a protein related to GABARAP, interacts with tubulin and GABAA receptor. *Biochemical and Biophysical Research Communications*, *325*(2), 639–648. https://doi.org/10.1016/J.BBRC.2004.10.072

Markin, V. S., & Albanesi, J. P. (2002). Membrane Fusion: Stalk Model Revisited. *Biophysical Journal*, *82*(2), 693–712. https://doi.org/10.1016/S0006-3495(02)75432-5

Martens, S. (2016). No ATG8s, no problem? How LC3/GABARAP proteins contribute to autophagy. *Journal of Cell Biology*, *215*(6), 761–763. https://doi.org/10.1083/jcb.201611116

Martens, S., & Fracchiolla, D. (2020). Activation and targeting of ATG8 protein lipidation. *Cell Discovery*, *6*(1). https://doi.org/10.1038/S41421-020-0155-1

Martens, S., & McMahon, H. T. (2008). Mechanisms of membrane fusion: disparate players and common principles. *Nature Reviews Molecular Cell Biology*, *9*(7), 543–556. https://doi.org/10.1038/nrm2417

Martin, S. R., & Schilstra, M. J. (2008). Circular Dichroism and Its Application to the Study of Biomolecules. *Methods in Cell Biology*, *84*, 263–293. https://doi.org/10.1016/S0091-679X(07)84010-6

Martinez-Vicente, M., Talloczy, Z., Wong, E., Tang, G., Koga, H., Kaushik, S., De Vries, R., Arias, E., Harris, S., Sulzer, D., & Cuervo, A. M. (2010). Cargo recognition failure is responsible for inefficient autophagy in Huntington's disease. *Nature Neuroscience*, *13*(5), 567–576. https://doi.org/10.1038/NN.2528

Maruyama, T., Alam, J. M., Fukuda, T., Kageyama, S., Kirisako, H., Ishii, Y., Shimada, I., Ohsumi, Y., Komatsu, M., Kanki, T., Nakatogawa, H., & Noda, N. N. (2021). Membrane perturbation by lipidated Atg8 underlies autophagosome biogenesis. *Nature Structural & Molecular Biology*, *28*(7), 583–593. https://doi.org/10.1038/s41594-021-00614-5

Maruyama, T., & Noda, N. N. (2017). Autophagy-regulating protease Atg4: structure, function, regulation and inhibition. *The Journal of Antibiotics*, *71*(1), 72–78. https://doi.org/10.1038/ja.2017.104

Matoba, K., Kotani, T., Tsutsumi, A., Tsuji, T., Mori, T., Noshiro, D., Sugita, Y., Nomura, N., Iwata, S., Ohsumi, Y., Fujimoto, T., Nakatogawa, H., Kikkawa, M., & Noda, N. N. (2020). Atg9 is a lipid scramblase that mediates autophagosomal membrane expansion. *Nature Structural & Molecular Biology*, *27*(12), 1185–1193. https://doi.org/10.1038/s41594-020-00518-w

Mayer, L. D., Hope, M. J., & Cullis, P. R. (1986). Vesicles of variable sizes produced by a rapid extrusion procedure. *Biochimica et Biophysica Acta (BBA) - Biomembranes*, *858*(1), 161–168. https://doi.org/10.1016/0005-2736(86)90302-0

Melia, T. J., Lystad, A. H., & Simonsen, A. (2020). Autophagosome biogenesis: From membrane growth to closure. *Journal of Cell Biology*, *219*(6). https://doi.org/10.1083/JCB.202002085/151729

Mercer, T. J., & Tooze, S. A. (2021). The ingenious ULKs: expanding the repertoire of the ULK complex with phosphoproteomics. *Autophagy*, *17*(12), 4491–4493. https://doi.org/10.1080/15548627.2021.1968615

Metlagel, Z., Otomo, C., Takaesu, G., & Otomo, T. (2013). Structural basis of ATG3 recognition by the autophagic ubiquitin-like protein ATG12. *Proceedings of the National Academy of Sciences of the United States of America*, *110*(47), 18844–18849. https://doi.org/10.1073/PNAS.1314755110

Mi, N., Chen, Y., Wang, S., Chen, M., Zhao, M., Yang, G., Ma, M., Su, Q., Luo, S., Shi, J., Xu, J., Guo, Q., Gao, N., Sun, Y., Chen, Z., & Yu, L. (2015). CapZ regulates autophagosomal membrane shaping by promoting actin assembly inside the isolation membrane. *Nature Cell Biology*, *17*(9), 1112–1123. https://doi.org/10.1038/ncb3215

Minton, A. P. (2016). Recent applications of light scattering measurement in the biological and biopharmaceutical sciences. *Analytical Biochemistry*, *501*, 4–22. https://doi.org/10.1016/J.AB.2016.02.007

Mizushima, N. (2020). The ATG conjugation systems in autophagy. *Current Opinion in Cell Biology*, *63*, 1–10. https://doi.org/10.1016/J.CEB.2019.12.001

Mizushima, N., Noda, T., & Ohsumi, Y. (1999). Apg16p is required for the function of the Apg12p–Apg5p conjugate in the yeast autophagy pathway. *The EMBO Journal*, *18*(14), 3888–3896. https://doi.org/10.1093/EMBOJ/18.14.3888

Mizushima, N., Sugita, H., Yoshimori, T., & Ohsumi, Y. (1998). A New Protein Conjugation System in Human: The counterpart of the yeast Apg12p conjugation system essential for autophagy. *Journal of Biological Chemistry*, *273*(51), 33889–33892. https://doi.org/10.1074/JBC.273.51.33889

Mizushima, N., Yamamoto, A., Hatano, M., Kobayashi, Y., Kabey, Y., Suzuki, K., Tokuhis, T., Ohsumi, Y., & Yoshimori, T. (2001). Dissection of autophagosome formation using Apg5-deficient mouse embryonic stem cells. *The Journal of Cell Biology*, *152*(4), 657–667. https://doi.org/10.1083/JCB.152.4.657

Montava-Garriga, L., & Ganley, I. G. (2020). Outstanding Questions in Mitophagy: What We Do and Do Not Know. *Journal of Molecular Biology*, *432*(1), 206–230. https://doi.org/10.1016/J.JMB.2019.06.032

Murakawa, T., Yamaguchi, O., Hashimoto, A., Hikoso, S., Takeda, T., Oka, T., Yasui, H., Ueda, H., Akazawa, Y., Nakayama, H., Taneike, M., Misaka, T., Omiya, S.,

Shah, A. M., Yamamoto, A., Nishida, K., Ohsumi, Y., Okamoto, K., Sakata, Y., & Otsu, K. (2015). Bcl-2-like protein 13 is a mammalian Atg32 homologue that mediates mitophagy and mitochondrial fragmentation. *Nature Communications*, *6*(1), 7527. https://doi.org/10.1038/ncomms8527

Nair, U., Jotwani, A., Geng, J., Gammoh, N., Richerson, D., Yen, W. L., Griffith, J., Nag, S., Wang, K., Moss, T., Baba, M., McNew, J. A., Jiang, X., Reggiori, F., Melia, T. J., & Klionsky, D. J. (2011). SNARE proteins are required for macroautophagy. *Cell*, *146*(2), 290–302. https://doi.org/10.1016/J.CELL.2011.06.022

Nakatogawa, H. (2013). Two ubiquitin-like conjugation systems that mediate membrane formation during autophagy. *Essays in Biochemistry*, *55*(1), 39–50. https://doi.org/10.1042/bse0550039

Nakatogawa, H. (2020). Mechanisms governing autophagosome biogenesis. *Nature Reviews. Molecular Cell Biology*, *21*(8), 439–458. https://doi.org/10.1038/S41580-020-0241-0

Nakatogawa, H., Ichimura, Y., & Ohsumi, Y. (2007). Atg8, a ubiquitin-like protein required for autophagosome formation, mediates membrane tethering and hemifusion. *Cell*, *130*(1), 165–178. https://doi.org/10.1016/J.CELL.2007.05.021

Nath, S., Dancourt, J., Shteyn, V., Puente, G., Fong, W. M., Nag, S., Bewersdorf, J., Yamamoto, A., Antonny, B., & Melia, T. J. (2014). Lipidation of the LC3/GABARAP family of autophagy proteins relies on a membrane-curvature-sensing domain in Atg3. *Nature Cell Biology*, *16*(5), 415–424. https://doi.org/10.1038/ncb2940

Nemos, C., Mansuy, V., Vernier-Magnin, S., Fraichard, A., Jouvenot, M., & Delage-Mourroux, R. égis. (2003). Expression of gec1/GABARAPL1 versus GABARAP mRNAs in human: predominance of gec1/GABARAPL1 in the central nervous system. *Molecular Brain Research*, *119*(2), 216–219. https://doi.org/10.1016/J.MOLBRAINRES.2003.09.011

Nguyen, N., Shteyn, V., & Melia, T. J. (2017). Sensing Membrane Curvature in Macroautophagy. *Journal of Molecular Biology*, *429*(4), 457–472. https://doi.org/10.1016/J.JMB.2017.01.006

Nguyen, T. N., Padman, B. S., & Lazarou, M. (2016a). Deciphering the Molecular Signals of PINK1/Parkin Mitophagy. *Trends in Cell Biology*, *26*(10), 733–744. https://doi.org/10.1016/J.TCB.2016.05.008

Nguyen, T. N., Padman, B. S., Usher, J., Oorschot, V., Ramm, G., & Lazarou, M. (2016b). Atg8 family LC3/GABARAP proteins are crucial for autophagosome–lysosome fusion but not autophagosome formation during PINK1/Parkin mitophagy and starvation. *Journal of Cell Biology*, *215*(6), 857–874. https://doi.org/10.1083/jcb.201607039

Nieva, J. L., Goñi, F. M., & Alonso, A. (1989). Liposome Fusion Catalytically Induced by Phospholipase C. *Biochemistry*, *28*(18), 7364–7367. https://doi.org/10.1021/BI00444A032

Nishimura, T., Tamura, N., Kono, N., Shimanaka, Y., Arai, H., Yamamoto, H., & Mizushima, N. (2017). Autophagosome formation is initiated at phosphatidylinositol synthase-enriched ER subdomains. *The EMBO Journal*, *36*(12), 1719–1735. https://doi.org/10.15252/EMBJ.201695189

Nixon, R. A., Wegiel, J., Kumar, A., Yu, W. H., Peterhoff, C., Cataldo, A., & Cuervo, A. M. (2005). Extensive Involvement of Autophagy in Alzheimer Disease: An Immuno-Electron Microscopy Study. *Journal of Neuropathology & Experimental Neurology*,

64(2), 113–122. https://doi.org/10.1093/JNEN/64.2.113

Noda, N. N., & Fujioka, Y. (2015). Atg1 family kinases in autophagy initiation. *Cellular and Molecular Life Sciences*, *72*(16), 3083–3096. https://doi.org/10.1007/S00018-015-1917-Z

Noda, N. N., & Inagaki, F. (2015). Mechanisms of Autophagy. *Annual Review of Biophysics*, *44*, 101–122. https://doi.org/10.1146/annurev-biophys-060414-034248

Noda, N. N., Ohsumi, Y., & Inagaki, F. (2010). Atg8-family interacting motif crucial for selective autophagy. *FEBS Letters*, *584*(7), 1379–1385. https://doi.org/10.1016/J.FEBSLET.2010.01.018

Noda, N. N., Satoo, K., Fujioka, Y., Kumeta, H., Ogura, K., Nakatogawa, H., Ohsumi, Y., & Inagaki, F. (2011). Structural basis of Atg8 activation by a homodimeric E1, Atg7. *Molecular Cell*, *44*(3), 462–475. https://doi.org/10.1016/J.MOLCEL.2011.08.035

Novak, I., Kirkin, V., McEwan, D. G., Zhang, J., Wild, P., Rozenknop, A., Rogov, V., Löhr, F., Popovic, D., Occhipinti, A., Reichert, A. S., Terzic, J., Dötsch, V., Ney, P. A., & Dikic, I. (2010). Nix is a selective autophagy receptor for mitochondrial clearance. *EMBO Reports*, *11*(1), 45–51. https://doi.org/10.1038/embor.2009.256

Obara, K., Sekito, T., Niimi, K., & Ohsumi, Y. (2008). The Atg18-Atg2 complex is recruited to autophagic membranes via phosphatidylinositol 3-phosphate and exerts an essential function. *The Journal of Biological Chemistry*, *283*(35), 23972–23980. https://doi.org/10.1074/JBC.M803180200

Ohashi, K., Otomo, C., Metlagel, Z., & Otomo, T. (2019). Structural Studies of Mammalian Autophagy Lipidation Complex. *Methods in Molecular Biology*, *1880*, 57–75. https://doi.org/10.1007/978-1-4939-8873-0_3

Ohsumi, Y. (2014). Historical landmarks of autophagy research. *Cell Research 2014 24:1*, *24*(1), 9–23. https://doi.org/10.1038/cr.2013.169

Okamoto, K. (2014). Organellophagy: Eliminating cellular building blocks via selective autophagy. *Journal of Cell Biology*, *205*(4), 435–445. https://doi.org/10.1083/JCB.201402054

Onishi, M., Yamano, K., Sato, M., Matsuda, N., & Okamoto, K. (2021). Molecular mechanisms and physiological functions of mitophagy. *The EMBO Journal*, *40*(3), 1–27. https://doi.org/10.15252/embj.2020104705

Osawa, T., Kotani, T., Kawaoka, T., Hirata, E., Suzuki, K., Nakatogawa, H., Ohsumi, Y., & Noda, N. N. (2019). Atg2 mediates direct lipid transfer between membranes for autophagosome formation. *Nature Structural & Molecular Biology*, *26*(4), 281–288. https://doi.org/10.1038/S41594-019-0203-4

Otomo, C., Metlagel, Z., Takaesu, G., & Otomo, T. (2013). Structure of the human ATG12~ATG5 conjugate required for LC3 lipidation in autophagy. *Nature Structural & Molecular Biology*, *20*(1), 59–66. https://doi.org/10.1038/NSMB.2431

Pickles, S., Vigié, P., & Youle, R. J. (2018). Mitophagy and Quality Control Mechanisms in Mitochondrial Maintenance. *Current Biology*, *28*(4), R170–R185. https://doi.org/10.1016/j.cub.2018.01.004

Planas-Iglesias, J., Dwarakanath, H., Mohammadyani, D., Yanamala, N., Kagan, V. E., & Klein-Seetharaman, J. (2015). Cardiolipin Interactions with Proteins. *Biophysical Journal*, *109*(6), 1282–1294. https://doi.org/10.1016/j.bpj.2015.07.034

Popelka, H., & Klionsky, D. J. (2021). Multiple structural rearrangements mediated by high-plasticity regions in Atg3 are key for efficient conjugation of Atg8 to PE during autophagy. *Autophagy*, *17*(8), 1805–1808. https://doi.org/10.1080/15548627.2021.1954457

Popelka, H., Reinhart, E. F., Metur, S. P., Leary, K. A., Ragusa, M. J., & Klionsky, D. J. (2021). Membrane Binding and Homodimerization of Atg16 Via Two Distinct Protein Regions is Essential for Autophagy in Yeast. *Journal of Molecular Biology*, *433*(5). https://doi.org/10.1016/J.JMB.2021.166809

Proikas-Cezanne, T., Takacs, Z., Dönnes, P., & Kohlbacher, O. (2015). WIPI proteins: Essential PtdIns3P effectors at the nascent autophagosome. *Journal of Cell Science*, *128*(2), 207–217. https://doi.org/10.1242/JCS.146258

Ravenhill, B. J., Boyle, K. B., von Muhlinen, N., Ellison, C. J., Masson, G. R., Otten, E. G., Foeglein, A., Williams, R., & Randow, F. (2019). The Cargo Receptor NDP52 Initiates Selective Autophagy by Recruiting the ULK Complex to Cytosol-Invading Bacteria. *Molecular Cell*, *74*(2), 320-329.e6. https://doi.org/10.1016/J.MOLCEL.2019.01.041

Ravikumar, B., Duden, R., & Rubinsztein, D. C. (2002). Aggregate-prone proteins with polyglutamine and polyalanine expansions are degraded by autophagy. *Human Molecular Genetics*, *11*(9), 1107–1117. https://doi.org/10.1093/HMG/11.9.1107

Romanov, J., Walczak, M., Ibiricu, I., Schüchner, S., Ogris, E., Kraft, C., & Martens, S. (2012). Mechanism and functions of membrane binding by the Atg5-Atg12/Atg16 complex during autophagosome formation. *The EMBO Journal*, *31*(22), 4304–4317. https://doi.org/10.1038/EMBOJ.2012.278

Ryan, T., Bamm, V. V., Stykel, M. G., Coackley, C. L., Humphries, K. M., Jamieson-Williams, R., Ambasudhan, R., Mosser, D. D., Lipton, S. A., Harauz, G., & Ryan, S. D. (2018). Cardiolipin exposure on the outer mitochondrial membrane modulates α-synuclein. *Nature Communications*, *9*(1), 817. https://doi.org/10.1038/s41467-018-03241-9

Saha, S., Panigrahi, D. P., Patil, S., & Bhutia, S. K. (2018). Autophagy in health and disease: A comprehensive review. *Biomedicine & Pharmacotherapy*, *104*, 485–495. https://doi.org/10.1016/J.BIOPHA.2018.05.007

Sani, M.-A., Dufourc, E. J., & Gröbner, G. (2009). How does the Bax-α1 targeting sequence interact with mitochondrial membranes? The role of cardiolipin. *Biochimica et Biophysica Acta (BBA) - Biomembranes*, *1788*(3), 623–631. https://doi.org/10.1016/j.bbamem.2008.12.014

Sawa-Makarska, J., Baumann, V., Coudevylle, N., von Bülow, S., Nogellova, V., Abert, C., Schuschnig, M., Graef, M., Hummer, G., & Martens, S. (2020). Reconstitution of autophagosome nucleation defines Atg9 vesicles as seeds for membrane formation. *Science*, *369*(6508). https://doi.org/10.1126/SCIENCE.AAZ7714

Schaaf, M. B. E., Keulers, T. G., Vooijs, M. A., & Rouschop, K. M. A. (2016). LC3/GABARAP family proteins: autophagy- (un)related functions. *The FASEB Journal*, *30*(12), 3961–3978. https://doi.org/10.1096/fj.201600698R

Scherz-Shouval, R., & Elazar, Z. (2011). Regulation of autophagy by ROS: physiology and pathology. *Trends in Biochemical Sciences*, *36*(1), 30–38. https://doi.org/10.1016/J.TIBS.2010.07.007

Schlattner, U., Tokarska-Schlattner, M., Ramirez, S., Tyurina, Y. Y., Amoscato, A. A., Mohammadyani, D., Huang, Z., Jiang, J., Yanamala, N., Seffouh, A., Boissan, M., Epand, R. F., Epand, R. M., Klein-Seetharaman, J., Lacombe, M.-L., & Kagan, V. E. (2013). Dual Function of Mitochondrial Nm23-H4 Protein in Phosphotransfer and Intermembrane Lipid Transfer. *Journal of Biological Chemistry*, *288*(1), 111–121. https://doi.org/10.1074/jbc.M112.408633

Schwarten, M., Mohrlüder, J., Ma, P., Stoldt, M., Thielmann, Y., Stangler, T., Hersch, N., Hoffmann, B., Merkel, R., & Willbold, D. (2009). Nix directly binds to GABARAP: a possible crosstalk between apoptosis and autophagy. *Autophagy*, *5*(5), 690–698. https://doi.org/10.4161/AUTO.5.5.8494

Sentelle, R. D., Senkal, C. E., Jiang, W., Ponnusamy, S., Gencer, S., Panneer Selvam, S., Ramshesh, V. K., Peterson, Y. K., Lemasters, J. J., Szulc, Z. M., Bielawski, J., & Ogretmen, B. (2012). Ceramide targets autophagosomes to mitochondria and induces lethal mitophagy. *Nature Chemical Biology*, *8*(10), 831–838. https://doi.org/10.1038/nchembio.1059

Settembre, C., Fraldi, A., Rubinsztein, D. C., & Ballabio, A. (2008). Lysosomal storage diseases as disorders of autophagy. *Autophagy*, *4*(1), 113–114. https://doi.org/10.4161/AUTO.5227

Shen, H. M., & Mizushima, N. (2014). At the end of the autophagic road: an emerging understanding of lysosomal functions in autophagy. *Trends in Biochemical Sciences*, *39*(2), 61–71. https://doi.org/10.1016/J.TIBS.2013.12.001

Shpilka, T., Weidberg, H., Pietrokovski, S., & Elazar, Z. (2011). Atg8: An autophagy-related ubiquitin-like protein family. *Genome Biology*, *12*(7), 1–11. https://doi.org/10.1186/GB-2011-12-7-226

Sica, V., Galluzzi, L., Bravo-San Pedro, J. M., Izzo, V., Maiuri, M. C., & Kroemer, G. (2015). Organelle-Specific Initiation of Autophagy. *Molecular Cell*, *59*(4), 522–539. https://doi.org/10.1016/J.MOLCEL.2015.07.021

Simunovic, M., Voth, G. A., Callan-Jones, A., & Bassereau, P. (2015). When Physics Takes Over: BAR Proteins and Membrane Curvature. *Trends in Cell Biology*, *25*(12), 780–792. https://doi.org/10.1016/J.TCB.2015.09.005

Singer, S. J., & Nicolson, G. L. (1972). The Fluid Mosaic Model of the Structure of Cell Membranes. *Science*, *175*(4023), 720–731. https://doi.org/10.1126/SCIENCE.175.4023.720

Sora, V., Kumar, M., Maiani, E., Lambrughi, M., Tiberti, M., & Papaleo, E. (2020). Structure and Dynamics in the ATG8 Family From Experimental to Computational Techniques. *Frontiers in Cell and Developmental Biology*, *8*, 420. https://doi.org/10.3389/FCELL.2020.00420

Sou, Y. S., Tanida, I., Komatsu, M., Ueno, T., & Kominami, E. (2006). Phosphatidylserine in Addition to Phosphatidylethanolamine Is an in Vitro Target of the Mammalian Atg8 Modifiers, LC3, GABARAP, and GATE-16. *Journal of Biological Chemistry*, *281*(6), 3017–3024. https://doi.org/10.1074/JBC.M505888200

Stadel, D., Millarte, V., Tillmann, K. D., Huber, J., Tamin-Yecheskel, B. C., Akutsu, M., Demishtein, A., Ben-Zeev, B., Anikster, Y., Perez, F., Dötsch, V., Elazar, Z., Rogov, V., Farhan, H., & Behrends, C. (2015). TECPR2 Cooperates with LC3C to Regulate COPII-Dependent ER Export. *Molecular Cell*, *60*(1), 89–104. https://doi.org/10.1016/J.MOLCEL.2015.09.010

Stepanyants, N., Macdonald, P. J., Francy, C. A., Mears, J. A., Qi, X., & Ramachandran, R. (2015). Cardiolipin's propensity for phase transition and its reorganization by dynamin-related protein 1 form a basis for mitochondrial membrane fission. *Molecular Biology of the Cell*, *26*(17), 3104–3116. https://doi.org/10.1091/mbc.E15-06-0330

Stolz, A., Ernst, A., & Dikic, I. (2014). Cargo recognition and trafficking in selective autophagy. *Nature Cell Biology*, *16*(6), 495–501. https://doi.org/10.1038/ncb2979

Struck, D. K., Hoekstra, D., & Pagano, R. E. (1981). Use of resonance energy transfer to monitor membrane fusion. *Biochemistry*, *20*(14), 4093–4099. https://doi.org/10.1021/BI00517A023

Suetsugu, S., Kurisu, S., & Takenawa, T. (2014). Dynamic shaping of cellular membranes by phospholipids and membrane-deforming proteins. *Physiological Reviews*, *94*(4), 1219–1248. https://doi.org/10.1152/PHYSREV.00040.2013

Sugawara, K., Suzuki, N. N., Fujioka, Y., Mizushima, N., Ohsumi, Y., & Inagaki, F. (2004). The crystal structure of microtubule-associated protein light chain 3, a mammalian homologue of Saccharomyces cerevisiae Atg8. *Genes to Cells*, *9*(7), 611–618. https://doi.org/10.1111/j.1356-9597.2004.00750.x

Szoka, F., & Papahadjopoulos, D. (1980). Comparative properties and methods of preparation of lipid vesicles (liposomes). *Annual Review of Biophysics and Bioengineering*, *9*, 467–508. https://doi.org/10.1146/ANNUREV.BB.09.060180.002343

Takahashi, Y., Liang, X., Hattori, T., Tang, Z., He, H., Chen, H., Liu, X., Abraham, T., Imamura-Kawasawa, Y., Buchkovich, N. J., Young, M. M., & Wang, H. G. (2019). VPS37A directs ESCRT recruitment for phagophore closure. *The Journal of Cell Biology*, *218*(10), 3336–3354. https://doi.org/10.1083/JCB.201902170

Tanida, I., Ueno, T., & Kominami, E. (2004). LC3 conjugation system in mammalian autophagy. *The International Journal of Biochemistry & Cell Biology*, *36*(12), 2503–2518. https://doi.org/10.1016/J.BIOCEL.2004.05.009

Tanida, I., Wakabayashi, M., Kanematsu, T., Minematsu-Ikeguchi, N., Sou, Y. S., Hirata, M., Ueno, T., & Kominami, E. (2006). Lysosomal turnover of GABARAP-phospholipid conjugate is activated during differentiation of C2C12 cells to myotubes without inactivation of the mTor kinase-signaling pathway. *Autophagy*, *2*(4), 264–271. https://doi.org/10.4161/AUTO.2871

Tsuboyama, K., Koyama-Honda, I., Sakamaki, Y., Koike, M., Morishita, H., & Mizushima, N. (2016). The ATG conjugation systems are important for degradation of the inner autophagosomal membrane. *Science*, *354*(6315), 1036–1041. https://doi.org/10.1126/science.aaf6136

Tsukada, M., & Ohsumi, Y. (1993). Isolation and characterization of autophagy-defective mutants of Saccharomyces cerevisiae. *FEBS Letters*, *333*(1–2), 169–174. https://doi.org/10.1016/0014-5793(93)80398-E

Turco, E., & Martens, S. (2016). Insights into autophagosome biogenesis from in vitro reconstitutions. *Journal of Structural Biology*, *196*(1), 29–36. https://doi.org/10.1016/J.JSB.2016.04.005

Turco, E., Witt, M., Abert, C., Bock-Bierbaum, T., Su, M. Y., Trapannone, R., Sztacho, M., Danieli, A., Shi, X., Zaffagnini, G., Gamper, A., Schuschnig, M., Fracchiolla, D., Bernklau, D., Romanov, J., Hartl, M., Hurley, J. H., Daumke, O., & Martens, S. (2019). FIP200 Claw Domain Binding to p62 Promotes Autophagosome Formation at Ubiquitin Condensates. *Molecular Cell*, *74*(2), 330-346.e11. https://doi.org/10.1016/J.MOLCEL.2019.01.035

Um, J.-H., & Yun, J. (2017). Emerging role of mitophagy in human diseases and physiology. *BMB Reports*, *50*(6), 299–307. https://doi.org/10.5483/BMBRep.2017.50.6.056

Valverde, D. P., Yu, S., Boggavarapu, V., Kumar, N., Lees, J. A., Walz, T., Reinisch, K. M., & Melia, T. J. (2019). ATG2 transports lipids to promote autophagosome biogenesis. *The Journal of Cell Biology*, *218*(6), 1787–1798. https://doi.org/10.1083/JCB.201811139

Van Meer, G., Voelker, D. R., & Feigenson, G. W. (2008). Membrane lipids: where they are and how they behave. *Nature Reviews Molecular Cell Biology*, *9*(2), 112–124. https://doi.org/10.1038/nrm2330

Vidal, R. L., Matus, S., Bargsted, L., & Hetz, C. (2014). Targeting autophagy in neurodegenerative diseases. *Trends in Pharmacological Sciences*, *35*(11), 583–591. https://doi.org/10.1016/J.TIPS.2014.09.002

Viguera, A. R., Mencía, M., & Goñi, F. (1993). Time-resolved and equilibrium measurements of the effects of poly(ethylene glycol) on small unilamellar phospholipid vesicles. *Biochemistry*, *32*(14), 3708–3713. https://doi.org/10.1021/BI00065A024

Villa, E., Marchetti, S., & Ricci, J.-E. (2018). No Parkin Zone: Mitophagy without Parkin. *Trends in Cell Biology*, *28*(11), 882–895. https://doi.org/10.1016/j.tcb.2018.07.004

von Muhlinen, N., Akutsu, M., Ravenhill, B. J., Foeglein, Á., Bloor, S., Rutherford, T. J., Freund, S. M. V., Komander, D., & Randow, F. (2012). LC3C, Bound Selectively by a Noncanonical LIR Motif in NDP52, Is Required for Antibacterial Autophagy. *Molecular Cell*, *48*(3), 329–342. https://doi.org/10.1016/j.molcel.2012.08.024

Walczak, M., & Martens, S. (2013). Dissecting the role of the Atg12-Atg5-Atg16 complex during autophagosome formation. *Autophagy*, *9*(3), 424–425. https://doi.org/10.4161/AUTO.22931

Wang, H., Sun, H.-Q., Zhu, X., Zhang, L., Albanesi, J., Levine, B., & Yin, H. (2015). GABARAPs regulate PI4P-dependent autophagosome:lysosome fusion. *Proceedings of the National Academy of Sciences*, *112*(22), 7015–7020. https://doi.org/10.1073/pnas.1507263112

Weidberg, H., Shvets, E., Shpilka, T., Shimron, F., Shinder, V., & Elazar, Z. (2010). LC3 and GATE-16/GABARAP subfamilies are both essential yet act differently in autophagosome biogenesis. *The EMBO Journal*, *29*(11), 1792–1802. https://doi.org/10.1038/EMBOJ.2010.74

Weiergräber, O. H., Mohrlüder, J., & Willbold, D. (2013). Atg8 Family Proteins. Autophagy and Beyond. In *Autophagy - A Double-Edged Sword - Cell Survival or Death?* IntechOpen. https://doi.org/10.5772/55647

Wesch, N., Kirkin, V., & Rogov, V. V. (2020). Atg8-Family Proteins. Structural Features and Molecular Interactions in Autophagy and Beyond. *Cells*, *9*(9), 2008. https://doi.org/10.3390/CELLS9092008

Wild, P., McEwan, D. G., & Dikic, I. (2014). The LC3 interactome at a glance. *Journal of Cell Science*, *127*(Pt 1), 3–9. https://doi.org/10.1242/JCS.140426

Wilson, M. I., Dooley, H. C., & Tooze, S. A. (2014). WIPI2b and Atg16L1: setting the stage for autophagosome formation. *Biochemical Society Transactions*, *42*(5), 1327–1334. https://doi.org/10.1042/BST20140177

Wirawan, E., Berghe, T. Vanden, Lippens, S., Agostinis, P., & Vandenabeele, P. (2011). Autophagy: for better or for worse. *Cell Research 2011 22:1*, *22*(1), 43–61. https://doi.org/10.1038/cr.2011.152

Wu, F., Watanabe, Y., Guo, X. Y., Qi, X., Wang, P., Zhao, H. Y., Wang, Z., Fujioka, Y., Zhang, H., Ren, J. Q., Fang, T. C., Shen, Y. X., Feng, W., Hu, J. J., Noda, N. N., & Zhang, H. (2015). Structural Basis of the Differential Function of the Two C. elegans Atg8 Homologs, LGG-1 and LGG-2, in Autophagy. *Molecular Cell*, *60*(6), 914–929. https://doi.org/10.1016/J.MOLCEL.2015.11.019

Xie, Z., Nair, U., & Klionsky, D. J. (2008). Atg8 controls phagophore expansion during autophagosome formation. *Molecular Biology of the Cell*, *19*(8), 3290–3298. https://doi.org/10.1091/MBC.E07-12-1292

Xin, Y., Yu, L., Chen, Z., Zheng, L., Fu, Q., Jiang, J., Zhang, P., Gong, R., & Zhao, S. (2001). Cloning, expression patterns, and chromosome localization of three human and two mouse homologues of GABA(A) receptor-associated protein. *Genomics*, *74*(3), 408–413. https://doi.org/10.1006/GENO.2001.6555

Xu, Y., Zhang, F., Su, Z., McNew, J. A., & Shin, Y. K. (2005). Hemifusion in SNARE-mediated membrane fusion. *Nature Structural & Molecular Biology*, *12*(5), 417–422. https://doi.org/10.1038/NSMB921

Yamamoto, H., Kakuta, S., Watanabe, T. M., Kitamura, A., Sekito, T., Kondo-Kakuta, C., Ichikawa, R., Kinjo, M., & Ohsumi, Y. (2012). Atg9 vesicles are an important membrane source during early steps of autophagosome formation. *Journal of Cell Biology*, *198*(2), 219–233. https://doi.org/10.1083/JCB.201202061

Yang, D., Zhang, W., Zhang, H., Zhang, F., Chen, L., Ma, L., Larcher, L. M., Chen, S., Liu, N., Zhao, Q., Tran, P. H. L., Chen, C., Veedu, R. N., & Wang, T. (2020). Progress, opportunity, and perspective on exosome isolation - Efforts for efficient exosome-based theranostics. *Theranostics*, *10*(8), 3684–3707. https://doi.org/10.7150/THNO.41580

Yang, & Klionsky. (2010). Eaten alive: a history of macroautophagy. *Nature Cell Biology 2010 12:9*, *12*(9), 814–822. https://doi.org/10.1038/ncb0910-814

Yang, L., Li, P., Fu, S., Calay, E. S., & Hotamisligil, G. S. (2010). Defective Hepatic Autophagy in Obesity Promotes ER Stress and Causes Insulin Resistance. *Cell Metabolism*, *11*(6), 467–478. https://doi.org/10.1016/J.CMET.2010.04.005

Ye, Y., Tyndall, E. R., Bui, V., Tang, Z., Shen, Y., Jiang, X., Flanagan, J. M., Wang, H. G., & Tian, F. (2021). An N-terminal conserved region in human Atg3 couples membrane curvature sensitivity to conjugase activity during autophagy. *Nature Communications*, *12*(1). https://doi.org/10.1038/S41467-020-20607-0

Yu, L., McPhee, C. K., Zheng, L., Mardones, G. A., Rong, Y., Peng, J., Mi, N., Zhao, Y., Liu, Z., Wan, F., Hailey, D. W., Oorschot, V., Klumperman, J., Baehrecke, E. H., & Lenardo, M. J. (2010). Termination of autophagy and reformation of lysosomes regulated by mTOR. *Nature*, *465*(7300), 942–946. https://doi.org/10.1038/nature09076

Yue, Z., Jin, S., Yang, C., Levine, A. J., & Heintz, N. (2003). Beclin 1, an autophagy gene essential for early embryonic development, is a haploinsufficient tumor suppressor. *Proceedings of the National Academy of Sciences of the United States of America*, *100*(25), 15077–15082. https://doi.org/10.1073/PNAS.2436255100

Zhao, H., & Lappalainen, P. (2012). A simple guide to biochemical approaches for analyzing protein-lipid interactions. *Molecular Biology of the Cell*, *23*(15), 2823–2830. https://doi.org/10.1091/MBC.E11-07-0645

Zhen, Y., Spangenberg, H., Munson, M. J., Brech, A., Schink, K. O., Tan, K. W., Sørensen, V., Wenzel, E. M., Radulovic, M., Engedal, N., Simonsen, A., Raiborg, C., & Stenmark, H. (2020). ESCRT-mediated phagophore sealing during mitophagy. *Autophagy*, *16*(5), 826–841. https://doi.org/10.1080/15548627.2019.1639301

Zheng, Y., Qiu, Y., Grace, C. R. R., Liu, X., Klionsky, D. J., & Schulman, B. A. (2019). A switch element in the autophagy E2 Atg3 mediates allosteric regulation across the lipidation cascade. *Nature Communications*, *10*(1). https://doi.org/10.1038/S41467-019-11435-Y

Zhou, F., Wu, Z., Zhao, M., Murtazina, R., Cai, J., Zhang, A., Li, R., Sun, D., Li, W., Zhao, L., Li, Q., Zhu, J., Cong, X., Zhou, Y., Xie, Z., Gyurkovska, V., Li, L., Huang, X., Xue, Y., … Segev, N. (2019). Rab5-dependent autophagosome closure by ESCRT. *Journal of Cell Biology*, *218*(6), 1908–1927. https://doi.org/10.1083/JCB.201811173

PUBLICATIONS

PUBLICATIONS

Iriondo, M. N., Etxaniz, A., Antón, Z., Montes, L. R., & Alonso, A. (2021). Molecular and mesoscopic geometries in autophagosome generation. A review. *Biochimica et Biophysica Acta - Biomembranes*, *1863*.

Iriondo, M. N.*, Etxaniz, A.*, Varela, Y. R., Ballesteros, U., Hervás, J. H., Montes, L. R., Goñi, F. M., & Alonso, A. (2022). LC3 subfamily in cardiolipin-mediated mitophagy: a comparison of the LC3A, LC3B and LC3C homologs. *Autophagy*, 1–19.

In preparation

Iriondo, M. N., Etxaniz, A., Varela, Y. R., Ballesteros, U., Lazaro M., Valle M., Fracchiolla D., Martens S., Montes, L. R., Goñi, F. M., & Alonso, A. Effect of ATG12–ATG5-ATG16L1 autophagy E3 complex on the ability of LC3/GABARAP proteins to induce vesicle tethering and fusion.

Other Publications

Ballesteros, U., Etxaniz, A., Iriondo, M. N., Varela, Y. R., Lázaro, M., Viguera, A. R., Montes, L. R., Valle, M., Goñi, F. M., & Alonso, A. (2022). Autophagy protein LC3C binding to phospholipid and interaction with lipid membranes. *International Journal of Biological Macromolecules*, *212*, 432–441.

Varela, Y. R., Iriondo, M. N., Etxaniz, A., Ballesteros, U., Montes, L. R., Goñi, F. M., & Alonso, A. Ceramide enhances binding of LC3/GABARAP autophagy proteins to cardiolipin-containing membranes (Accepted with minor revision in *International Journal of Biological Macromolecules*)

ACKNOWLEDGEMENTS

ACKNOWLEDGEMENTS

The present PhD Thesis has been performed at the “Instituto Biofisika” (UPV/EHU, CSIC) and the Department of Biochemistry and Molecular Biology, Faculty of Science and Technology, University of the Basque Country (UPV/EHU) under the supervision of Prof. Alicia Alonso Izquierdo and Dr. Lidia Ruth Montes Burgos. The author was recipient of a predoctoral fellowship from UPV/EHU (PIF program year 2016) and a predoctoral FPU fellowship from the Spanish Ministry of Science Innovation and Universities (FPU16/05873). The work was supported in part by the Spanish Ministerio de Ciencia e Innovacion (MCI), Agencia Estatal de Investigacion (AEI) and Fondo Europeo de Desarrollo Regional (FEDER) (grant No. PGC2018-099857- B-I00), by the Basque Government (Eusko Jaurlaritza IT1270-19), by Fundacion Ramón Areces (CIVP20A6619), by Fundacion Biofisica Bizkaia and by the Basque Excellence Research Centre (BERC) program of the Basque Government.

The author is indebted to Prof. Félix Mª Goñi for his valuable assistance throughout the thesis. The author is also grateful to Prof. Sascha Martens and Dr. Dorotea Fracchiolla (Max Perutz Labs, Vienna, Austria) for the opportunity to collaborate through a three months stay and to Isaac Santos, Melisa Lázaro and Dr. Mikel Valle from CIC Biogune for their collaboration in the project. She is also indebted to Dr. Asier Etxaniz, Yaiza Varela, Uxue Ballesteros, Dr. Emilio José González Ramirez, Dr. Javier Hervás, Maider Garnica, Araceli Marcos and Dr. Jesus Sot from the Instituto Biofisika (UPV/EHU, CSIC) for their valuable opinions and discussion throughout the thesis.